# THÈSE

**En vue de l'obtention du**

# DOCTORAT DE L'UNIVERSITÉ DE TOULOUSE

**Délivré par :**

Institut National Polytechnique de Toulouse (INP Toulouse)

**Discipline ou spécialité :**

Energétique et Transferts

---

## Présentée et soutenue par :

M. NAJIB BELGACEM

le jeudi 14 avril 2016

## Titre :

MODELISATION MIXTE CONTINUE - RESEAU DE PORES DES TRANSFERTS DIPHASIQUES CATHODIQUES D'UNE PILE A COMBUSTIBLE PEMFC

---

**Ecole doctorale :**

Mécanique, Energétique, Génie civil, Procédés (MEGeP)

**Unité de recherche :**

Institut de Mécanique des Fluides de Toulouse (I.M.F.T.)

**Directeur(s) de Thèse :**

M. MARC PRAT

**Rapporteurs :**

M. BRUNO AUVITY, POLYTECH NANTES

Mme SOPHIE DIDIERJEAN, UNIVERSITE DE LORRAINE

**Membre(s) du jury :**

M. YANN BULTEL, INP DE GRENOBLE, Président

M. JOEL PAUCHET, CEA GRENOBLE, Membre

M. MARC PRAT, INP TOULOUSE, Membre

# Remerciements

*Mes premiers remerciements sont à Marc Prat mon directeur de thèse qui m'a accordé sa confiance. Ses conseils, son suivi et ses aides sont très précieuses durant toute la thèse.*

*Merci beaucoup Joël pour tous les échanges qu'on a eu durant la thèse. Ton regard critique envers mes résultats m'a bien aidé. Tu as allégé les moments difficiles avec ton sens humain.*

*Dominique grand merci pour tous tes aides, ton soutien et tous les échanges.*

*Samira ne change pas ;), merci pour ton grand humour et tes gâteaux …*

*Merci Beaucoup Pierre-André, Arnaud, Frèd, Tristan, Yohan, Marie, Inès, Marion.*

*Emeline merci pour les cafés tous les matins, les sorties mêmes qu'elles n'étaient pas nombreuses.*

*Je remercie également mes amis qui m'ont bien soutenus: Anis, Meycèn, Mahmoud, Ayoub (Arfaoui et Nouri), Oussama…,un merci spécial à mes amis de Nantes qui ont une place particulière dans mon cœur.*

*Merci Samir et Brahim.*

*Merci mes frères Mohamed, Hedi et Taher.*

*Merci Rim et Ibtissèm.*

*Merci à toutes mes belles sœurs.*

*Je dédie ce travail à mes parent : Mabrouk et Fatma*

# Résumé

Cette thèse présente une contribution à l'étude des transferts d'eau au sein des piles à combustible de type PEMFC, un aspect clé de cette technologie. Une approche de simulation numérique est développée en couplant un modèle de type réseau de pores dans la couche de diffusion (DM), une approche mixte continue –réseau de pore dans la couche microporeuse (MPL) et une modélisation par compartiments dans la couche active. L'approche développée prend en compte les transferts couplés de chaleur et d'eau via notamment la modélisation des phénomènes de changement de phase dans la DM et la MPL (évaporation et condensation). Dans une première partie, nous étudions le cas où l'eau migre dans l'assemblage MPL-DM directement en phase liquide. L'impact de la variation de pression dans la phase gazeuse sur la distribution de la phase liquide est étudié. L'épaisseur optimale de la MPL est également étudiée. Dans une seconde partie, nous étudions des situations où l'eau se forme par condensation dans la couche de diffusion. Nous étudions tout d'abord l'impact des propriétés de la couche de diffusion et de la MPL sur le diagramme de condensation. Ensuite nous analysons l'impact de la formation de l'eau liquide sur la distribution de courant locale. Enfin, l'impact de la mouillabilité sur les figures de condensation est étudié. Cette dernière étude est vue comme un premier pas vers l'étude des mécanismes de dégradation dans le régime de condensation.

# Contenu

**Partie I** : *Scénario injection*

**Chapitre 1** : *Influence of transverse gas pressure gradient on liquid water invasion in GDL*

**Chapitre 2** : *Liquid invasion from multiple inlet sources and optimal gas access in a two-layer thin porous medium*

**Partie II** *Scénario condensation*

**Chapitre 3** *Modeling*

**Chapitre 4** : *Calage et validation des modèles*

**Chapitre 5** : *Gas diffusion layer condensation diagram in proton exchange membrane fuel cells*

**Chapitre 6**: *Impact of liquid water formation on the current local distribution at the cathode gas diffusion layer-catalyst layer interface in proton exchange membrane fuel cells*

**Chapitre 7** : *Impact of the wettability on condensation pattern in the gas diffusion layer*

**Conclusion et perspectives**

# Introduction

Les besoins mondiaux en énergie ne cessent d'augmenter. À ce jour, ces besoins sont couverts principalement par les énergies fossiles. Ces sources d'énergie ne sont pas renouvelables et elles contribuent pour une grande part au problème du réchauffement climatique.

Dans ce contexte, le transport figure parmi les secteurs les plus consommateurs en énergie et beaucoup de travaux sont entrepris pour trouver une alternative aux moteurs thermiques qui soit fiable et économiquement compétitive. Pour ce qui est de l'automobile par exemple, les efforts se concentrent autour de motorisations d'origine électrique. Deux principales technologies sont mis en œuvre : les systèmes utilisant un système de stockage de l'électricité dans des batteries et ceux s'appuyant sur la technologie des piles à combustible (PAC) basse température. Une pile à combustible est un système de conversion de l'énergie chimique en énergie électrique, offrant une bonne solution au problème de stockage de l'énergie. Les PAC sont l'objet d'intenses recherches et développements à travers le monde, notamment en Amérique du nord, au Japon et bien sûr en Europe. Les efforts actuels visent notamment à améliorer les performances, la durée de vie de ces systèmes et en minimiser le cout. Ces efforts visent aussi à étendre l'applicabilité des PAC. Pour ne citer qu'un exemple hors de l'automobile, MyFc est une société d'innovation suédoise qui développe et industrialise des solutions pour alimenter les appareils électroniques portatifs. Un de ces produits le PowerTrekk est un chargeur à pile à combustible à prix abordable (199 €) compatible avec de nombreux objets nomades comme les tablettes, les téléphones portables, les appareils photos, ….

Figure 1 : PowerTrekk : chargeur à pile à combustible

Dans le secteur transport, Toyota a commercialisé très récemment une voiture fonctionnant avec la technologie PAC : la Mirai . Celle-ci est commercialisée depuis décembre 2015 au Japon (avec une commercialisation en France prévue en 2017). Son cout hors taxes est estimé à 66000 € en Allemagne. Son énergie est produite par une pile à combustible à membrane échangeuse de proton (PEMFC pour son acronyme anglais) capable de produire une

puissance maximal de 114kW pour alimenter une moteur électrique de puissance 113 kW (154 ch DIN).

Figure 2 : Toyota Mirai

Elle a une autonomie de 500Km et se ravitaille en 3 minutes comme une voiture à essence. Elle contient notamment deux réservoirs d'hydrogène stockés sous une pression de 700 bars. Pour plus des détails voir le site internet suivant :

http://www.moteurnature.com/actu/2014/toyota-mirai-hydrogene-pile-a-combustible.php

La Mirai est un exemple de voitures fonctionnement purement à l'hydrogène. Il existe aussi des voitures hybrides électrique/hydrogène. Par exemple, l'utilitaire Renaud Kongo ZE H2 est une voiture électrique qui contient une pile à combustible. Celle-ci est utilisée pour recharger la batterie, ce qui permet d'augmenter l'autonomie du véhicule.

Dans ce contexte, cette thèse a pour objet les PEMFC. Elle a été financée par un projet européen from the European Union's Seventh Framework Programme (FP7/ 2007-2013) for the Fuel Cells and Hydrogen Joint Technology Initiative. Il s'agit du projet IMPACT "IMPACT— Improved Lifetime of Automotive Application Fuel Cells with ultra-low Pt-loading" (grant agreement n°303452).

Une PEMFC est un dispositif électrochimique produisant du courant pour une tension donnée. Le schéma d'une cellule élémentaire et de ses principales couches constitutives est présenté sur la Figure 2. Dans les applications, les cellules sont mises en série (pour augmenter la tension) ou en parallèle (pour augmenter la densité de courant) dans un assemblage appelé stack (Fig.3). Chaque cellule est alimentée par un système de canaux en hydrogène (coté anode) et en air (coté cathode). Les réactions chimiques se produisent dans les couches catalytiques (couches actives de la Fig.3). Des couches additionnelles appelées couches de diffusion (GDL ou gas diffusion layers) sont placées entre les couches actives et les plaques portant les canaux d'alimentation en hydrogène et air. Les GDLs ont pour but d'homogénéiser les flux électriques, de chaleur et de masse entre les couches actives et la zone des canaux.

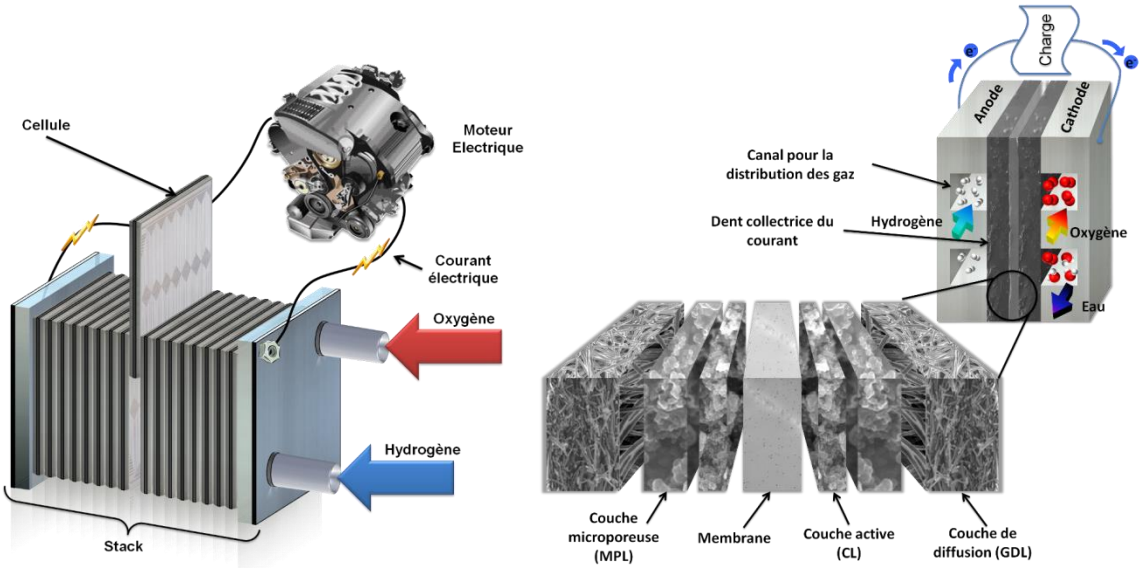


Figure 3 : Cellules assemblées en stack (à gauche). La figure de droite montre les différentes couches constitutives d'une cellule.

Le rôle de la GDL est de garantir le transport des charges (électrons) (par sa structure solide en carbone), le transfert des gaz (dans les pores), et de contrôler l'eau liquide dans le MEA (traitement hydrophobe).
Elle a ainsi un rôle très important sur les performances des PEMFC (Williams et al, 2004; Park et al., 2012). Des expériences montrent que la MPL a un rôle également important sur les performances (Park et al., 2006; Karan et al., 2007).
La GDL est une composante clé pour assurer une bonne gestion de l'eau liquide dans le MEA ((Mathias et al., 2003; Wood, 2006; Wood and Borup, 2010; Li et al., 2008). Elle joue ainsi un rôle crucial sur l'équilibre : maintenir une bonne hydratation d'ionomer (pour avoir une bonne conductivité protonique de la membrane) sans avoir produit beaucoup d'eau liquide qui bloquerait le passage des réactifs vers la CL.
Ainsi, il s'avère très important de mieux comprendre le transport de l'eau liquide dans la GDL, et spécialement de pouvoir analyser plus précisément l'écoulement diphasique et la diffusion des gaz dans la GDL.
La GDL est composé d'un support de diffusion DM (Diffusion Medium) et d'une couche microporeuse MPL( Micro Porous Layer) (figure 4).
Le DM est une structure poreuse constituée de fibres de carbone (8 - 10 µm de diamètre), avec parfois un liant. Un traitement hydrophobe (généralement à base de PTFE) est introduit dans le DM en général par imprégnation.
La MPL est également une structure poreuse, mais à base de noir de carbone (CB) avec un agent hydrophobe (en général également PTFE) qui assure la résistance mécanique. Elle est déposée sur le DM et selon les propriétés du DM (Par exemple sa mouillabilité et sa porosité) et de la MPL (Par exemple sa viscosité), la MPL peut pénétrer ou non à l'intérieur du DM (pas de pénétration de la MPL sur la figure 4). La MPL peut aussi avoir des fissures sur sa surface (figure 5).

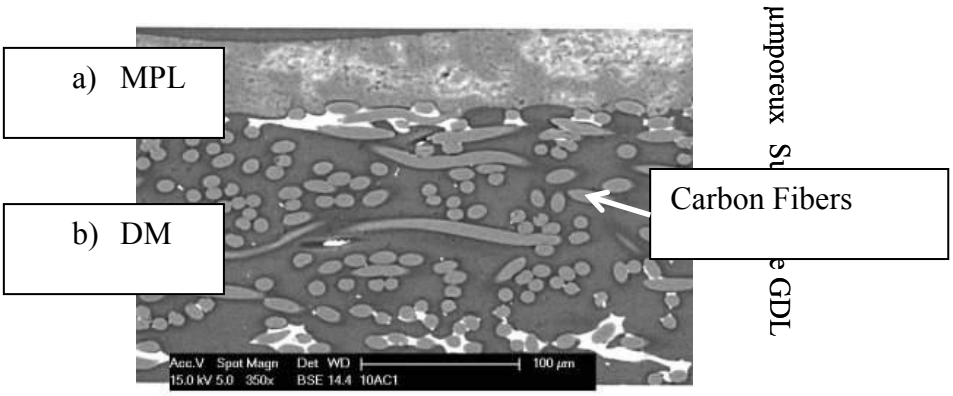


Figure 4 : image SEM d'une GDL avec la MPL a) et le DM (b) (image du CEA); Les fibres de carbone sont en gris

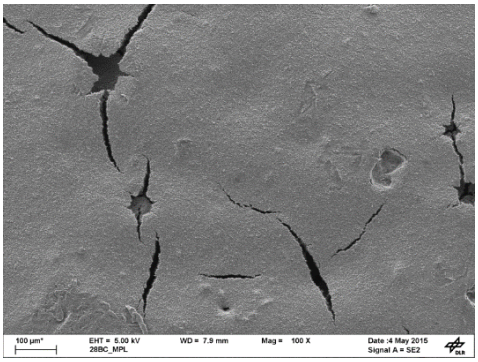

Figure 5: Vue de la surface d'une MPL avec quelques fissures

**Gestion de l'eau, transfert de chaleur, durabilité**

Les problèmes de durabilité constituent sans doute le principal frein à la commercialisation massive de la technologie PEMFC. A titre indicatif, une pile a typiquement une longévité de quelques milliers d'heures si bien qu'il n'est pas possible d'espérer effectuer plus de 100 000 km dans le cas de l'application automobile. C'est particulier gênant lorsqu'il s'agit de l'élément le plus coûteux de la voiture. Ces problèmes de dégradation sont en réalité intiment liés à deux autres aspects clé de cette technologie, la gestion de l'eau et les transferts de chaleur au sein de la pile, que ce soit à l'échelle d'une cellule unique de laboratoire ou à l'échelle d'un stack. La gestion de l'eau est classiquement présentée comme le problème d'assurer une humidification correcte de la membrane (afin d'assurer un bon transport des protons H+ à travers cette membrane) tout en évitant de noyer des GDLs ce qui a pour conséquence de limiter sévèrement l'accès des gaz aux couches actives. Le problème de la gestion de l'eau ne peut en fait être découplé de celui des transferts de chaleur en raison de l'importance des phénomènes de changement de phase liquide-vapeur au sein de la pile. Les transferts de chaleur et notamment les hétérogénéités spatiales de température jouent un rôle clé dans les mécanismes de dégradation, e.g. Nandjou (2015), Abbou (2015) si bien qu'en réalité c'est pour une large part une meilleure compréhension du triptyque transfert d'eau, transfert thermique, dégradation qui doit être développée pour améliorer la technologie PEMFC.

Dans ce contexte et compte tenu du grand nombre de travaux dédiés ces vingt dernières années aux PEMFC, on peut s'étonner que les mécanismes contrôlant les transferts de l'eau au sein d'une cellule, ne soient pas complétement élucidés. Il s'agit là d'un point crucial si l'on veut espérer une stratégie de développement organisée qui aille au-delà des stratégies expérimentales courantes par essais – erreurs dont le défaut essentiel est que très souvent, on se retrouve en incapacité d'expliquer les résultats obtenus faute d'une compréhension suffisante de ce qui se passe au sein de la pile.
Comme noter dans Straubhaar (2015), même le cas des GDL, a priori plus simple compte tenu notamment du fait que les GDLs ne sont pas le siège des réactions électrochimiques et qu'au moins le medium de diffusion (DM) peut être imagé par tomographie X ou par absorption de neutrons, reste un sujet d'études.
Si par exemple, on se limite comme dans Straubhaar (2015) aux études s'appuyant sur des modèles de réseaux de pores (pore network models (PNM)), techniques de modélisation que nous utilisons également dans ce travail, on peut faire le constat suivant. Pratiquement toutes les études avant le travail de Straubhaar (2015), sont basées sur le scenario, défini comme le scénario #1, où l'eau entre en phase liquide dans le GDL depuis la couche active voisine (ce scenario est illustré sur la Fig. 6a)

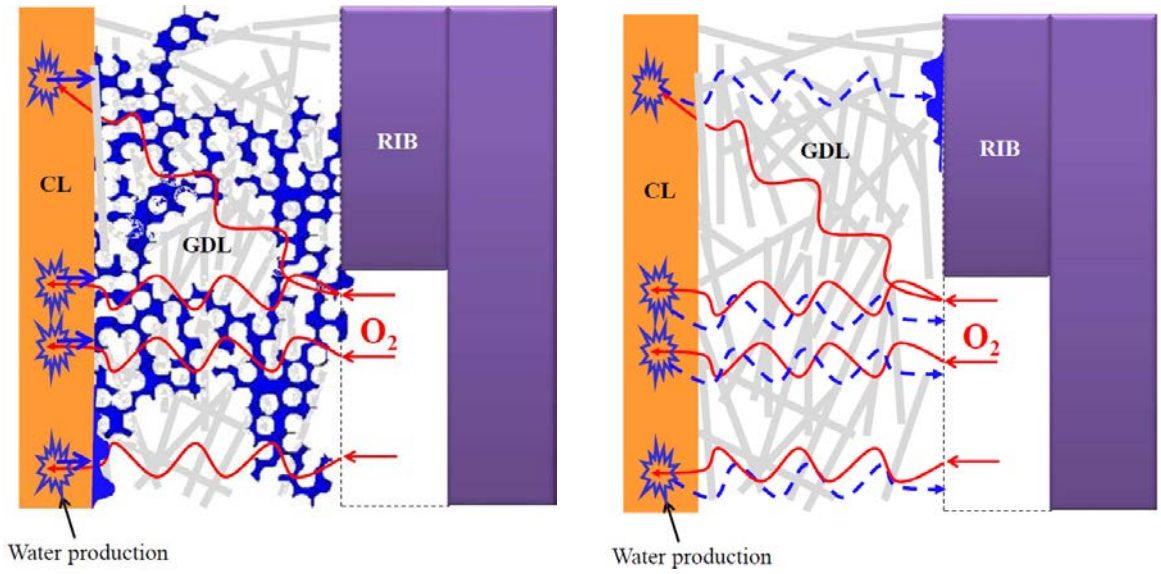


a) b)

Figure 6: Schémas illustratifs des deux situations de base en ce qui concerne la phase, liquid ou vapeur, sous laquelle l'eau entre dans la GDL depuis la couche active (CL) : a) scenario #1, eau entrant sous forme liquide (en bleu), (b) scenario #2; eau entrant dans la GDL sous forme vapeur (lignes pointillées bleues), (tiré de Straubhaar et al. 2016).

A la différence de tous ces travaux, voir Straubhaar et al. (2016) pour une revue bibliographique, le scenario privilégié dans la thèse de Straubhaar (2015), dit scenario #2 sur la Fig.6b, est un scénario selon lequel l'eau entre dans la GDL sous forme vapeur à l'interface CL – GDL. Selon ce scenario, l'eau liquide peut se former dans la GDL (et en particulier dans le DM) si l'humidité relative dans le canal et la densité de courant sont suffisamment fortes

par condensation. A la différence du scenario #1, ce scenario est intimement lié aux transferts thermiques car la condensation est d'autant plus probable que la variation de température est notable à travers la GDL.
Comme montré dans Straubhaar (2015), les simulations réseau de pores du scenario de condensation sont en accord qualitatif avec plusieurs mesures expérimentales et observations in situ, du moins pour une température de fonctionnement classique proche de 80°C.
La présente thèse s'est déroulée en même temps que ce changement de paradigme, i.e. du scénario #1 au scénario #2. Ceci explique que nous avons travaillé à la fois selon les hypothèses du scenario #1 (première partie de la thèse) et du scenario #2 (seconde partie de la thèse) quand il est devenu clair que le scénario de condensation paraissait la façon la plus appropriée de comprendre la formation de l'eau dans la GDL.
Même si il n'y a plus beaucoup de doutes quant à la pertinence du scénario de condensation aux températures assez élevées (i.e. 80°C), il est à noter cependant que la situation n'est pas encore clarifiée aux températures « froides ». Il n'est donc pas du tout à exclure que le scenario # 1 (injection liquide) mérite toujours considération, ne serait-ce que pour les températures froides par exemple.
Dans ce contexte, la thèse est ainsi organisée en deux grandes parties. La première est basée sur le scenario #1. On y discute deux points. Le premier (Chap.1) est dédié à une étude courte sur le possible impact de l'écoulement de la phase gazeuse au sein du DM sur les figures d'invasion. Le second (Chap. 2) est une étude sur le rôle de la MPL sur l'accès de l'oxygène vers la couche active dans le cadre du scenario #1. Ce chapitre correspond à l'article Belgacem et al. (2016).
La deuxième partie est formée de 5 chapitres (Chap. 3-7) est basée sur le scénario de condensation. On présente tout d'abord un modèle couplant les transferts entre la membrane la couche active et la GDL (MPL + DM). Ce modèle a comme originalité de s'appuyer sur une modélisation réseau de pores pour ce qui concerne le DM. Le Chapitre 4 décrit comment les paramètres du modèle du chapitre 3 ont été spécifiés. Les trois chapitres qui suivent sont dédiés à l'exploitation de ce modèle. Le chapitre 5 étudie l'impact de différents paramètres sur le diagramme de condensation (le diagramme de condensation donne en fonction de l'humidité relative dans le canal la densité de courant critique à partir de laquelle l'eau se forme par condensation dans le DM). Le chapitre 6 s'intéresse à l'impact de la formation de l'eau liquide sur la distribution de densité de courant à l'interface couche active – GDL. Le Chapitre 6 donne un aperçu sur l'impact des conditions de mouillabilité sur les distributions de phase liquide et gaz dans le DM lors de la condensation.
Pour tous ces chapitres, on se place à l'échelle dent canal.

Enfin, il est à noter qu'il est souvent question de dégradation dans le modèle du chapitre 2. La simulation de mécanismes de dégradation fait partie des objectifs majeurs du projet européen « Impact » qui a financé cette thèse. Ces simulations sont renvoyées à l'après thèse car il n'a pas été possible d'avancer suffisamment sur cette partie dans le cadre de la thèse.

**Références**

S.Abbou, Phénomènes locaux instationnaires dans les piles à combustible à membrane (PEMFC) fonctionnant en mode bouché (dead-end), Thèse Université de Lorraine, (2015).

N.Belgacem, T.Agaësse, J. Pauchet, M. Prat, Liquid invasion from multiple inlet sources and optimal gas access in a two-layer thin porous medium, Transport in Porous Media, DOI 10.1007/s11242-016-0630-1 (2016)

F.Nandjou, Local study of temperature distribution in P.E.M fuel cells for automotive applications. Correlation between local temperature and degradations, Ph.D thesis, Grenoble Alpes University, (2015).

B.Straubhaar, Pore network modelling of condensation in gas diffusion layers of PEMFC, Ph.D thesis, Toulouse University (2015)

Straubhaar B., J.Pauchet, M. Prat, Pore network modelling of condensation in gas diffusion layers of proton exchange membrane fuel cells, submitted (2016

# *Partie I: Scénario injection*

Chapter 1

# Influence of transverse gas pressure gradient on liquid water invasion in GDL

**Abstract**

In this chapter, we study from pore network simulations the possible impact of transverse gas flow within the diffusion medium (DM) of the GDL at the rib –channel scale on liquid water invasion patterns and oxygen access to the catalyst layer (CL). The study is performed considering scenario #1, that is assuming liquid water enters the DM in liquid phase from the adjacent CL or MPL.

## 1. Introduction

In this chapter, only the diffusion medium on the cathode side is considered assuming that water enters the DM in liquid phase from the MPL / CL area (scenario #1). We implicitly refer to the serpentine channel configuration on the bipolar plate. Because of the gas pressure drop within the serpentine channel, a total pressure difference exists between two close meanders of the serpentine channel. This induces a gas flow within the DM below the rib from the upstream channel section to the downstream channel section. In this context, the objective is to evaluate the possible impact of the transverse gas flow within the DM on the liquid invasion patterns within the DM. The work is based on pore network (PN) simulations developed in 2D and 3D domains. It must be pointed out that the impact of the transverse gas flow on liquid invasion patterns has not been addressed in the literature, at least the one based on PN simulations. A schematic of the situation investigated is shown in Fig.1.

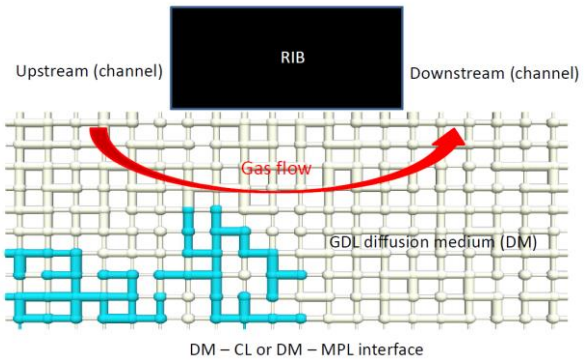


Figure 1 Schematic of the gas transverse flow between serpentine channel upstream section and downstream section on each side of the rib.

## 2. Pore network model

The computational domain contains between one to three unit cells (a unit cell at the rib – channel scale typically corresponds to a rib and two half channel sections, or to two half rib and one channel). Examples of unit cell used in the present chapter are depicted in Fig.2 (2D) and Fig.3 (3D).

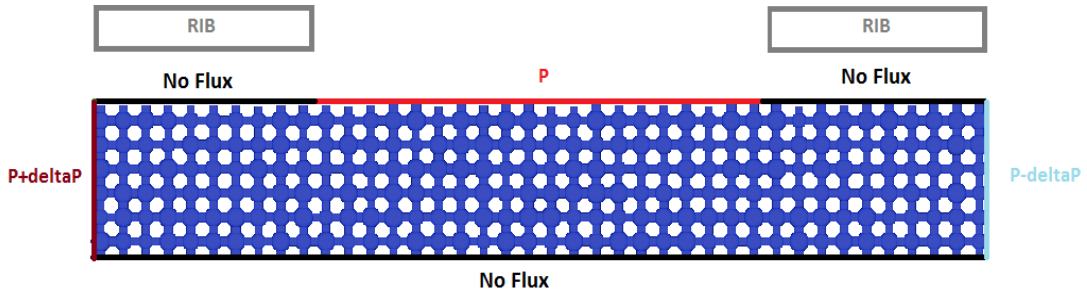


Figure 2: 2D unit cell with gas pressure boundary conditions.

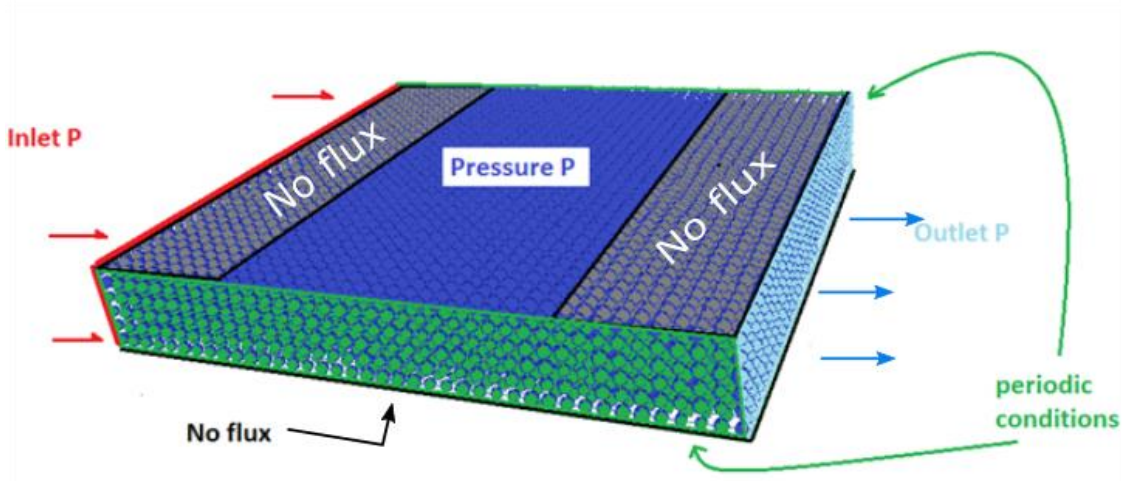


Figure 3: 3D unit cell with gas pressure boundary conditions

As in several previous works, e.g. Rebai et al. (2009), Ceballos et al. (2011), (2013), the DM is represented as a square network (2D) or a cubic network (3D) of pores interconnected by narrower channels (as illustrated in Fig.4). The distance between two pores (two neighbour intersections in the network) is referred to as the lattice spacing. The lattice spacing is denoted by $a$. As in Rebai et al. (2009), we took $a \approx 50\mu m$. The size of the computational domain in

the in-plane directions in Figs.2 and 3 is $L=2mm$ (this corresponds to the size of the rib plus twice the half channel width).

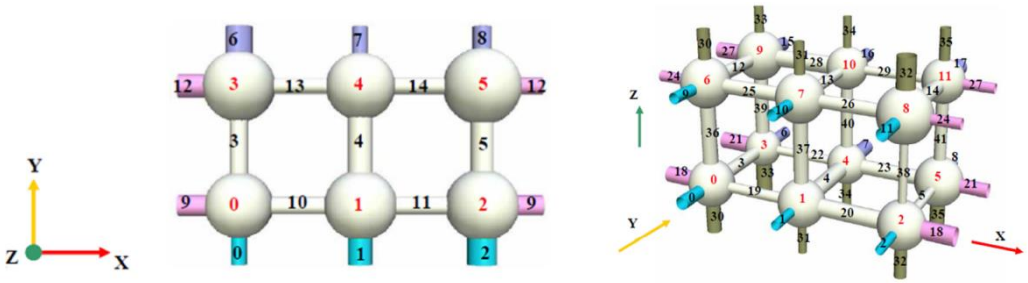


Figure 4: 2D square network (left) and 3D cubic network (right).

Expressed in lattice spacing units, the network size is therefore *40xl* in 2D and *40 x 40 x l* in 3D where *l* refer to the DM thickness.The DM thickness is typically in the range *[170 – 400] µm*. This amounts to considering networks of size *40 x N* with *N* in the range [4, 8] in 2D (networks of size *40 x 40 x N* in 3D). Therefore, there are 40 pores along an in-plane direction and between 4 to 8 pores in the through-plane direction. The narrower channels between two pores are referred to as throats or bonds. Their sizes, denoted by $d_t$, are randomly distributed over the network according to a given probability density function (p.d.f.) within the range $[d_{tmin}, d_{tmax}]$ with $d_{t\min}$ =20 µm, $d_{t\max}$ =34µm.

## 3. Gas pressure computation

Compared to previous works considering scenario #1, e.g. Rebai et al. (2009), Ceballos et al. (2011), (2013), the main new feature here lies in the fact that the total gas pressure varies within the DM. The method to compute the pressure field in the gas phase within the pores occupied by the gas phase in the network is somewhat classical, e.g. Gostick et al. (2007).

The flow rate $q_{ij}$ between two adjacent gas pores *i* and *j* is expressed using a Poiseuille like expression as

$$q_{ij} = g_{h,ij}(P_j - P_i) \qquad (1)$$

where $g_{h,ij}$ is the hydraulic conductance of the throat between pore $i$ and pore $j$, $g_{h,ij} = \frac{d_t^4}{128\,\mu a}$ where $\mu$ is the gas viscosity. Then we express the volume conservation at each pore of network (note that the variation of gas density with the pressure is neglected),

$$\sum_{j}^{n} g_{h,ij}(P_j - P_i) = 0 \qquad (2)$$

Solving numerically Eq.(2) with appropriate boundary conditions yields the gas pressure in each pore occupied by the gas phase pore within the DM.

The pressure boundary conditions are presented in Fig.2 (2D) and Fig.3 (3D). As can be seen, we impose different pressure values on the lateral surfaces of network and at the channel / DM surface. The idea is to take into account the transverse pressure difference resulting from the pressure drop within the serpentine channel. Assuming that the channel upstream is on the left and the channel downstream on the right in Figs. 2 and 3, the highest pressure value P+ΔP is imposed on the left lateral edge (2D) or surface (3D) of network whereas a lower pressure P-ΔP is imposed along the boundary on the right. The pressure $P$ is imposed at the DM - channel interface. This procedure is straightforwardly extended when more than one unit cell is considered as illustrated in Fig. 5.

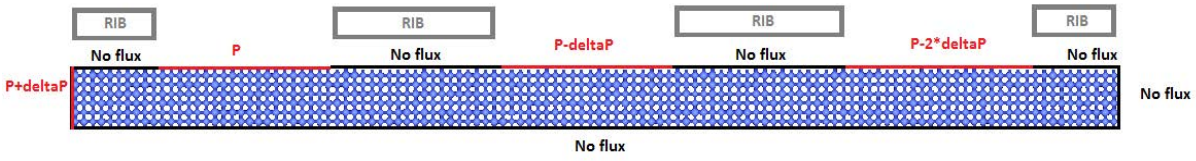


Figure 5: Gas pressure boundary conditions in a three cells network.

## 4. Liquid water invasion PN algorithm in the presence of a non-uniform gas pressure

According to scenario #1, water is supposed to enter the DM in liquid phase from the DM / MPL or DM / CL interface. The DM is supposed to be perfectly hydrophobic ($\theta \sim 110$ °) and it is widely admitted that the invasion is essentially by capillary forces, i.e. viscous forces can be neglected in the liquid phase, see Rebai et al. (2009) for more details. Under these circumstances, the liquid invasion can be simulated using the classical invasion percolation

algorithm, e.g. Wilkinson and Willemsen (1983). An invasion capillary pressure threshold is assigned to each throat as (Laplace's law),

$$p_{\text{cth}} = \frac{4\gamma \cos\theta_g}{d_t} \qquad (3)$$

with $\theta_g = 180° - \theta$ ($\theta_g$ is the contact angle measured in the gas phase); γ is the surface tension. Then, the IP algorithm simply consists in invading the network each throat at a time (together with the throat adjacent pore not yet filled with liquid) selecting at each step the throat located on the liquid-gas interface of lowest invasion capillary threshold. This is when the total gas pressure is uniform. When the gas pressure $P$ is not uniform the liquid pressure $P_l$ necessary to invade a throat is given by the equation

$$p_{\text{cth}} = \frac{4\gamma \cos\theta_g}{d_t} = P(x,y,z) - P_l(x,y,z) \qquad (4)$$

From Eq.(4), we thus define a throat invasion potential as

$$\varphi_{th} = P(x,y,z) - p_{cth} \qquad (5)$$

The algorithm then simply consists in selecting at each step the throat of greatest potential. Naturally, the classical IP invasion rule is recovered when the gas pressure is uniform. Thus here the invasion threshold depends not only on the throat size but also on the gas pressure.

The invasion is performed until breakthrough, that is until the liquid phase reaches the channel.

A last point concerns the injection boundary condition at the DM – CL or DM – MPL interface. As pointed out in Ceballos and Prat (2010), the classical boundary condition used in IP simulation is to assume that the pressure in the liquid along this interface is uniform. It was argued in Ceballos and Prat (2010) that such a boundary condition is not adapted to GDL on the grounds that the water is produced through a series of discrete sites in the CL. This led to propose a different boundary condition referred to as a multiple injection boundary condition. With this boundary conditions, a fraction of the injection throats present at the DM inlet (=DM – CL or DM – MPL interface) are considered as injection throats. In what follows we have used a variant of the multiple injection BC combined with the IP invasion rule

computed from the potential given by Eq.(50). The procedure was as follows. A number $n_i$ of injection throats at the DM inlet is chosen randomly (between 1 and 40 in 2D and 1 and 40x40 in 3D). Then the IP invasion rule was applied starting with the selected $n_i$ injection throats.

## Estimate of gas pressure difference across the unit cell

Wang et al. (2010) presented a series of experimental and numerical studies analyzing velocity and pressure drop within the channel of the bipolar plate. These results are summarized in Table 1.

The cells referred to as 12-11 corresponds to a channel width equal to 1mm, see Wang et al. (2011).The total pressure drop over the plate is 1375 Pa, which corresponds to a pressure drop $\Delta P$ = 125 Pa between the two sides of a rib. This pressure variation can be compared to the range of invasion capillary pressure thresholds (Eq.(3)): $\delta p_{\text{cth}} = \frac{4\gamma\cos\theta_g}{d_{t\min}} - \frac{4\gamma\cos\theta_g}{d_{t\max}} =$ 1688 Pa. Thus, $\Delta P / \delta p_{\text{cth}} \sim 7\%$ which shows that the impact of gas pressure variation is not negligible (in fact the impact is expected to be greater than estimated here because the range of throats typically selected in the invasion percolation process is narrower than considered here; the narrower throats are actually not invaded).

Note that the gas pressure field is recomputed after each invasion (with no flow rate boundary condition on the liquid throats in contact with the gas phase). Thus the pressure drop increases locally within the network as the network is invaded by the liquid phase. The variations of temperature with the DM are neglected.

Calculated pressure drops at the operating voltage of 0.3 V.

| Cells | $\Delta p$ (Pa) | $W_{\text{cell}}$ (W/m$^2$) | $W_p$ (W/m$^2$) | $W_{net}$ (W/m$^2$) |
|---|---|---|---|---|
| 8–7 | 323 | 24638.69 | 6.11 | 24632.58 |
| 10–9 | 817 | 27886.83 | 15.44 | 27871.39 |
| 12–11 | 1375 | 28976.71 | 25.99 | 28950.72 |
| 16–15 | 2370 | 29900.32 | 44.79 | 29855.53 |
| 22–21 | 4100 | 30364.95 | 77.51 | 30287.44 |
| 38–37 | 17200 | 30524.82 | 325.14 | 30199.68 |

Table 1: pressure drop along bipolar plates

# Simulations

## 1.1.Gas pressure field structure

6 Fig. 6 shows the structure of the pressure field in a dry DM. As can be seen the pressure gradients are concentrated below the ribs.

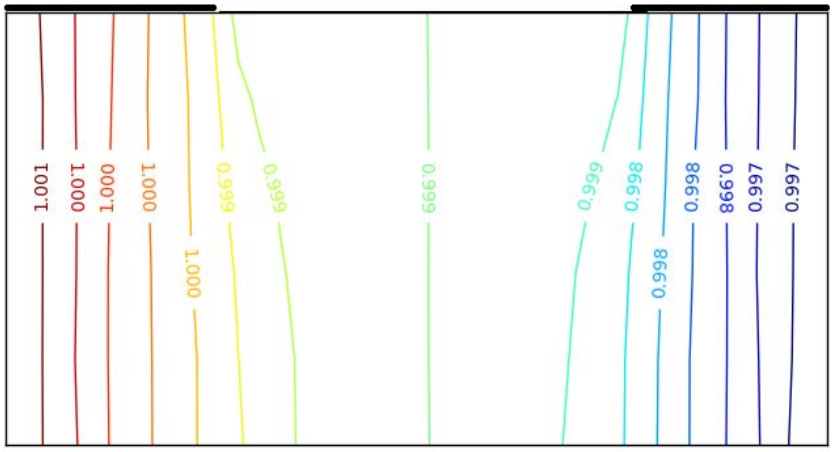


Figure 6: Gas pressure field structure in a dry DM in a transverse cross sect of the unit cell. The gas pressure was made dimensionless using the pressure at the channel – DM surface.

Since the gas pressure is greater below the upstream rib and lower below the downstream rib, it is expected from Eq.(5) that the liquid invasion will be easier in the region of the downstream rib where the gas pressure is lower.

## 1.2. Liquid water invasion patterns

Fig. 7 and Fig.8 show examples of liquid invasion patterns in 2D and 3D unit cell respectively, when the transverse gas pressure difference is varied.

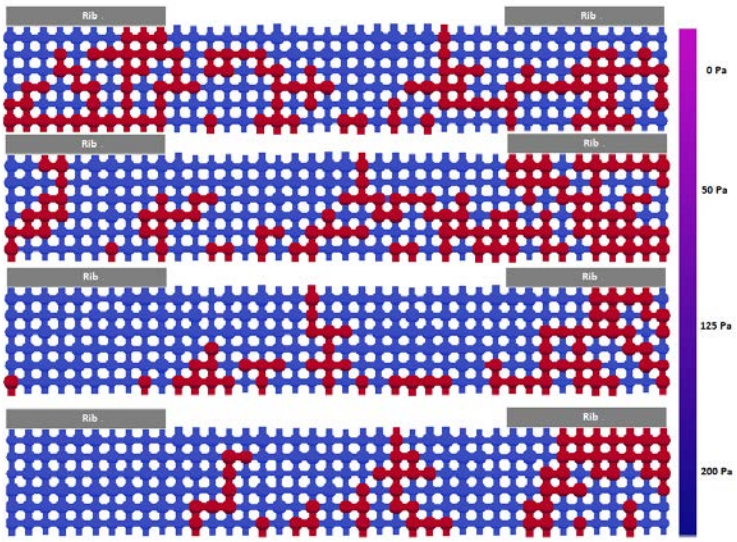


Figure 7: Liquid water (in red) invasion patterns for various transverse gas pressure differences in 2D network.

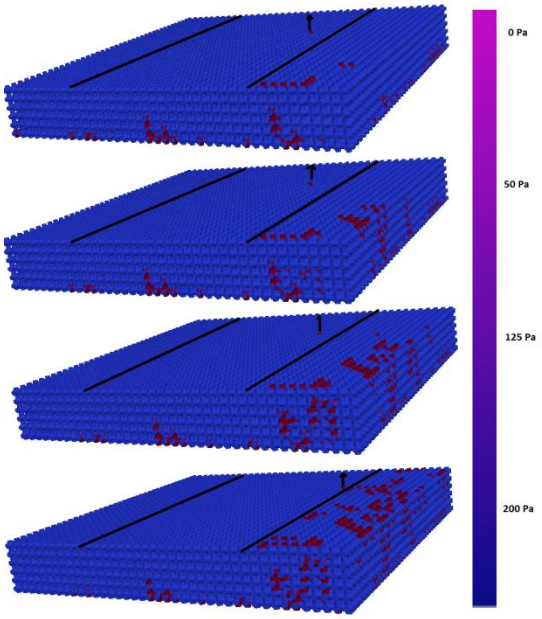


Figure 8: Liquid water (in red) invasion patterns for various transverse gas pressure differences in 3D network.

These figures illustrate the impact of the transverse gas pressure variations on the pattern with as expected a preferential invasion of the region below the downstream rib when the transverse gas pressure variation is sufficiently high.

Fig. 9 shows similar results for the 2D computational domain with three unit cells (note that a no gas flow boundary condition is imposed on the right lateral edge of network in this case (this would corresponds to a series of three unit cells with the one the most on the right corresponding to the channel exit).

The displacement of the liquid patterns toward the downstream region is still more marked.

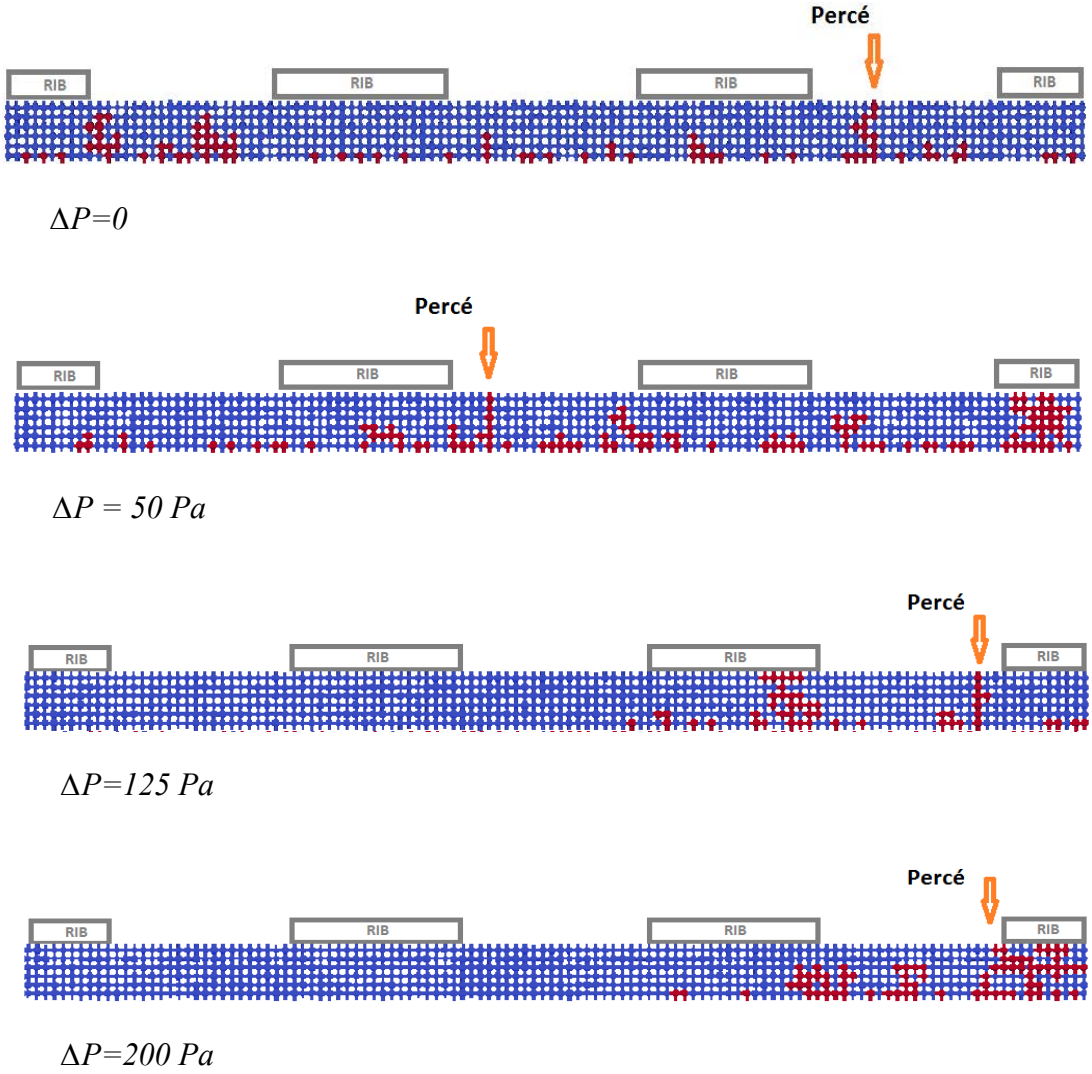


Figure 9: Liquid water (in red) invasion patterns for various transverse gas pressure differences in 2D three unit cells network.

## Influence of transverse gas pressure gradient on saturation

7. The saturation is defined as the volume fraction of the pore space occupied by liquid water. The saturation was computed at the end of invasion. The saturation was actually computed in the three cells depicted in Fig.10 for various transverse gas pressure differences. The results are summarized in Tables 2 and 3. Note that the results presented in Tables 2 and 3 are mean values over 10 realizations of network.

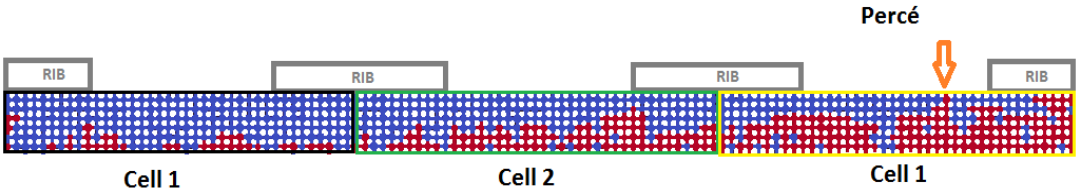


Figure 10: The 3 cells considered for the computation of the saturation.

| **ΔP(Pa)** | 0 | 50 | 125 | 200 |
|---|---|---|---|---|
| **Cell 1** | 0.16 | 0.05 | 0.001 | 0 |
| **Cell 2** | 0.15 | 0.13 | 0.03 | 0.01 |
| **Cell 3** | 0.156 | 0.29 | 0.29 | 0.2 |

Table 2: Mean saturation (over 10 network realizations) in the 3 cells in 2D network as a function of transverse gas pressure difference. Note that the indicated pressure difference corresponds to the pressure variation over one cell (the total pressure difference over the three cells is therefore three times this value).

| ΔP(Pa) | 0 | 50 | 125 | 200 |
|---|---|---|---|---|
| **Cell 1** | 0.042 | 0.005 | 0 | 0 |
| **Cell 2** | 0.041 | 0.02 | 0.003 | 0.0002 |
| **Cell 3** | 0.04 | 0.04 | 0.032 | 0.04 |

Table 3: Mean saturation (over 10 network realizations) in the 3 cells in 3D network as a function of transverse gas pressure difference. Note that the indicated pressure difference corresponds to the pressure variation over one cell (the total pressure difference over the three cells is therefore three times this value).

Figure 11 shows the through plane mean saturation profiles. It can be seen that the transverse pressure difference has relatively little impact on the saturation in the two rows of pores located next to the CL. This can be understood since the transverse gas pressure difference actually increases locally as the liquid pattern develops since less and less space is available for the gas flow. The impact is quite significant when the liquid approaches breakthrough.

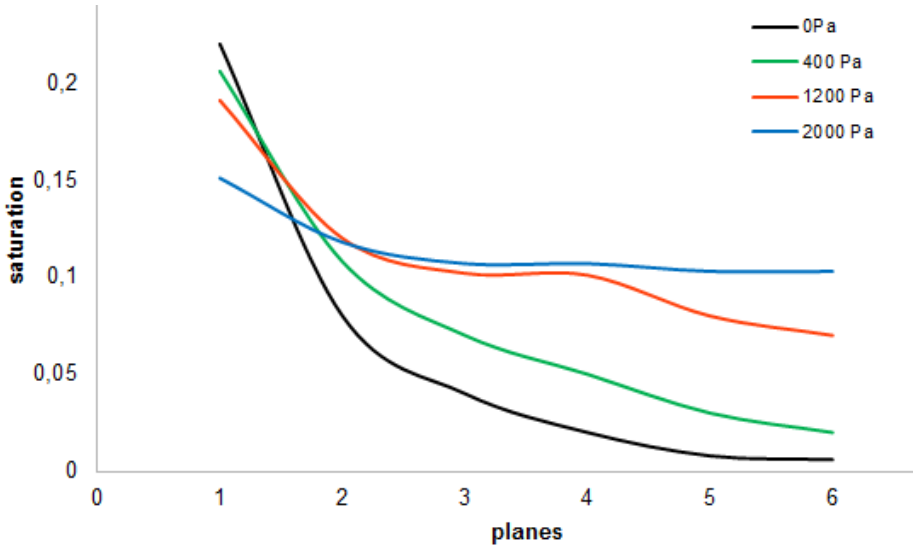


Figure 11: Influence of transverse gas pressure difference on through-plane saturation profiles (3D one cell network). The saturation is a mean saturation over 10 realizations of network. The channel – rib – DM interface is on the right, the CL on the left.

# Influence of transverse gas pressure gradient on effective diffusion coefficient

## 8.

### 1.3. Computational method

The effective diffusion coefficient of the DM is computed considering only the diffusion as transport mechanism of the gas components. This is justified by the fact that the Peclet number is smaller than 1. In other terms, the gas flow can have an impact on the liquid invasion pattern but the convective transport of the gas species transport can be neglected.

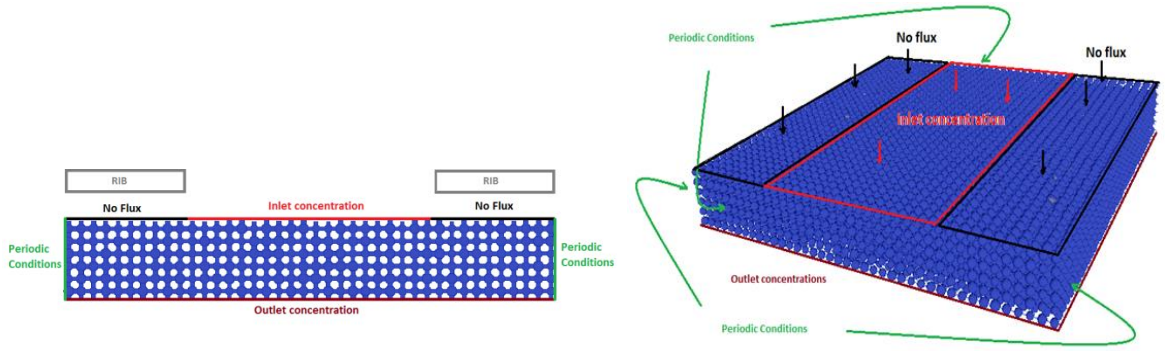


**1 cell networks**

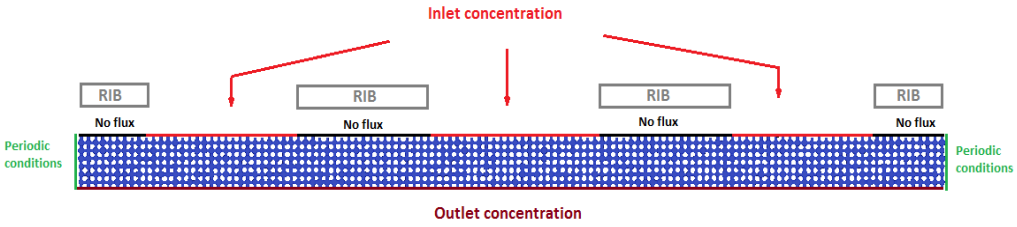


**3 cells network**

Figure 12: Boundary conditions for the computation of the diffusive transport in gas phase.

The PN computation of the effective diffusion coefficient is described in Gostick et al. (2007). The procedure is analogous to the one used for the computation of the gas pressure field. The diffusive flow rate $n_{ij}$ of species $A$ in stagnant species $B$ between two adjacent gas pores $i$ and $j$ is expressed as

$$n_{ijA} = g_{d,ij}(\ln x_{Bj} - \ln x_{Bi}) \quad (6)$$

where $x_{B,j}$ is species $B$ molar fraction in pore $j$, and $x_{B,i}$ is species $B$ molar fraction in pore $i$. $g_d$ is the diffusive conductance between the two pores. $g_d$ is expressed for a tube of length $l$ and diameter $d$ as

$$g_{d,ij} = \frac{cD_{AB}d^2}{l} \quad (7)$$

where $c$ is the molar density of the mixture and $D_{AB}$ is the binary diffusion coefficient. The diffusive conductance between the two pores is computed as the harmonic average of the conductance of the throat between the two pores and the conductances of half pore $i$ and half pore $j$,

$$\frac{1}{g_{d,ij}} = \frac{1}{g_{d,pi}} + \frac{1}{g_{d,t}} + \frac{1}{g_{p,j}} \quad (8)$$

The next step is to express the mass conservation in each gas pore of network as

$$\sum_{j}^{n} g_{d,ij}(\ln x_{Bj} - \ln x_{Bi}) = 0 \quad (9)$$

which leads to a linear system which can be solved with appropriate boundary conditions to obtain the molar fraction of species $B$ in each pore. There is no transport in the pores occupied by liquid.

The boundary conditions are summarized in Fig.12 for the various computational domains.

Figure 13 below shows two examples of molar fraction fields so obtained in the pore network.

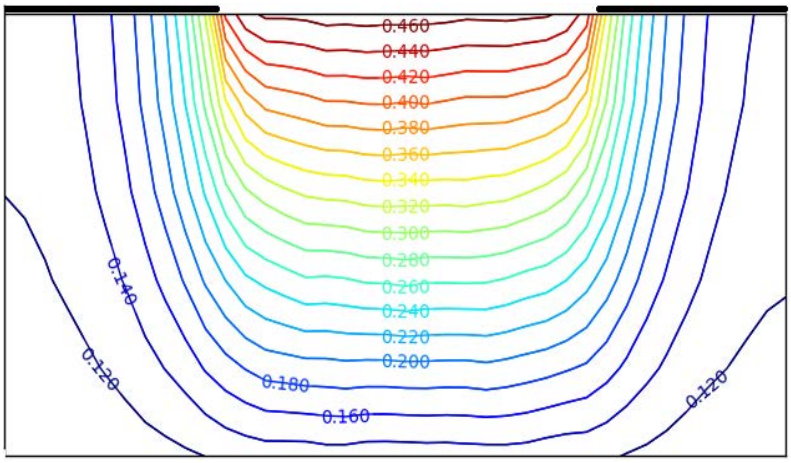


**one cell 2D network**

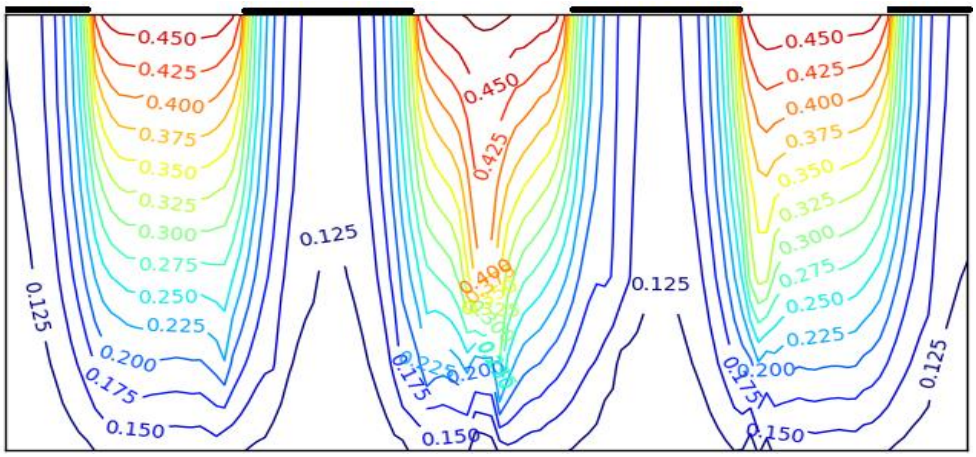


**three cells 2D Network**

Figure 13: Examples of A species molar fraction isocontour lines in 1 cell and 3 cells 2D network.

Once the molar fraction is computed, it is easy to determine the diffusive flow rate $N_A$ of species $A$ in the through plane direction (we simply sum up the diffusive flow rate in every throat located in a plane perpendicular to the through plane direction). We then express that this diffusive flow rate in the through plane direction must be equal to the macroscopic expression of the diffusive flow rate using Fick's law,

$$N_A = \frac{cD_{eff}A_n}{h}(\ln x_{Bj} - \ln x_{Bi}) \qquad (10)$$

where $x_{B,in}$ and $x_{B,out}$ are the inlet and outlet mole fractions of stagnant species B, $h$ is the thickness of the DM and $A_n$ is the cross-section area of the network in the in plane directions ($A_n$= *(40-1)x(40-1)$a^2$* in the 40 *x* 40 *x l* network). This enables one to determine the effective through plane diffusive coefficient $D_{eff}$ from Eq.(10).

## 1.4. Impact of *ΔP* on effective through plane diffusion coefficient

To show the effect of transverse pressure gradient on effective diffusion coefficient in one cell network, we proceed as follows:

- a transverse pressure difference is imposed.
- Molar fraction boundary conditions are imposed (as depicted in Fig.12).
- Start liquid invasion and at every step of invasion compute overall saturation and effective diffusion coefficient.

Figure 14 shows the variation of the effective diffusion coefficient as a function of overall saturation for different values of transverse pressure difference.

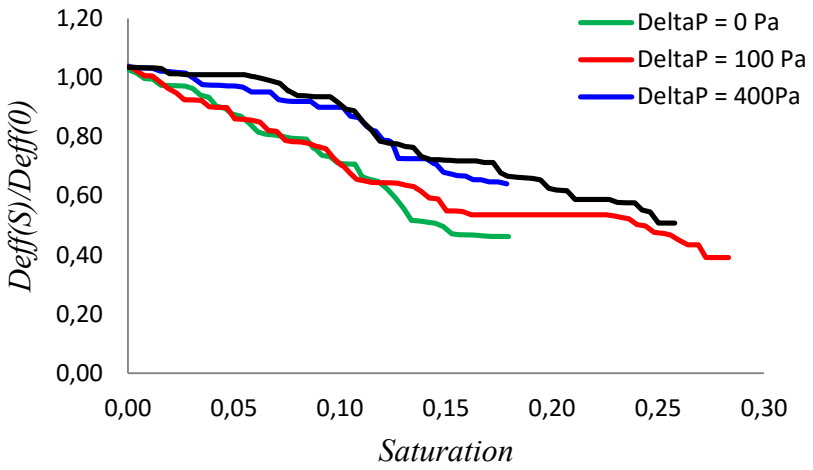


Figure 14: Effective diffusion coefficient as a function of overall saturation for different value of transverse gas pressure difference in a one cell 2D network (results are mean values over 10 realizations of network).

As can be seen the effective diffusion coefficient increases for a given overall saturation with the transverse gas pressure difference $\Delta P$. This is of course in line with the impact of $\Delta P$ on the liquid water invasion patterns (as depicted for example in Fig.7 and Fig.8). The liquid tends to accumulate in the region of lower gas pressure when $\Delta P$ is sufficiently high. This increases comparatively the fraction of the DM-CL (or DM-MPL) interface free of liquid and thus available for the gas access (as well illustrated in Fig. 9 for example). Although the gas access to the CL is globally improved when $\Delta P$ is increased, this is not true in the region of lower gas pressure. Since liquid tends to accumulate in this region, the gas access to the CL is clearly less good in this region compared to the situation where there is no impact of the transverse gas flow.

## 9. Conclusion

The results presented in this chapter suggest that the magnitude of the gas flow induced by the transverse gas pressure difference between the upstream and downstream serpentine channel sections adjacent to a rib is sufficient to impact the liquid water invasion pattern in the diffusion medium (DM). Although only scenario #1 was considered in this chapter, this should also hold in the case of scenario #2 (condensation). The possible impact of the transverse gas flow strongly depends on the throat size distribution in the diffusion medium. For instance, if the distribution is broader than considered in this chapter, the impact will be less.

Consistently with the impact on the liquid gas phase distribution, the transverse gas flow can globally improve the gas access to the CL if sufficient to promote the accumulation of liquid in the lower gas pressure region. However, the gas access in the latter is then clearly less good.

**References**

L.Ceballos, M.Prat, Invasion percolation with multiple inlet injections and the water management problem in Proton Exchange Membrane Fuel Cells, *J. of Power Sources* 195, pp. 825–828 (2010).

L. Ceballos, M. Prat, and P. Duru ,Slow invasion of a nonwetting fluid from multiple inlet sources in a thin porous layer. *Phys. Rev. E* **84**, 056311 (2011)

L. Ceballos, M. Prat, Slow invasion of a fluid from multiple inlet sources in a thin porous layer: influence of trapping and wettability, *Phys. Rev. E* **87**, 043005 (2013)

M. Rebai, M. Prat, Scale effect and two-phase flow in a thin hydrophobic porous layer. Application to water transport in gas diffusion layers of proton exchange membrane fuel cells, *Journal of Power Sources* 192, 534–543 (2009).

J. T. Gostick, M. A. Ioannidis, M. W. Fowler , M. D. Pritzker, Pore network modeling of fibrous gas diffusion layers for polymer electrolyte membrane fuel cells, *Journal of Power Sources* 173, 277–290 (2007).

X. D. Wang, W. M. Yan , Y.-Y. Duan, F. B. Weng, G. B. Jung, C. Y. Lee, Numerical study on channel size effect for proton exchange membrane fuel cell with serpentine flow field, *Energy Conversion and Management* 51, 959–968 (2010)

D.Wilkinson, J.F.Willemsen, Invasion percolation : a new form of percolation theory, J.Phys.A Math.Gen. **16,** 3365-3376 (1983).

Chapter 2

# Liquid invasion from multiple inlet sources and optimal gas access in a two-layer thin porous medium

Ce chapitre correspond à l'article éponyme paru dans Tranport in Porous Media: N.Belgacem, T.Agaësse, J. Pauchet, M. Prat, Liquid invasion from multiple inlet sources and optimal gas access in a two-layer thin porous medium, Transport in Porous Media, DOI 10.1007/s11242-016-0630-1 (2016). Il s'agit d'une contribution à un numéro spécial de cette revue sur les milieux poreux minces (thin porous media). Ceci explique le parti-pris de présenter le problème étudié de manière générique plutôt que directement liée aux PEMFC dans l'idée d'intéresser aussi des lecteurs ne connaissant pas les PEMFCS. Ce parti-pris n'est évidemment a priori pas adapté à ce manuscrit pour lequel la problématique liée à la pile peut être posée d'entrée. D'un autre côté, on peut estimer que le lecteur familier des piles ne sera en réalité pas gêné par le parti-pris en question, si bien qu'il a été décidé de n'apporter aucune modification ici par rapport à l'article.

Le sujet central est la modélisation des transferts à travers l'assemblage MPL-DM. Compte tenu de la très forte différence en taille de pores (de deux à trois ordres de grandeurs environ) entre la MPL et le DM, une approche brutale réseau de pores est numériquement impossible à l'échelle dent-canal en raison de la taille du réseau qu'il faudrait utiliser pour représenter la MPL. L'objectif essentiel de l'article est de montrer comment une solution peut être construite en exploitant des données statistiques obtenues sur des réseaux de taille numériquement calculables (sur des PC). Comme l'indique explicitement le titre, ce travail a été effectué dans le cadre du scenario #1 (invasion en phase liquide)

**Abstract** This study builds upon previous work on single layer percolation in thin layers to incorporate a second layer with significantly different pore sizes and to study the impact of the resulting water configuration on gas phase mass transport. Liquid water is injected at the assembly inlet through a series of independent injection points. The challenge is to ensure the transport of the liquid water while maintaining a good diffusive transport within the gas phase. The beneficial impact of the fine layer on the gas diffusion transport is shown. It is further shown that there exists a narrow range of fine layer thicknesses optimizing the gas transport. The results are discussed in relation with the water management issue in polymer electrolyte membrane fuel cells. Additional discussions, of more general interest in the context of thin porous system, are also offered.

**Keywords** Thin porous media. Invasion percolation. Pore network simulation. Polymer electrolyte fuel cell,

## Introduction

As discussed in Prat and Agaësse (2015), the modeling of transport phenomena in TPM poses specific questions. This is notably so because the traditional modelling tools, such as for instance the classical volume-averaged transport equations, cannot often be used at all or cannot be used in their traditional forms, e.g. (Quin and Hassanizadeh 2014). This is especially true for the TPM with only a few pores over their thickness because the traditional concept of

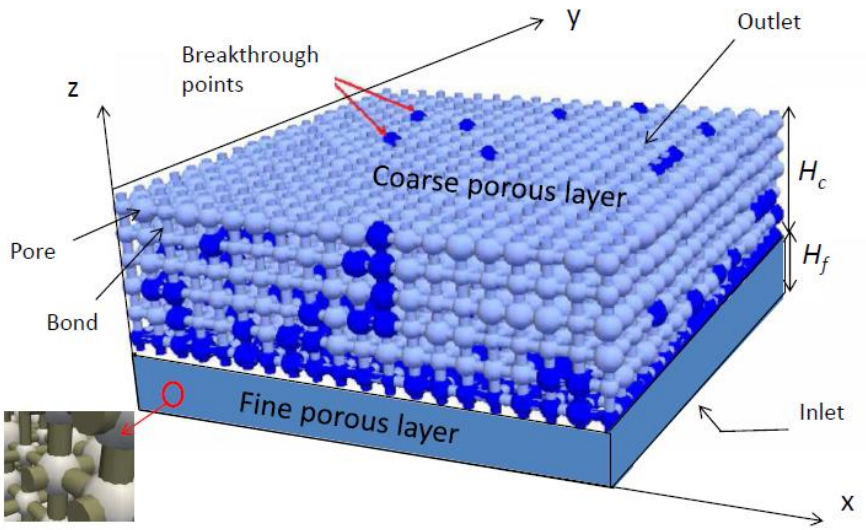


**Fig. 1** Sketch of the problem considered in this study. Liquid water (in blue) is injected at the inlet of the fine layer through a series of independent injection bonds and percolates through the assembly up to the outlet where it forms droplets (referred to as breakthrough points). A gaseous species is transported by diffusion between the outlet surface and inlet surface in the gas phase (pores and bonds shown in light blue-grey in the coarse layer; the various phases are not illustrated in the fine layer).

length scale separation underlying the classical Darcy scale equations is not satisfied over the thickness. In the present article, we consider a quite different approach, not based on volume averaged or thickness averaged equations or any other types of up-scaled partial differential

equations (PDE). Instead, transfer "laws" are established from a series of extensive pore-network simulations and it is showed how these laws can be used to predict the properties of the considered thin system. The idea is not to determine local fields but rather to determine the response of the entire thin system. Thus, from a methodological standpoint, the objective is to enrich the TPM tool box with the consideration of an approach not based on up-scaled PDE.

The approach is presented from the consideration of the problem depicted in Fig. 1. A thin hydrophobic porous medium is formed by the assembly of two porous layers. The lateral extension of this system is typically on the order of 2 – 3 mm. A coarser porous layer is on top. The thickness of this layer is typically on the order of 200 - 300 μm with an average pore size of 30-50 μm. A thinner porous layer, hereafter called the fine layer, forms the bottom layer. The average pore size in this layer is on the order of 500 nm, thus about ten times smaller than in the coarse layer. The system inlet is formed by the bottom surface of the fine layer whereas the outlet is formed by the coarse layer top surface (Figure 1). Initially all the pores are occupied by the gaseous phase. The latter is a mixture of several species and we will be interested in the diffusive transport of one of these species across the two-layer assembly between the outlet and the inlet (gas transport is on average in the direction opposite to that of liquid flow ). Liquid water is then injected at the inlet, thus at the entrance of the fine layer until it reaches the outlet on top of the coarse layer. This corresponds to the liquid breakthrough. It is assumed that all the water reaching the outlet is immediately removed owing to the gas flow existing along the outlet surface. This means that there is no influence of transfers at the outlet surface on the gas – liquid distribution within the porous system.

At the inlet liquid water is injected through a series of independent injection points. Let denote the number of injection points by $N_i$. $N_i$ can vary between 1 and $N_{imax}$ where $N_{imax}$ is the number of entry pores at the fine layer inlet.

The objective is then to predict the number of breakthrough points at the system outlet, the liquid saturation in both the fine layer and the coarse layer and to characterize the gas access to the inlet. As discussed in Ceballos and Prat (2010), breakthrough points correspond to droplet formation spots at the outlet surface. Those droplets represent observable data. Determining their number is therefore interesting to characterize the two phase flow in the system under study.

This problem was studied in previous publications, i.e. (Ceballos and Prat 2010; Ceballos et al. 2011; Ceballos and Prat 2013). However, the system was formed only by the coarse layer without the fine layer. The impact of the fine layer was thus not studied. Hence, this study builds upon previous work on single layer percolation in thin layers to incorporate (a) a second layer with significantly different pore sizes but otherwise similar behavior and (b) the impact of the resulting water configuration on gas phase mass transport. Also, we provide in the present article simple theoretical arguments supporting the detailed numerical results reported in Ceballos and Prat (2011). Additional pore network simulations on random networks are also presented to confirm the universal nature of the results used in the present work.

This problem is inspired from a situation encountered in a polymer electrolyte membrane fuel cell (PEMFC), e.g. (Barbir 2005). However, there is no need to be familiar with PEMFC to understand the present article. The PEMFC terminology is not used in what follows except in a sub-section in section 5 where the results are briefly discussed in relation with PEMFC. This sub-section can be skipped by readers not interested in PEMFC.

The paper is organized as follows. The main results presented in previous papers and useful for the present paper are briefly recalled in section 2 together with the theoretical arguments. The properties of fine layer are given in section 3. The main part of the paper, i.e. the study of the fine layer – coarse layer assembly is presented in section 4. Discussions are presented in section 5. These notably include a brief discussion of main results in relation with the water management issue in PEMFC and a discussion about the modelling of the fine layer – coarse layer interface. Conclusions are presented in section 6.

## 2. Literature review

Capillarity controlled two – phase flows in thin layers have motivated many studies in recent years in relation with the problem of the water management in PEMFC, a crucial aspect of this technology. As for the present work, many of these studies are based on a PNM approach, e.g. Sinha et Wang (2007), Markicevic et al. (2007), Bazylak et al. (2008), Hinebaugh et al. (2010), Lee et al. (2009, 2010, 2014), Gostick (2013), Wu et al. (2013), Fazeli et al. (2015), Quin (2015).

The majority of these studies used the traditional invasion percolation algorithm, e.g. Wilkinson and Willemsen (1983), Sheppard et al. (1999). However, as discussed in Ceballos and Prat (2010), the boundary condition of uniform pressure at the inlet used in classical IP simulations can be questioned in the context of PEMFC studies. In particular, the classical boundary condition is not consistent with the in situ observations showing several breakthrough points at the outlet of the thin layer since only one breakthrough point is obtained using the traditional version of the IP algorithm. This led to the consideration of a different inlet boundary condition, where the non-wetting fluid is injected through a series of independent injection points at the inlet. As shown in Ceballos and Prat (2010), the surface density of breakthrough points is then consistent with the observations. The impact of this boundary condition was then studied in details in Ceballos et al. (2011) and Ceballos and Prat (2013). We are not aware of previous works in the context of IP theory where the IP variants proposed in Ceballos and Prat (2010) and Ceballos et al. (2011) were studied.

In this section, we recall some of the results presented in Ceballos et al. (2011) and Ceballos and Prat (2013) which are useful for the present study. These results were obtained using a simple cubic pore network. In this model, the pores are located at the nodes of a cubic mesh. Two adjacent pores are connected by a narrower channel called bond. The size of the cubic network was denoted by $L \times L \times H$, where $H$ was the porous medium thickness or $N_x \times N_y \times N_z$ (with $N_x = N_y$) measured in number of pores along each direction of a Cartesian coordinate system. In this pore network model, the inlet is formed by $N_x^2$ bonds oriented in the $z$

direction giving access to the $N_x^2$ pores located in the first x - y plane of pores. Liquid is injected through these bonds, which are thus referred to as "injection points" or "injection bonds". The number of injection points was defined via the fraction $n_i$ of injection points at the inlet, $n_i = N_i / N_x^2$, where $N_i$ is the number of injection points. Thus $n_i = 1$ for example corresponds *to* $N_i = N_{imax} = N_x^2$. The injection bonds were randomly selected at the inlet when $n_i < 1$. The impact of $n_i$ was explored varying $n_i$ in the range [0.02, 1]. Thus fractions of inlet injection bonds lower than 2% were not considered.

The pore network was hydrophobic and the liquid water injection was supposed to be sufficiently slow for viscous effects to be negligible compared to capillary effects. Gravity effects are also negligible so that water invasion was simulated using a variant of the invasion percolation (IP) algorithm (Wilkinson and Willemsen 1983). The variant lies in the boundary condition (multiple independent injection points versus a reservoir type condition with the classical IP algorithm) and the consideration of the coalescence phenomenon between liquid paths originating from different liquid injection points.

## 2.1 Liquid invasion simulation algorithm

We used the simultaneous IP algorithm referred to as the sequential algorithm in Ceballos et al. (2011). The algorithm can be summarized as follows:

1) the network is fully saturated by the gas phase initially

2) a first liquid flow path is computed using the standard IP algorithm without trapping starting from a first injection point (selected at random among the inlet active bonds or sequentially). The computation of this step stops at breakthrough, that is when the liquid water reaches the outlet.

3) the simulation is repeated starting from a second injection bond at the inlet. This second invasion stops either when the flow path generated from this second injection point merges into the flow path associated with the first injection bond (flow path coalescence) or at breakthrough, i.e. when the liquid injected from the second inlet bond reaches the outlet through a path independent from the path connected to the first injection point.

4) the procedure is repeated starting successively from all the other injection bonds at the inlet.

Simulations were performed with this algorithm over many realizations of the cubic network varying the thickness of the layer. The results were ensemble-averaged over the number of considered realizations. The results of interest for the present work are presented in Figures 2 - 4. These results were obtained for $N_x = N_y = 20$ and $N_x = N_y = 40$, varying $N_z$ using random distributions of bond and pore sizes.

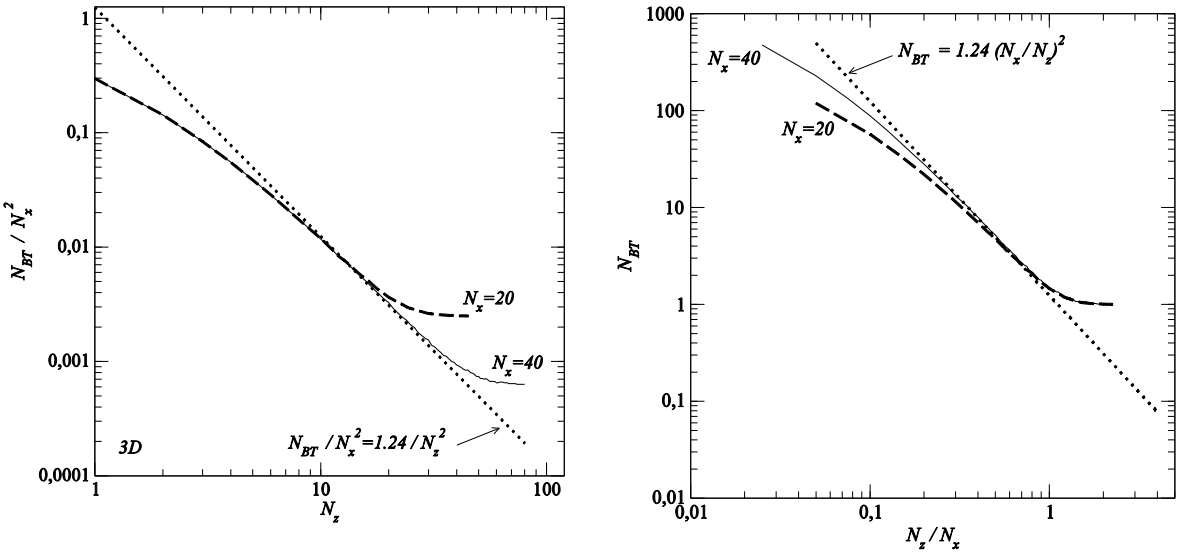


a) b)

**Fig. 2** a) Probability that an outlet bond is a breakthrough point as a function of network thickness $N_z$ when all inlet bonds are active at the inlet ($n_i$ =100%). b) Average number of breakthrough points $N_{BT}$ as a function of porous layer relative thickness $N_z$ / $N_x$ when all pores are active at the inlet ($N_i$ =$N_{max}$) ($n_i$ =100%). The results are shown for two network lateral sizes ($N_x$ = $N_y$ = 20 and $N_x$ = $N_y$ = 40).

## 2.2 Breakthrough points

Fig.2a shows the probability that an outlet bond is a breakthrough point as a function of network thickness $N_z$ whereas Fig.2b shows the average number of breakthrough points $N_{BT}$ as a function of porous layer relative thickness $N_z$ / $N_x$ when all pores are active at the inlet ($n_i$ =1).

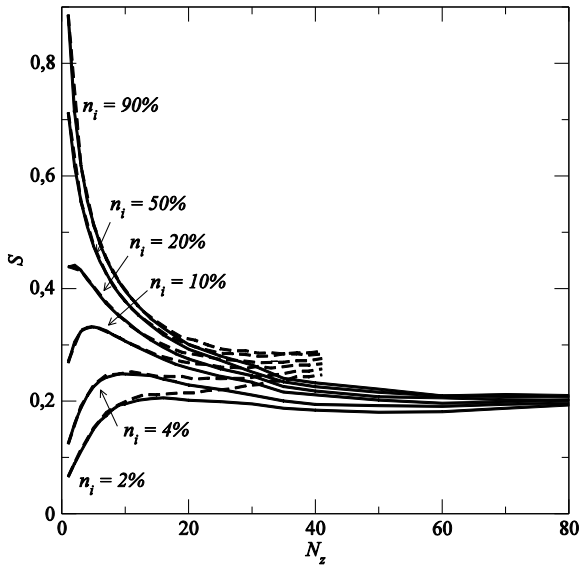


**Fig. 3** Mean overall liquid saturation as a function of porous layer thickness for various injection point fraction $n_i$ for two network lateral sizes ($N_x$ = $N_y$ = 20 (dashed lines) and $N_x$ = $N_y$ = 40 (solid lines)).

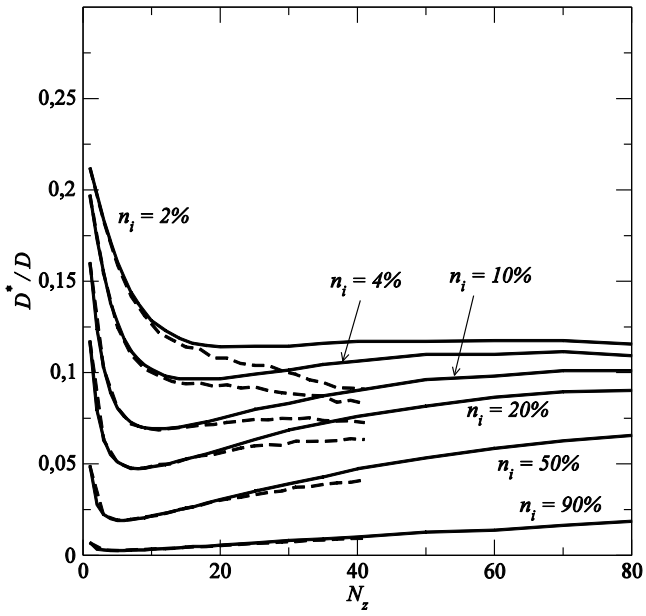


**Fig. 4** Variation of effective diffusion coefficient as a function of network thickness for various injection point fraction $n_i$ for two network lateral sizes ($N_x = N_y = 20$ (dashed lines) and $N_x = N_y = 40$ (solid lines)).

Four regions can be distinguished in Fig.2a depending on the thickness $N_z$ of the system: 1) the ultrathin system region when the system is sufficiently thin, i.e. $N_z \leq 10$, 2) the power law region for larger thicknesses right after the region of ultrathin systems where $N_{BT} / N_x^2 \propto N_z^{-2}$, 3) a transition region between the power law region and region #4, 4) the thick systems characterized by only one breakthrough point (plateaus on the right-hand side in Fig. 2a, noticing that only the beginning of plateaus is shown).

As can be seen from Fig.2a, the behaviors of ultrathin and thin systems (power-law region) is independent of lateral size, which means that $N_{BT} / N_x^2$ only depends on $N_z$ in the ultrathin and thin porous medium domain. It is of course interesting to determine the range of validity of the universal behaviors corresponding to the ultrathin and the thin systems. As can be seen from Fig.2b, the power law regime characterizing the thin systems is observed up to $N_z / N_x \approx 0.8$. Thus, for a given lateral size $N_x$, the universal behaviours are obtained as long as $N_z \leq 0.8\, N_x$. Universal behaviors mean here independent of lateral size. This can be expressed as

$$N_{BT} / N_x^2 = f(N_z, n_i) \text{ if } N_z \leq 0.8\, N_x \qquad (1)$$

where $f$ is a function depending only on $N_z$ for a given $n_i$.

Additional information not considered in the previous works is the distribution of breakthrough points at the outlet. There is no reason to expect something different from a homogeneous distribution (as long as $N_{BT}$ is not too small, i.e. in the regime corresponding to Eq.(1) ). Assuming that the breakthrough points are evenly distributed at the surface, the mean distance $d$ between two neighbour breakthrough points is then given by

$$\frac{d}{a} = \frac{2}{\sqrt{\pi f(N_z, n_i)}} \qquad (2)$$

where $a$ is the lattice spacing (distance between two neighbour pores in the network).

### 2.3 Overall liquid saturation

Somewhat similarly as for the breakthrough point statistics, the results reported in (Ceballos et al. 2011) show that the overall liquid saturation at the end of displacement only depends on $N_z$ for a given fraction $n_i$ of injection bonds at the inlet as long as $N_z < 20$. Thus,

$$S = f_s(N_z, n_i) \text{ if } N_z < 20 \qquad (3)$$

This is illustrated in Fig.3.

## 3. Single layer additional results

### 3.1 Diffusion coefficient

The gas phase is a binary mixture of two species A and B. The gas access is characterized by the diffusive flux of species B through the layer for a given concentration difference $\Delta c$ imposed across the layer. This flux, denoted by $J$, can be expressed as

$$J \approx \frac{D^*}{H} \Delta c \qquad (4)$$

where $D^*$ is the effective diffusion coefficient of the layer; $D^*$ can be computed from pore network simulations. We used the method described in Gostick et al. (2007).

Variations of $D^*$ as a function of layer thickness computed from pore network simulations are shown in Fig.4. Again an "universal" behavior is observed for the sufficiently thin systems,

$$\frac{D^*}{D} = f_D(N_z, n_i) \text{ if } N_z \leq 20. \qquad (5)$$

where $D$ is the molecular diffusion coefficient of the considered species.

Note also the non-monotonous variation of $D^*$ as a function of $N_z$. This non-monotonous variation may appear as counter-intuitive since the variation of saturation in Fig.3 is monotonously decreasing. In fact, the expected result is that the diffusive flux $J$ decreases with $N_z$ and this is indeed what is obtained (as shown in Fig.6a in Ceballos and Prat (2013)). From Eq.(4) $D^*$ can thus be interpreted as the product of an increasing function of $N_z$ ( $H = aN_z$, where $a$ is the distance between two pores in the network) and a decreasing function of $N_z$ (= $J$). This can be expressed mathematically as $\frac{\partial D^*}{\partial H} \propto H\frac{\partial J}{\partial H} + J$ where $\frac{\partial J}{\partial H} < 0$ and $J > 0$. In the range of very low thicknesses, the variation of $D^*$ is dominated by the term $H\frac{\partial J}{\partial H}$, and thus $\frac{\partial D^*}{\partial H} < 0$ whereas the variation for greater $N_z$ is dominated by the term $J$, leading to $\frac{\partial D^*}{\partial H} > 0$ .

## 3.2 Simple theoretical considerations

The universal behavior regarding the number of breakthrough points described in subsection 2.2 can be predicted from a simple argument. We consider the situations where $N_z < N_x$. Figure 5 shows a pore network numerical simulation of the considered invasion scenario for $n_i$ = 1. A colored cluster in the figure corresponds to the liquid cluster associated with one breakthrough point. Thus, there are 6 breakthrough points in this example. This figure clearly suggests that the system can be decomposed into a finite number of independent regions (the

lateral limiting surfaces of a region act as capillary barriers for the liquid present in the adjacent regions). The liquid phase in each region is connected to only one breakthrough point.

Here we make the simplifying assumption that the size of an elementary region is approximately equal to its thickness. Thus, we decompose the system into a number of elementary cubes of lateral size $N_z$. There are $N_b$ elementary cubes with $N_b = \left(N_x / N_z\right)^2$.

Suppose now that the number of breakthrough points is the same (in an average sense) for each cube independently of thickness $N_z$. This number is denoted by $N_e$. We do not take $N_e = 1$ a priori because we do not know whether the size of each elementary cube corresponds to the size of the clusters illustrated in Fig.5, noting that the image in Fig.5

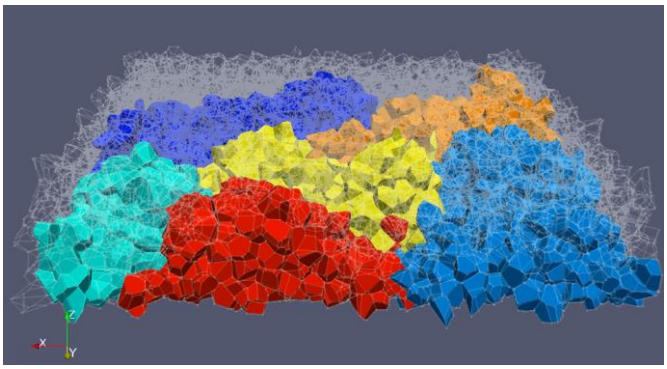

**Fig. 5** The multiple injection scenario leads to the formation of a series of independent liquid occupied regions in the network. Each region is shown with a different color and is connected to only one breakthrough point. Hence each breakthrough point is associated with a well-defined and individualized region of the system.

is for a small network and is merely illustrative. Then the total number of breakthrough points is simply given by,

$$N_{BT} \approx N_e \left(N_x / N_z\right)^2 \qquad (6)$$

leading to

$$\frac{N_{BT}}{N_x^2} \approx \frac{N_e}{N_z^2} \qquad (7)$$

which perfectly corresponds to the power law regime depicted in Fig.2a.

The numerical results on a cubic network indicate that $N_e \approx 1.24$. In fact, the numerical results for a network of size $N_x \times N_x \times N_x$ show that the number of breakthrough points is one with a probability $P_1$ , two with probability $P_2$ and three with probability $P_3$ (see Fig.7b in Ceballos et al. (2011)) with $P_1 + P_2 + P_3 \approx 1$ provided that $N_x$ is not too small. Hence the probability of having more than three breakthrough points is negligible. Thus the prefactor $N_e$ should be equal to $N_e \approx P_1 + 2P_2 + 3P_3$.The numeral value 1.24 is consistent with the values of $P_1$, $P_2$ and $P_3$ reported in Fig.7b in Ceballos et al. (2011).

Naturally, the consideration of elementary cube becomes meaningless when $N_z \geq N_x$, i.e. $N_z / N_x \geq 1$, which is also consistent with the numerical results. The latter indicates that the scaling given by Eq.(6) actually holds up to $N_z / N_x \approx 0.8$.

The numerical study indicates that the power law behavior does not hold for the ultrathin systems corresponding approximately to $N_z \leq 10$. The variation of probability $\frac{N_{BT}}{N_x^2}$ with the thickness is slower than predicted by Eq.(7) for $N_z \leq 10$. This reflects the fact that the number of breakthrough points can vary much more than between 1 and 3 from one elementary cube to another when $N_z \leq 10$. This is shown in Fig.8 in Ceballos et al. (2011) which indicates that the number of breakthrough points follows a Gaussian distribution when $N_z < 10$.

Showing that Eq.(7) (with $N_e \approx 1.24$) overestimates the probability $\frac{N_{BT}}{N_x^2}$ for the ultrathin systems is easy. To this end, consider a system formed by a single layer of pores ($N_z = 1$) for the case $n_i = 1$. Applying Eq.(7) leads to $\frac{N_{BT}}{N_x^2} \approx 1.24$. Each pore in this layer is connected to 4 neighbor pores located in the same horizontal plane (we recall that a simple cubic network is considered) and to a vertical inlet bond and a vertical outlet bond. The probability for the liquid to go straight from the inlet bond to the outlet bond (where it forms a breakthrough point) is therefore only 1/5. Thus it is clear that the total of breakthrough points $N_{BT}$ is necessary significantly lower than $1.24\,N_x^2$, which is the value given by Eq.(6). A more refined analysis of this probability is as follows. Consider an outlet bond. As just discussed the probability for this outlet bond to be a breakthrough point because of direct invasion from immediate neighbor inlet bond is 1/5. However, water can also reach the pore adjacent to the considered outlet bond from neighboring pores with probability 2/5 (we consider the sequential algorithm assuming that two of the four neighboring pores have been invaded

before the considered pore is activated). Then the probability of invading the outlet bond from a path originating from the two considered neighbor pores is 1/4 (the inlet bond cannot be invaded). This leads to $\frac{N_{BT}}{N_x^2} \approx \frac{1}{5} + \frac{2}{5} \times \frac{1}{4} \approx 0.3$, which almost exactly corresponds to the numerical results for $N_z = 1$ in Fig.2a.

### 3.3 On the universal nature of results from PN simulations on random networks

In order to confirm that the results discussed in previous sections are generic and not specific to cubic networks, a few simulations were performed over unstructured networks.

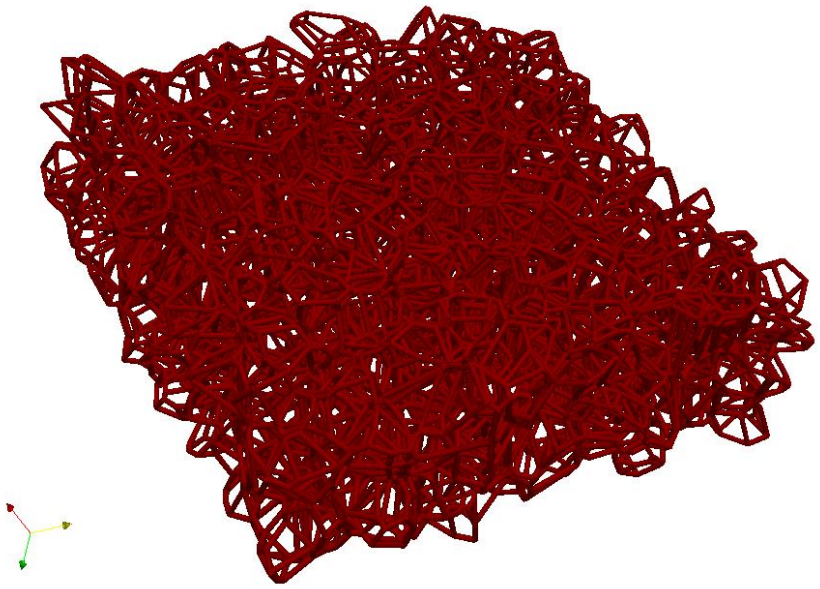

**Fig. 6** Example of generated fiber image generated using the method described in Gostick (2013). The Voronoi lines (fibers) create polyhedral cages that define pore bodies.

The model used in this section has a random 3D architecture based on Delaunay tessellations to represent the pore space and Voronoi tessellations to represent the fiber structure. This model is illustrated in Fig.6 (see also Fig.5) and the procedure for generating it is described in details in Gostick (2013). This procedure is therefore not described again here. This type of network is referred to as a Voronoi network in the following.

Similarly as for the cubic network, $N_z$ is the number of pores (a pore corresponds to a polyhedral cage in Fig.6) in the through plane direction whereas $N_x$ is the number of cages (pores) in the in-plane directions ($N_y = N_x$).

Fig.7 shows the average number of breakthrough points $N_{BT}$ as a function of porous layer relative thickness $N_z / N_x$ when all pores are active at the inlet ($n_i$ =1) obtained for Voronoi networks of lateral size $N_x = 30$ and $N_x = 40$, respectively.

As can be seen from Fig.7, the results obtained with the Voronoi network are consistent with the power law behavior obtained with the cubic network. In particular, the data for the network size $N_x = 40$ are consistent with the exponent 2 of the power law. The conclusion is that the results shown in Fig.7 are a sufficiently clear indication that the results discussed in previous sections are generic of thin systems.

## Fine layer

**4.**

The average pore size in the thin layer is much smaller than in the coarse layer. As an example, consider a thin layer of 50 μm in thickness and of 2.6 mm in lateral size. The lattice spacing $a_f$ is 700 nm. The fine layer is thus represented by a 3715 × 3715 ×72 pore network ($N_{xf} = N_{yf}$ =3715, $N_{zf}$ = 72). Pore network simulations in such a big network would be computationally extremely long, if even feasible. Therefore the fact of knowing "universal" laws is here crucial. Note that the subscript " $f$ " is used to label the data relative to the fine layer.

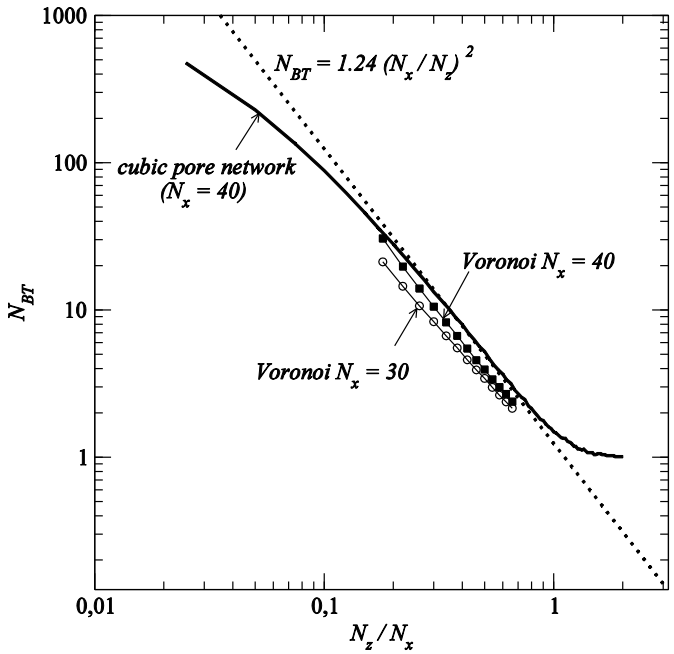


**Fig. 7** Average number of breakthrough points $N_{BT}$ as a function of porous layer relative thickness $N_z / N_x$ when all pores are active at the inlet ($N_i = N_{max}$) ($n_i$ =100%). The results are shown for two Voronoi network lateral sizes ($N_x = N_y = 30$ and $N_x = N_y = 40$, averaged over 1500 realizations) together with the results for a cubic network of lateral size $N_x = N_y = 40$

## 4.1 Breakthrough points

In relation with the results shown in Fig. 2, we first note that $N_{zf} / N_{xf} \leq 0.8$ ($N_{zf} / N_{xf} = 0.019$). Thus the system is in the universal regime. Secondly, $N_{zf} \geq 10$. Thus, we can use the power law relationship to obtain the number of breakthrough point. As an example consider the case $n_{if} = 1$. Applying Eq.(7) (with $N_e = 1.24$) yields $N_{BT} \approx 3300$, to be compared with the number of injection points $N_i = 3715^2$. Hence $N_{BT} / N_i \approx 2\ 10^{-4}$, which illustrates the efficiency of liquid path coalescence process. Also it can be noted that the thickness corresponding to the end of the power law regime, i.e. $N_{zf} / N_{xf} \approx 0.8$ corresponds to $N_{zf} \approx 2972$ for this network lateral size. Similarly, other properties such as the overall saturation and the diffusion coefficient, can be predicted using the data obtained from the simulations over much smaller networks presented in section 2. How to construct these data is the main objective of the present section.

## 4.2 Overall liquid saturation

The objective is to determine the variation of $S_f$ as a function of $N_{zf}$ for different fraction $n_{if}$ in the range [0.02, 0.9]. Fig.3 shows the results obtained with networks of size 20 x 20 x $N_z$ and 40 x 40 x $N_z$. The obvious and expected result is that the saturation increases with increasing $n_i$ for a given thickness. There is absolutely no reason to expect a different tendency in a large network such as the 3715 x 3715 x $N_{zf}$ network used to represent the fine layer.

One problem is that the results shown in Fig.3 cannot be directly applied because the variation of $S_f$ with thickness $N_{zf}$ and $n_{if}$ also depends on lateral size $N_{xf}$ for $N_{zf} > 20$. The situation is as follows. For $N_{zf} < 20$, the variation of $S_f$ with $N_{zf}$ is independent of lateral size $N_{xf}$ and thus the values determined on network of relatively small lateral extensions and shown in Fig.3 are also the ones expected with a large a network in this range of thicknesses. For $N_{zf} \approx 2\ N_{xf}$, there is only one breakthough point and there is a clear dependence of saturation with lateral size $N_{xf}$ as also illustrates in Fig. 3. Since the system is at the percolation threshold (only one breakthrough point) at $N_{zf} \approx 2\ N_{xf}$ , it is tempting to make use of the percolation scaling $S \propto N_x^{d_f - 3}$, where $d_f$ is the fractal dimension of the percolation cluster ($d_f = 2.52$ in 3D). According to the results presented in Ceballos et al. (2011), see the inset in Fig.12b in this reference, this is a quite reasonable idea. Thus suppose we know the saturation $S_{Nx1}$ at $N_{z1} \approx 2N_{x1}$ for a network of lateral size $N_{x1}$ then the saturation $S_{Nx2}$ at $N_{z2} \approx 2N_{x2}$ for a network of lateral size $N_{x2}$ is expected to be

$$S_{Nx2} \approx S_{Nx1} \left( \frac{N_{x1}}{N_{x2}} \right)^{3-d_f} \qquad (8)$$

, which consistently with available numerical simulations predicts that $S$ at $N_{zf} \approx 2\ N_{xf}$ decreases with increasing lateral size (this is illustrated in Fig.3).

From the data available for networks of lateral size $N_x = 40$, we therefore know for any larger size the saturation for the thicknesses lower than 20 (there are identical to the ones for the network of lateral size 40) and the saturation at $N_{zf} \approx 2\ N_{xf}$, which is given using obvious notations by $S_f(2N_{xf}) = S_f(2N_{x40})\left(\frac{N_{x40}}{N_{xf}}\right)^{3-d_f}$. For our network of lateral size $N_{xf} = 3715$, this means that we know the saturations for the thickness lower than 20 and at $N_{zf} = 7430$. The question is then how to estimate the saturation between $N_{zf} = 20$ and $N_{zf} = 7430$.

From the shape of the curves shown in Fig. 3, we decided to perform power law adjustments, i.e.

$$S_f = \eta N_{zf}^{\chi} \qquad (9)$$

between the values limiting the range of variations of $S_f$. This gave the variations shown in Figure 8 whereas the values of coefficients of the power law adjustments for the various $n_{if}$ are given in Table 1

## 4.3 Diffusion coefficient

The next step is to evaluate the effective diffusion coefficient of the fine layer for the various $n_{if}$. Figure 4 shows the variations obtained from simulations on networks of size 20 x 20 x $N_z$

and 40 x 40 x $N_z$. A natural idea based on the approach prevailing for traditional porous media is to try to express $D^*$ as a function of liquid saturation $S$.

However, combining the results of Fig.3 and Fig.4 leads to the results shown in Fig.9. Interestingly, contrary to traditional porous media, there is not a one to one relationship between $D^*$ and $S$. This is another illustration of the scale dependence of results in a thin system for the situation considered in the present article. See also García-Salaberri et al. (2015) for further discussion on the relationship between $D^*$ and $S$ in thin systems.

Since searching for simple relationships between $D^*$ and $S$ is not appropriate here, we proceed similarly as for constructing the saturation profiles. This means that we are interested in the variation of $D^*$ as functions of $N_{zf}$ and $n_{if}$ rather than $S$.

As illustrated in Fig.4, we first note that the values of $D_f^*$ are independent of lateral size $N_{xf}$ for $N_{zf} < 20$. Then, we estimate $D_f^*$ for $N_{zf} = 2N_{xf}$. For this thickness, we know that the invading phase, i.e. the liquid phase, forms a percolation cluster (there is only one breakthrough point). The defending phase (the gas phase) is therefore well connected (except of course when $n_{if}$ approaches 100%). In others terms, the gas phase is far from a percolation threshold and thus traditional relationship expressing the variation of $D_f^*$ with saturation should be acceptable for this thickness.

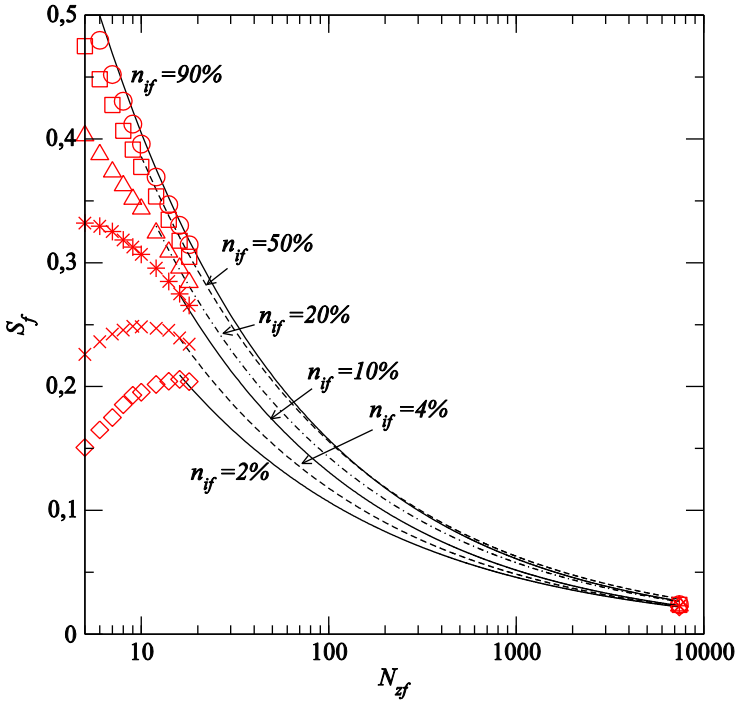


**Fig. 8** Constructed variation of overall saturation as a function of layer thickness for various fractions of inlet injection bonds $n_{if}$ for the 3715 x 3715 x $N_{zf}$ network used to represent the fine layer. The symbols on the left corresponds to the "universal" values (i.e. independent of lateral size) obtained on a smaller network for $N_{zf} < 20$. The symbols on the right corresponds to the saturations computed using the percolation scaling (Eq.(8)). These saturations are actually very close for the various $n_{if}$ and the symbols on the right are therefore almost superposed one on top of another. The lines correspond to the power law adjustments (Eq.(9), see text).

Table 1. Coefficients of power law (Eq.(9)) for various $n_{if}$

| $n_{if}$ (%) | $\eta$ | $\chi$ |
|---|---|---|
| 2 | 0.579 | -0.367 |
| 4 | 0.697 | -0.386 |
| 10 | 0.840 | -0.403 |
| 20 | 0.877 | -0.355 |
| 50 | 0.956 | -0.394 |
| 90 | 1.044 | -0.411 |

As an example we took a classical relationship of the form,

$$\frac{D_f^*(S_f)}{D} = \alpha(1-S_f)^{1.5} \qquad (10)$$

and determined the numerical coefficient $\alpha$ from the results of invasion percolation simulations reported in Ceballos and Prat (2013). This gave $\alpha$ = 0.23.

Eq.(10) is used to determine $D_f^*$ at $N_{zf} = 2N_{xf}$ from the saturations determined for this thickness as explained previously (i.e. using Eq.(8)).

Then from the shape of the curves shown in Fig. 4, we again decided to perform power law adjustments, i.e.

$$\frac{D_f^*}{D} = \eta_D N_{zf}^{\chi_D} \qquad (11)$$

between the values limiting the range of variations of $D_f^*$. This gave the variations shown in Fig.10 whereas the values of coefficients of the power law adjustments for the various $n_{if}$ are given in Table 2

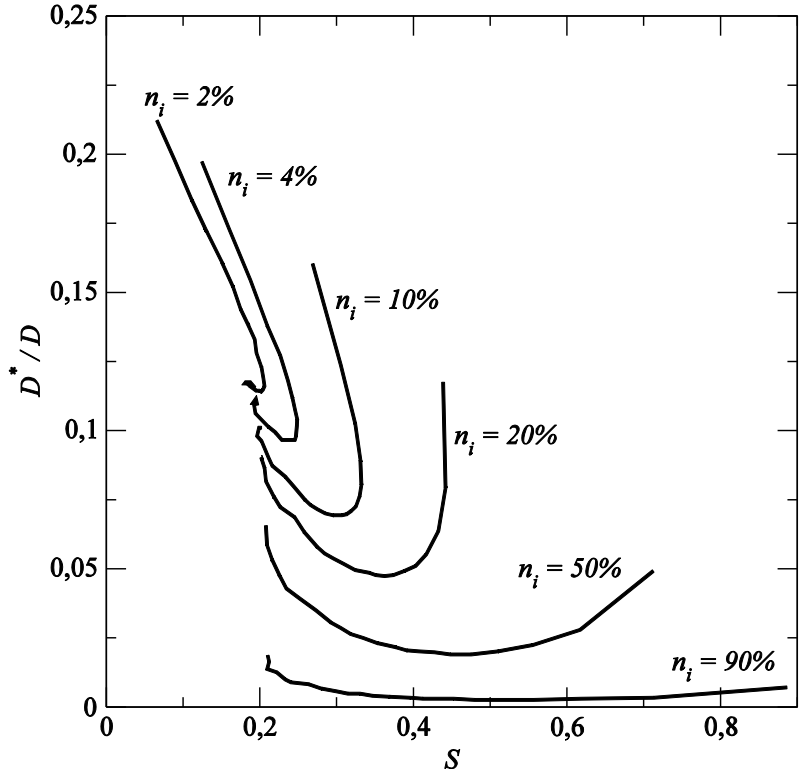


**Fig. 9** Variation of diffusion coefficient with saturation for various fractions of inlet injection bonds $n_i$ from simulations on *40 x 40 x* $N_z$ networks. The curves are obtained by combining the data shown in Fig.3 and Fig.4 for the *40 x 40 x* $N_z$ networks.

## 5. Fine layer – coarse layer assembly

The objective of this section is to show how the behavior of the fine layer – coarse layer assembly can be predicted from the results presented in the previous sections taking advantage of the established "universal" laws. Also, the objective is to illustrate why the presence of the fine layer can be extremely beneficial to gas access across the coarse layer.

A first problem lies in the nature of the assembly. Here we make the simple assumption that the interface between the fine layer and the coarse layer is sharp. In other terms, this interface has no particular properties. This point is further commented in section 5.

As before, we are interested in the number of breakthrough points at the outlet of coarse layer, the overall saturations in the layers and the gas access through the assembly.

The dimensions and other properties of the fine layer are those given in Section 3. As an example, we consider a coarse layer of 200 µm in thickness with a lattice spacing $a_c$ of 40 µm. This corresponds to a 65 × 65 × 5 network. Thus we have a 65 × 65 × 5 network coupled

with a 3715 × 3715 × $N_{zf}$ network, where $N_{zf}$ is the thickness of the fine layer (measured in fine layer lattice spacing unit $a_f$).

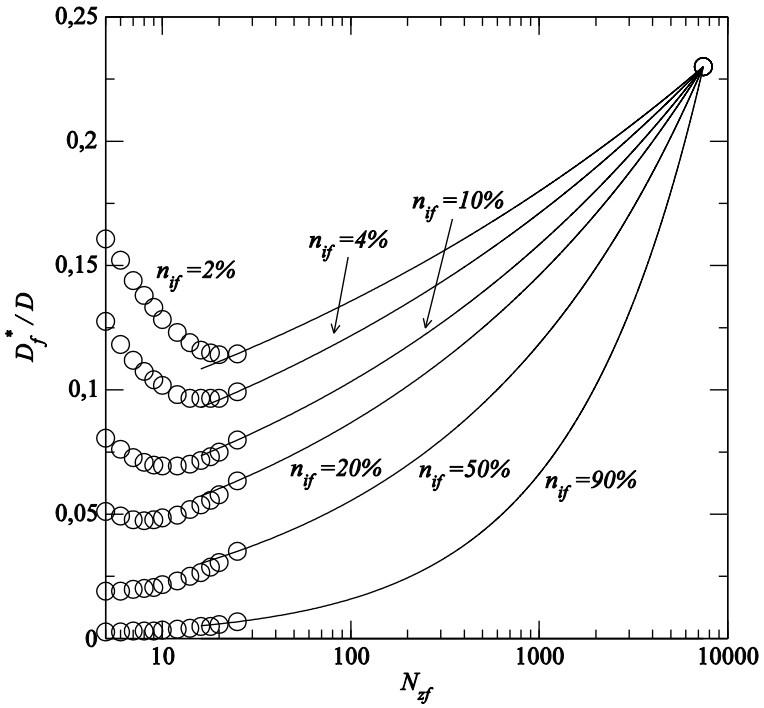


**Fig. 10** Constructed variation of diffusion coefficient as a function of layer thickness for various fractions of inlet injection bonds $n_{if}$ for the 3715 x 3715 x $N_{zf}$ network used to represent the fine layer. The symbols on the left corresponds to the "universal" values (i.e. independent of lateral size) obtained on a smaller network for $N_{zf} < 30$. The symbol on the right corresponds to the saturations computed using the percolation scaling (Eq.(8)). These saturations are actually very close for the various $n_{if}$ leading to indiscernible variations at $N_{zf} = 2\ N_{xf}$ (= 7430) for the various values of $n_{if}$. The lines correspond to the power law adjustments (Eq.(11), see text).

Table 2. Coefficients of diffusion coefficient power law (Eq.(11)) for various $n_{if}$

| $n_{if}$ (%) | $\eta_D$ (x10) | $\chi_D$ |
|---|---|---|
| 2 | 0.772 | 0.122 |
| 4 | 0.617 | 0.148 |
| 10 | 0.439 | 0.186 |
| 20 | 0.306 | 0.226 |
| 50 | 0.121 | 0.330 |
| 90 | 0.0091 | 0.620 |

The reference case is the case where there is no fine layer and all bonds at the coarse layer inlet are injection points ($n_{ic}$ =1). The impact of the fine layer on transport in the coarse layer is illustrated by varying the thickness of the fine layer without modifying the coarse layer.

## 5.1 Impact of fine layer thickness on the number of breakthrough points at coarse layer outlet

We are first interested in the minimal fine layer thickness $N_{zfmin}$ above which the gas transfer become possible across the assembly.

According to Eq.(1), the number of breakthrough points $N_{BTf}$ at the fine layer – coarse layer interface can be expressed as,

$$N_{BTf} / N_{xf}^2 = f(N_{zf}, n_{if}) \text{ if } N_{zf} \leq 0.8\, N_{xf} \qquad (12)$$

The number of inlet bonds at the inlet of coarse layer is $N_{xc}^2$. Assuming that the fine layer breakthrough points are evenly distributed at the fine layer – coarse layer interface, we can first estimate the fine layer thickness $N_{zfmin}$ for which the number of fine layer breakthrough points is about equal to the number of inlet bonds at the coarse layer inlet. This thickness is given by the equation,

$$N_{BTf} = f(N_{zfmin}, n_{if})\ N_{xf}^2 = N_{xc}^2 \qquad (13)$$

As discussed in §2, $f(N_{zf}, n_{if}) \approx \frac{1.24}{N_{zf}^2}$ independently of $n_{if}$ as long as $N_{zf}$ is greater than about 20 (over the range [0.02 – 1] of $n_i$ considered in Ceballos et al. 2011). Under these circumstances we deduce from Eq.(13) that ,

$$N_{zfmin} \approx 1.1135 \frac{N_{xf}}{N_{xc}} \qquad (14)$$

In our case ($N_{xf}$ =3715, $N_{xc}$ = 65), this gives $N_{zfmin}$ ≈63. Hence $N_{zf}$ must be greater than $N_{zfmin}$ for having gas percolating paths across the coarse layer - fine layer assembly. For $N_{zf} \leq N_{zfmin}$ all inlet bonds at the inlet of coarse layer are invaded by liquid, which blocks the gas access.

The situation $N_{zf} \leq N_{zfmin}$ also corresponds to a maximum of breakthrough points at the outlet of coarse layer since all coarse layer inlet bonds are injection bonds.

To determine the number $N_{BTc}$ of breakthrough points at the coarse layer outlet for $N_{zf} > N_{zfmin}$, we first have to determine the fraction $n_{ic}$ of coarse layer inlet bonds which are injection bonds. Again we assume that the fine layer breakthrough points are evenly distributed at the fine layer – coarse layer interface, which leads to,

$$n_{ic} = \frac{N_{BTf}}{N_{xc}^2} = \frac{1.24}{N_{zf}^2}\frac{N_{xf}^2}{N_{xc}^2} \qquad (15)$$

Then we need to know how $N_{BTc}$ varies for fixed coarse layer dimensions ($N_{xc}$ = 65, $N_{zc}$ = 5) as a function of $n_{ic}$. According to the results reported in Ceballos et al. (2011), the coarse layer is sufficiently thin for the "universal" behaviors characterized in Ceballos et al. ( 2011) to apply. So we made a fit of the data reported in Ceballos et al. (2011) for the case $N_z$ = 5 to obtain,

$$\frac{N_{BTc}}{N_{xc}^2} = \frac{2.585\ln(100 n_{ic}) + 4.4605}{400} \qquad (16)$$

Combining Eq.(15) and Eq.(16) leads to the desired relationship between the number of breakthrough points at the outlet of the assembly as a function of fine layer thickness,

$$\frac{N_{BTc}}{N_{xc}^2} = \frac{2.585}{400}\ln\left(\frac{124}{N_{zf}^2}\frac{N_{xf}^2}{N_{xc}^2}\right) + \frac{4.4605}{400} \qquad (17)$$

Applied to our example, this leads to the results shown in Fig.11. As can be seen, increasing

$N_{zf}$ above $N_{zfmin}$ has a clear impact on the number of breakthrough points at the coarse layer outlet. The number of breakthrough points is decreasing with an increasing fine layer thickness, which is first indication that the presence of a sufficiently thick fine layer should improve the gas access.

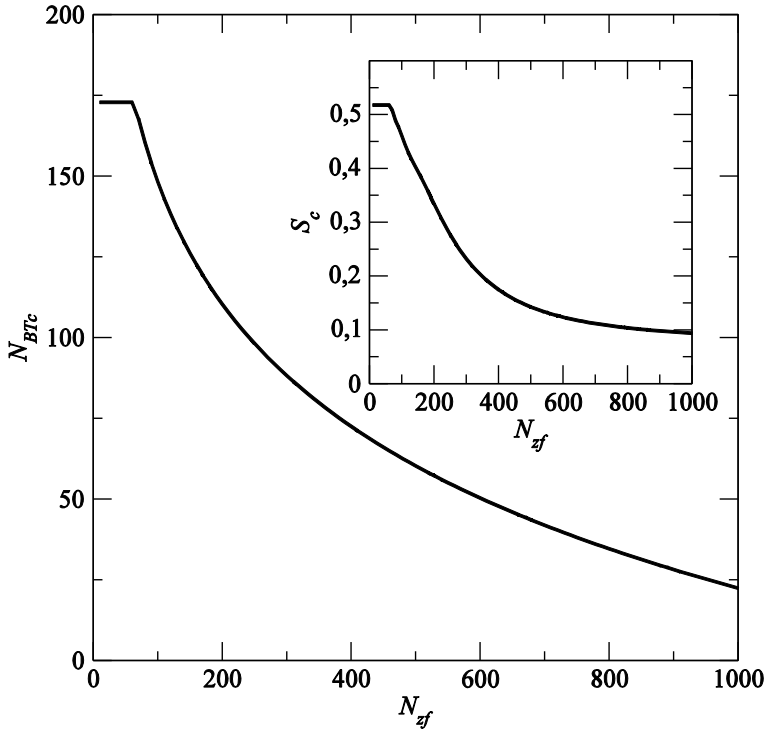


**Fig. 11** Number of breakthrough points at the coarse layer outlet as a function of fine layer thickness $N_{zf}$. As an order of magnitude, 100 breakthrough points correspond to a density of 15 droplets per mm$^2$ at the surface of the assembly for our example. The inset shows the mean overall liquid saturation in coarse layer as a function of fine porous layer thickness $N_{zf}$.

## 5.2 Impact of fine layer thickness on overall liquid saturation in coarse and fine layer

For evaluating the evolution of global saturation $S_c$ in the coarse layer we need again a relationship between $S_c$ and $n_{ic}$ for a fixed network size in the "universal" domain. As can be seen from Fig.3, $S_c$ only depends on $n_{ic}$ for $N_z$ = 5 (and thus does not depend on lateral dimension). The variation of $S_c$ with $n_{ic}$ for this thickness is shown in Fig.12. We then made a polynomial fit from the data reported in Ceballos et al. (2011) and shown in Fig.12 in order to easily compute $S_c$ as a function of $n_{ic}$.

Combined with Eq.(15) this leads for our example to the results depicted in Fig.13 showing the variation of overall saturation in coarse layer as a function of fine layer thickness.

As can be seen increasing the fine layer thickness significantly decreases the liquid saturation in coarse layer when $N_{zf} > N_{zfmin}$. As depicted in Fig. 8, the effect of thickness increase is also to reduce the overall saturation in the fine layer. An interesting difference between the fine and the coarse layer is that the variation of saturation in the coarse layer for a given assembly (i.e. a given fine layer thickness) is independent of $n_{if}$ (for the range of $n_{if}$ considered) whereas the saturation in the fine layer does depend on $n_{if}$ (as illustrated in Fig.8).

## 5.3 Impact of fine layer thickness on gas access and gas transport

As discussed in § 4.1, the fine layer thickness $N_{zf}$ must be greater than $N_{zfmin}$ for the gas transfer to be possible across the assembly.

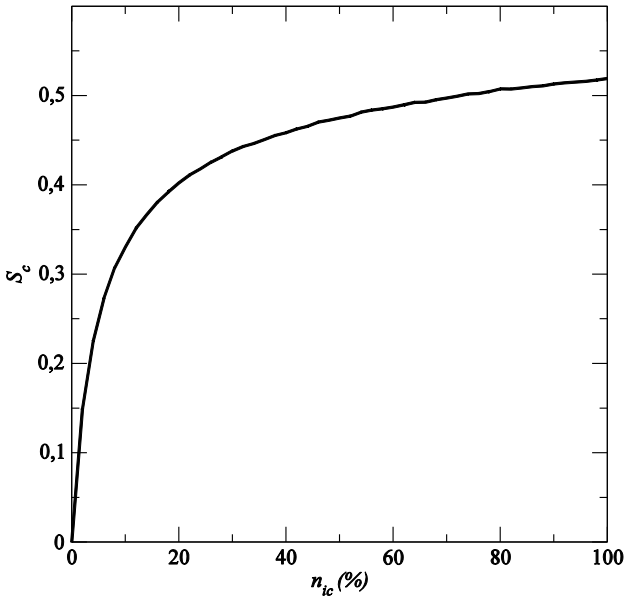


**Fig. 12** Mean overall liquid saturation in coarse layer as a function of fraction of injection bonds at layer inlet.

Note that the gas transfer as a dissolved species in the liquid is not considered. Thus gas transfer is only possible when the gas phase percolates through the assembly. For $N_{zf} \leq N_{zfmin}$ all inlet bonds at the inlet of coarse layer are invaded by liquid, which blocks the gas access.

In what follows, we consider again the case of the diffusive transfer of species B in the gas phase formed by the binary mixture of two species A and B.

Then the gas access is again characterized by the diffusive flux across the assembly for a given concentration difference $\Delta c$ imposed across the assembly. This flux, denoted by $J$, can be expressed as

$$J \approx \left( \frac{H_f}{D_f^*(N_{zf}, n_{if})} + \frac{H_c}{D_c^*(S_c)} \right)^{-1} \Delta c \qquad (18)$$

where $H_f$ and $H_c$ are the thicknesses of fine and coarse layers respectively; $D_f^*(N_{zf}, n_{if})$ and $D_c^*(S_c)$ are the effective diffusion coefficient of fine and coarse layers respectively. As reference flux we use the flux across a perfectly dry coarse layer,

$$J_{ref} \approx \frac{D_c^*(0)}{H_c} \Delta c \qquad (19)$$

which leads to express Eq.(18) in dimensionless form as

$$\frac{J}{J_{ref}} \approx \left( \frac{H_f}{D_f^*(N_{zf}, n_{if})} + \frac{H_c}{D_c^*(S_c)} \right)^{-1} \frac{H_c}{D_c^*(0)} \qquad (20)$$

Eq.(20) can be also expressed as

$$\frac{J}{J_{ref}} \approx \left( \frac{N_{zf}\, a_f}{D_f^*(N_{zf}, n_{if})} + \frac{N_{zc} a_c}{D_c^*(S_c)} \right)^{-1} \frac{N_{zc} a_c}{D_c^*(0)} = \frac{1}{\frac{D_c^*(0)}{D_f^*(N_{zf}, n_{if})} \frac{N_{zf}\, a_f}{N_{zc} a_c} + \frac{D_c^*(0)}{D_c^*(S_c)}} \qquad (21)$$

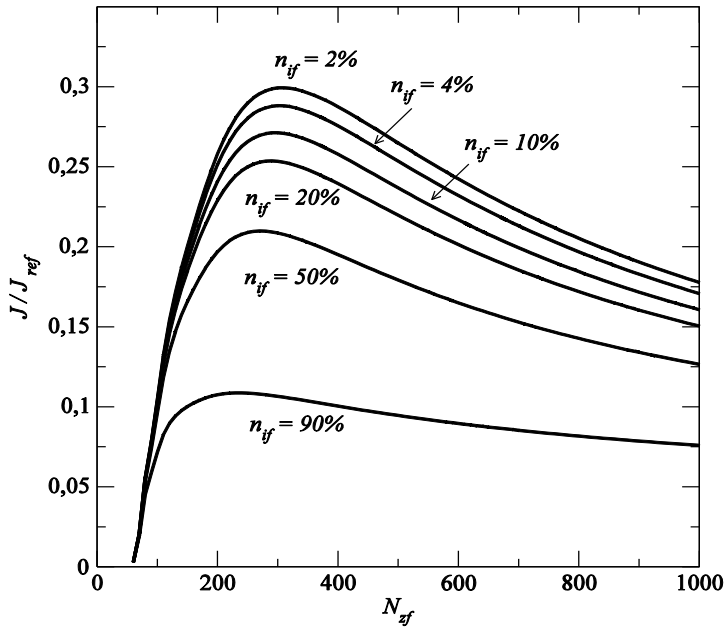


**Fig. 13** Variation of gas diffusive flux through the fine layer – coarse layer assembly as a function of fine porous layer thickness $N_{zf}$ for various fractions of inlet injection bonds $n_{if}$.

To make use of Eq.(21), we need to know $D_f^*(N_{zf}, n_{if})$ and $D_c^*(S_c)$. For $D_f^*(N_{zf}, n_{if})$ we use the results presented in § 3.3 and illustrated in Fig. 10. For the coarse layer, one can directly use the results shown Fig.4. From the results shown in Fig.4 for $N_z$ =5, we can express $D_c^*(S_c)$ as

$$\frac{D_c^*(S_c)}{D} = 0.23 - 0.44 S_c \qquad (22)$$

Fig.13 shows the variation of $J/J_{ref}$ as a function of $N_{zf}$ for our example. We first recall that no transfer is possible, i.e. $J = 0.$, in the absence of the fine layer owing to the flooding of coarse layer inlet bonds. Thus the fine layer has clearly a beneficial effect since it makes possible the gas transfer owing to the impact of fine layer on the number of flooded bonds at the coarse layer inlet. Then the most striking and interesting result is that the variation of $J/J_{ref}$ is not monotonous but shows a maximum. Thus there are a range of fine layer thicknesses, around $N_{zf}$ = 300 in Fig. 13, which leads to an optimal gas transfer. Interestingly, the optimal thickness only slightly depends on $n_{if}$ over the range of $n_{if}$ considered.

To understand the results shown in Fig.13, one should remember that increasing the fine layer thickness increases the diffusive resistance due to the fine layer but also decreases the diffusive resistance in the coarse layer owing to the decrease in the coarse layer saturation $S_c$. This can further analyzed by expressing Eq.(21) as

$$\frac{J}{J_{ref}} = \frac{1}{R_{fine} + R_{coarse}} \qquad (23)$$

where $R_{fine} = \frac{D_c^*(0)}{D_f^*(N_{zf}, n_{if})} \frac{N_{zf}\, a_f}{N_{zc} a_c}$ and $R_{coarse} = \frac{D_c^*(0)}{D_c^*(S_c)}$ represent resistances to diffusive transport in the gas phase in the fine layer and the coarse layer respectively.

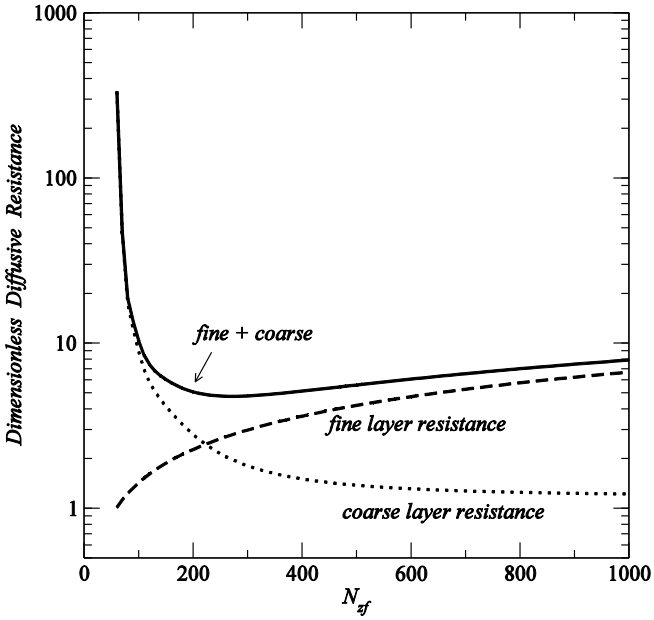


**Fig. 14** Variation of fine layer and coarse layer diffusive resistances a function of fine porous layer thickness $N_{zf}$ for the case $n_{if} = 0.5$

As an example, the variations of $R_{fine}$ and $R_{coarse}$ as a function of $N_{zf}$ are shown in Fig.15 for the case $n_{if} = 0.5$. For sufficiently low $N_{zf}$, the liquid saturation in the coarse layer is high (see Figure 13), close to the saturation corresponding to the gas percolation threshold. As a result the coarse diffusive resistance is by far dominant. Then this resistance decreases rapidly with the increase in the fine layer thickness owing to the impact of the fine layer on the coarse layer saturation and diffusion coefficient (see Figure 13 and Eq.(22)). The fine layer resistance progressively increases with $N_{zf}$ until both resistances are comparable. This corresponds to the optimal fine layer thicknesses. Further increase in the fine layer thickness leads to the increase in the overall resistance owing to the increase of fine layer resistance, which progressively becomes the dominant resistance.

# 6. Discussions

## 6.1 On the fine layer – coarse layer interface

In the present investigation, the interface between the fine layer and the coarse layer was considered as sharp. In fact, we implicitly assumed that the two layers could be prepared independently and then just press one onto the other with negligible deformation and negligible overlap between the two layers. However, in practice, the fine layer is often obtained by depositing and agglomerating fine particles on the coarse layer. As a result a non-negligible fraction of the fine layer can actually penetrate into the coarse layer. Under these circumstances, the system can actually be described in terms of at least three regions:

the region of the coarse layer far from the fine layer which is free from fine layer material, the fine layer formed as a result of the agglomeration of particles and a transition region where both solid phase belonging to the coarse layer and the fine layer material are present together.

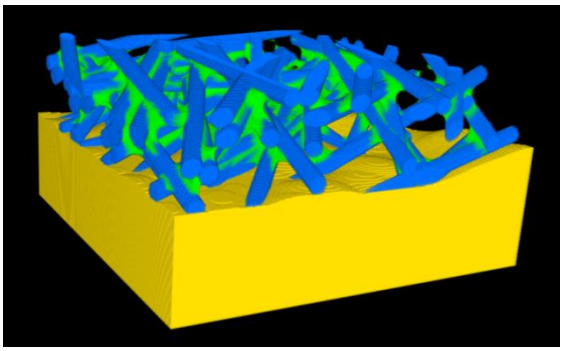

a)

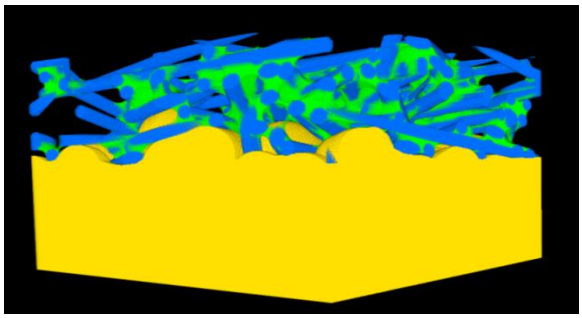

b)

**Fig. 15** a) Illustration of the situation considered in the present article where the transition between the fine layer (in yellow) and the coarse layer (represented as a fibrous material with fiber in blue and binder in green) is sharp, b) illustration of the situation with interpenetration of the fine layer and the coarse layer.

This is illustrated in Fig. 15b. Thus, as discussed in Prat and Agaësse (2015), the interfacial region between the two layers must then be considered as a transition region between the two regions. The transition region was referred to as the "third layer" in Prat and Agaësse (2015). In contrast with the sharp interface, transport properties must be determined also for the transition region. For example, Eq.(23) must be expressed as

$$\frac{J}{J_{ref}} = \frac{1}{R_{fine} + R_{transition} + R_{coarse}} \qquad (24)$$

where $R_{transition}$ is the diffusive resistance due to the transition region. Naturally, assigning transport properties to the transition region is not an obvious task. Also the transition between the two main layers can be progressive (the concentration in particles penetrating into the coarse layer can vary with the distance from coarse layer inlet), which makes the transition layer still more difficult to characterize. It can be surmised that the transition region can have a great impact on transport properties on the whole assembly. This of course depends notably on the thickness of transition region compared to the thicknesses of the two other regions. It is difficult to go further without considering a specific example. Thus here the message is simply that the fine layer – coarse layer assembly we have considered in the previous section can be an overly simplified representation of the assembly and that further work is needed to study systems such as the one illustrated in Fig.15b.

## 6.2 Comparison with a previous work

Interestingly a problem similar to the one considered in section 4 was studied in Nam and Kaviany (2003) but using traditional volume average equations, such as the generalized Darcy's law. As in the present work, they found a range of fine layer thicknesses optimizing the gas diffusion transport. However, the impact of the fine layer was quite weak. By contrast, the impact is quite significant in our study. To explain the difference, we first note that considering discrete injection points cannot be made accurately within the framework of the continuum approach. More importantly, the relevance of traditional continuum approach for studying the considered problem is highly questionable. This is discussed in Rebai and Prat (2009). First there is an obvious lack of length scale separation as regards the coarse layer (only five pore sizes thick in our example). Second, it is well known that the capillarity dominated regime considered in the present work and which is also supposed to prevail for the case studied by Nam and Kaviany (2003) is a regime that cannot be described properly with the traditional continuum two-phase flow model, e.g. (Rebai et Prat 2009; Lenormand et al. 1988). This is an example of thin porous medium specificity, i.e. traditional concepts can be inappropriate or at best can lead to very approximate results.

## 6.3 Applications to PEMFC

This section can be skipped by readers not familiar with PEMFC. In the context of PEMFC, the coarse layer corresponds to the gas diffusion layer (GDL), the fine layer to the microporous layer (MPL). First, it can be noted that we considered a scenario in which liquid water forms in the catalyst layer (the catalyst layer (CC) is a fine porous layer adjacent to the MPL where the electrochemical reaction takes place and water is produced). Although this scenario has been considered in many papers, it is likely that liquid – vapor phase change phenomena, e.g. evaporation and condensation, are also a key factor in this system, e.g. (Straubhaar et al. 2015 and references therein). If one accepts that liquid water enters the MPL – GDL assembly from the CC, then the consideration of multiple independent injection points

at the inlet comes from the fact that water formed in different points within the volume of the CC, e.g. (Ceballos and Prat 2010; El Hannach et al. 2011,2012) for more details.

Several experimental studies have shown that the presence of the MPL had a beneficial impact on the fuel cell performance. The present study provides a piece of explanation in relation with the general problem of the water management in PEMFC. In brief, adding the MPL improves the oxygen access to the CC and reduces the risk of flooding of the GDL.

However, the situation in a fuel cell is more complex than considered in the present study. For example, the GDL outlet surface is not entirely free. A significant fraction of this surface is occluded by the ribs of the bipolar plate. The GDL is compressed differently below the rib and below the channel. We considered isotropic networks whereas the GDL is an anisotropic medium. Also, considering a thick transition region (as discussed in section 5.1) would be more realistic. The GDL is often considered as only partially hydrophobic, e.g. (Ceballos and Prat 2013) whereas we have assumed a perfectly hydrophobic assembly. In brief, several aspects need to be incorporated in the modelling for extending the results presented in the present paper. Nevertheless, we believe that the present work well illustrates one of the possible beneficial impacts of the MPL-GDL assembly, namely its impact on the gas access, compared to the situation where the MPL is not present.

## 7. Conclusion

Thin porous media represent a special class of porous media for which classical models based on the traditional continuum approach to porous media cannot be adapted owing to the lack of length scale separation over the thickness.

As an illustrative example, we considered a situation where the thin porous medium was formed by the assembly of a fine layer and a coarse layer. We studied a situation, inspired from a situation considered in relation with the water management problem in PEMFC, where liquid water was injected at the assembly inlet and the gas present at the outlet must percolate through the assembly.

It was first show how laws or relationships governing different variables of interest could be established from pore network simulations over single layers. Then these relationships were used to study the impact of fine layer thickness on gas diffusion transport properties of the assembly.

It was shown that the consideration of the fine layer had a beneficial impact on gas transport and that there exists a narrow range of fine layer optimal thicknesses. Furthermore, the optimal thicknesses were found to be only slightly sensitive to the fraction of injection bonds at the fine layer inlet.

Although the main result, i.e. the existence of a range of optimal thicknesses, is expected to be quite general, several points deserve further investigations. For example, the coarse layer thickness was not varied. It is likely that the optimal thickness depends on the coarse layer thickness. More importantly, the data for large networks were extrapolated from data on small networks. Extensive pore network simulations on larger networks than the ones considered in previous works are desirable to confirm the validity of the extrapolation methods proposed in the present work.

A perhaps still more interesting issue in the context of thin porous media would be to analyze more properly the impact of the transition region between the fine layer and the coarse layer. Here we simply assume a sharp interface between the two layers. In many thin systems, the consideration of this interface as a transition region of a certain thickness having specific properties seems more appropriate.

**Acknowledgements**

The research leading to these results has received funding from the European Union's Seventh Framework Programme (FP7/ 2007-2013) for the Fuel Cells and Hydrogen Joint Technology Initiative under grant agreement n°303452, "IMPACT— Improved Lifetime of Automotive Application Fuel Cells with ultra-low Pt-loading".

**References**

Barbir, F.: PEM Fuel Cells: theory and practice. Elsevier Academic Press (2005)

Bazylak, A. V Berejnov, B Markicevic, D Sinton, N Djilali, Numerical and microfluidic pore networks: Towards designs for directed water transport in GDLs, *Electrochimica Acta* 53 (26), 7630-7637, 2008.

Ceballos, L., Prat M.: Invasion percolation with multiple inlet injections and the water management problem in Proton Exchange Membrane Fuel Cells. J. of Power Sources **195**, 825–828 (2010)

Ceballos, L., Ph.D thesis, University of Toulouse, France (2011)

Ceballos, L. , Prat, M., Duru P.:Slow invasion of a nonwetting fluid from multiple inlet sources in a thin porous layer. Phys. Rev. E **84**, 056311 (2011)

Ceballos, L. , Prat, M.: Slow invasion of a fluid from multiple inlet sources in a thin porous layer: influence of trapping and wettability. Phys. Rev. E **87**, 043005 (2013)

El Hannach, M., Prat, M., Pauchet, J.: Pore Network Modelling: application to multiphase transport inside the cathode catalyst layer of proton exchange membrane fuel cell. Electrochimica Acta **56**, 10796– 10808 (2011)

El Hannach, M., Prat, M., Pauchet, J.: Pore Network Model of the Cathode Catalyst Layer of Proton Exchange Membrane Fuel Cells: analysis of water management and electrical performance. International Journal of Hydrogen Energy **37** (24), 18996–19006 (2012)

M Fazeli, J Hinebaugh, A Bazylak, Investigating Inlet Condition Effects on PEMFC GDL Liquid Water Transport through Pore Network Modeling, *Journal of The Electrochemical Society*, 162 (7) F661-F668 (2015)

García-Salaberri, P.A., Hwang, G., Vera, M., Weber, A.Z., Gostick J.T.:Effective diffusivity in partially-saturated carbon-fiber gas diffusion layers: Effect of through-plane saturation distribution. International Journal of Heat and Mass Transfer 86, 319-333 (2015).

Gostick, J.T, Ioannidis M.A., Fowler M.W., Pritzker M.D.: Pore network modeling of fibrous gas diffusion layers for polymer electrolyte membrane fuel cells. J. Power Sources **173,** 277–290 (2007).

Gostick, J.T.: Random pore network modeling of fibrous PEMFC gas diffusion media using Voronoi and Delaunay tessellations. J. Electrochemic. Soc. **160** (8), F731-F743 (2013)

Hinebaugh, J. and Fishman, Z. and Bazylak, A. Unstructured Pore Network Modeling with Heterogeneous PEMFC GDL Porosity Distributions, *Journal of the Electrochemical Society*, Vol. 157, pp. B1651-B1657 (2010)

K. J. Lee, J. H. Nam, and C. J. Kim, Pore-network analysis of two-phase water transport in gas diffusion layers of polymer electrolyte membrane fuel cells, *Electrochim. Acta* **54**, 1166-1176 (2009).

KJ Lee, JH Kang, JH Nam, CJ Kim, Steady liquid water saturation distribution in hydrophobic gas-diffusion layers with engineered pore paths: An invasion-percolation pore-network analysis, *Journal of Power Sources* 195 (11), 3508-3512 (2010).

KJ Lee, JH Kang, JH Nam, Liquid water distribution in hydrophobic gas-diffusion layers with interconnect rib geometry: An invasion-percolation pore-network analysis, *International Journal of Hydrogen Energy* 39, 6646-6656 (2014).

Lenormand, R., Touboul, E., Zarcone, C.: Numerical models and experiments on immiscible displacements in porous media. J. Fluid Mech. **189**, 165-187 (1988).

Markicevic, B., Bazylak, A. and Djilali, N. Determination of transport parameters for multiphase flow in porous gas diffusion electrodes using a capillary network model. 2, *Journal of Power Sources*, Vol. 171, pp. 706-717. (2007)

Nam, J.H., Kaviany M., Effective diffusivity and water saturation distribution in single-and two-layer PEMFC diffusion medium. Int .J. Heat Mass Transf. **46**,4595-4611 (2003).

Prat,M., Agaësse, T.: Thin porous media, Chapter 4 in Handbook of Porous Media 3rd Edition, Edited by K.Vafai, Taylor & Francis (2015).

Qin,C.Z., Hassanizadeh, S.M. : Multiphase flow through multilayers of thin porous media: General balance equations and constitutive relationships for a solid–gas–liquid three-phase system. Int .J. Heat Mass Transf. **70**: 693-708 (2014).

C. Quin, Water Transport in the Gas Diffusion Layer of a Polymer ElectrolyteFuel Cell: Dynamic Pore-Network Modeling Journal of the Electrochemical Society, 162 (9) F1036-F1046 (2015)

Rebai, M., Prat, M.: Scale effect and two-phase flow in a thin hydrophobic porous layer. Application to water transport in gas diffusion layers of PEM fuel cells, J. of Power Sources **192,** 534-543 (2009).

Adrian P Sheppard, Mark A Knackstedt, W V Pinczewski, Muhammad Sahimi, Invasion percolation: new algorithms and universality classes. Journal of Physics A: Mathematical and General, Volume 32, Number 49 L521–L529 (1999).

Sinha PK, Wang CY. Pore-network modeling of liquid water transport in gas diffusion layer of polymer electrolyte fuel cell. *Electrochimica Acta* ;52:7936-45 (2007).

Straubhaar, B., Pauchet, J., Prat,M.: Water transport in gas diffusion layer of a polymer electrolyte fuel cell in the presence of a temperature gradient. Phase change effect. Int. J. of Hydrogen Energy, **40** (35), 11668–11675 (2015).

Wilkinson, D., Willemsen, J.F.: Invasion percolation : a new form of percolation theory, J.Phys.A Math.Gen. **16,** 3365-3376 (1983).

Wu R., Xun Zhu, Qiang Liao, Rong Chen, Guo-Min Cui, Liquid and oxygen transport in defective bilayer gas diffusion material of proton exchange membrane fuel cell, *International Journal of Hydrogen Energy*, 38 (10), pp 4067–4078 (2013).

# *Partie II: Scénario condensation*

# Chapter 3
# Modeling

## 1. Introduction

As mentioned in the introduction, the model is developed so as to be able in a near future to model MEA degradation by coupling the loss of PTFE in the GDL and the loss of catalyst surface in the catalyst layer. Many studies have been done to model catalyst layer degradation and much less to model GDL degradation. To our knowledge, this is a first attempt to couple these two phenomena in a single approach.

This final objective has driven the developments presented in this chapter.

Pore Network Modeling (PNM) approach has shown its interest to model two-phase flows inside GDL and has especially demonstrated that mixed-wettability of GDL (with the presence of hydrophobic pores and of hydrophilic pores) is a key aspect on two-phase pattern and gas diffusion (Pulloor, 2011), and that hydrophobicity loss (with the increase of the number of hydrophilic pores) can have a huge influence on PEMFC durability (Pauchet et al, 2012). On this basis, PNM will be used here to model transport phenomena in GDL.

Some recent works (Straubhaar et al., 2016) have confirmed that the most probable water transfer scenario inside GDL is the condensation scenario (liquid water is due to condensation that appears inside the GDL due to temperature and water vapor gradients); for this reason, our PNM will include condensation scenario as described in (Straubhaar et al., 2016). This is conisderer as a major progress compared to the works cited above that did consider the injection scenario for which liquid water comes from the catalyst layer.

As the local fields are different between rib and channel (Rachidi, 2011; Freunberger, 2006), degradation is suspected to be also non-uniform. For this reason, our model is developed at the rib/channel scale (Figure 3) and focuses on the cathode side as most of the degradation due to water management appears on the cathode side.

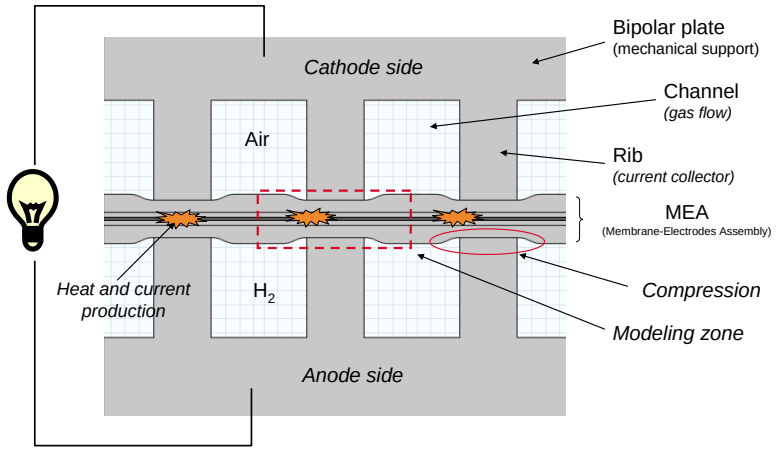


Figure 3 : Description of rib/channel pattern

Compressibility of the GDL below the rib is taken into account in the model which accounts for liquid and gas transport, heat transfer, electron and proton transfers and electrochemistry.

Another important aspect is that the model aims at being compared to durability test protocols to check its consistency with real degradation of PEMFC. During these experiments, current density is an input and the electrical potential is recorded as a function of time (constant or cycling, Figure 4) to derive the degradation rate (µV/h). This means that the model shall also be capable to do so. As described in the next paragraphs, this request to modify the classical electrochemical relationships used to model the catalyst layer in order to calculate V as a function of *i* instead of *i* as a function of V as usual

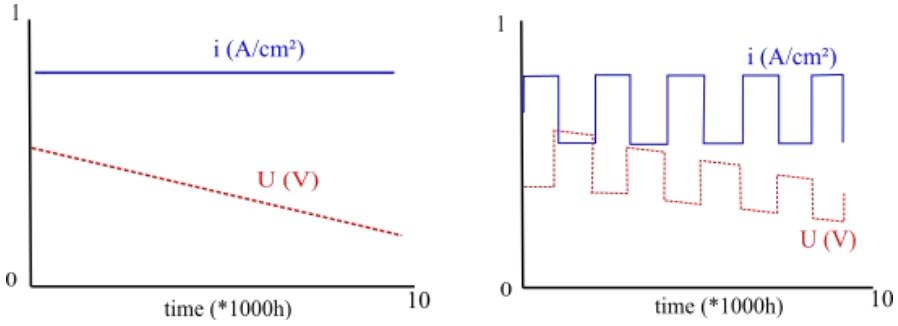


Constant current Cycling current

Figure 4 : Typical degradation protocols used for PEMFC

In this chapter we describe the 3D model developed at rib/channel scale on the cathode side, coupling the membrane, the catalyst layer, the MPL and the DM. It allows studying one and two-phase transfers inside a cathode, the difference between rib and channel, and will be used in the future to couple degradation of the GDL to the one of the catalyst layer.

We first describe the geometry under consideration, then the physical models used in the different cathode layers, the 3D PNM approach applied to the DM, the (PNM-finite difference model) used for the MPL, the (2D + 0D model) approaches used for the catalyst layer and membrane, and the algorithm for single and two-phase situations (meaning without and with liquid water in the GDL).

The model proposed here allows taking into account major transfers using the efficiency of PNM to simulate two-phase transfers. This model will allow analyzing condensation diagrams (chapter 5), the influence of liquid water on current density distribution (chapter 6), and a first analysis on PTFE loss inside GDL (chapter 7). Degradation of catalyst layer and the coupling between GDL and catalyst layer degradations will be studied after the thesis, based on the model presented here.

## 2. Geometry

The geometry under consideration Figure 5 is based on the one described in Figure 3 restricted to the cathode side: GDL (DM and MPL), catalyst layer and membrane.

As this work focuses on degradation on the cathode side, only the cathode side is modeled. This allows also restricting the simulation domain as some simulations are time consuming. Obviously this leads to making some assumptions on the anode side, which is modeled as a BC applied to the membrane. This model could be extended in the future to include the anode also but this would need to improve the simulation efficiency to reduce the simulation time.

The air gas channel is modeled as a boundary condition applied to the DM. This model could be easily extended to include the bipolar plate to set the temperature BC close to the cooling circuit and not to the rib, which would be more realistic.

The geometry is 3D with extension into y direction (flow direction in the channel). This hypothesis is not useful when only single phase transports are considered in the cathode as boundary conditions applied along z are uniform. Nevertheless, even with uniform BC in y direction, this 3D extension in y is mandatory when liquid water formation by condensation is considered, at least with the PNM approach considered.

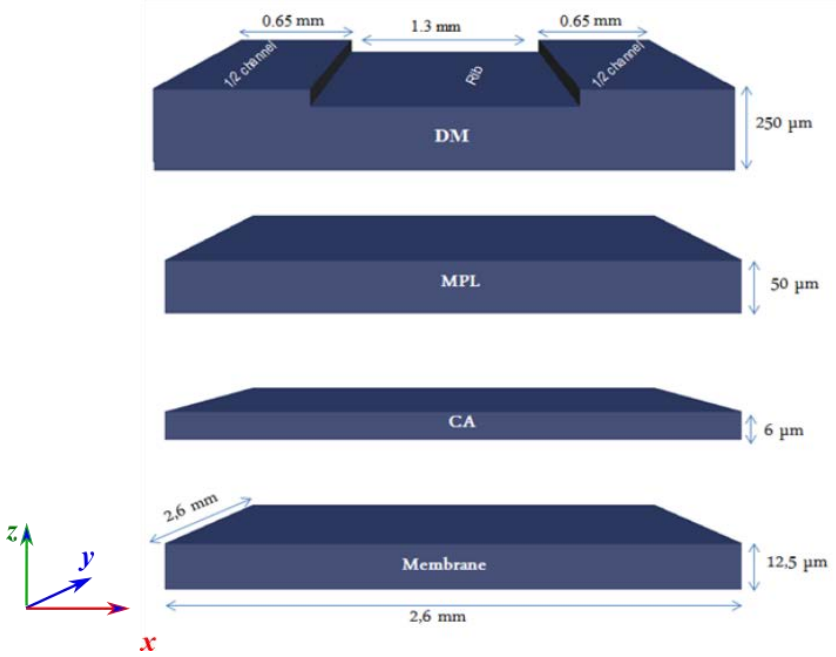


Figure 5 : Geometry modeled

# 3. Physical models

## 3.1. Single-phase situation

### 3.1.1. GDL

In the GDL (Micro-Porous Medium and Diffusion Medium), we consider gas, thermal and electrical transports.

Azote is considered as a stagnant gas in which water vapor and oxygen diffuses according to Fick's law

$$J_{H_2O} = -D_{eff}.\nabla c_{H_2O}$$

$$\nabla.J_{H_2O} = 0.$$

$$J_{O_2} = -D_{eff}.\nabla c_{O_2}$$
$$\nabla.J_{O_2} = 0.$$

Heat transfer is modeled according to Fourier's law

$$q = -\lambda_T.\nabla T$$
$$\nabla.q = 0.$$

and electron transport thanks to Ohm's law

$$i = -\sigma_e.\nabla\psi_e$$
$$\nabla.i = 0$$

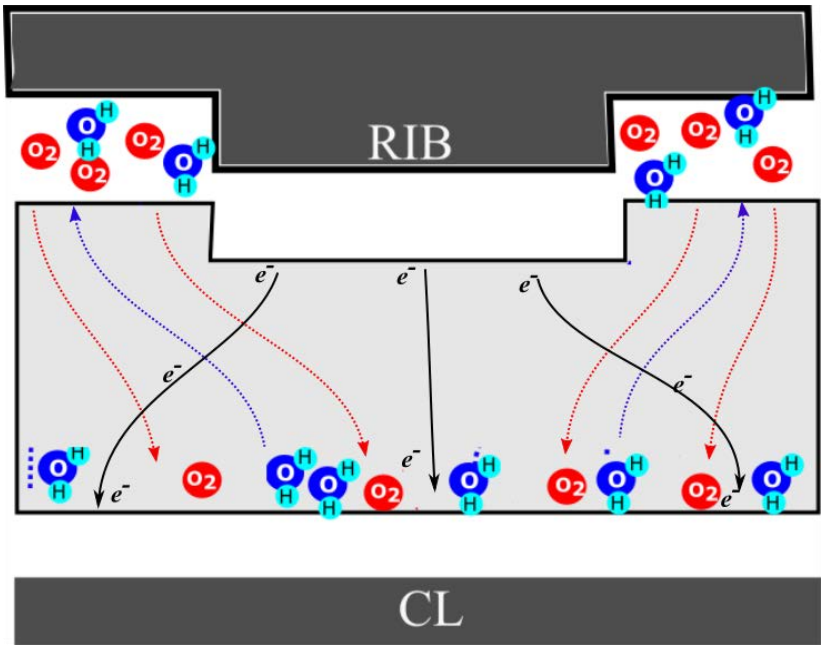


Figure 6: Sketch of transfers inside the GDL in the case of one-phase situation. The MPL and DM are not distinguished in this Figure.

The anisotropy of the DM is taken into account in the model with different values of the transport properties in the in-plane directions and the through plane direction (see Chapter 4). The MPL is considered as isotropic.

### 3.1.2. Cathode catalyst Layer

Oxygen Reduction Reaction

ORR is used as the baseline for cathode electrochemical behavior

$$\frac{1}{2}O_2 + 2H^+ + 2e^- \rightarrow H_2O$$

The Nernst equation is used for the computation of the thermodynamical potential:

$$E_{rev} = \frac{\Delta H - T\Delta S}{nF} + \frac{RT}{nF} ln\left(a_{O_2}^{\frac{1}{2}} a_{H_2} a_{H_2O}^{-1}\right)$$

with the activities $a_i$ relating to the different gases

$$\begin{cases} a_{H_2O} = \dfrac{P_{H_2O}}{P_{sat}} \\ a_{O_2} = \dfrac{P_{O_2}}{P_{ref}} \\ a_{H2} = \dfrac{P_{H2}}{P_{ref}} \end{cases}$$

$R = 8.3$ (J/(mol.K)) Perfect gas constant

$F = 96485.3$ (A/mol) Faraday constant

$\Delta H = -242$ (kJ/mol)

$\Delta S = -44$ (J/mol)

$P_{ref}$ is the reference pressure (1 bar)

The Butler-Volmer equation (Erdey-Gruz, 1930; (Mann et al., 2000; Mann et al., 2006) gives the relation between current production rate $i_{bv}$ and the overpotential η:

$$i_{bv} = i_0 \left( exp\left(\frac{\alpha nF}{RT}\eta\right) - exp\left(-\frac{(1-\alpha)nF}{RT}\eta\right)\right)$$

with the exchange current density $i_0$ expressed as:

$$i_0 = n.k_0.exp\left(-\frac{A_0}{RT}\right)\left(a_{O_2}^{\gamma_{O_2}}\right)^{1-\alpha}\left(a_{H_2O}^{-\gamma_{H_2O}}\right)^{\alpha}$$

and

$k_0 = 4.2.10^{-8}\ (m.s^{-1})$

$A_0 = 24360\ (J.mol^{-1})$

$\alpha = 0.6$

$\gamma_{O_2} = 0.41$

$\gamma_{H_2O} = 2.04$

These variables have been fitted on specific experiments at CEA (Chameau project 2010) and the sign of $\gamma_{H_2O}$ is discussed in chapter 4.

The overpotential $\eta$ is defined as $\psi_c = E_{rev} + \eta + \phi_c$ with $\psi_c$ the electronic potential and $\phi_c$ the protonic potential.

The heat flux produced by the ORR is modeled as $q = \left(\frac{\Delta H}{nF} - \psi_c\right) i_{bv}$ for which we assume that part of it $(1 - \beta'_q)q$ is transferred to the anode side through the membrane

and the oxygen consumption and water vapor production as

$$j_{O2} = \frac{i_{bv}}{4F}$$

$$j_{H2O} = -\frac{i_{bv}}{2F}$$

for which we assume that part of it $(1 - \beta'_v)j_{H_2O}$ is transferred to the anode side through the membrane

Modification of Butler-Volmer relationship

The model aims at simulating degradation experiments in which current density is fixed (constant or cycling, Figure 4) and electrical potential is measured as a function of time. This means that the current density is an input of the model and the voltage is an output. The BV equation needs thus to be "inversed" to calculate the electrical voltage as a function of current density.

If the overpotential $|\eta| >> 0$ then $\exp\left(\frac{\alpha nF}{RT}\eta\right) << \exp\left(-\frac{(1-\alpha)nF}{RT}\eta\right)$ (as the activation overpotential is by definition negative at the cathode side) which leads to $\eta = -\frac{RT}{(1-\alpha)nF} ln\left(-\frac{i_{bv}}{i_0}\right)$, called below the "Large η" curve

If the overpotential $\eta \sim 0$ then the two exponentials of BV are of the same order of magnitude and a first order series expansion leads to the classical "Small η" relationship:

$$\eta = \frac{RT}{nF}.\frac{i_{bv}}{i_0}$$

We can then compute and plot the same polarization curve in two ways:

- by applying directly BV equations, with η as an input and then calculating *i*, which is named below the "direct" polarization curve
- by applying an inversed formulation of BV equations, with *i* as an input and then calculating $\eta$, which is named below the "inversed " polarization curve; this is that formulation that is to be used in our case

The comparison between the two curves will allow checking the accuracy of the "inversed" polarization" curve calculation.

We then have calculated the "Linear inversed" polarization curve by applying the formulation of η far away from 0 "Large η" combined with the one close to 0 ("Small η" slope) as defined above.

As shown in Figure 7, the "direct" polarization curve (in red) is not correctly modeled in this case (in green) as the linearization by "Small η" does not ensure continuity of the polarization

curve. Figure 5 shows also that the "inversed" formulation using only one exponential (black curve) is not consistent, as already said above. We have then chosen an alternative approach consisting in linearizing BV law at low current densities but ensuring the polarization curve continuity (see details below). This models very well the "direct" curve as shown in Figure 7.

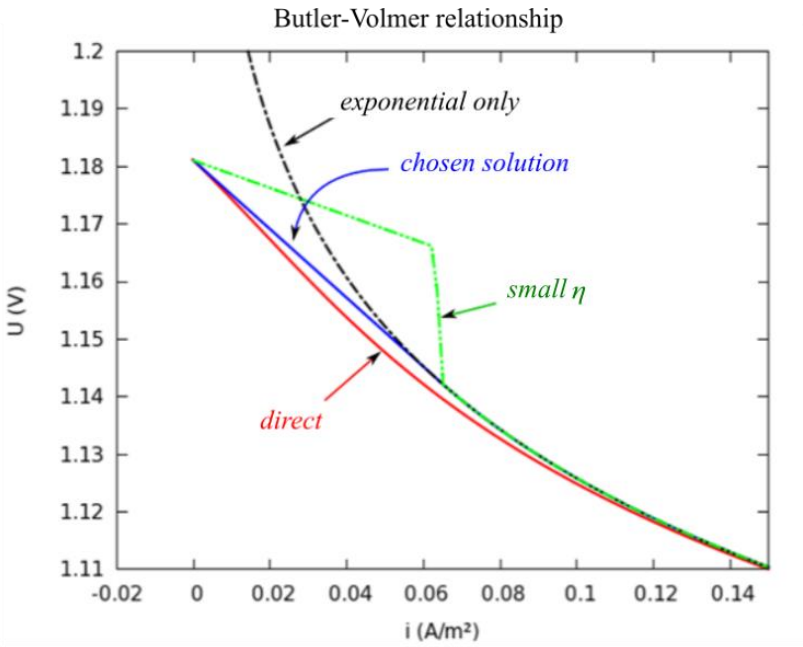


Figure 7 : linearization of the relationship of Butler-Volmer

In order to ensure continuity of the polarization curve, we applied the following procedure.

We define the critical current density $i_{critical}$ in the "direct" polarization curve such as its tangent crosses the point (i=0; U= $E_{rev}$).

Tangent equation can be written as:

$$y = f'(i_{critical})(x - i_{critical}) + f(i_{critical})$$

With $f = E_{rev} - \eta = E_{rev} - \frac{RT}{nf}\frac{1}{1-\alpha} ln\left(\frac{i_{bv}}{i_0}\right)$ and $f' = -\frac{RT}{nf}\frac{1}{1-\alpha}\frac{1}{i_{bv}}$

This gives:

$$y = -\frac{RT}{nf}\frac{1}{1-\alpha}\frac{1}{i_{critical}}(x - i_{critical}) + E_{rev} - \frac{RT}{nf}\frac{1}{1-\alpha}\ln\left(\frac{i_{critical}}{i_0}\right)$$

$$y = -\frac{RT}{nf}\frac{1}{1-\alpha}\frac{1}{i_{critical}}x + \left(\frac{RT}{nf}\frac{1}{1-\alpha} + E_{rev} - \frac{RT}{nf}\frac{1}{1-\alpha}ln\left(\frac{i_{critical}}{i_0}\right)\right)$$

To ensure also (i=0; U= $E_{rev}$):

$$\left(\frac{RT}{nf}\frac{1}{1-\alpha} + E_{rev} - \frac{RT}{nf}\frac{1}{1-\alpha}ln\left(\frac{i_{critical}}{i_0}\right)\right) = E_{rev}$$

$$\frac{RT}{nf}\frac{1}{1-\alpha}\left(1 - ln\left(\frac{i_{critical}}{i_0}\right)\right) = 0$$

Then $i_{critical}$ is the solution of $ln\left(\frac{i_{bv}}{i_0}\right) = 1$.

Linearized function becomes:

$$L(\eta) = \begin{cases} -\frac{RT}{(1-\alpha)nF}\frac{1}{i_{critical}}i_{bv} & si\ i_{bv} < i_{critical} \\ -\frac{RT}{(1-\alpha)nF}ln\left(-\frac{i_{bv}}{i_0}\right) & si\ i_{bv} \geq i_{critical} \end{cases}$$

The continuity of the "inversed" polarization curve is thus ensured and

$$\lim_{i \to i^{+}_{critical}} L(\eta) = \lim_{i \to i^{-}_{critical}} L(\eta)$$

The final system to be solved is thus,

if $i > i_{critical}$:

$$\begin{cases} j_{O_2} = \dfrac{i_{bv}}{4F} & (i) \\ j_{H_2O} = -\dfrac{i_{bv}}{2F} & (ii) \\ E_{rev} = \dfrac{\Delta H - T\Delta S}{nF} + \dfrac{RT}{nF} ln\left(a_{O_2}^{\frac{1}{2}} a_{H_2} a_{H_2O}^{-1}\right) & (iii) \\ \psi_c = E_{rev} + \eta + \phi_c & (iv) \\ \eta = -\dfrac{RT}{(1-\alpha)nF} ln\left(-\dfrac{i_{bv}}{i_0}\right) & (v) \\ q = \left(\dfrac{\Delta H}{nF} - \psi_c\right) i_{bv} & (vi) \\ \phi_c = \phi_a + R_m i_{bv} \end{cases}$$

and if $i \leq i_{critical}$:

$$\begin{cases} j_{O_2} = \dfrac{i_{bv}}{4F} & (i) \\ j_{H_2O} = -\dfrac{i_{bv}}{2F} & (ii) \\ E_{rev} = \dfrac{\Delta H - T\Delta S}{nF} + \dfrac{RT}{nF} ln\left(a_{O_2}^{\frac{1}{2}} a_{H_2} a_{H_2O}^{-1}\right) & (iii) \\ \psi_c = E_{rev} + L(\eta) + \phi_c & (iv) \\ q = \left(\dfrac{\Delta H}{nF} - \psi_c\right) i_{bv} & (v) \\ \phi_c = \phi_a + R_m i_{bv} \end{cases}$$

### 3.1.3. Membrane

Protonic resistance is modeled as a function of the water content λ and the local temperature as (1)

$$\sigma_m = (33.75\lambda - 21.41).exp\left(-\frac{1268}{T}\right)$$

with λ, the number of water molecules per sulfonic group modelled as (Sammes, 2006)

$$\begin{cases} \lambda = 0.043 + 17.81 a_{H_2O} - 39.85 a_{H_2O}^2 + 36 a_{H_2O}^3 & If \quad 0 < a_{H_2O} < 1 \\ \lambda = 14 + 1.4\left(a_{H_2O} - 1\right) & If \quad 1 < a_{H_2O} < 3 \\ \lambda = 16.8 & If \quad a_{H_2O} > 3 \end{cases}$$

## 3.2. Two-phase situation

The mechanisms of water transfers inside a GDL are still not fully understood (see for instance Straubhaar, 2015): liquid injection from the cathode catalyst layer (injection scenario) and/or condensation/evaporation inside the GDL (condensation scenario) due to temperature and water vapor gradients in the GDL thickness (Figure 8).

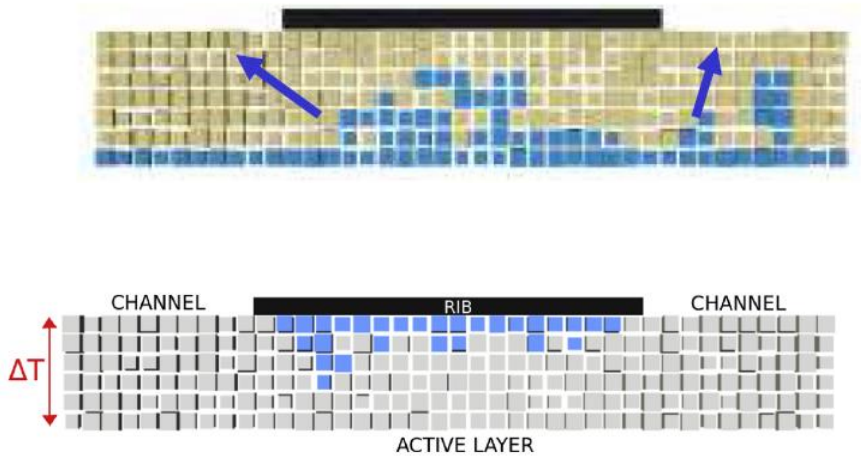


Figure 8: Schematic of injection (top) and condensation (bottom) scenarii (Straubhaar, 2015). Liquid water in blue.

Nevertheless, some recent numerical studies (Straubhaar, 2015; Straubhaar 2016) suggest that water condensation inside the GDL might be the major liquid water formation mechanism involved, at least for a PEMFC operating around 80°C. This is consistent with the condensation scenario studied here as relative water humidity increases from the catalyst layer to the rib/channel interface, as illustrated in Figure 9.

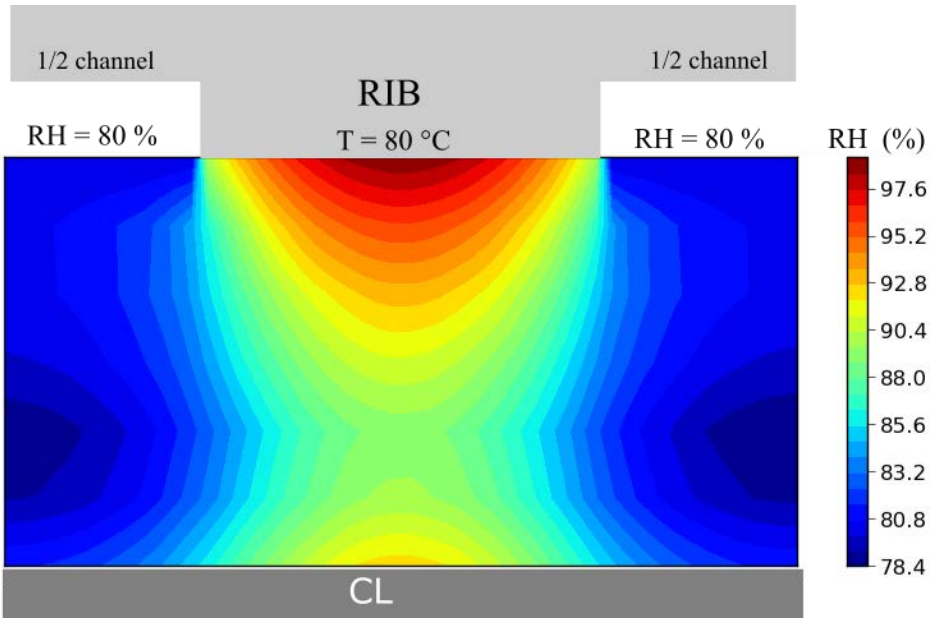


Figure 9 : Local relative humidity in a through-plane slice in GDL for $i$ = 0.8 A/cm²

In some cases, liquid water can be present in the DM close to the MPL but cannot enter the MPL due to a too high capillary pressure inside the MPL.

Under this hypothesis, the liquid water formation modeling in this work is a two-steps approach, as described in (Straubhaar, 2015):

- condensation points are calculated as a function of local conditions (water partial vapor and saturation pressure)
- then the growth of the liquid clusters (formed by condensation) is calculated as a function of local conditions and capillary forces

Note here that the influence of liquid water is taken into account only for gas (oxygen Figure 10 and water vapor) diffusion. According to (2), it could be interesting to include also the influence of liquid water on electrical and thermal conductivities to improve our model.

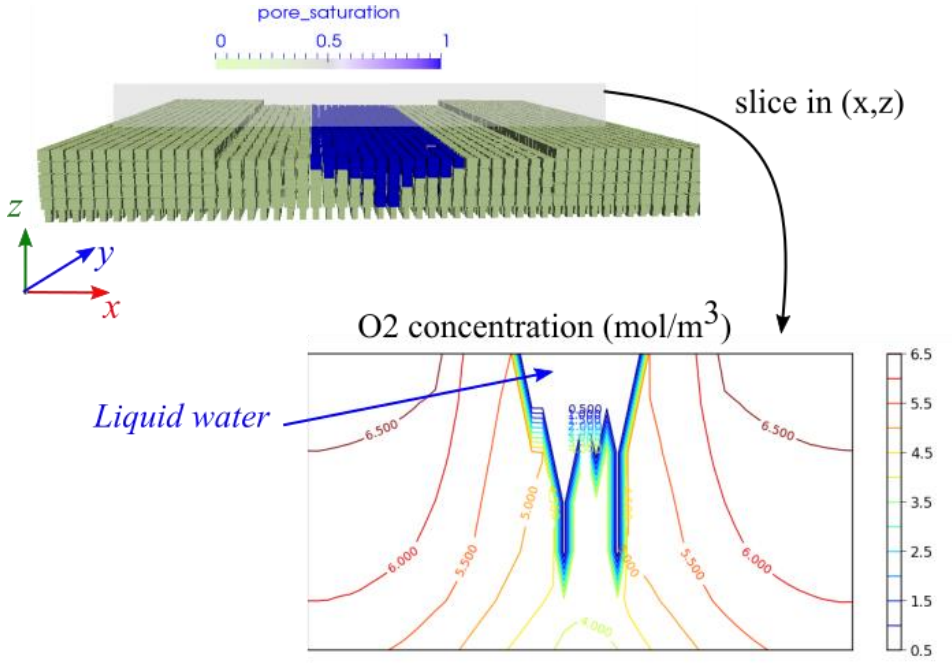


Figure 10 : Impact of liquid water (in blue) produced by condensation on oxygen diffusion in GDL (RH = 80%, T = 80°C, I = 1A/cm²,O2 = 20%)

Liquid water as shown in Figure 10 (blue color) occupies an area below the rib. Consequently this area is no alimented by oxygen any more

## 3.3. Boundary conditions (BC)

The bipolar plate is made of the gas channel and of the rib (Figure 11).

Boundary Conditions at the interface between channel and GDL

Gas concentrations applied as BC on the GDL/channel interface are defined as a function of relative humidity (RH), oxygen relative partial pressure ($P_{O2}$), nitrogen relative partial pressure ($P_{N2}$), gas temperature (T) and total pressure ($P_{tot}$) of gases in the channel as

$$\begin{cases} P_{tot} = P_{H_2O} + P_{O_2} + P_{N_2} \\ P_{H_2O} = x_{H_2O} P_{tot} = RH.P_{sat} \\ P_{O_2} = x_{O_2}(P_{tot} - P_{H_2O}) \\ P_{sat} = exp\left(23.1961 - \frac{3816.44}{T - 46.13}\right) \text{ (Springer et al. 1991)} \end{cases}$$

with $x_i = \frac{n_i}{n_{tot}}$

Assuming ideal gas behavior, we obtain the gas concentrations

$$\begin{cases} c_{H_2O} = \dfrac{P_{H_2O}}{RT} \\ c_{O_2} = \dfrac{P_{O_2}}{RT} \end{cases}$$

In the case of two-phase flows, we assume that the liquid that arises from the GDL evaporates at the interface GDL/channel (no droplet formation on the GDL surface).

Thus at the interface channel/GDL, the following conditions are applied:

- Dirichlet conditions on $C_{H2O}$, $C_{O2}$, $T_c$
- Free exit on liquid water
- Zero flux on electrical potential (current density is zero)

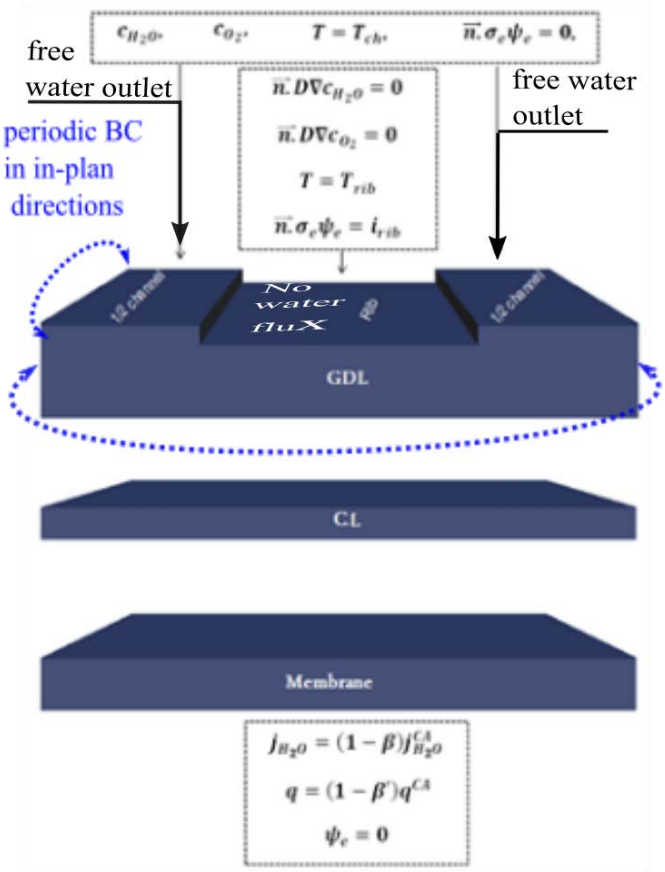


Figure 11: Transfers inside the GDL and boundary conditions in the case of one-phase situation

Thus at the interface rib/GDL, the following conditions are applied:

- Dirichlet conditions on $T_r$, V
- Zero flux on liquid water, vapor water

Boundary Conditions at the interface between membrane and anode

The anode is not included in our cathode model and is modeled as a BC applied to the membrane assuming that $\phi_a = \psi_a = 0$.

The net water and heat fluxes through the membrane from the cathode to the anode are modeled as $(1-\beta'_v)j_{H_2O}$ and $(1-\beta'_q)q$ where $(\beta'_q)$ and $(\beta'_v)$ are partition coefficients implicitly characterizing the membrane water and heat transport properties.

Boundary Conditions on the lateral surfaces

Periodic conditions are applied on both lateral surfaces for each flux (heat, electrical current, liquid water, vapor water, and $O_2$).

# 4. Numerical modeling

## 4.1. Pore Network Modeling in the Diffusion Medium

### 4.1.1. Introduction

Classical continuous modeling based on averaged Generalized Darcy equations is questionable in the case of DM as scale separation is weak, i.e. Rebai and Prat (2009). Another drawback is that the local information of DM (structure, wettability…) is taken into account through effective parameters and thus these models are not well adapted to analyze the efficiency of DM as a function of its local properties, i.e. the impact of non-homogeneities at the rib –channel scale.

The approach used in this work is thus based on an alternative method, pore network modeling, that allows taking into account the local properties of DM. Also, the pore network approach is adapted to try to propose improvements of GDL from simulations.

Pore Network Modeling (PNM) is a mesoscale approach well suited to simulating two-phase transports in porous media at the scale of the microstructure. It has been initially developed for analyzing soils and rocks properties (Blunt, 1997; Blunt, 1998) and especially as regards

the multiphase (oil, liquid) transport (relative permeabilities) or equilibrium (capillary pressure curve) properties. PNM has been applied in the last ten years to analyze liquid transfers in GDL (Chapuis, 2008; Chapuis, 2007; Pulloor, 2011; Hinegaugh, 2010; Sinha, 2008; Gostick, 2007; Ceballos, 2013; Ceballos, 2010; Rebai, 2009) in the case of liquid injection when liquid water is supposed to be formed in the cathode catalyst layer and then enters the GDL. It allowed proposing some first analysis of the influence of wettability (Pulloor, 2011), pore size distribution (Gostick, 2007) on effective transport properties (gas diffusion, relative permeability, capillary pressure…) and then compared to experimental results (Chapuis, 2008; Gostick, 2007; Pulloor, 2011). PNM has shown that classical approaches are not always suited to predict two-phase transports in thin porous media such as GDL, e.g. Rebai and Prat (2009).

Some more recent models, e.g. Straubhaar (2015); Straubhaar et al. (2016), take into account water condensation in the GDL which is suspected to be the major liquid water formation mechanism inside a MEA. The present work is thus based on the assumption that condensation inside the GDL is the driving mechanism for liquid appearance inside the GDL.

PNM is based on the representation of a porous medium by a network of pores (spherical or cubic) and throats (cylindrical or rectangular) connecting the pores. Networks can be structured (as for the cubic network shown in Fig.10a ) or unstructured (morphological) (as for the example shown in Fig.10b)). In the case of regular networks, the distance between the pores is constant and called the lattice spacing. Pores and throats sizes are inputs of the models are can be given by Mercury intrusion porosimetry or more recently by image analysis (Agaesse, 2016).

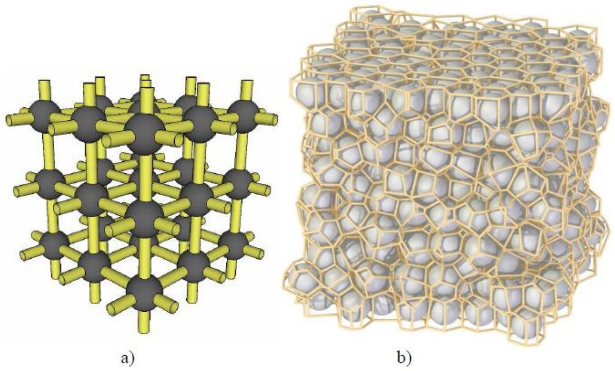


Figure 12 : Example of a structured (a) and unstructured (b) PNM

## 4.2. Application to the DM

The GDL modeled is the SGL 25BC which is the one used as the reference GDL in the IMPACT project. The DM under consideration is thus SGL 25BA (with no MPL).

The PSD and TSD are defined as follows.

The diameter of the throat $d_t$ is randomly assigned in the range [20µm, 34µm] using a Weibull's law as in (5):

$$d_t = d_{t_{min}} + (d_{t_{max}} - d_{t_{min}}) \left[ \left\{ -\delta \, ln\left( \lambda' \left( 1 - exp\left( -\frac{1}{\delta} \right) \right) \right) + exp\left( -\frac{1}{\delta} \right) \right\}^{\frac{1}{\gamma}} \right]$$

with $\delta = 0.1$ , $\gamma = 4.7$, and $\lambda'$ is random number drawn in the interval [0,1].

Once this task is done the diameter of pores is calculated. We initialize the diameter of each pore as the maximum of the diameters of its neighboring throats. And then we adjust the pores diameters by multiplying them by a coefficient to get the desired porosity of the DM.

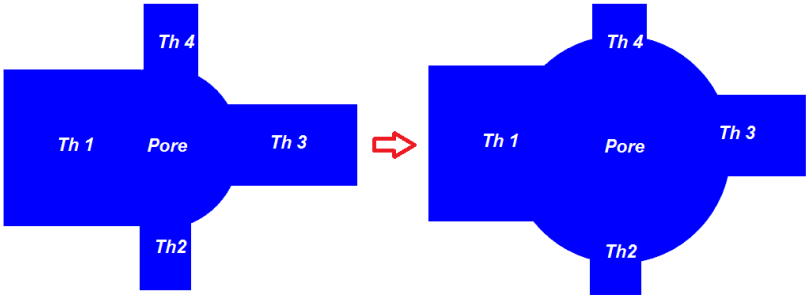


Figure 13 : TSD adjusting pore diameter to get the porosity

Network dimensions

- Lattice spacing $= 50\ \mu m$
- Porosity $\epsilon = 0.8$
- Network size : 52 x 52 x 5

General formulation of mass conservation at each pore $i$ surrounded by pores $j$ is controlled by ensuring

$$\sum_{j\ surrounding\ i} j_{i,j} = P_i$$

where $P_i$ is the local production in pore i and/or the flux applied at the BC of pore i, and $j_{i,j}$ is the flux between pores i and j.

*For electron transfer*,

this leads to $j_{i,j} = g_{i,j}\,(\psi_i - \psi_j)$ with the local conductance

$$g_{i,j} = \beta_e \frac{\sigma_e S_{i,j}}{l_{i,j}}$$

where

- $\sigma_e$ is the local electrical conductivity of the carbon fibers (61000 S/m)
- $S_i$ is the local surface of the throat ($m^2$)
- $l_i$ is the length of the throat (m)
- $\beta_e$ accounts for anisotropy of the GDL

*For heat transfer*:

$$j_{i,j} = g_{i,j}\,(T_i - T_j)$$

$$g_{i,j} = \beta_T \frac{\lambda S_{i,j}}{l_{i,j}}$$

where

- $\lambda$ is the local thermal conductivity of the carbon fibers (129 W/(m.K))
- analogy between electrical and thermal transfer is assumed to calculate the in-plane thermal conductivity

$$\frac{\lambda_{T_{//}}}{\lambda_{T_\perp}} = \frac{\sigma_{e_{//}}}{\sigma_{e_\perp}}$$

*For gas diffusion*:

$$j_{i,j} = g_{i,j}\,(C_i - C)$$

$$g_{i,j} = \beta_C \frac{D_{bin} S_{i,j}}{l_{i,j}}$$

and

- $D_{bin}$ binary coefficient diffusion
  - Water vapor in air : 0.260 cm²/s (Incropera)
  - Oxygen in air : $3.2.10^{-5}.\left(\frac{T}{353}\right)^{1.5}.1/p$ where p is the absolute pressure (Alink, 2013)
- $\beta_C$ is a fitting parameter that allows finding the correct effective gas diffusion conductivity as measured through-plane and in-plane

Solid and fluid networks

In the DM, two networks are thus created: one "fluid network" for the fluid transfers and one "solid network" for electric and thermal transfers.

We consider in the DM that we have the same N number of pores for the solid network and for the fluid network. This is not really consistent with reality as the fluid network should be inserted in the solid network (carbon fibers). This assumption has no influence on the simulations as we consider no fluid/solid interactions.

In the MPL a standard finite volume technique approach on a cubic Cartesian grid is used using the DM lattice spacing as spatial step. So each computational node of the MPL next to the DM s in fact connected to one solid and to one fluid pore in the DM. This assumption will thus help connecting the MPL and CL to the DM as described in 4.5. In fact, the method for the MPL is exactly equivalent to a standard finite volume as long as there is no liquid water formation by condensation in the MPL.We actually consider that the computational nodes in the MPL computational domain can be also regarded as "pores", only to test if condensation can occur in the MPL "pores" (the quotation marks are here to recall that a "realistic" pore network description of the MPL would require a much finer discretization than considered here since the pore sizes in the MPL are orders of magnitude smaller than in the DM). It turns out that condensation rarely occurs in the MPL "pores" in the simulations presented later in the manuscript. In those simulations, liquid condensation, if any, mainly occurs in the DM.

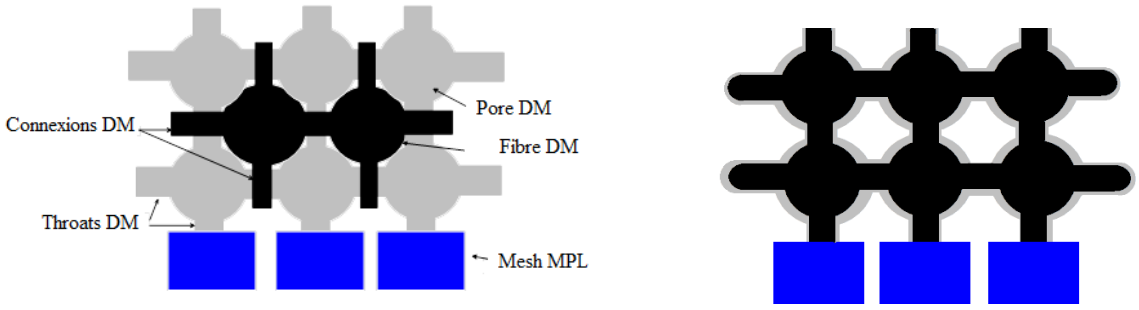


Figure 14 : Solid and fluid networks in the DM as modeled (right) and as in "reality" (left)

In the case of two-phase transfers

Only gas diffusion is modified by liquid water assuming that gas cannot diffuse in pore / throat fully invaded by liquid water. In partially invaded throats or pores we simply multiply local conductance by $(1 - Sat_i)$ where $Sat_i$ is the local water saturation of pore/throat i

$$g_{i,j} = \beta_C (1 - Sat_i) \frac{D_{bin} S_{i,j}}{l_{i,j}}$$

Particular case:

The above rules can lead to unrealistic results when some pores in the first plane of the MPL (the one connected to the CL) are fully occupied by liquid water since the concentration in oxygen and water vapor is not defined in these pores. As a result, the adjacent CL nodes would not produce electricity anymore, which is not representative and would be simply due to the too coarse representation of the MPL in our approach. To avoid this problem. we impose a minimum of oxygen and vapor pressure in CL nodes:

$$P_{O_2 \min} = 100\ Pa \sim 0.5\% \text{ of injected oxygen in channels using air condition}$$

$$P_{H_2O \min} = 100\ Pa \sim 0.2\% \text{ of injected vapor in channels using for RH = 100\%}$$

A more satisfactory approach would have been to a impose a minimum gas conductance in the liquid throat and pores on the ground that the liquid does not fully filled the throats and pores in reality and that passages remain for the gas in the corners of the pores and throats. Also, it can be argued that imposing the saturation vapor pressure at the local temperature would be more realistic. However, this situation, i.e. condensation in MPL, is rare in the simulations presented later in the manuscript and therefore this questionable aspect of the modelling is assumed to have a little impact, if any, on the results presented in Chapters 6 and 7.

*Input parameters*

The input parameters are described in chapter 4 as they are linked to the comparison with experimental results.

## 4.3. Micro Porous Layer and Catalyst Layer

A continuum description is used with some additional hypotheses to model the transport phenomena in the MPL and the catalyst layer (CL)

MPL

The same physical models as for the DM are used with some additional assumptions.

The MPL is meshed in the in-plane directions with the same in-plane mesh (52*52 pores/nodes) and lattice spacing as the DM in order to connect each node of the MPL to a pore of the DM. Two nodes are used in the thickness (Figure 15). Transfers in the plane are thus computed. The MPL is not compressed by the rib as the MPL is much harder than the MPL.

*Input parameters*

The input parameters are described in chapter 4 as they are linked to the comparison with experimental results.

Catalyst layer

The catalyst layer is meshed the same way as the MPL (Figure 15)

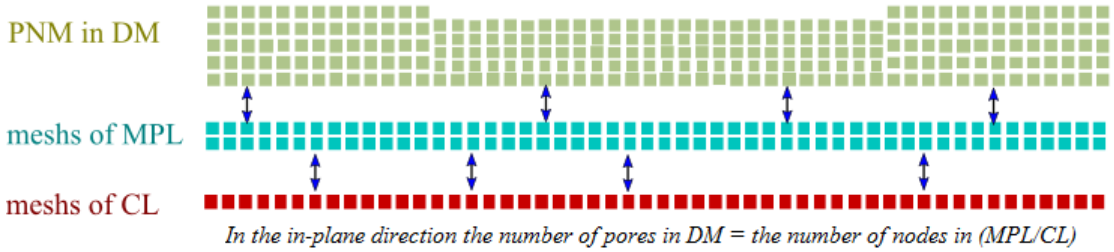


Figure 15: meshing of the DM, MPL and catalyst layer

## 4.4. Membrane

In the membrane, the water content and the proton resistance are calculated as described in 3.1.3.

## 4.5. Interface conditions between the layers (IC)

Interface conditions are defined at the different interfaces between the layers.

We assume no jump condition between the layers.

DM/MPL

Each cell of the MPL is connected to the corresponding throat of the GDL, for fluid and solid transfers (Figure 14).

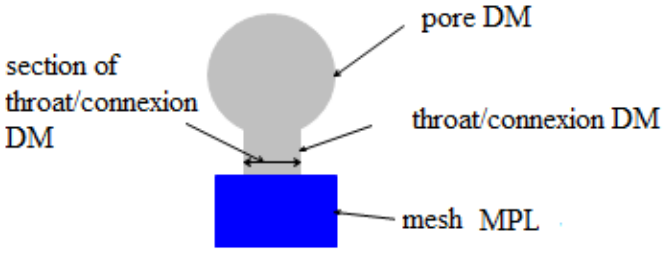


1.1.

Figure 16 : Connection between the MPL and the DM

Since the MPL and DM transport problems are discretized together over a single computational domain the continuity of variables and fluxes at the DM/MPL interface are automatically satisfied.

$$\begin{cases} j_{H_2O}^{MPL} S_{node} = j_{H_2O}^{PNM} S_{throat} (\, mol.s^{-1}) \\ j_{O_2}^{MPL} S_{node} = j_{O_2}^{PNM} S_{throat} \, (\, mol.s^{-1}) \\ i_{bv} S_{pt} = i^{PNM} S_{connexion} \, (A) \\ q^{MPL} S_{node} = q^{PNM} S_{connexion} \, (W) \end{cases}$$

MPL/CL

Each cell of the CL is connected to a fluid and to a solid cell of the MPL.

We assume the continuity of local fluxes of gases, heat and electrical current and a zero flux of local proton current.

CL/membrane

Each cell of the membrane is connected to a fluid cell of the CL.

We assume the continuity of local fluxes of water vapor, heat and protonic current and a zero flux of local electronic current density. Oxygen flux (to reflect oxygen permeation through the membrane) is an input of the model (generally set to zero in the simulations presented in this work).

## 4.6. Algorithm

The local current density distribution is set uniform as an initialization step. Then the heat flux is calculated assuming electrical potential. This is necessary to evaluate whether condensation occurs or not. We can compute then potential .And by imposing this potential value in then interface MPL/CL and the current density in the interface BP/RIB we can resolve electrical problem. The resolution give us a new current density distribution so why we use iterative method. We stop iterations when $i^{n+1} \cong i^n$

The algorithm is summarized in Figure 17.

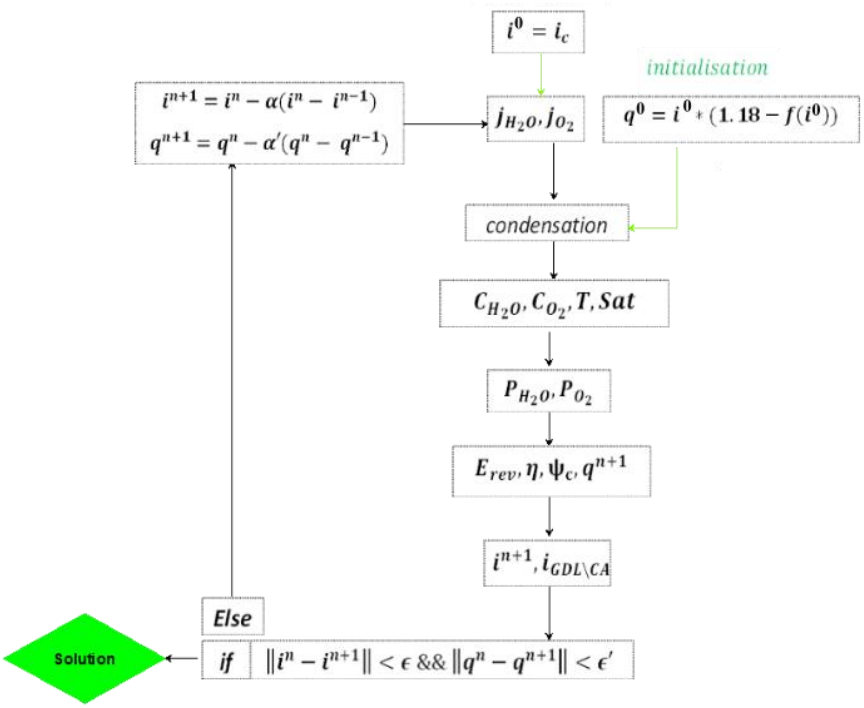


Figure 17 : Algorithm

Note: $\alpha, \alpha'$,are two parameters of the iterative method in the interval [0,1[

Regarding the condensation step we use the same algorithm as the one proposed in (Straubhaar, 2015). Note that all the liquid throats and pores are reset to dry when a new step in the iteration procedure is performed. If there is no liquid water formation this step leads only to compute the local relative humidity in pores.

The condensation algorithm is briefly described below:

- Nucleation step
  - Compute relative humidity in every pore $RH = \frac{P_{H_2O}}{P_{sat}}$.
  - Identify the pores where $RH >= n_c$ with $n_c$ is the nucleation parameter ($\eta_c$ = 1 generally, a value greater than 1 would reflects a possible supersaturation effect in the pore).
    - If $RH < n_c$ in all the pores then there is no condensation
    - otherwise we impose $RH = n_c$ in pores where $RH \geq n_c$ and we recalculate the $RH$ field to test possible appearance of new nucleation sites.
    - This step is stopped if there is no new condensation point anymore and we go to the invasion step
- Invasion step
  - We use classical percolation invasion algorithm (Ceballos, 2013) considering that groups of first neighbor nucleation points form liquid clusters:
    - We compute the mass flow rate of vapor water $\sum_{neighboring\ pores} J_{H_2O}$ at the periphery of each liquid cluster at each invasion step :
      - If $\sum_{neighboring\ pores} J_{H_2O} < 0$ we assume that there is more vapor condensing at the periphery of the considered cluster than liquid water evaporating. Under these circumstances, there is a net liquid water production and the cluster can growth
      - otherwise we assume that the considered cluster has reached an equilibrium and cannot grow any more. (condensation is balanced by evaporation)
    - We stop when each cluster reach a condensation –evaporation equilibrium status or when liquid water reaches the channel.

## 5. Conclusion

In this chapter, we have proposed a model coupling a pore network model (PNM) for describing the transfers in the diffusion medium (DM), a volume-finite like approach in the MPL and 0D models in the catalyst layer and the membranes. The advantage of the PNM is to allow the modeling of the liquid water formation by condensation in the DM using a state-of –

the art condensation PN algorithm (Straubhaar, 2015). Compared to the work of Straubhaar, (2015), the novelty lies in the consideration of the MPL and the coupling with the CL. As a result, this model allows computing the distribution of the current density at the CL /MPL interface or the MPL/GDL interface, as well as other fields like the gas composition or the temperature, whereas the current density distribution was an input data and not an outcome of the computation in the simpler model proposed in Straubhaar (2015).

**References**

(Agaesse, 2016) Validation of pore network simulations of ex-situ water distributions in a gas diffusion layer of proton exchange membrane fuel cells with X-ray tomographic images; Tristan Agaesse; Adrien Lamibrac, Dr; Felix N Büchi,Dr; Joel Pauchet; Marc Prat, Dr ; submitted

(Blunt, 1997) M.J. Blunt, Pore level modeling of the effects of wettability, Soc. Petrol. Eng. J. 2 (1997) 494-510.

(Blunt, 1998) M.J. Blunt, Physically-based network modeling of multiphase flow in intermediate-wet porous media, J. Petrol Sci. Eng. 20 (1998) 117-125.

(Ceballos, 2010) L. Ceballos, M. Prat, Invasion percolation with inlet multiple injections and the water management problem in proton exchange membrane fuel cells, J. Power Sources 195 (2010) 825-828.

(Ceballos, 2013) L. Ceballos, M. Prat, P. Duru, Slow invasion of a nonwetting fluid from multiple inlet sources in a thin porous layer; L. Ceballos and M. Prat; Phys. Rev. E 87, 043005

(Chameau 2010): Project Chameau, Synthèse des études de modélisation des performances ;

(Chapuis, 2007) O. Chapuis, M. Prat, Influence of wettability conditions on slow evaporation in two-dimensional porous media, Phys. Rev. E 75 (2007) 046311.

(Chapuis, 2008) O. Chapuis, M. Prat, M. Quintard, E. Chane-Kane, O. Guillot, N. Mayer, Two-phase flow and evaporation in model fibrous media: Application to the gas diffusion layer of PEM fuel cells, J. Power Sources 178 (2008) 258-268.

(El Hannach, 2011) Simulation et analyse des mécanismes de transfert diphasique dans les couches catalysts de piles à combustible PEMFC; PhD Thesis, University of Toulouse, France, 2011

(T. Erdey-Gruz , 1930) T. Erdey-Gruz and M. Volmer Z. Phys. Chem. (A) 150 (1930) 203-213.

(Freunberger, 2006) Stefan A. Freunberger, Mathias Reum, Jörg Evert, Alexander Wokau, and Felix N. Büchia; Measuring the Current Distribution in PEFCs with Sub-Millimeter Resolution; Journal of The Electrochemical Society, 153-11- A2158-A2165, 2006-

(Gostick, 2007) J.T. Gostick, M.A. Ioannidis, M.W. Fowler, M.D. Pritzker, Pore network modeling of fibrous gas diffusion layers for polymer electrolyte membrane fuel cells, J. Power Sources 173 (2007) 277-290.

(Hinegaugh, 2010) J. Hinebaugh, A. Bazylak, Condensation in PEM Fuel Cell Gas Diffusion Layers: A Pore Network Modeling Approach, J. Electrochem. Soc. 157 (2010) B1382-B1390.

(Karan et al., 2007) Karan, K., Atiyeh, H., Phoenix, A., Halliop, E., Pharoah, J., and Peppley, B. (2007). An experimental investigation of water transport in PEMFCs. Electrochemical and Solid-State Letters, 10(2) : B34_B38.

(LaManna, 2014) J. M. LaManna, S.Chakraborty, J. J. Gagliardo, M. M. Mench, Isolation of transport mechanisms in PEFCs using high resolution neutron imaging, *Int. J. of Hydrogen Energy* 39, 3 3 8 7 - 3 3 9 6 (2014)

(Li et al., 2008) Li, H., Tang, Y., Wang, Z., Shi, Z., Wu, S., Song, D., Zhang, J., Fatih, K., Zhang, J., Wang, H., Liu, Z., Abouatallah, R., and Mazza, A. (2008). A review of water Flooding issues in the proton exchange membrane fuel cell. Journal of Power Sources, 178(1) : 103-117.

(Mann, 2000) Ronald F. Mann, John C. Amphlett, Michael A.I. Hooper, Heidi M. Jensen,

Brant A. Peppley, Pierre R. Roberge, Development and application of a generalised steady-state electrochemical model for a PEM fuel cell; Journal of Power Sources 86-2000. 173–180

(Mann, 2006) R.F. Mann, J.C. Amphlett, B.A. Peppley, C.P. Thurgood, Application of Butler–Volmer equations in the modelling of activation polarization for PEM fuel cells, Journal of Power Sources 161 (2006) 775–781.

(Mathias et al., 2003) Mathias, M., Roth, J., Fleming, J., and Lehnert, W. (2003); Handbook of Fuel Cells : Fundamentals, Technology, Applications, chapter 42 Diffusion media materials and characterization, pages 517_537.

(Park et al., 2006) Park, S., Lee, J.-W., and Popov, B. N. (2006). E_ect of carbon loading

in microporous layer on PEM fuel cell performance. Journal of Power Sources, 163(1) :

357_363.

(Park et al., 2012) A review of gas diffusion layer in PEM fuel cells: Materials

and designs ; Sehkyu Park, Jong-Won Lee, Branko N. Popov, international journal of hydrogen energy 3 7 ( 2 0 1 2 ) pp. 5 8 5 0 - 5 8 6 5

(Pauchet et al, 2012) J. Pauchet, M. Prat, P. Schott, S. Pulloor Kuttanikkad; Performance loss of Proton Exchange Membrane Fuel Cell due to hydrophobicity loss in Gas Diffusion Layer: analysis by multiscale approach combining Pore Network and Performance Modeling; International Journal of Hydrogen Energy, Volume 37, Issue 2, January 2012, Pages 1628-1641;

(Pulloor, 2011) S. Pulloor Kuttanikkad, M. Prat, J. Pauchet, Pore-network simulations of two-phase flow in a thin porous layer of mixed wettability: Application to water transport in gas diffusion layers of proton exchange membrane fuel cells, J. Power Sources 196 (2011) 1145-1155.

(Rachidi, 2011) S. Rachidi Développement et exploitation d'une micro-instrumentation pour les piles à combustible de type PEMFC, Ph-D thesis, 12/12/2011, Grenoble, France

(Rebai, 2009) M. Rebai, M. Prat, Scale effect and two-phase flow in a thin hydrophobic porous layer. Application to water transport in gas diffusion layers of proton exchange membrane fuel cells, J. Power Sources 192 (2009) 534-543.

(Sadeghifar, 2013) H.Sadeghifar, N.Djilali, M.Bahrami, Effect of PTFE on thermal conductivity of gas diffusion layers of PEM fuel cells, Proceedings of the ASME 2013 11th Fuel Cell Science, Engineering and Technology Conference FuelCell2013, July 14-19, Minneapolis, MN, USA (2013)

(Sinha, 2008) P.K. Sinha, C.Y. Wang, Chem. Eng. Sci. Liquid water transport in a mixed-wet gas diffusion layer of a polymer electrolyte fuel cell, 63 (2008) 1081-1091.

(1) T. E. Springer, T. A. Zawodzinski et S. Gottesfeld, Polymer electrolyte fuel cell model, Journal of The Electrochemical Society, vol. 138, no. 8, p. 2334_2342, 1991.

(Straubhaar, 2015) B.Straubhaar, J.Pauchet, M. Prat, Water transport in gas diffusion layers of PEM fuels cells in presence of a temperature gradient. Phase change effect, *Int. J. of Hydrogen Energy*, 40 (35) 11668–11675 (2015)

(Straubhaar, 2016) B.Straubhaar, J.Pauchet, M. Prat, Pore network modelling of condensation in gas diffusion layers of proton exchange membrane fuel cells, submitted (2016)

(Williams et al., 2004) Williams, M. V., Begg, E., Bonville, L., Kunz, H. R., and Fenton, J. M. (2004a). Characterization of gas di_usion layers for PEMFC. Journal of The Electrochemical Society, 151(8) : A1173_A1180.

(Wood, 2006) Wood, D. L. (2006). Fundamental material degradation studies during longterm operation of hydrogen/air PEMFCs. PhD thesis, University of New Mexico.

(Wood and Borup, 2010) Wood, D. L. and Borup, I. R. L. (2010). Estimation of mass-transport overpotentials during long-term PEMFC operation. Journal of The Electrochemical Society, 157(8) : B1251_B1262.

# Chapitre 4
# Calage et validation des modèles

## 1. Introduction

L'objectif de ce chapitre est de définir les valeurs des divers paramètres des modèles de GDL (MPL et DM), couche active et membrane, tels que décrits au chapitre 3. Ceci se fera en déterminant les paramètres des modèles permettant de retrouver, lorsque les mesures sont disponibles, les valeurs mesurées (ou les tendances expérimentales) pour les couches séparées et/ou assemblées. Les résultats obtenus sont décrits dans les paragraphes suivants.

Comme décrit dans le chapitre 3, le modèle développé permet de simuler les cas de fonctionnement sans eau liquide (monophasique) ainsi que ceux avec eau liquide dans la DM (diphasique), l'eau liquide étant produite par condensation dans la DM (nous considérons qu'il n'y a pas d'eau liquide dans la MPL ni dans la CA).

Dans ce chapitre, nous nous intéressons au cas en régime monophasique pour lequel nous disposons de mesures de certains paramètres intrinsèques pour la GDL.

Pour le cas en diphasique, nous n'avons pas fait de comparaisons avec l'expérience dans la mesure où nous n'avons pas identifié de mesures expérimentales de coefficients intrinsèques (coefficient de diffusion relative des gaz, courbe de pression capillaire…) dans ce régime de fonctionnement par condensation.

## 2. Modèle de la GDL

La GDL étudiée est la SGL 25BC dont le support de diffusion (DM) est la SGL 25BA.

Dans un premier temps, les paramètres du modèle de la DM sont calés sur les mesures expérimentales disponibles pour la SGL 25BA puis dans un second temps ceux du MPL sont calés de manière à ce que la GDL simulée (DM + MPL) ait les mêmes propriétés que celles mesurées pour la SGL 25BC.

Comme les données expérimentales ne sont pas toutes disponibles et que les résultats existants montrent une grande variabilité des valeurs mesurées (Figure 19), l'objectif est de définir les paramètres du modèle GDL représentant « correctement » une GDL réelle.

### 2.1. SGL 25BA (sans MPL)

Dans ce paragraphe, le modèle est constitué uniquement de la DM. Il est décrit chapitre 3, § 3.1.1 et schématisé Figure 18.

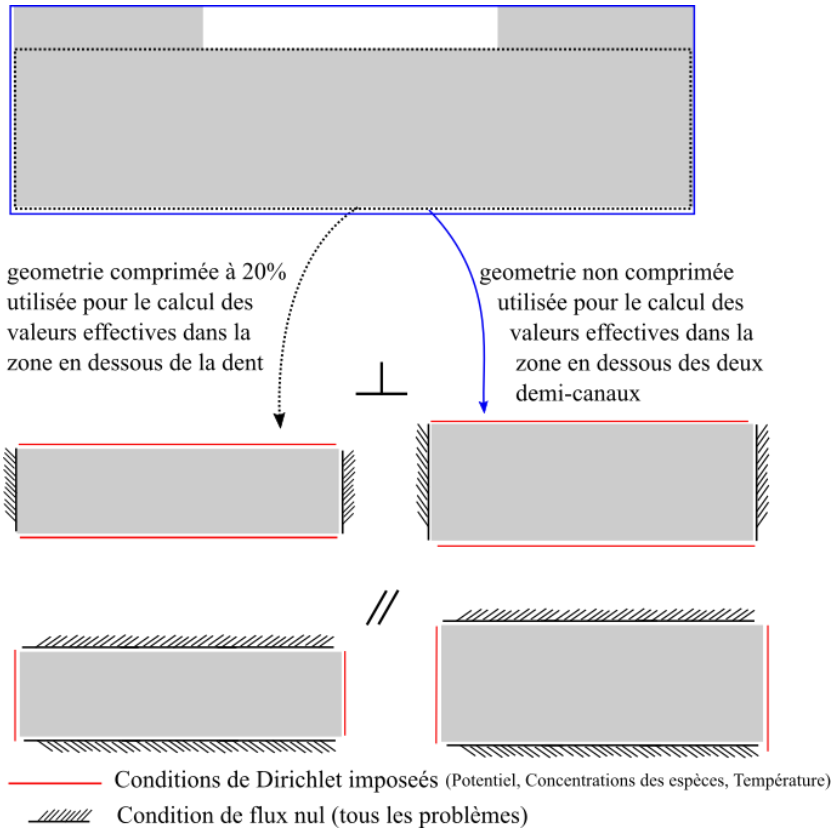


Figure 18 : Représentation du modèle utilisé pour le calage des paramètres de la DM

Pour chaque phénomène physique étudié (transport électronique, chaleur, gaz), des conditions de Dirichlet sont imposées sur les faces de la GDL.

Prise en compte de l'anisotropie

Comme le montrent certaines mesures expérimentales obtenues au CEA (Figure 19), la GDL est fortement anisotrope et ses propriétés dépendent de son écrasement. Elles sont donc différentes sous la dent et sous le canal.

Dans la suite, nous avons considéré que la GDL est comprimée à 20% sous la dent (comme pour les essais) et non comprimée sous le canal.

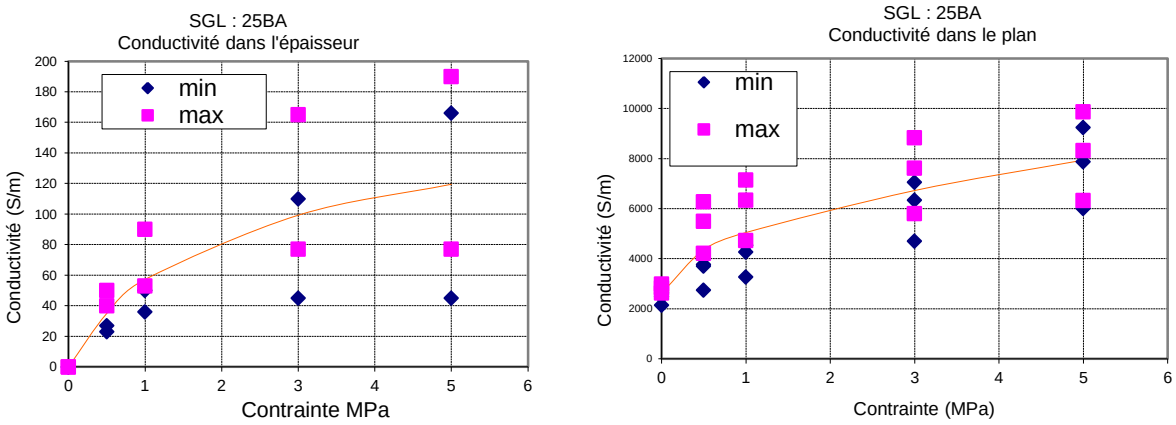


Figure 19 : Conductivités électriques mesurées de la SGL 25BA dans l'épaisseur (à gauche) et dans le plan (à droite)

Afin de prendre ces effets en compte, pour chaque type de transfert simulé (chaleur, électrons, diffusion des gaz) nous intégrons dans le calcul des conductances locales un coefficient de tortuosité β différent dans l'épaisseur et dans le plan et différent pour la zone sous la dent et pour celle sous le canal.

Dans ce qui suit, on note // les grandeurs relatives au transfert dans le plan de la GDL (in-plane) et $\perp$ celles relatives au transfert dans l'épaisseur de la GDL (through-plane).

Forme générale des conductances

Le flux de la grandeur X du pore i vers le pore j est donné par $j_{i,j} = g_{i,j}\,(X_i - X_j)$ avec $g_{i,j}$ la moyenne harmonique des conductances locales $g_i$ des deux demi-pores et du lien qui les connecte (Figure 20) :

$$\frac{1}{g_{i,j}} = \frac{1}{g_{p_i}} + \frac{1}{g_{p_j}} + \frac{1}{g_{th}}$$

$$g_i = \beta \frac{X_e S_i}{l_i}$$

et

- $S_i$ la section de référence du lien/pore dans le lequel passe le flux (m²)
- $l_i$ la longueur de ce lien (m)
- $X_e$ le coefficient représentatif du mode de transfert de la grandeur X
- β le coefficient de tortuosité

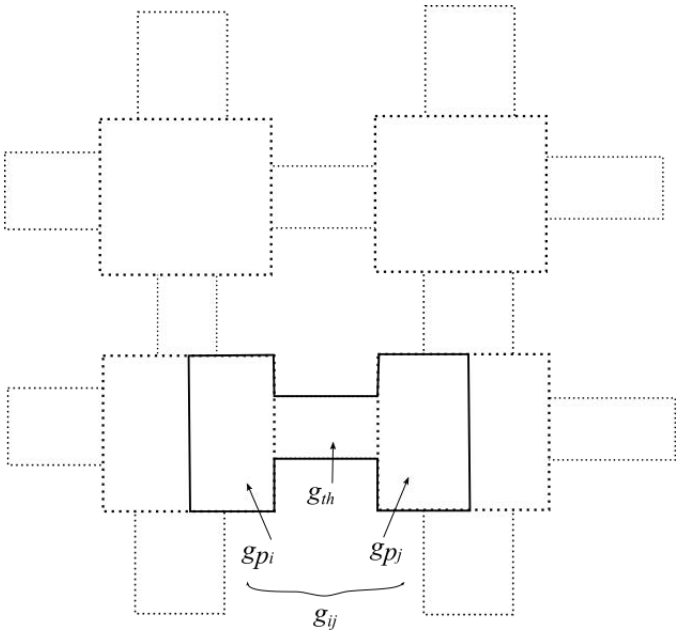


Figure 20 : Conductances locales

Dans les tableaux ci-dessous, on présente :

- Les propriétés effectives expérimentales de la SGL 25BA (lorsqu'elles sont disponibles, sinon nous précisons la GDL sur laquelle les mesures ont été réalisées)
- Ces mêmes propriétés calculées par notre modèle PNM sur la DM (propriétés effectives PNM dans le tableau)
- Les valeurs des coefficients de tortuosité $\beta_i$ qui permettent au modèle PNM de correspondre aux valeurs expérimentales effectives de la SGL 25BA
- Les valeurs des coefficients intrinsèques de transfert de la DM correspondant

Cas de la diffusion des gaz

$$g_i = \beta_i \frac{D_{bin} S_i}{l_i}$$

avec $D_{bin}$ le coefficient de diffusion binaire

- de l'oxygène dans l'air : 0.35 cm²/s (Alink, 2013)
- de la vapeur d'eau dans l'air : 0.260 cm²/s (Incropera)

Les données expérimentales disponibles sont rares car les essais sont difficiles. Dans les cas où les mesures ne sont pas disponibles pour la SGL 25BA, nous avons utilisé celles disponibles pour d'autres supports.

| Diffusion des gaz | Dent | | Canal | |
|---|---|---|---|---|
| | // | ⊥ | // | ⊥ |
| $D_{eff}/D_{bin}$ Valeurs expérimentales | --- | --- | ~ 0.6 (Freudenberg, Chameau 2010) ~ 0.6 (Rashapov and Gostick 2016 )(SGL 25 BA) | • ~ 0.29 ±0.08 (pour $D_{bin}$ = 0.35 cm²/s) (Lamanna and Kandlikar 2011)<br>• Entre 0.08 et 0.12 (James, Choi, and Pharoah 2012) (SGL 34BA) |
| $D_{eff}/D_{bin}$ Valeurs effectives (PNM) | 0.5 | 0.117 | 0.6 | 0.2 |
| $\boldsymbol{\beta_i}$ | 1 | 0.4 | 1 | 0.4 |

Tableau 1 : calage des paramètres de diffusion des gaz de la DM (SGL 25BA)

La comparaison avec les mesures expérimentales d'une GDL non comprimée (sous le canal) conduisent à une valeur de βi égale à 1 dans le plan, ce qui tend à montrer que le réseau de pores considéré représente correctement la diffusion des gaz dans le plan, et qu'au premier ordre il n'est pas nécessaire d'intégrer une tortuosité. Notons néanmoins que cette conclusion est liée à la valeur « moyenne » expérimentale de 0.2 sur laquelle nous avons fait les comparaisons. L'utilisation d'une autre valeur (les résultats expérimentaux sont très dispersés) aurait conduit à une conclusion différente.

Par défaut et en l'absence de valeurs expérimentales, nous avons utilisé les mêmes valeurs de tortuosité pour la GDL comprimée (sous la dent), même si ce point est discutable compte-tenu du fait que la compression déforme la structure ; on pourrait notamment s'attendre à une augmentation de la tortuosité dans le plan lorsque la compression augmente.

Cas du transport électrique

$$g_i = \beta_i \frac{\sigma_e S_i}{l_i}$$

Où $\sigma_e$ est la conductivité électrique du carbone (61000 S/m) qui constitue les fibres de la couche de diffusion.

| Transport électrique | Dent | | Canal | |
|---|---|---|---|---|
| | // | ⊥ | // | ⊥ |
| Valeurs expérimentales (S/m) | 2800~ 5800 (mesures CEA) | 250 (mesures CEA) | 2612 ± 270 (mesures CEA, 25BA) 2516 ~ 5790 (mesures CEA, SGL 24 BA) | 138 (mesures CEA) < 190 (site Sigracet) |
| Valeurs effectives (PNM) (S/m) | 5000 | 254 | 4000 | 138 |
| $\boldsymbol{\beta_i}$ | 1 | 4.2e-2 | 0.8 | 2.2e-2 |

Tableau 2 : Calage des paramètres électriques de la DM (SGL 25BA)

Les propriétés mesurées au CEA (Chameau 2010) correspondent à des compressions de 25% (et non de 20% comme nécessaire dans notre étude). De plus les mesures à 0% de compression dans le plan (Figure 19) sont considérées comme imprécises.

Pour définir alors les valeurs cibles à atteindre par le modèle, nous avons utilisé ces mesures de la manière suivante :

- dans le plan :
    - sous le canal (0% de compression), la valeur cible choisie (4000 S/m) est plus élevée que celle mesurée (Figure 21)
    - sous la dent (20% de compression), la valeur cible (5000 S/m) est définie par une interpolation linéaire entre la valeur cible à 0% de compression et la valeur expérimentale à 25% de compression
- dans l'épaisseur :
    - sous le canal (0% de compression) les valeurs cibles sont celles mesurées expérimentalement
    - sous la dent (20% de compression), les valeurs cibles sont définies par une interpolation linéaire entre la valeur cible à 0% de compression et la valeur expérimentale à 25% de compression

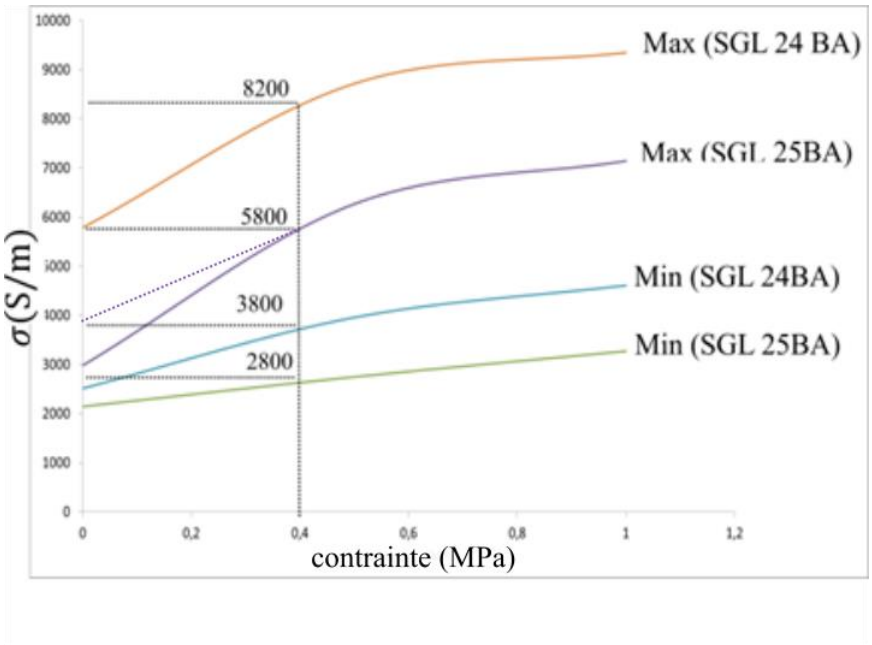


Figure 21 : Conductivité electrique dans le plan d'une SGL 25BA et une SGL 24BA (les valeurs a 0 MPa sont extrapolées) : La compression à 20% correspond à une contrainte de 0.4 MPa

La tortuosité dans l'épaisseur est très inférieure à celle dans le plan. Ceci peut s'expliquer par le fait que le transfert électrique dans le plan se fait principalement par les fibres (orientées principalement dans le plan de la GDL) alors que le transfert électrique dans l'épaisseur est fortement lié aux contacts électriques entre les fibres. Comme cette résistance de contact entre les fibres n'est pas prise en compte dans notre modèle, la tortuosité estimée dans l'épaisseur intègre donc non seulement l'effet de structure mais également les résistances de contact.

Cas du transport thermique

$$g_j = \tau_j \frac{\lambda_T S_j}{l_j}$$

Où $\lambda_T$ est la conductivité thermique du carbone (129 W/(m.K))

Les valeurs de la conductivité thermique dans le plan sont déterminées par analogie avec le problème électrique :

$$\frac{\lambda_{T_{//}}}{\lambda_{T_\perp}} = \frac{\sigma_{e_{//}}}{\sigma_{e_\perp}}$$

| Conductivité thermique | Dent | | Canal | |
|---|---|---|---|---|
| | // | ⊥ | // | ⊥ |
| Valeurs expérimentales (W/m/K) | --- | • ~ 0.237 (épaisseur 190µm), ~0.12 (épaisseur 100µm) (*)<br>• ~ 0.6 W/m/K Mesures CEA (Chameau, 2010) | --- | |
| Valeurs effectives (PNM) (W/m/K) | 6.9 | 0.35 | 4.9 | 0.17 (**) |
| $\beta_i$ (-) | 0.75 | 0.026 | 0.6 | 0.013 |

Tableau 3 : Calage des paramètres thermiques de la DM (SGL 25BA)

(*) Adapté de (Thomas, 2014) pour estimer la valeur à 20% de compression qui nous intéresse…

(**) Calé sur une valeur interne CEA

## 2.2. SGL 25BC (avec MPL)

Dans ce paragraphe, le modèle est constitué de la DM (avec les paramètres déterminés dans le paragraphe précédent) et de la MPL (dont les paramètres vont être déterminés ci-dessous).

Le modèle numérique de la MPL est décrit chapitre 3, § 3.1.1 et 3.4.2.

La MPL est représentée par un réseau de compartiments de taille 52 x 52 x 2 (Figure 22). Cela nous permet de connecter chaque pore du premier plan du DM avec un compartiment de la MPL. Pour plus de détails voir chapitre modélisation.

On considère ici que la MPL a une épaisseur de 50 µm et qu'il n'y a pas pénétration de la MPL dans la DM. Ce dernier point pourrait être une amélioration future du modèle.

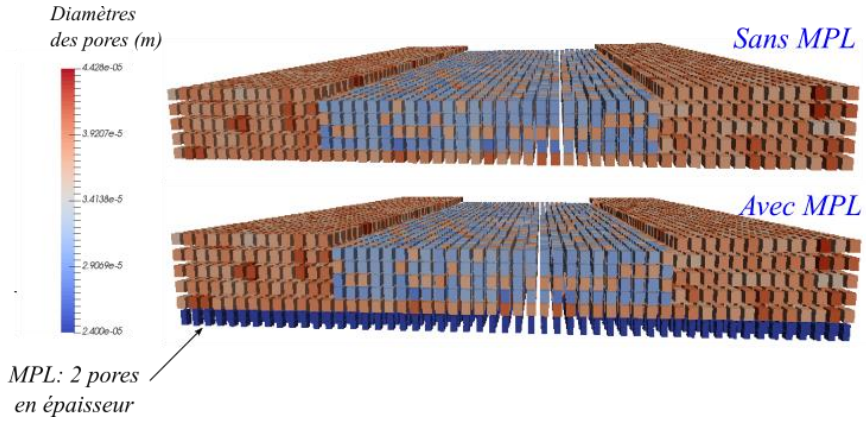


Figure 22 : Prise en compte de la MPL

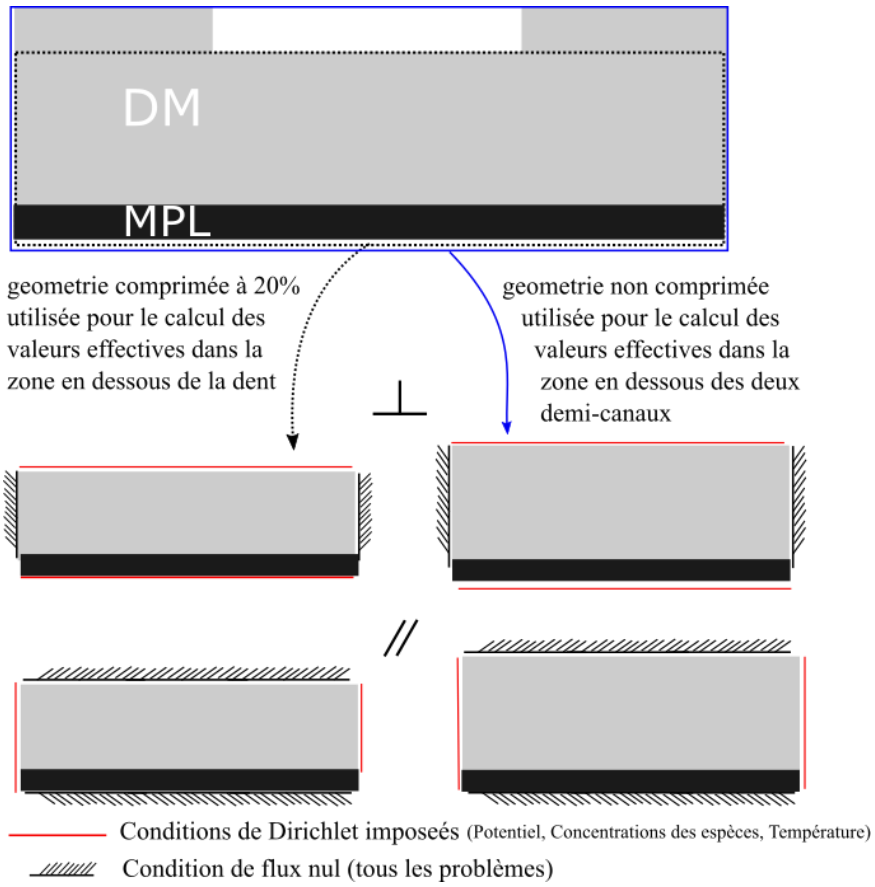


Figure 23 : Représentation du modèle utilisé pour le calage des paramètres de la MPL

Pour chaque phénomène physique étudié (transport électronique, chaleur, gaz), des conditions de Dirichlet sont imposées sur les faces de la GDL.

On considère que la MPL est beaucoup moins déformable que la DM et qu'elle ne se comprime donc pas sous la dent. D'autre part, sa structure granulaire lui confère un comportement isotrope. En conséquence, les propriétés de la MPL sont considérées comme isotropes et identiques sous la dent et sous le canal.

Comme la taille des pores de la MPL est très petite devant la taille du compartiment, les conductances de la MPL ne sont pas directement reliées à la structure locale de la MPL, contrairement au cas de la DM. L'exercice de calage et validation consiste donc à trouver les valeurs des conductances locales (et non des coefficients de tortuosité comme pour la DM) qui permettent de trouver les bonnes propriétés effectives de notre matériau de référence (SGL 25 BC) en tenant compte du calage déjà réalisé sur la SGL 25 BA.

Dans les tableaux ci-dessous, on présente :

- Les propriétés effectives expérimentales de la SGL 25BC (lorsqu'elles sont disponibles, sinon nous précisons la GDL sur laquelle les mesures ont été réalisées)
- Ces mêmes propriétés calculées par notre modèle PNM sur l'assemblage DM + MPL (valeurs effectives PNM dans le tableau)
- Les valeurs des conductances du MPL qui permettent au modèle PNM de correspondre aux valeurs expérimentales effectives de la SGL 25BC
- Les valeurs des coefficients intrinsèques de transfert de la MPL correspondant à ces conductances

Cas de la diffusion des gaz

| Diffusion des gaz | Dent | | Canal | |
|---|---|---|---|---|
| | // | ⊥ | // | ⊥ |
| $D_{eff}/D_{bin}$ Valeurs expérimentales | --- | --- | --- | ~ 0.17 (*) |
| $D_{eff}/D_{bin}$ Valeurs effectives (PNM) | 0.5 | 0.08 | 0.6 | 0.1 (**) |
| $g_j$ (MPL)($m^3/s$) | 1.9 x $10^{-9}$ | 1.9 x $10^{-9}$ | 1.9 x $10^{-9}$ | 1.9 x $10^{-9}$ |
| $D_{eff}/D_{bin}$ (MPL) | 0.04 | 0.04 | 0.04 | 0.04 |

Tableau 4 : calage des paramètres de diffusion des gaz de la SGL 25BC

(*) valeur extraite de (Lamanna, 2011) pour $D_{bin}$ = 0.35 $cm^2/s$ (vapeur d'eau à 1bar et 80°C)

(**) valeur estimée à partir de mesures CEA sur la GDL Freudenberg H23T1015C1 et conservée par manque de temps, même s'il aurait été préférable de prendre la valeur déduite de (Lamanna, 2011).

Ces résultats confirment que la MPL diffuse beaucoup moins bien les gaz que la DM dans toutes les directions. Elle contribue à réduire fortement la diffusion effective totale de la GDL.

Cas du transport électrique

Comme pour la 25BA, les propriétés mesurées au CEA (Chameau 2010) correspondent à des compressions de 25% (et non de 20% comme nécessaire dans notre étude). De plus les mesures à 0% de compression dans le plan sont considérées comme imprécises.

Pour définir alors les valeurs cibles à atteindre par le modèle, nous avons procédé comme pour la 25BA:

- dans le plan :
    - sous le canal (0% de compression), la valeur cible choisie (4300 S/m) respecte la variation des valeurs expérimentales
    - sous la dent (20% de compression), la valeur cible (5500 S/m) est définie par une interpolation linéaire entre la valeur cible à 0% de compression et la valeur expérimentale à 25% de compression
- dans l'épaisseur :
    - sous le canal (0% de compression) les valeurs cibles sont celles mesurées expérimentalement
    - sous la dent (20% de compression) les valeurs cibles sont celles mesurées expérimentalement

| Transport électrique | Dent | | Canal | |
|---|---|---|---|---|
| | // | ⊥ | // | ⊥ |
| Valeurs expérimentales (S/m) | 3412 ~ 7148 (mesures CEA) | --- | 2815 ~ 4891 (mesures CEA) | <195 (site Sigracet 100 Pa) |
| Valeurs effectives (PNM) (S/m) | 5500 | 300 | 4300 | 170 |
| $g_j$ (MPL) (S) | 0.2 | 0.2 | 0.2 | 0.2 |
| Valeurs effectives de la MPL (S/m) | 2500 | 2500 | 2500 | 2500 |

Tableau 5 : Calage des paramètres électriques de la SGL 25BC

On constate ici que la MPL est plus conductrice électrique que la DM dans l'épaisseur mais moins conductrice que la DM dans le plan.

Dans le plan, ceci peut s'expliquer par une meilleure conduction électrique le long des fibres de la DM (orientés majoritairement dans le plan de la DM) qui assurent un meilleur transport électrique que les points de contact entre les grains.

Dans l'épaisseur, le transport est majoritairement lié aux contacts (entre les fibres pour la DM et entre les grains pour la MPL), mais comme la MPL est moins poreuse (~ 40%) que la DM (~ 80%), le transport effectif est meilleur dans la MPL.

Cas du transport thermique

| Conductivité thermique | Dent | | Canal | |
|---|---|---|---|---|
| | // | ⊥ | // | ⊥ |
| Valeurs expérimentales (W/m/K) | --- | ~ 0.235 (*) (12) | --- | --- |
| Valeurs effectives (PNM) (W/m/K) | 4.6 | 0.25 | 4.3 | 0.17 |
| $g_j$ (MPL) (W/K) | 2 | 2 | 2 | 2 |
| Valeurs effectives de la MPL (W/m/K) | 2.5 | 2.5 | 2.5 | 2.5 |

Tableau 6 : Calage des paramètres thermiques de la SGL 25BC

(*) Adapté de (Thomas, 2014) pour estimer la valeur à 20% de compression qui nous intéresse

Notons ici que les valeurs estimées par notre démarche pour le MPL (2.5 W/m/K) sont environ 10 fois plus élevées que certaines valeurs récemment publiées (0.2 W/m/K) obtenues de manière numérique (Thomas, 2014).

On constate ici également que la MPL est plus conductrice thermiquement que la DM dans l'épaisseur mais moins conductrice que la DM dans le plan. Ceci peut s'expliquer de la même manière que pour le transport électrique, par analogie.

### 2.3. Influence des paramètres de calage

Pour analyser l'importance de ce calage nous comparons quelques résultats avant et après calage, dans le cas de la géométrie étudiée avec les dents et les canaux.

A chaque fois, nous imposons des conditions de Dirichlet sur les deux faces de la GDL (coté couche active et coté dent/canal).

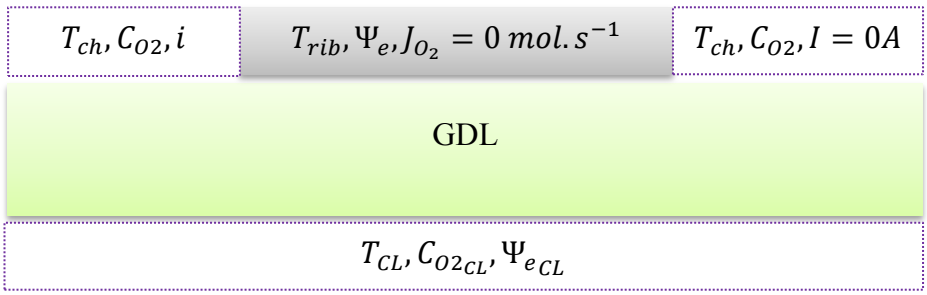


Figure 24 : modèle de la GDL pour l'analyse de l'effet des paramètres de calage

Les paramètres après calage définis aux paragraphes précédents pour la MPL et la DM.

Avant le calage tous les coefficients de tortuosité pour tous les problèmes sont pris égaux à 1.

Après calage | Avant calage

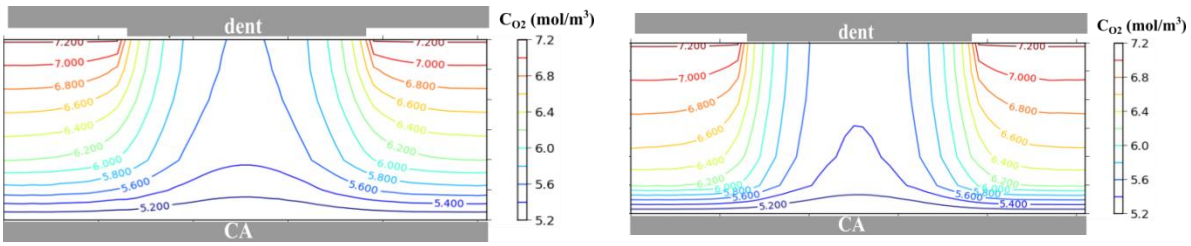


**Problème de diffusion des gaz :** La MPL diffuse moins que la DM ; la zone en dessous de la dent est mieux alimentée en oxygène après calage

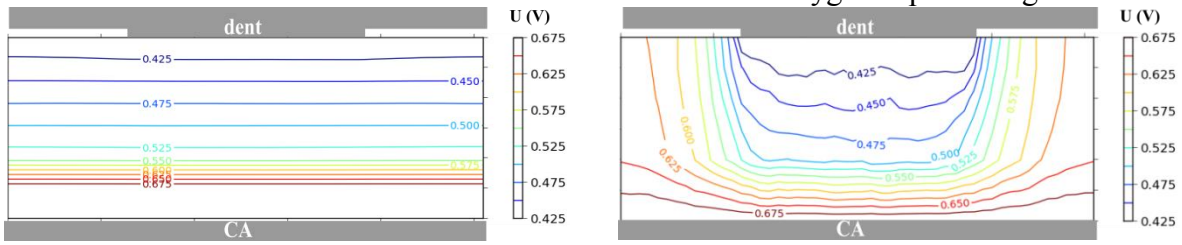


**Problème électrique :** la MPL conduit mieux que la GDL à travers le plan et le calage lisse l'effet de la dent vu le rapport entre la conductivité électrique dans le plan et à travers le plan

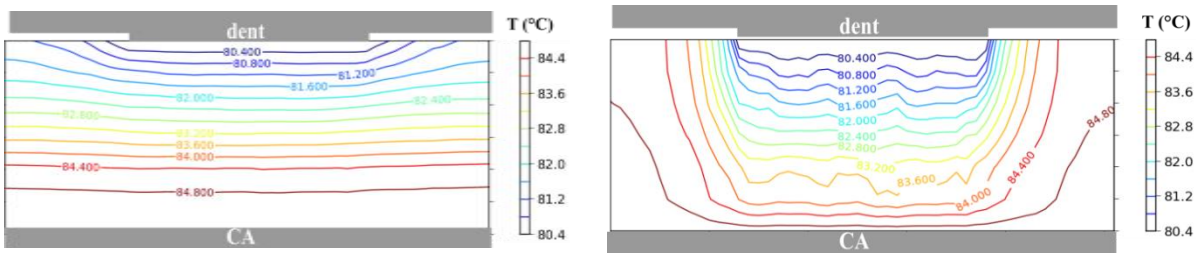


**Problème thermique :** les conclusions sont identiques au problème électrique, vu l'analogie que nous adaptons entre les transferts électrique et thermique

## 3. Modèle de la CA

### 3.1. Introduction

Comme détaillé dans le chapitre modélisation (chapitre 3), la couche active est prise en compte dans les conditions aux limites de la MPL. A chaque compartiment de la MPL est associé un compartiment de la couche active dont le modèle est basé sur la relation de Butler-Volmer inversée, telle que décrite au chapitre 3.

Cette inversion permet d'exprimer le potentiel en fonction de la densité de courant demandée. Les paramètres sont issus d'expériences réalisées au CEA.

Dans ce paragraphe, sauf mention particulière, le modèle est constitué de la CA seule ; il est décrit chapitre 3, § 3.1.2.

## 3.2. Détermination des paramètres

En vue de valider ce modèle, nous analysons sa sensibilité à certains paramètres comme la valeur de l'humidité relative dans les canaux, la fraction de l'oxygène et la température.

Nous discutons également la valeur de $\gamma_{H2O}$ relatif à l'activité de la vapeur d'eau dans la relation de Butler-Volmer.

Le cas de référence (conditions définies dans le canal) dans la suite des calculs est défini par

| HR | $O_2$ | T | P | $P_N$ |
|---|---|---|---|---|
| 80 % | ***20 %*** (fraction molaire dans l'air sec) | 80 °C | 1.5 bar | 0.9 bar |

### 3.2.1. Sensibilité à l'humidité relative (HR)

Le gaz transporté dans les canaux est composé de l'oxygène, l'azote et la vapeur d'eau :

$$P_{tot} = P_{H_2O} + P_{O_2} + P_N$$

La variation de $P_{H_2O}$ entraine donc soit :

1. une variation de $P_{tot}$, avec $P_{O_2}$ constant
2. une variation $P_{O_2} + P_N$ et $P_{tot}$ reste fixe, dans ce cas aussi on peut supposer que $P_{O_2}$ ne varie pas et que $P_N$ varie.

Dans tous les résultats qui suivent je choisis l'option 1.

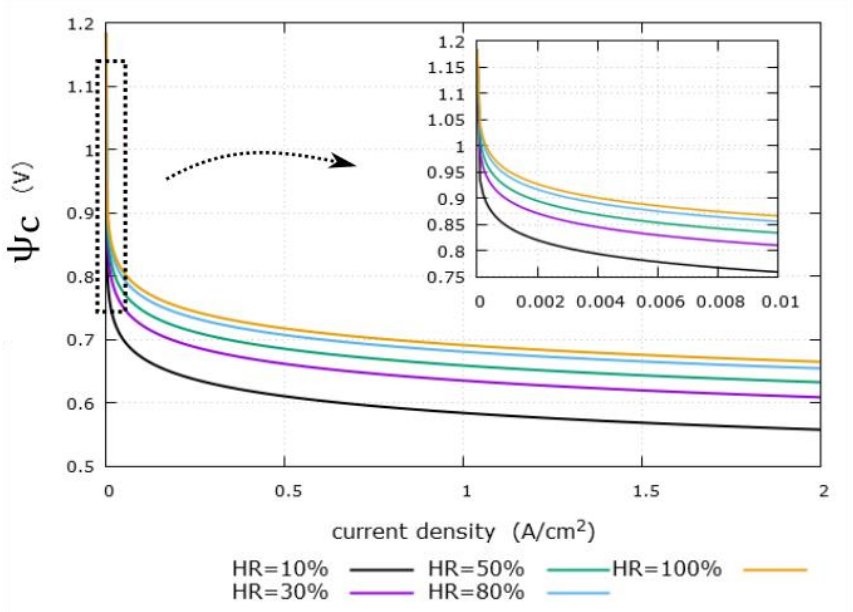


Figure 25 : Simulation de l'effet de HR sur les performances

A titre d'illustration, des résultats expérimentaux sont donnés (Figure 26) comme exemple de la sensibilité des performances à l'humidité relative des gaz. La tendance de notre modèle est la bonne même si les sensibilités sont plus importantes que celles obtenues expérimentalement. Ceci peut être lié au fait que les couches actives utilisées (Figure 26) sont différentes de celles pour lesquelles le calage a été effectué dans (Chameau, 2010). Pour être plus précis, il aurait été nécessaire de refaire le calage de ces paramètres mais cela représente un travail conséquent qui dépasse le cadre de ce travail.

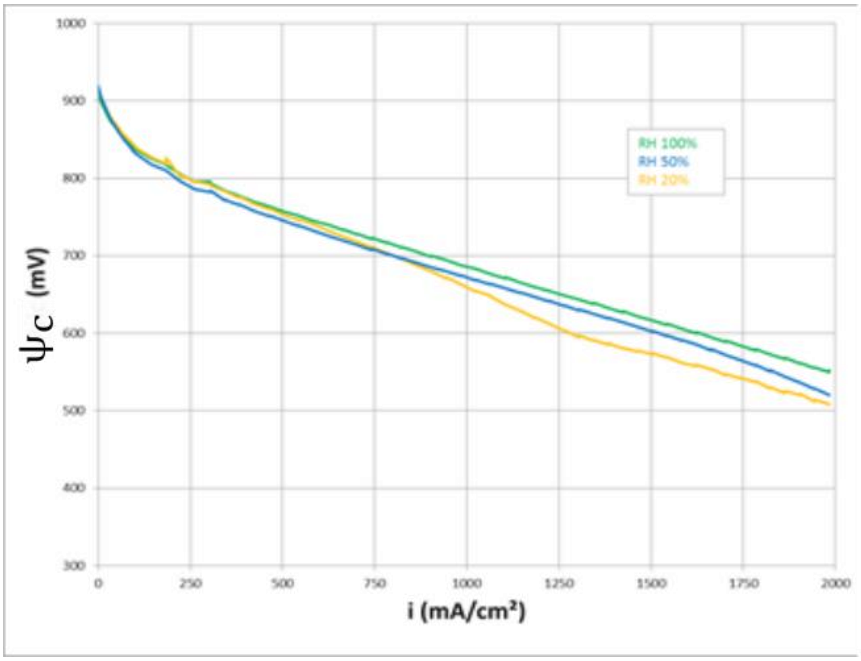


Figure 26 : Exemple de résultats expérimentaux pour la GDL 25B

### 3.2.2. Sensibilité à l'oxygène ($O_2$)

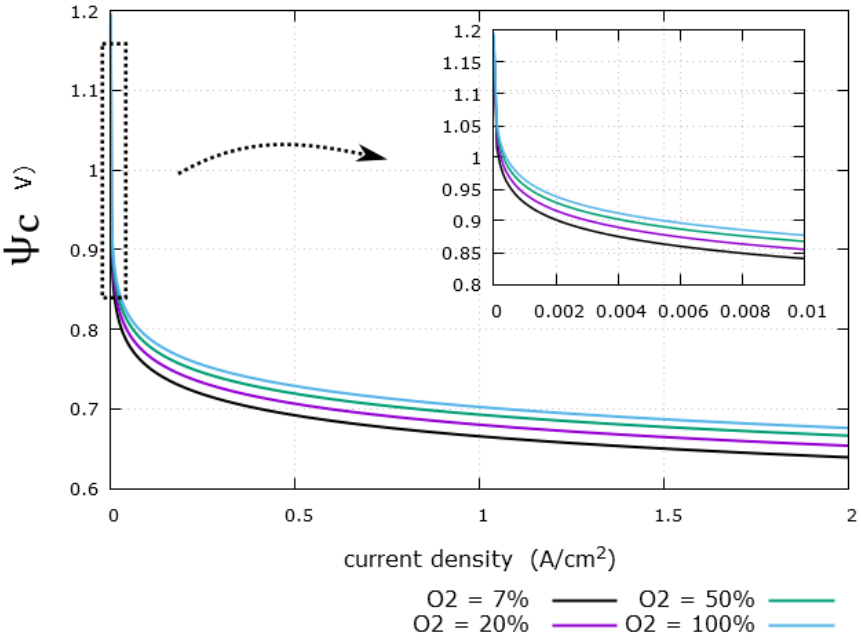


Figure 27 : Effet de la fraction de l'oxygène sur les performances

L'effet de l'oxygène illustré dans la Figure 27 est qualitativement en cohérence avec les résultats des expériences ; l'augmentation de la fraction d'oxygène entraîne une augmentation des performances.

### 3.2.3. Sensibilité à la température (T)

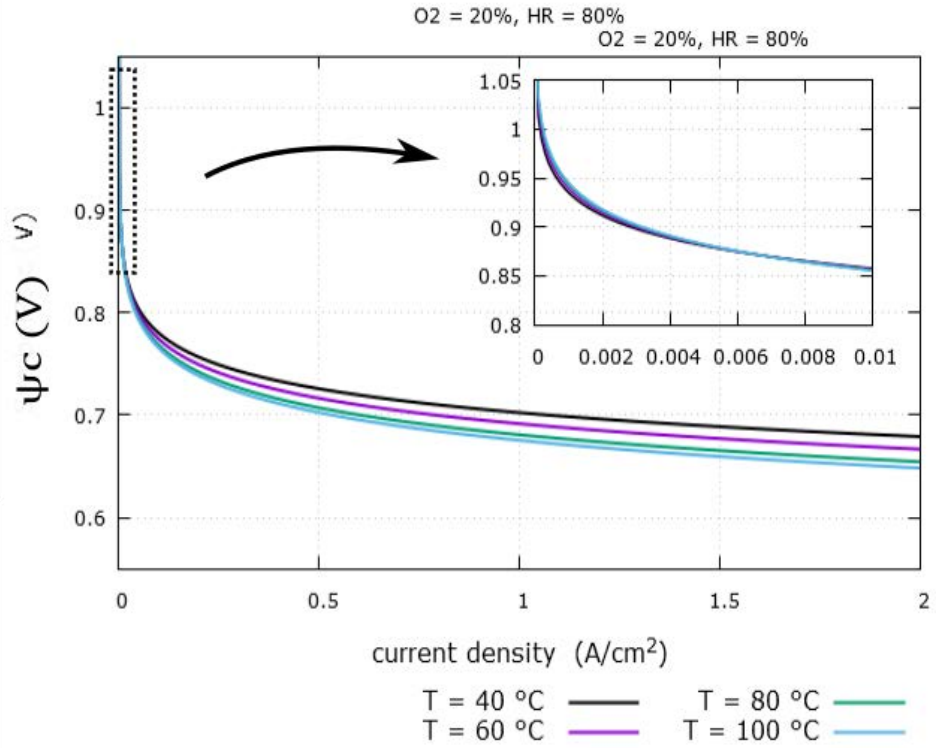


Figure 28 : Effet de la température sur les performances RH = 80% et O2 = 20%

Sans tenir compte de la membrane ni de l'effet de la température sur les activités des réactifs, la Figure 28 montre une augmentation des performances lorsque la température augmente.

## 4. Modèle de la membrane

Le modèle de membrane est décrit chapitre 3, § 3.1.3.

La membrane modélisée (membrane Nafion d'épaisseur 12.5 µm) est prise en compte uniquement par sa résistance Ohmique qui dépend de la température et de l'humidité relative (voir chapitre modélisation pour plus de détails) :

$$\sigma_m = (33.75\lambda - 21.41).exp\left(-\frac{1268}{T}\right)(\text{S/M})$$

Le chargement en eau $\lambda$ est le nombre de molécules d'eau par site sulfoné :

$$\lambda = 0.043 + 17.81a_{H_2O} - 39.85a_{H_2O}^2 + 36a_{H_2O}^3$$

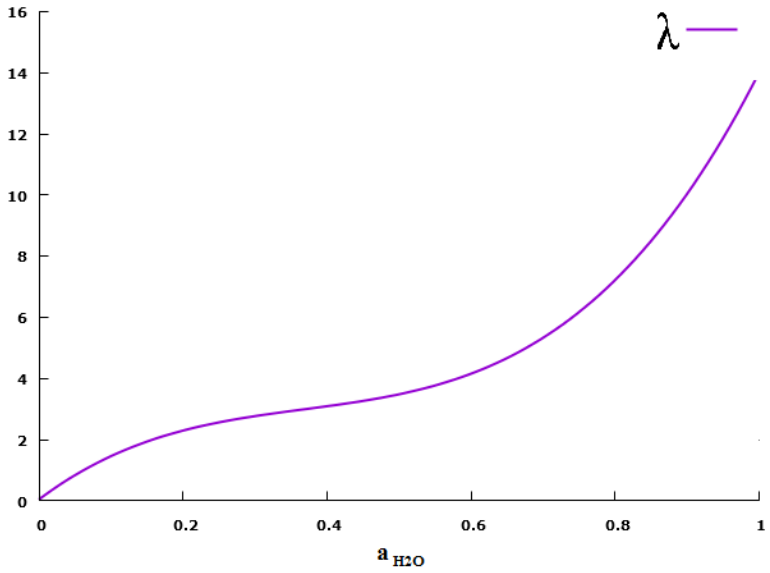


Figure 29 : variation du ʌ en fonction de l'activité de la vapeur d'eau

Les courbes Figure 30 montrent la variation de la résistance ohmique de la membrane en fonction de ces deux paramètres.

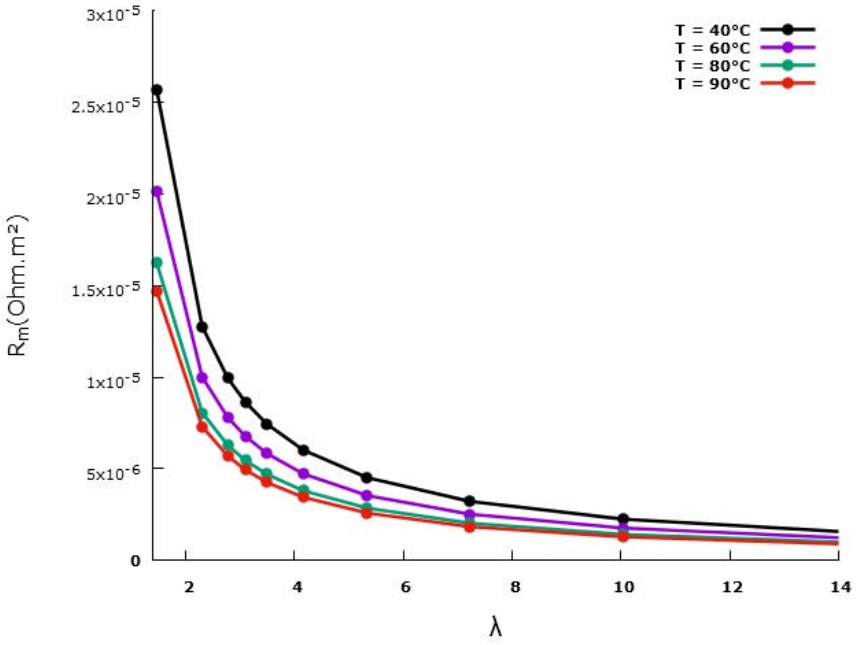


Figure 30 : Effet de la température et de Λ sur la résistance Ohmique de la membrane

La membrane est d'autant plus conductrice des protons que son chargement en eau λ et sa température sont élevés

## 5. Couplage couche active et membrane

Certains paramètres ont un double effet à la fois sur la couche active et sur la membrane, comme par exemple l'humidité relative et la température. C'est pour cette raison que dans ce paragraphe nous analysons la sensibilité de HR et de T sur un modèle qui couple les modèles de GDL et de couche active, tels que décrits précédents.

(a) Effet HR

(b) Effet T

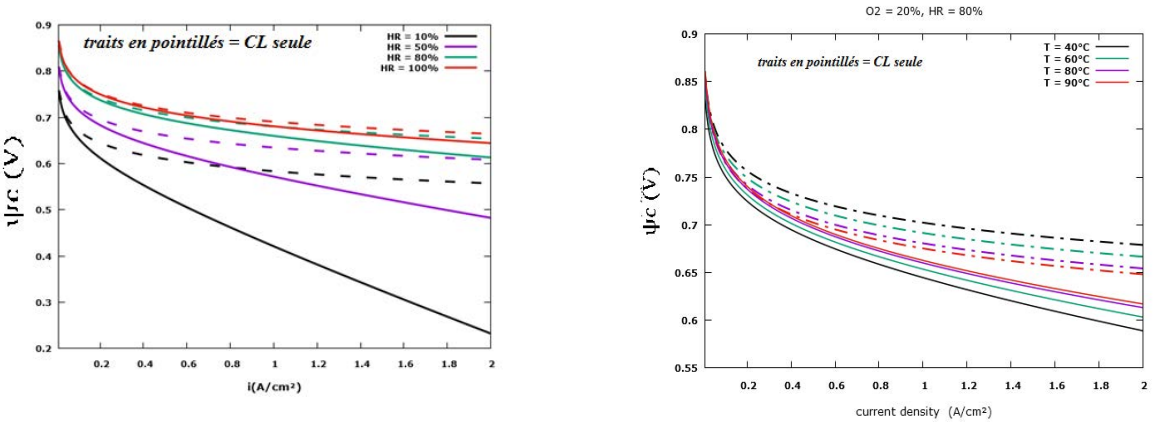


Figure 31 : Effet de la prise en compte de la membrane : sensibilité à l'humidité relative et à la température, couche active seule (traits en pointillés) et avec la membrane (traits en continus)

La Figure 31 (a) montre que le système est plus sensible à l'humidité relative en ajoutant la membrane à la couche active. Par exemple à très faible HR (= 10%) la membrane est sèche et les performances chutent rapidement. Cette figure prouve également que pour les fortes HR la membrane est peu influente sur les performances ce qui est cohérent avec l'effet de HR sur sa résistance protonique.

La Figure 31 (b) montre que, dans le cas de la couche active seule, les performances sont meilleures avec de faibles températures, cependant en rajoutant la membrane les tendances s'inversent : On a des meilleures performances avec des fortes températures et dans ce cas la membrane n'a pas un grand effet (pour des faibles densités de courant) car elle est mieux conductrice. Mais pour des températures inférieures à 60°C, la résistance protonique de la membrane augmente et les performances chutent.

Dans le cas où on intègre la GDL (Figure 32), les performances diminuent et on commence à voir la limite de diffusion » au-delà de 1.5 A/cm².

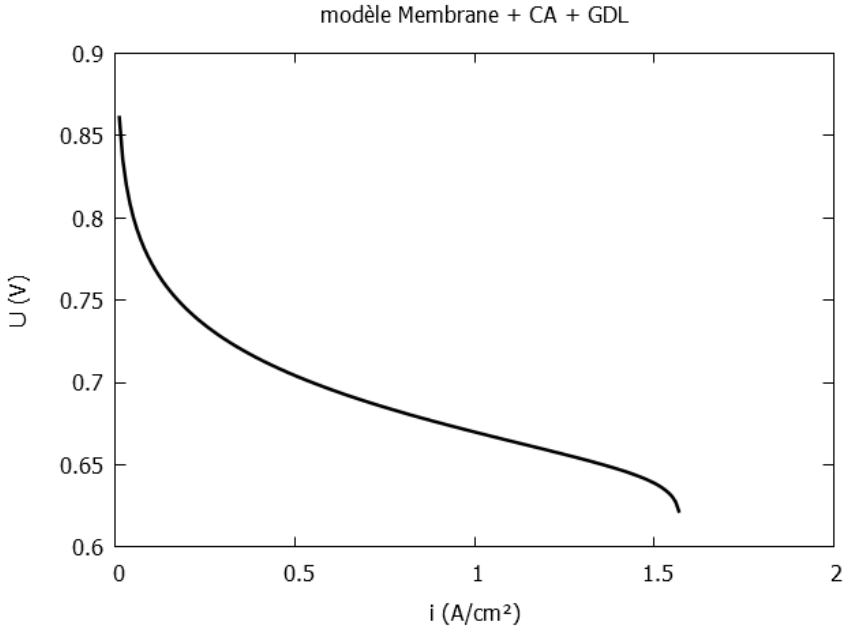


Figure 32 : Effet de la prise en compte de la GDL

## 6. Conclusion

Les modèles numériques de DM, MPL, couche active et membrane ont été comparés à des expériences afin de définir les valeurs les plus pertinentes des paramètres de ces modèles.

Ces modèles vont être maintenant exploités pour étudier les diagrammes de condensation (chapitre 5), l'impact de l'eau liquide sur la distribution de courant entre la dent et le canal (chapitre 6) et l'impact des conditions de mouillabilité sur les distributions de phase liquide et gaz dans la DM (chapitre 7).

**Références**


1. Springer TE, Zawodzinski TA, Gottesfeld S. Polymer Electrolyte Fuel Cell Model. J Electrochem Soc. 1991;138(8):2334.

2. Sadeghifar H, Djilali N, Bahrami M. Effect of PTFE on Thermal Conductivity of Gas Diffusion Layers of PEM Fuel Cells. Proc ASME 2013 11th Fuel Cell Sci Eng Technol Conf FuelCell2013. 2013;1–11.

3. Oberholzer P, Boillat P, Siegrist R, Kästner A, Lehmann EH, Scherer GG, et al. Simultaneous neutron imaging of six operating PEFCs: Experimental set-up and study of the MPL effect. Electrochem commun [Internet]. Elsevier B.V.; 2012;20(1):67–70. Available from: http://dx.doi.org/10.1016/j.elecom.2012.03.038

4. Gostick JT, Ioannidis MA, Fowler MW, Pritzker MD. Pore network modeling of fibrous gas diffusion layers for polymer electrolyte membrane fuel cells. J Power Sources. 2007;173(1):277–90.

5. Pauchet J, Prat M, Schott P, Kuttanikkad SP. Performance loss of proton exchange membrane fuel cell due to hydrophobicity loss in gas diffusion layer: Analysis by multiscale approach combining pore network and performance modelling. Int J Hydrogen Energy. 2012;37(2):1628–41.

6. Straubhaar B, Pauchet J, Prat M. Water transport in gas diffusion layer of a polymer electrolyte fuel cell in the presence of a temperature gradient. Phase change effect. Int J Hydrogen Energy [Internet]. Elsevier Ltd; 2015;40(35):11668–75. Available from: http://dx.doi.org/10.1016/j.ijhydene.2015.04.027

7. Ceballos L, Prat M. Slow invasion of a fluid from multiple inlet sources in a thin porous layer: Influence of trapping and wettability. Phys Rev E - Stat Nonlinear, Soft Matter Phys. 2013;87(4):1–18.

8. Alink R, Gerteisen D. Modeling the liquid water transport in the gas diffusion layer for polymer electrolyte membrane fuel cells using a water path network. Energies. 2013;6(9):4508–30.

9. Rashapov RR, Gostick JT. In-Plane Effective Diffusivity in PEMFC Gas Diffusion Layers. Transp Porous Media [Internet]. Springer Netherlands; 2016; Available from: http://link.springer.com/10.1007/s11242-016-0648-4

10. Lamanna JM, Kandlikar SG. Determination of effective water vapor diffusion coefficient in pemfc gas diffusion layers. Int J Hydrogen Energy [Internet]. Elsevier Ltd; 2011;36(8):5021–9. Available from: http://dx.doi.org/10.1016/j.ijhydene.2011.01.036

11. James JP, Choi H-W, Pharoah JG. X-ray computed tomography reconstruction and analysis of polymer electrolyte membrane fuel cell porous transport layers. Int J Hydrogen Energy [Internet]. 2012 Dec [cited 2016 Jan 14];37(23):18216–30. Available from: http://www.sciencedirect.com/science/article/pii/S0360319912018794

12. Thomas A, Maranzana G, Didierjean S, Dillet J, Lottin O. Thermal and water transfer in PEMFCs: Investigating the role of the microporous layer. Int J Hydrogen Energy [Internet]. 2014 Feb [cited 2016 Feb 11];39(6):2649–58.

# Chapter 5
# Gas diffusion layer condensation diagram in proton exchange membrane fuel cells.

**Abstract**

For given operating conditions, the condensation diagram gives the local critical current density marking the onset of liquid water formation by condensation in the GDL as a function of the relative humidity in the gas channel. The GDL is free of liquid water for current densities lower than the critical one. The model presented in Chapter 3 is used to explore the impact of the operating temperature and the GDL and MPL transport properties as well as other parameters on the condensation diagram.

## 1. Introduction

As discussed in Straubhaar et al. (2016), there is no doubt that the condensation of water vapor is a major mechanism of liquid water formation in the cathode gas diffusion layer (GDL) of proton exchange membrane fuel cell (PEMFC), at least for PEMFC operating at not too low temperatures, i.e. typically around 80°C. As shown in Straubhaar et al. (2016), the occurrence of liquid water by condensation in a GDL depends on various factors, such as the operating conditions and the properties, thermal and diffusive properties in particular, of the PEMFC components. For a given system and given operating conditions, the formation of liquid water is expected for a sufficiently high current density $i$ and a sufficiently high relative humidity $RH_{ch}$ in the feeding gas (air or oxygen) channel. For lower values in current density and / or relative humidity, the water formed in the catalyst layer (CL) can actually be totally transferred in vapor phase through the GDL. Under these circumstances, there is no liquid water in the GDL. The GDL is dry. A dry GDL is the most favorable situation as regards the oxygen access to the CL since liquid water is a barrier to the oxygen transport within the GDL.

As illustrated in Fig.1, this led to introduce the concept of condensation diagram, e.g. Straubhaar et al. (2015), Straubhaar et al. (2016). For a given system, this diagram gives the operating conditions ($i$, $RH_{ch}$) leading to a dry GDL or a wet GDL, i.e. a GDL with liquid water formed by condensation. The line in Fig.1 marking the boundary between the "dry" operating conditions and the "wet" boundary conditions corresponds to the curve $i_c(RH_{ch})$, where $i_c$ is, for a given $RH_{ch}$, the "critical" current density, i.e. the minimum current density leading to condensation.

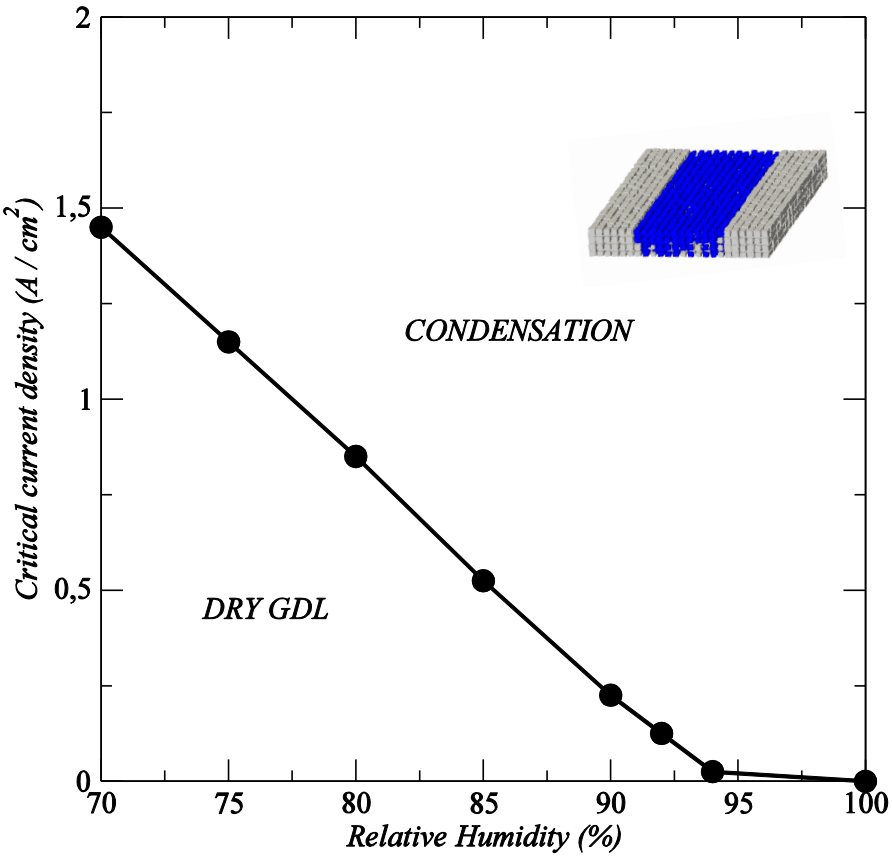


Fig.1: Condensation diagram. It corresponds to the reference case defined in § 3.1

As in Straubhaar et al. (2016). the condensation diagram depicted in Fig.1 was obtained from numerical simulations. Although the concept could of course be used in relation with experimental data, e.g. such as the ones provided in Oberholzer and Boillat (2014) for example, the condensation diagram is also studied in the present paper from numerical simulations. To construct the diagram, the method consists in determining the local relative humidity fields with the GDL, i.e. $RH = p_v(x,y,z) / p_{vs}(T(x,y,z))$, where $p_v$ is the local water vapor partial pressure, $p_{vs}(T(x,y,z))$ is the water vapor saturation pressure and $T$ is the local temperature. Condensation is supposed to occur when there is at least one point within the GDL where

$$RH \geq \eta \qquad (1)$$

The parameter $\eta$ is referenced to as the nucleation parameter, i.e. Straubhaar et al. (2016). It reflects the fact that the onset of condensation may occur for a local relative humidity slightly greater than 1.

The model used for the present study is significantly more advanced than the one used in Straubhaar et al. (2016). In the latter, the micro porous layer (MPL) was not considered and the current density distribution at the interface between the GDL and the Catalyst Layer (CL) was an input data. There was no coupling between the GDL and the CL. As a result, the oxygen transport was actually not computed. By contrast, the MPL is included in the model used in the present paper, coupling with the CL is performed and the electrical and oxygen transports are computed. This opens up the possibility to study the impact of much more parameters on the condensation diagram under presumably much more representative conditions.

The description of the model is relatively long. Although this is of course an important contribution of the present paper, we believe that many readers will not be interested in the details of the modeling but mostly on the discussion of the condensation diagram. For this reason, the model is presented in the Appendix so that we can concentrate on the main results in the main text.

The paper is organized as follows. As just mentioned, the computational model is mostly presented in the Appendix. The computational domain is described in section 2. Results on the condensation diagram are presented in section 3. A conclusion is presented in section 4.

## 2. Computational domain and model

In the following, we consider the GDL as a two-layer porous system, made of the "fibrous" Diffusion Medium (DM) and of the "granular" Micro-Porous-Medium (MPL) coated on the DM (Fig. 2). The MPL penetration into the DM is not considered in this study.

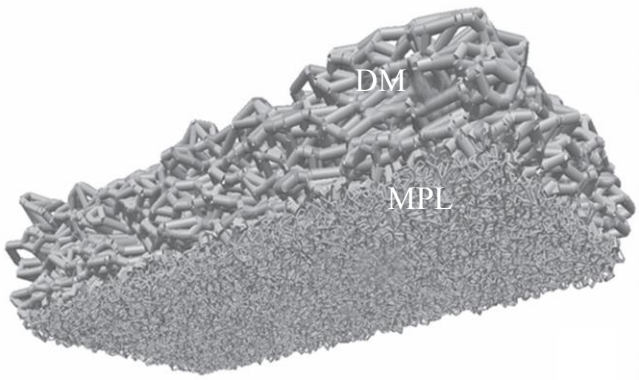


Fig.2. Computer-generated model of GDL as a DM / MPL assembly.

The computational domain considered in the study is depicted in Fig.3. It corresponds to an elementary unit cell containing a bipolar plate rib and two gas half channels. The geometrical dimensions of the various layers are specified in Fig.3. For the GDL, the indicated thickness corresponds to the uncompressed GDL, i.e. below the channels.

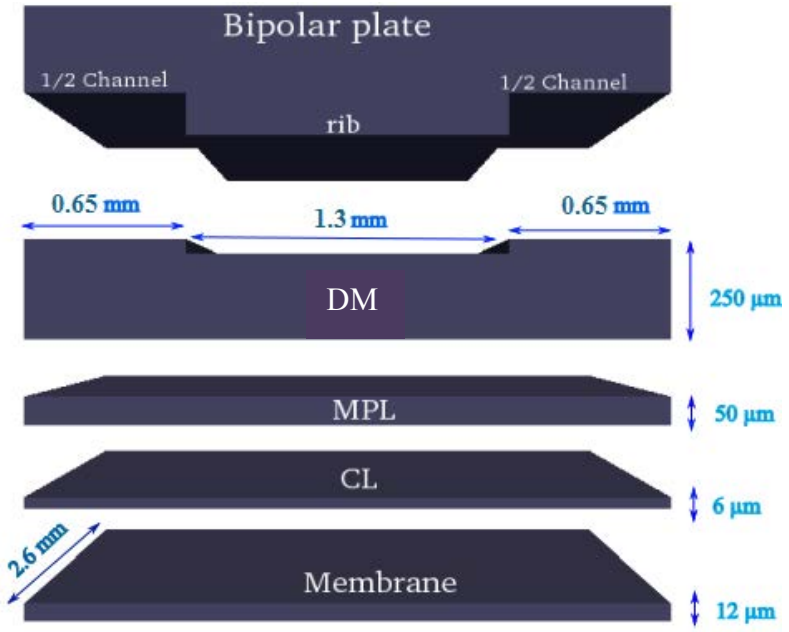


Fig.3: The computational domain is a unit cell of a full PEMFC cell.

| | *Effective thermal conductivity* ($Wm^{-1}K^{-1}$) | *Effective electrical conductivity* (S/m) | *Effective diffusion coefficient* | *Thickness (microns)* | *Porosity* |
|---|---|---|---|---|---|
| *Symbol* | $\lambda$ | $\sigma$ | $D^*/D$ | | |
| | 2.5 | 2500 | 0.04 | 50 | 0.4 |

Table 1: MPL properties.

| | *DM thickness (µm)* | | *Porosity* | |
|---|---|---|---|---|
| *Symbol* | $\delta_c$ | $\delta_{uc}$ | $\varepsilon_c$ | $\varepsilon_{uc}$ |
| | 200 | 250 | 0.72 | 0.8 |
| | *Effective thermal conductivity* ($Wm^{-1}K^{-1}$) | | | |
| *symbol* | $\lambda_{//c}$ | $\lambda_{//uc}$ | $\lambda\perp_c$ | $\lambda\perp_{uc}$ |
| | 6.9 | 4.9 | 0.35 | 0.17 |
| | *Effective electrical conductivity* (S/m) | | | |
| *symbol* | $\sigma_{//c}$ | $\sigma_{//uc}$ | $\sigma\perp_c$ | $\sigma\perp_{uc}$ |
| | 5000 | 4000 | 254 | 138 |
| | *Effective diffusion coefficient (-)* | | | |
| *symbol* | $D_{//c}/D$ | $D_{//uc}/D$ | $D\perp_c/D$ | $D\perp_{uc}/D$ |
| | 0.5 | 0.6 | 0.12 | 0.2 |

Table 2: DM properties (corresponding to SGL 25 BC).

The properties of the various layers have been specified from various sources, internal to CEA or from the literature. There are summarized in Tables 1- 2 for the MPL and the GDL. The procedure was as follows. First we specified the properties of the DM starting from known values for SGL25BA. Then the properties of the MPL/DM assembly were specified so as to reproduce available experimental data for the SGL 25BC. In particular, the diffusion coefficient of the MPL was specified so as to obtain a value for the assembly consistent with the results reported in LaManna and Kandlikar (2011).

The useful properties of the other layers, namely the catalyst layer (CL) and the membrane are given in the Chapter 3 together with the model used to compute the condensation diagram.

As described in Chapter 3, the GDL is represented by a 52 x 52 x 7 Rebai et al (2009), Gostick et al (2007) pore network (the figures indicate the number of pores along the directions of a Cartesian grid). Actually, the pore network representation is not essential as long as there is no liquid water within the GDL. Under these circumstances, the computation of the oxygen and water vapor transfer over the pore network is in fact not different than when using a classical finite volume method on a Cartesian grid. Actually, a pore network approach was chosen in the prospect of computing liquid water formation and transport since as discussed in previous works, e.g. Straubhaar et al. (2016) and references therein, pore network models are well adapted to describe the liquid phase distribution in a thin system such as a GDL. This is also for this reason that a 3D computational domain has been chosen as 3D is mandatory to simulate correctly the growth and coalescence of liquid water clusters, e.g. Straubhaar et al. (2016).

## 3. Results

## 3.1 Definition of a reference case

A reference case is first defined. It corresponds to the values of operating conditions and parameters reported in Tables 1-2 and Table 3. Typically, we will vary the values of only one parameter at a time, the values of the other parameters corresponding to the reference values.

Table 3. Reference conditions ($T$ is the bipolar plate temperature equal to the gas temperature, $P$ the total gas pressure, $p_{O2}$ the oxygen partial pressure in the channel) and reference values for partition coefficients $\beta_{H2O}$ and $\beta_T$ and nucleation parameter $\eta$.

| $T$ (°C) | $P$ (bar) | $p_{O2} / P$ | $\beta_T$ | $\beta_{H2O}$ | $\eta$ |
|---|---|---|---|---|---|
| 80 | 1.5 | 0.21 | 0.8 | 0.8 | 1 |

As described in Chapter 3, the partition coefficients $\beta_{H2O}$ and $\beta_T$ correspond to the fractions of the water production rate and heat production rate respectively directed toward the cathode GDL, the complementary fractions (1-$\beta_{H2O}$) and (1-$\beta_T$) correspond to the fractions of these production rates directed toward the anode GDL.

Note that the oxygen partial pressure will not be varied and will always have the value specified in Table 3.

As discussed in the introduction the occurrence of condensation is directly related to the local relative humidity field in the GDL $RH = p_v(x,y,z) / p_{vs}(T(x,y,z))$. From the expression of $RH$, it can be inferred that condensation onset points should first roughly correspond to points of higher vapour partial pressures, which means the points in the GDL located the farthest from the channel since the channel corresponds to a region of the GDL where the vapour pressure is minimum. This is illustrated in Fig. 4, which schematically shows that the water vapor diffusion paths to the channel are longer from the region below the rib than from the region right below the channel.

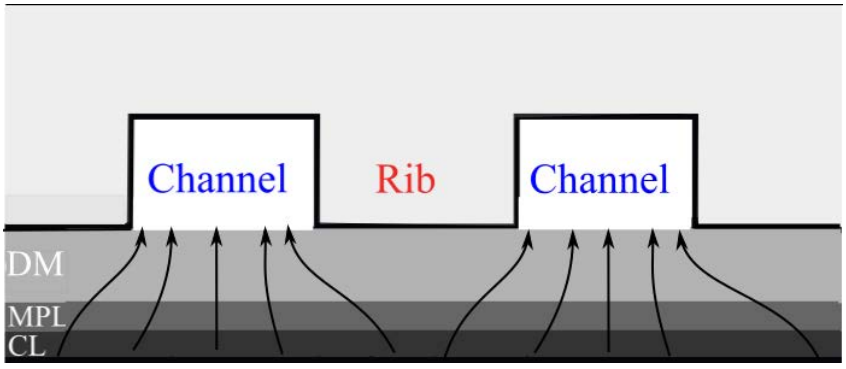


Fig.4: Schematic illustration of the water vapor diffusion paths within the GDL. The longer diffusion paths between the region below the rib and the channel imply greater water vapor partial pressure in the region of the GDL below the rib.

Then since the saturation vapour pressure $p_{vs}$ is an increasing function of the temperature, the occurrence of condensation is more likely in a region of lower temperature. Since the lowest temperature within the GDL is right below the rib, the most likely location of first condensation spots is the region of the GDL in contact with the middle of the rib. This is illustrated in Fig. 5.

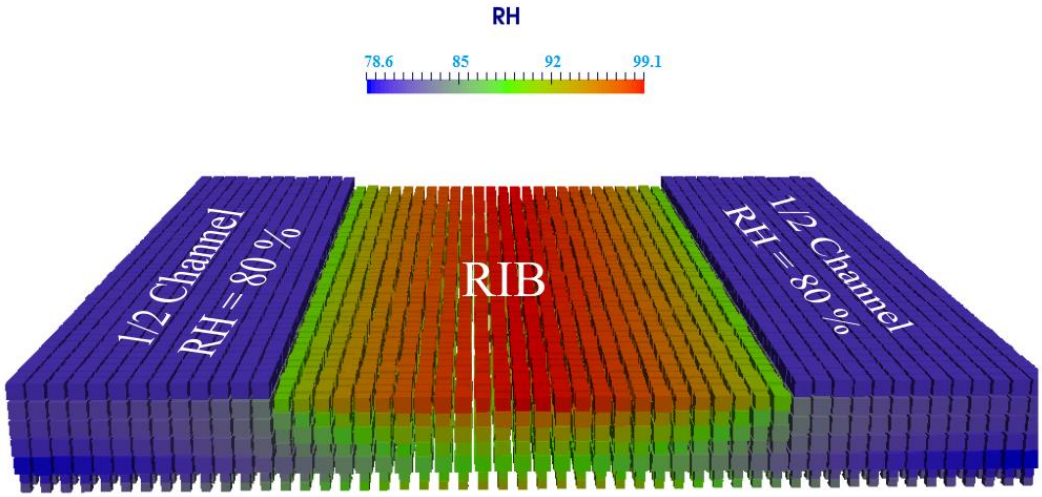


a)

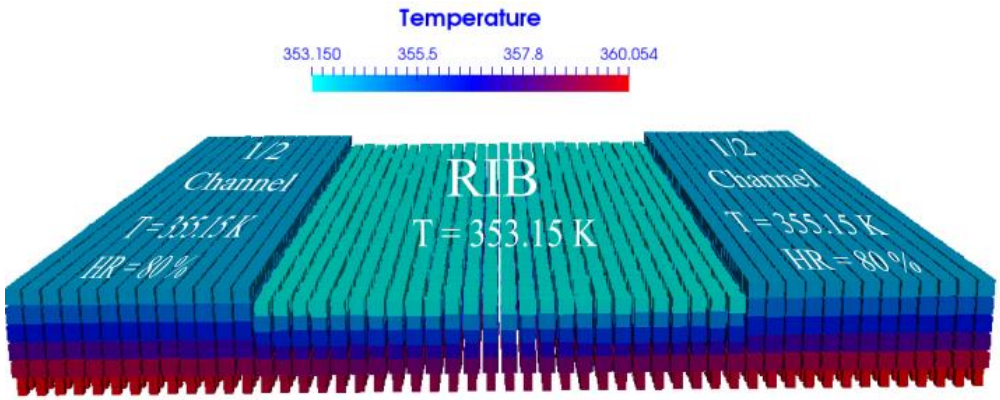


b)

Fig.5: Example of local relative humidity field (a) and temperature field within the GDL at critical current density for the reference case ($RH_{ch}$ = 80%) )

From these considerations, it is obvious that the parameters affecting the condensation diagram are the parameters affecting the temperature and vapor pressure distributions right below the rib. In what follows, the impact of some of these parameters on the condensation diagram is explored.

### 3.2 Impact of nucleation parameter

As can be seen from Fig.6, the nucleation parameter has not a great impact on the condensation diagram. Increasing the nucleation parameter makes the condensation to occur for a greater value of the local vapor partial pressure, i.e. a greater water production. Therefore, the critical current increases with an increasing nucleation parameter. It is expected that the nucleation parameter is close to 1 since condensation is generally expected to occur without significant metastability effects. Since, its impact is relatively weak, all the simulations presented in the next sub-sections were performed for the reference value ($\eta$ = 1).

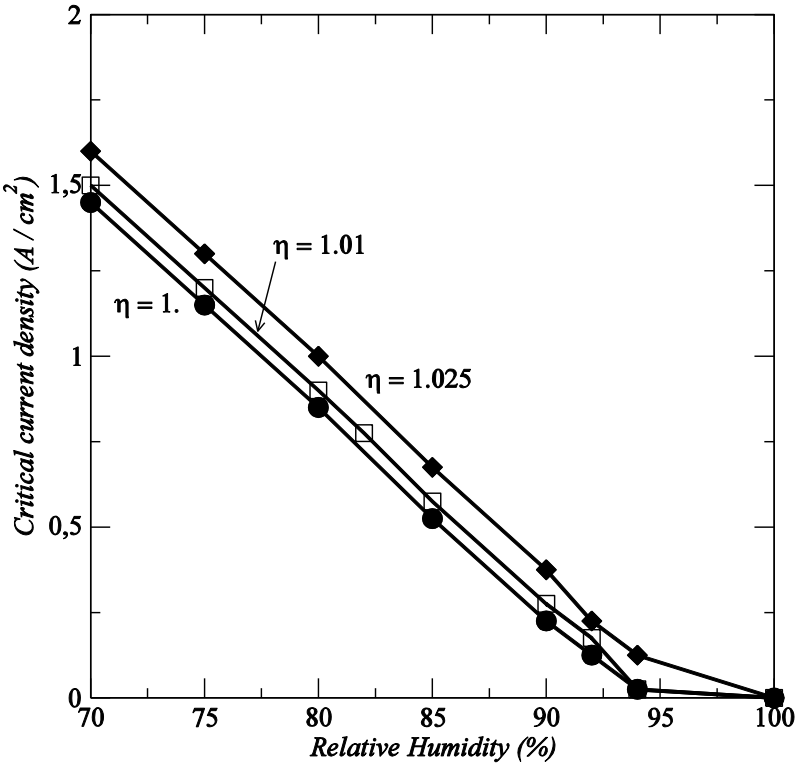


Fig.6: Impact of nucleation parameter on condensation diagram.

### 3.3 Impact of operating temperature

As depicted in Fig.7, the operating temperature has a strong impact on the condensation diagram. This is explained by the strongly non-linear variation of the vapor saturation pressure with temperature ($p_{vs}$ = 7375 Pa, 19920 Pa and 47360 Pa for $T$ = 40°C, 60°C and 80°C respectively). For a given relative humidity in the channel, the critical current marking the onset of condensation decreases with a decreasing temperature. This is in line with the neutron radiographs reported in La Manna et al. (2014) (see Fig.3 in this reference).

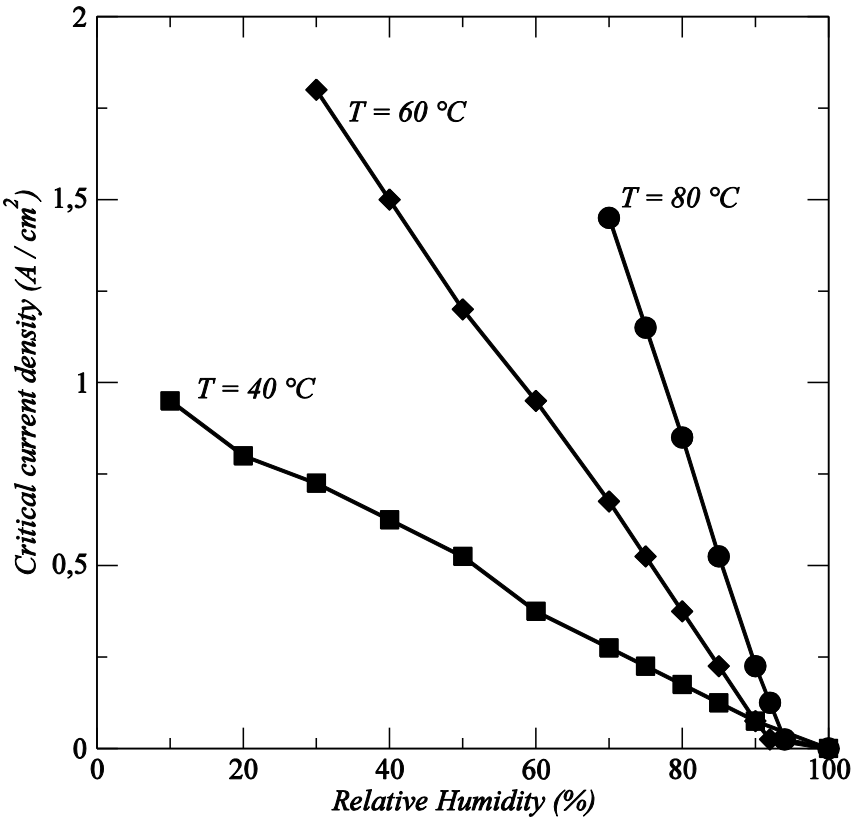


Fig.7: Impact of temperature on condensation diagram.

### 3.4 Impact of partition coefficients $\beta_{H2O}$ and $\beta_T$

Varying $\beta_T$ between 0.5 and 1 (the reference value is 0.8) has no effect on the condensation diagram. This somewhat unexpected result is explained by the fact that the temperature right below the rib in the GDL is actually imposed by the bipolar plate temperature (80°C in the reference case) and thus only marginally affected by the heat flux imposed at the GDL/CL interface.

By contrast, $\beta_{H2O}$ has a significant impact on the condensation diagram. This is illustrated in Fig.8. Decreasing $\beta_{H2O}$ decreases the incoming water vapour flux at the GDL /CL interface of the cathode GDL, thereby decreasing the vapour partial pressure right below the rib middle region area. Therefore, this makes the condensation to occur for a comparatively greater critical current (all other things being equal). This is line with the results reported in Oberholzer and Boillat (2014) showing that increasing the relative humidity on the anode side favors the formation of liquid water on the cathode side if we make the reasonable assumption that increasing the relative humidity on the anode side amounts to decreasing the fraction of

water production directed toward the anode and thus the fraction of the water production directed toward the cathode.

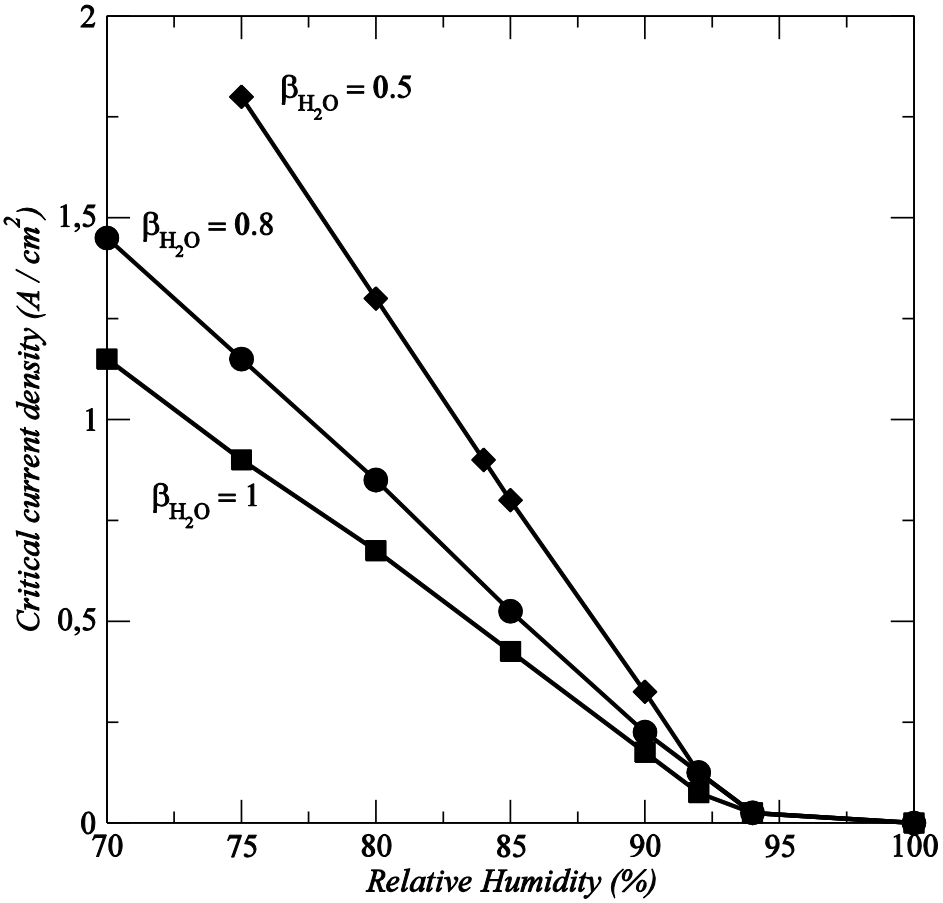


Fig.8: Impact of water production partition coefficient on condensation diagram.

### 3.5 Impact of channel – rib size

Modifying the diffusion path between the rib middle region and the channel can be expected to have an influence on the condensation diagram. Reducing the size of the rib reduces the length of the diffusion path and thus the value of the vapor partial pressure below the rib middle region. As illustrated in Fig. 9, this makes the condensation to occur for a greater critical current density.

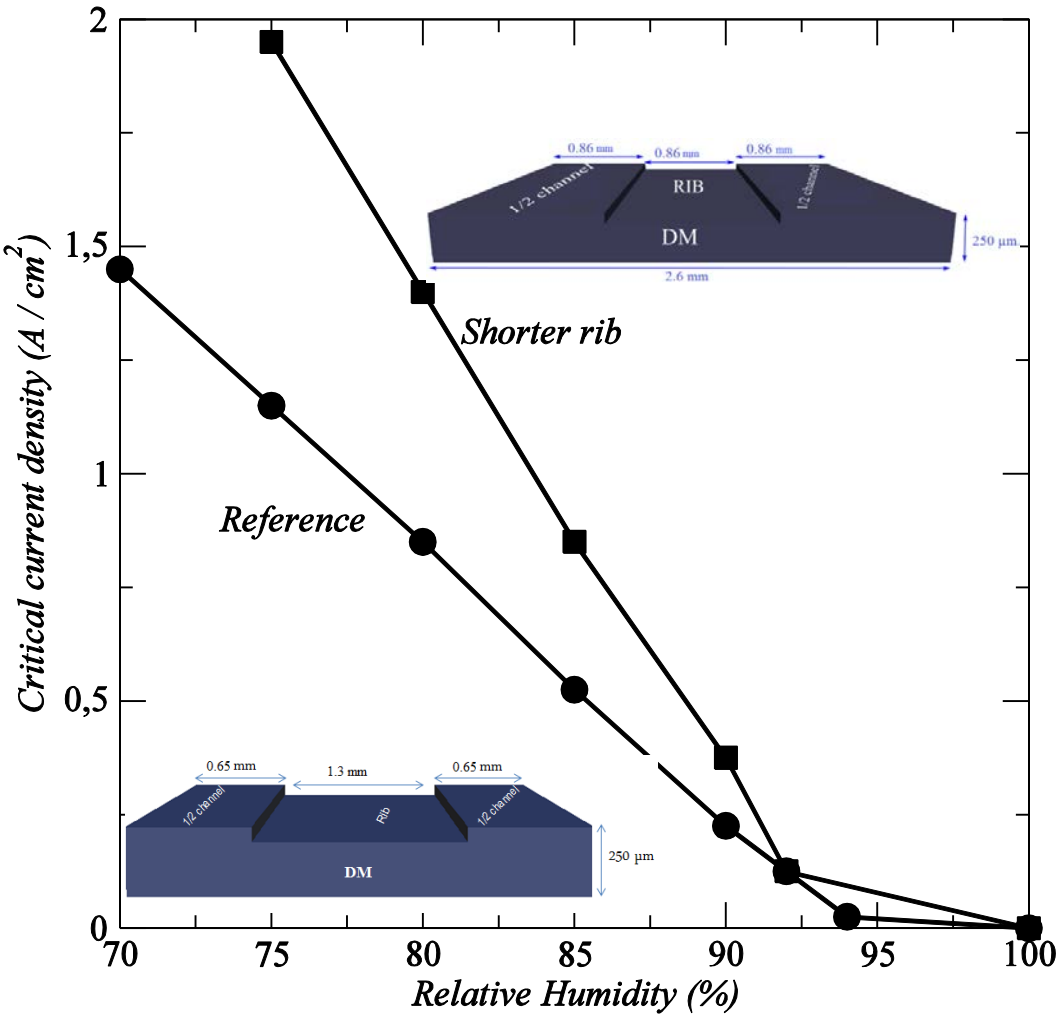


Fig.9: Impact of channel – rib size on condensation diagram.

## 3.6 Impact of GDL and MPL transport properties

Since the temperature below the rib is essentially imposed by the bipolar plate temperature, it is expected that the thermal properties of the DM – MPL assembly are not very sensitive parameters regarding the condensation diagram. Dividing or multiplying the MPL thermal conductivity by a factor 3 has actually no impact on the condensation diagram. This is also consistent with the fact that the thermal resistance of the GDL assembly is mainly due to the DM owing to the comparatively small thickness of the MPL. A similar observation is made as regards the electrical conductivity.

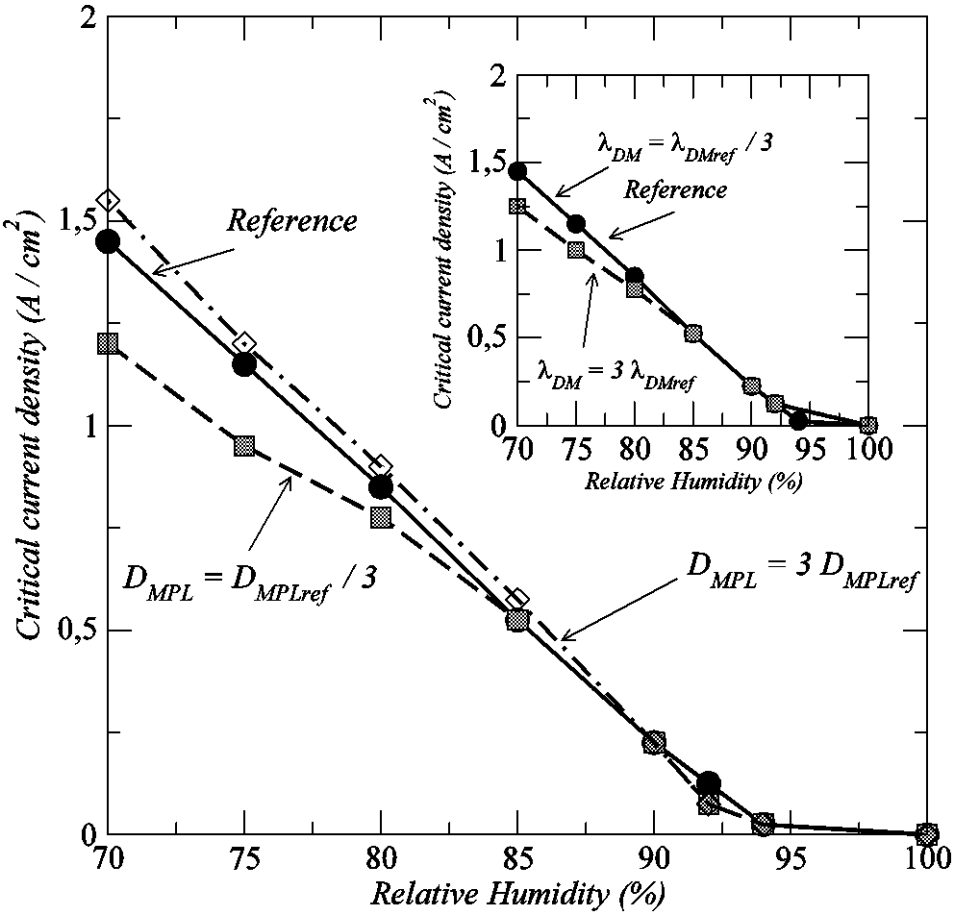


Fig.10: Impact of MPL effective diffusion coefficient on condensation diagram. The inset shows the impact of DM through plane thermal conductivity on condensation diagram. Note that the DM in-plane thermal conductivity is not varied. Only the through plane thermal conductivity is varied.

As can be seen from the inset in Fig.10, modifying the DM through plane thermal conductivity has no impact when it is divided by a factor 3 (from $\lambda\perp_c$ = 0.35 W m$^{-1}$ K$^{-1}$ to 0.12 W m$^{-1}$ K$^{-1}$ as regards the compressed region of the DM for example) but has some impact when multiplied by a factor 3 (from $\lambda\perp_c$ = 0.35 W m$^{-1}$ K$^{-1}$ to 1.05 W m$^{-1}$ K$^{-1}$). This is interpreted as follows. Decreasing the DM thermal conductivity increases the thermal gradient, making the coldest region still more confined below the central part of the rib (where the temperature is imposed by the bipolar plate temperature). This would explain why there is no impact when the DM through plane thermal conductivity is decreased by a factor

3. By contrast, the temperature variation across the GDL is less when the thermal conductivity is increased, making the region where the temperature is close to the bipolar plate temperature of larger extent within the DM. Assuming for simplicity that the vapor partial pressure field is unchanged, this will modify the position of the first condensation spots, i.e. further inside the DM, through the impact of the temperature on the local relative humidity $RH = p_v(x,y,z) / p_{vs}(T(x,y,z))$. In other terms, the DM is globally at a lower temperature. Thus the effect is somewhat similar to reducing the operating temperature. Consistently with the results shown in the inset in Fig.9, this makes the critical current density lower, at least when the relative humidity in the channel is lower than 85 %.

The situation is somewhat different as regards the effective diffusion coefficients since these coefficients affect the field $p_v(x,y,z)$ within the DM and in particular the values of this field right below the middle of the rib. As illustrated in Fig.11, this holds for the DM effective diffusion coefficients. As can be seen the impact is quite significant. Increasing (decreasing respectively) the DM through plane effective diffusion coefficient makes the critical current density greater (lower respectively) than for the reference case. Note that the DM in-plane effective diffusion coefficient was not varied. It was set at the reference value. Interestingly, as illustrated in Fig. 10, this also holds for the MPL diffusion coefficient in spite of the MPL small thickness. To explain the results shown in Fig.10, one can notice that the through plane diffusive conductance $D_{eff}/\delta$ is not significantly different between the DM and the MPL for the reference situation ( $(D\perp_c / \delta_{cDM}) / (D_{MPL} / \delta_{MPL}) \approx 0.75$). As a result, changing the MPL effective diffusion coefficient has an impact on $p_v(x,y,z)$. Then decreasing the effective diffusion coefficient of the MPL increases the values of $p_v(x,y,z)$ in the DM below the rib, leading to a comparatively lower critical current density. Increasing the MPL effective diffusion coefficient has the opposite effect as illustrated in Fig. 10. However, the influence is less marked than when the MPL effective diffusion is decreased (when the relative humidity is less than about 80% in Fig. 10). This can be also explained from the consideration of the diffusive conductance ratio $(D\perp_c / \delta_{cDM}) / (D_{MPL} / \delta_{MPL})$ which is equal to 0.75 for the reference case and to 2.25 and 0.25 when $D_{MPL}$ is decreased by a factor 3 and increased by a factor 3 respectively. The relative variations of this ratio are 2 and 0.7 respectively, thus higher when the $D_{MPL}$ is decreased by a factor 3.

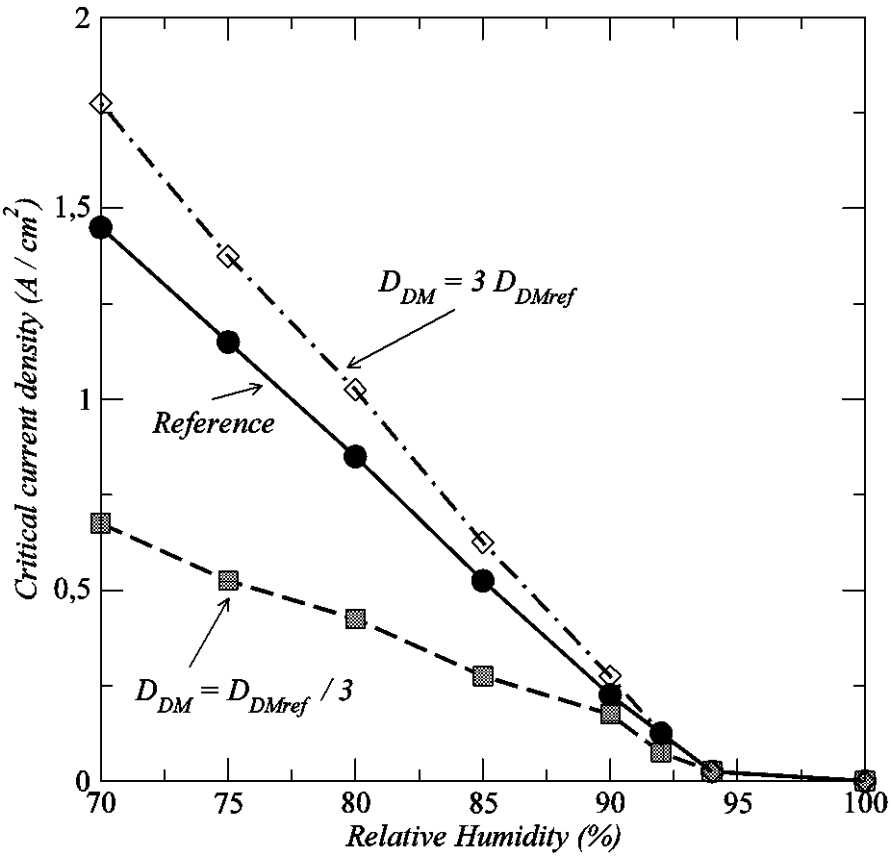


Fig.11: Impact of DM through plane effective diffusion coefficient on condensation diagram. Note that the DM in-plane effective diffusion coefficient is not varied. It is set at the reference value.

## 3.7 Comparison of GDL with and without MPL

Somewhat surprisingly the condensation diagram is not strongly modified when the MPL is removed. This is illustrated in Fig. 12. This can be explained in part as follows. First we note that the thermal conductance is much lower in the DM than in the MPL ($\lambda_{\perp c} / \delta_{cDM}$) / ($\lambda_{MPL} / \delta_{MPL}$) ≈ 0.03). As a result, removing the MPL should not modify the temperature field within the DM since the thermal resistance of the DM – MPL assembly is dominated by the DM thermal resistance. This is illustrated in Fig.13 showing that the temperatures at the inlet of the DM (the inlet of the DM corresponds to the GDL / CL interface in the absence of MPL and to the DM/MPL interface when a MPL is present) are very close between the case with MPL and the case without MPL. It can be noted, however, that the MPL tends to smooth out the temperature variation at the DM inlet.

Second, it can be noted from Fig.10 than increasing the MPL diffusive conductance has less effect than reducing the MPL diffusive conductance. This is because the diffusive conductance of the assembly tends to be progressively dominated by the DM diffusive resistance.

Nevertheless, the comparison between Fig.10 and Fig.12 indicates that removing the MPL has an impact similar to one obtained in increasing the MPL effective diffusion by a factor 3.

However, the effect on the critical current density is reversed. This is surprising since one could expect that the situation without MPL should amount to increasing the MPL effective diffusion by an "infinite" factor. The slight impact of the MPL on the condensation diagram (Fig.12) is consistent with the distributions of water vapor and oxygen partial pressures at the DM /CL interface (case without MPL) and DM /MPL interface reported in Fig.14. As can be seen the distributions are quite close. The fact that the water vapor partial pressure is slightly greater at the DM inlet in the absence of MPL is consistent with the results on the condensation diagram depicted in Fig.12.

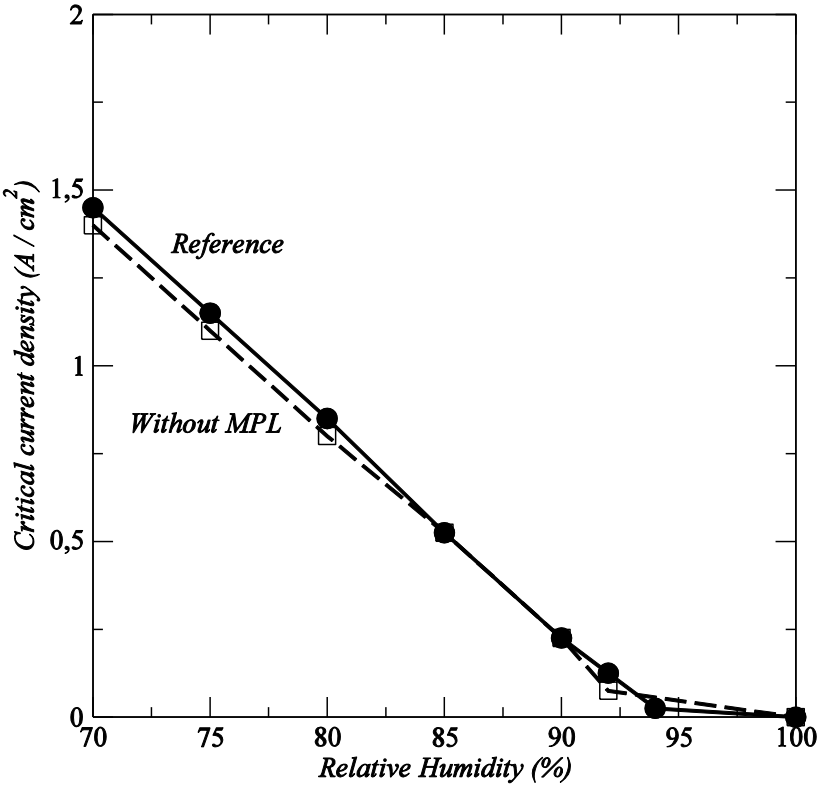


Fig.12: Impact of MPL on condensation diagram.

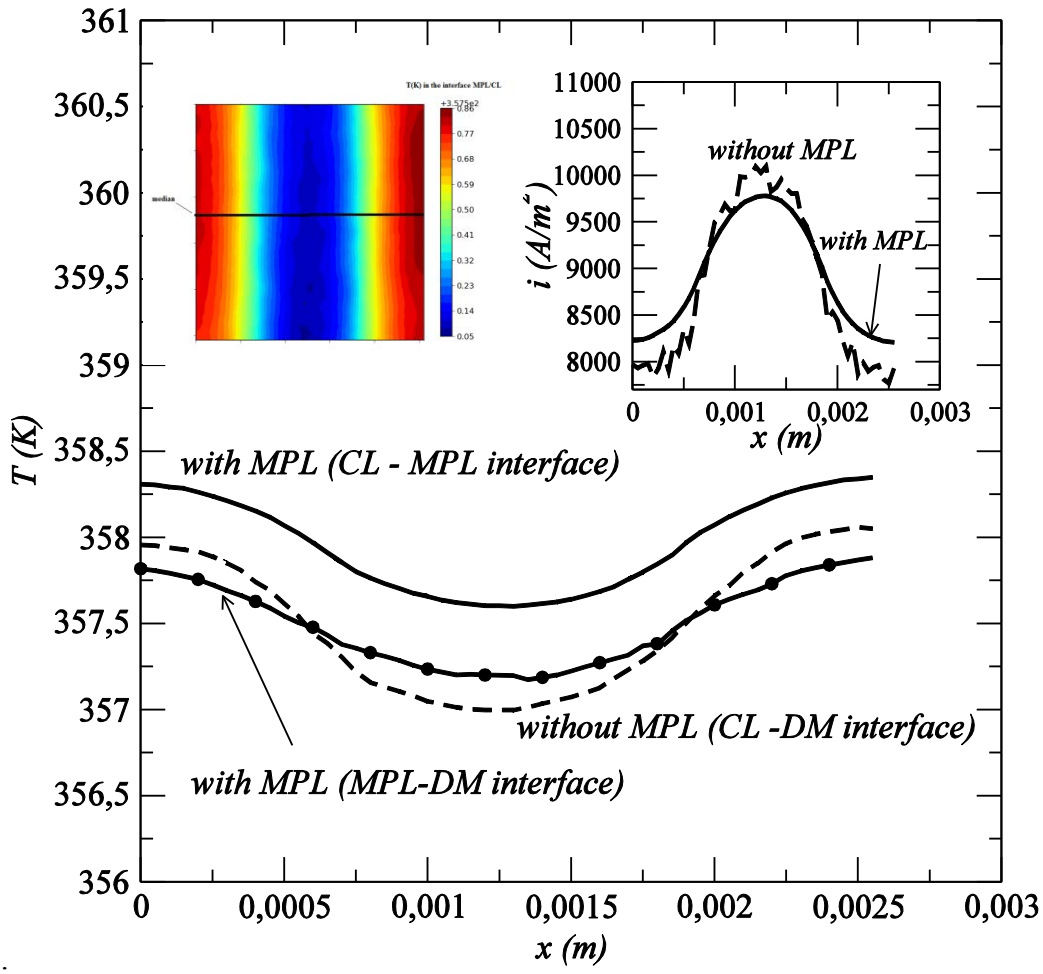


Fig.13: Transverse temperature distribution at the GDL / CL interface and at the MPL / DM interface (case with MPL) for the reference case and *RH* = 75%. The inset shows the transverse current density distribution at the CL / GDL interface. The color map shows the temperature distribution over the GDL / CL interface. The transverse profiles shown in the figures correspond to the black solid line crossing the color map in the middle,

Also the relative position of the curves (MPL / DM) and (CL /DM) in Fig.14 are fully consistent with the condensation diagrams presented in Fig.10 and in Fig.12. The fact that removing the MPL has a reverse impact on the condensation diagram that simply increasing the MPL diffusive conductance could be due to the more non-uniform temperature distribution at the DM inlet depicted in Fig.13 for the case without MPL, noting that the temperature is colder below the rib region is this case compared to the situation with MPL (the rib region corresponds to the minimum temperature in Fig.13). A colder temperature corresponds to a lower critical current. The temperature difference is however quite weak (less than 0.3 K). Thus further analysis will be desirable to fully explain the somewhat unexpected reversal revealed by our simulations.

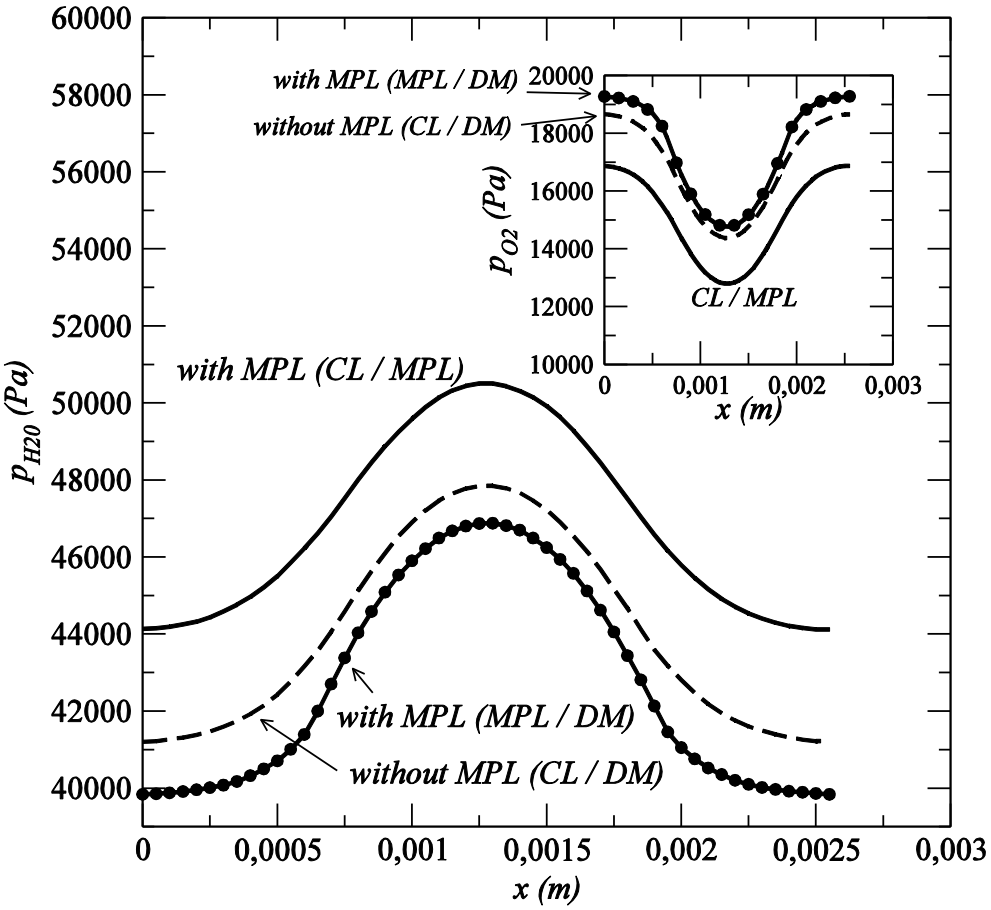


Figure 14 : Transverse distributions of oxygen and water vapor partial pressures at the GDL / CL interface and the MPL / DM interface (case with MPL) for the reference case and *RH* = 75%.

## 4. Conclusion

The condensation diagram characterizes the conditions when the GDL is free of liquid water, which might be seen as the most favorable conditions to operate the fuel cell since there is no liquid water obstructing the oxygen access to the catalyst layer.

In this paper, the impact of various parameters on the condensation diagram was investigated from numerical simulations coupling the mass, electrical and heat transfers between the various layers forming the cathode. As expected the operating temperature has a strong impact. For given operating conditions, the critical current density marking the onset of the liquid water formation by condensation in the GDL, decreases with temperature. The impact of water partition coefficient is also strong which is seen as being in accordance with the experimental results showing an impact of the relative humidity on the anode side on the occurrence of liquid water on the cathode side. Our results also indicate that using narrower rib allows operating with a dry GDL at greater current densities.

The thermal properties of the GDL or the MPL were not found to be sensitive parameters. This was explained by the fact that the temperature at the most likely location of incipient

condensation is essentially imposed by the operating temperature (temperature of the bipolar plate). The effective diffusive coefficients were found to be sensitive parameters, which is consistent with the structure of water vapor diffusive paths within the GDL.

In our case, it was shown that decreasing the effective diffusion coefficient of the MPL had a detrimental effect (the critical current density is smaller). However, this highly depends on the diffusive conductance of each layer of the GDL – MPL assembly. For example, if the MPL diffusive conductance is significantly greater than the GDL diffusive conductance, the effective diffusion coefficient of the MPL is not a sensitive parameter (unless it is reduced drastically). This type of consideration can help designing improved GDL. Hence, playing with the MPL diffusion properties to enhance the critical current density is meaningful only if the MPL diffusive conductance is comparable (or greater) to the GDL diffusive conductance.

**References**

J.T.Gostick, M.A. Ioannidis, M.W. Fowler, M.D. Pritzker, Pore network modeling of fibrous gas diffusion layers for polymer electrolyte membrane fuel cells, *Journal of Power Sources* 173, 277–290 (2007)

J. M. LaManna, S.Chakraborty, J. J. Gagliardo, M. M. Mench, Isolation of transport mechanisms in PEFCs using high resolution neutron imaging, *Int. J. of Hydrogen Energy* 39, 3 3 8 7 - 3 3 9 6 (2014)

J.M. LaManna, S.G. Kandlikar Determination of effective water vapor diffusion coefficient in pemfc gas diffusion layers *Int. J. of Hydrogen Energy* 36, 5021-5029 (2011)

P. Oberholzer and P. Boillat, Local characterization of PEFCs by differential cells: systematic variations of current and asymmetric Relative Humidity *Journal of The Electrochemical Society*, 161 (1) F139-F152 (2014)

M.Rebai, M.Prat, Scale effect and two-phase flow in a thin hydrophobic porous layer. Application to water transport in gas diffusion layers of proton exchange membrane fuel cells *Journal of Power Sources* 192, 534–543 (2009)

B.Straubhaar, J.Pauchet, M. Prat**,** Water transport in gas diffusion layers of PEM fuels cells in presence of a temperature gradient. Phase change effect, *Int. J. of Hydrogen Energy*, 40 (35) 11668–11675 (2015)

B.Straubhaar, J.Pauchet, M. Prat, Pore network modelling of condensation in gas diffusion layers of proton exchange membrane fuel cells, submitted (2016)

chapter 6

# Impact of liquid water formation on the current local distribution at the cathode gas diffusion layer–catalyst layer interface in proton exchange membrane fuel cells.

## Abstract

Experimental results based on in-situ measurements of the current density distribution at the interface between the catalyst layer and the gas diffusion layer on the cathode side at the rib – channel scale shows an interesting variation of the distribution as the mean current density is increased. It is found that the current density below the rib median axis rather corresponds to a local maximum in current density at low mean current densities and to a minimum when the mean current density is sufficiently high. Also, the higher the current density, the more marked the minimum. We show that a similar reversal effect can be obtained from numerical simulations provided that the formation of liquid water in the region of the gas diffusion layer below the rib due to condensation is taken into account.

## 1. Introduction

It is well known that water management is a key issue in PEMFC technology. Improving the water management is still largely an open issue. In this prospect, it is clear than any improvement in the understanding of the liquid water formation and migration into the membrane electrode assembly (MEA) is useful. Consider the gas diffusion layer (GDL) on the cathode side. Somewhat surprisingly, a literature review, e.g. Straubhaar et al. (2016), shows that two quite different mechanisms of water formation in the GDL have been considered. Namely, i) formation of liquid water resulting from the capillarity controlled invasion in liquid phase at the interface between the GDL and the catalyst layer (CL), ii) condensation of the water vapor within the GDL. Thus, water enters the GDL from the CL in vapor phase in the latter case whereas it enters the GDL in liquid phase in the first scenario. The pore network simulations of the condensation scenario reported in Straubhaar et al. (2016) are in agreement, at least qualitatively, with several experimental in – situ observations. Thus, there is little doubt that the condensation of water vapor is a major mechanism of liquid water formation in the GDL. Note, however, that the simulations presented in Straubhaar et al. (2016) were performed for a temperature of 80°C. Although this temperature is considered as a typical operating temperature in many applications, lower operating temperatures are also possible. It is unclear whether condensation is still the dominant mechanism of liquid formation in GDL as the operating temperature is decreased. In any case, it is interesting to confirm the relevance of the condensation scenario in the upper range of temperatures, i.e. close to 80°C.

In the present chapter, further confirmation of the relevance of the condensation scenario is sought from the distribution of the current density at the CL-GDL interface. The objective is to compare this distribution for different average current densities obtained on the one hand

experimentally and on the other hand from numerical simulations with liquid formation by condensation.

The chapter is organized as follows. Some experimental results of interest are briefly described in section 2. Some features of the modelling are recalled in Section 3. Main results of simulations are presented in section 4. A conclusion is presented in section 5.

## 2. Experiments

Current distribution at scales smaller than the rib-channel scale were reported in Freunberger et al. (2006). It was shown that the current density tends to become less and less uniform as the average current is increased and that the minimum current tends to localize below the rib areas. The interpretation was not fully conclusive because the liquid water formation could not be detected. In other terms, the possible impact of the liquid water on the measured current density distributions could not be assessed. Somewhat similar experimental results were obtained by Rachidi (2011). Here also it was not possible to relate the current density minimum variation with the possible impact of liquid formation. One can refer to Rachidi's Ph.D manuscript for a detailed description of the experimental set-up and measurement methods. The main results obtained by Rachidi and of interest for the present study are shown in Figs.1-2. As indicated in Fig.1, they were obtained at the rib –channel scale.

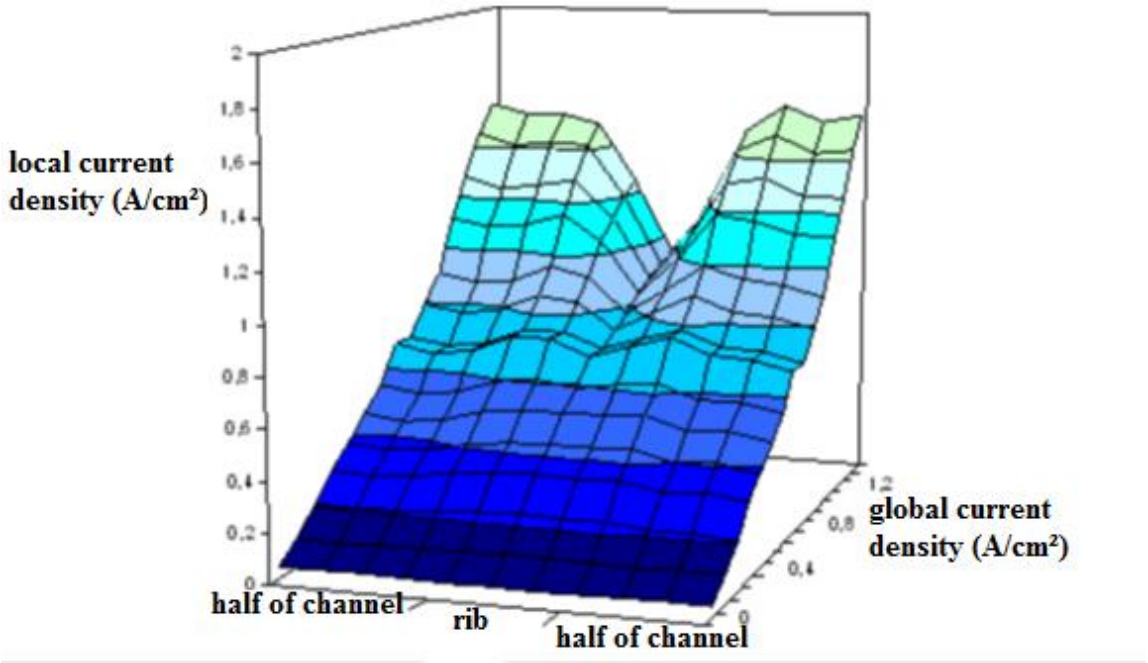


Figure 1: Typical type of rib –channel scale results obtained by Rachidi (2011). Note the position of the rib and the channels, $P_{O2}$ / $P$= 21%, *RH = 80% , P = 1.5 bar, T= 80°C.*

As can be seen from Fig.1, the transverse current densities distribution varies with both the relative humidity in the channel and the mean current density. For the three RH tested, the transverse current density is uniform at the CL-GDL interface for a sufficiently low mean current density (approximately $\bar{i} < 0.2$ A / cm$^2$). Then, as the mean current density is increased, the local current density tends to be slightly higher in the region of the CL-GDL interface located below the rib than below the channel (this corresponds to mean current densities approximately in the range [0.2 – 0.6 A / cm$^2$]). This trend is reversed in the range of the highest mean current densities ($\bar{i} > 0.6$ A / cm$^2$). The local current density is then significantly lower in the region of the interface located below the rib. As can be seen also from Fig.1, the non-uniformity of the local current density at high mean current density significantly increases as *RH* is increased. The difference in local current density between the regions below the channels and the region below the centre line of the rib can be as high as about 0.5 A/cm$^2$ for the highest tested mean current density ($\bar{i} \approx 1.35$ A/cm$^2$).

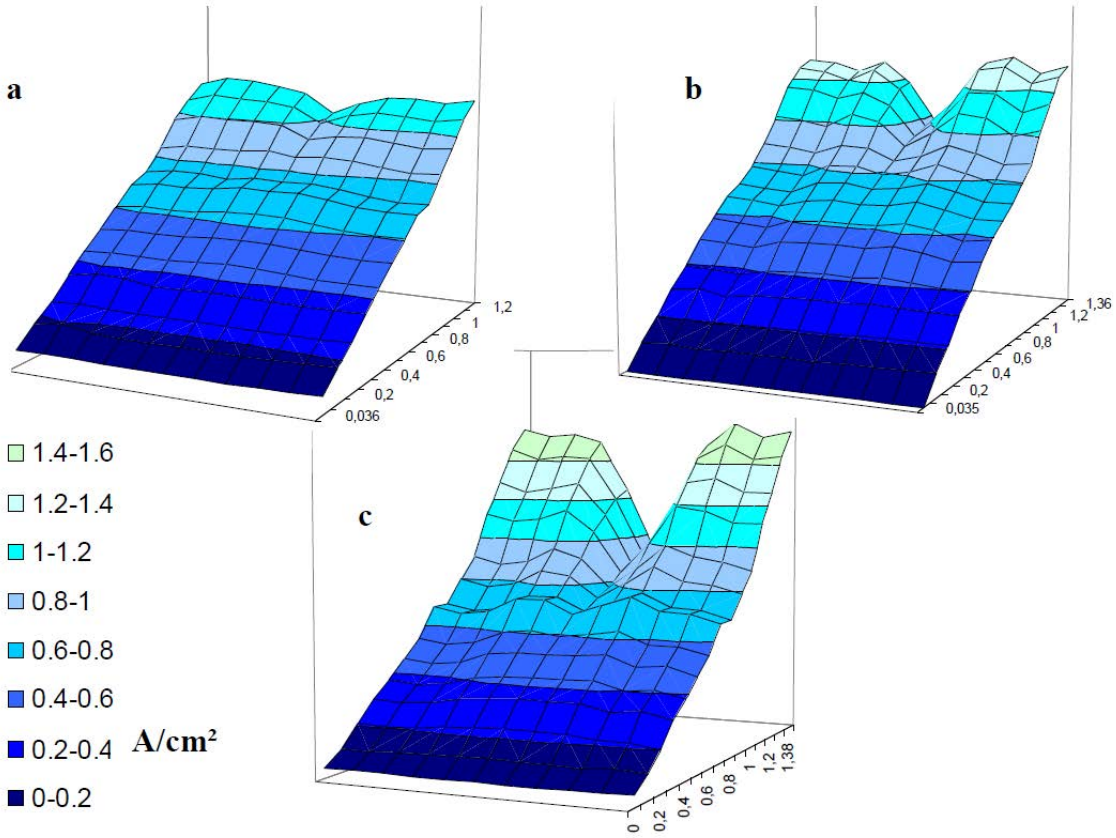


Figure 2: Transverse current density distributions as a function of mean current density ($P_{O2}$ / $P$ = 21%) a) *RH = 30%,* b) *RH = 50%,* c) *RH = 80% , P = 1.5 bar, T= 80°C.*

## 3. Modelling

The computational model is the one described in Chapter 3 and is therefore the same as the one used in Chapter 5 for the study of the condensation diagram. However, an important difference compared to Chapter 5 is that the simulations of liquid water formation n GDL are carried out (only dry GDL were considered in Chapter 5).

It should be noted that results shown in Fig. 2 where obtained with a GDL Freudenberg H2315T10AC1 whereas the parameters in our model were specified so as to represent a SGL 25BC. We believe that the problem, i.e. the impact of liquid water, is generic and therefore can be studied, at least qualitatively, using the parameters corresponding to SGL 25BC.

As sketched in Fig.3, the GDL is considered as a two-layer porous system, made of a "fibrous" Diffusion Medium (DM) and of a Micro-Porous-Layer (MPL) coated onto the DM. The MPL penetration into the DM is not considered in this study.

The computational domain considered in the study is depicted in Fig.3. It corresponds to an elementary unit cell containing a bipolar plate rib and two gas half channels similarly as for the experimental domain shown in Fig.1. The geometrical dimensions of the various layers are specified in Fig.3. For the GDL, the indicated thickness corresponds to the uncompressed GDL, i.e. below the channels.

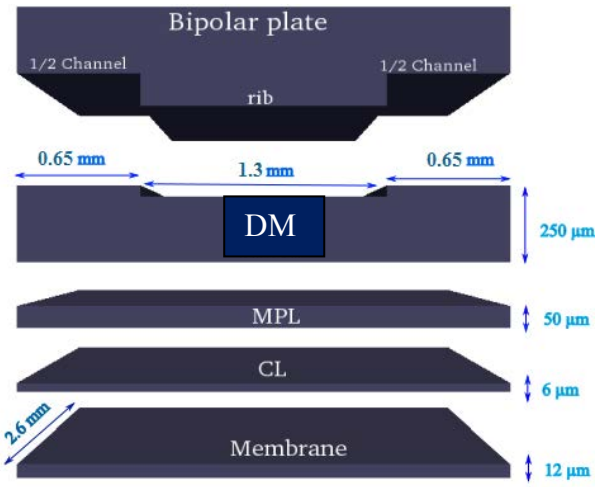


Figure 3: Computational domain.

The properties of the various layers have been specified as explained in previous chapters. There are summarized in Tables 1- 2 for the MPL and the GDL.

The useful properties of the other layers, namely the catalyst layer (CL) and the membrane are given in Chapter 3 together with the model used to compute the current density distribution.

Table 1 : MPL properties.

| | *Effective thermal conductivity* ($Wm^{-1}K^{-1}$) | *Effective electrical conductivity* (S/m) | *Effective diffusion coefficient* | *Thickness* (*µm*) | *Porosity* |
|---|---|---|---|---|---|
| *Symbol* | $\lambda$ | $\sigma$ | $D^*/D$ | | |
| | 2.5 | 2500 | 0.04 | 50 | 0.4 |

Table 2: DM properties (corresponding to SGL 25 BC).

| | *DM thickness* (*µm*) | | *Porosity* (%) | |
|---|---|---|---|---|
| *Symbol* | $\delta$ | $\delta_{uc}$ | $\varepsilon_c$ | $\varepsilon_{uc}$ |
| | 200 | 250 | 0.72 | 0.8 |
| | *Effective thermal conductivity* ($Wm^{-1}K^{-1}$) | | | |
| *symbol* | $\lambda_{//c}$ | $\lambda_{//uc}$ | $\lambda\perp_c$ | $\lambda\perp_{uc}$ |
| | 6.9 | 4.9 | 0.35 | 0.17 |
| | *Effective electrical conductivity* (S/m) | | | |
| *symbol* | $\sigma_{//c}$ | $\sigma_{//uc}$ | $\sigma\perp_c$ | $\sigma\perp_{uc}$ |
| | 5000 | 4000 | 254 | 138 |
| | *Effective diffusion coefficient (-)* | | | |
| *symbol* | $D_{//c}/D$ | $D_{//uc}/D$ | $D\perp_c/D$ | $D\perp_{uc}/D$ |
| | 0.5 | 0.6 | 0.12 | 0.2 |

The GDL is represented by a $52\times52\times7$ cubic pore network (the figures indicate the number of pores along the directions of a Cartesian grid), see Chapter 3 for more details. As discussed for instance in Straubhaar et al. (2016), the pore network (PN) representation is convenient for simulating the formation of liquid water by condensation in the DM. To this end, the condensation PN algorithm described in Straubhaar et al. (2016) is used. The main features of this algorithm are summarized in Chapter 3.

4. Numerical simulations

## 4.1 Condensation diagram

As discussed in some details in Chapter 5, the condensation diagram gives the operating conditions ($\bar{i}$ , *RH*) leading to a dry GDL or a wet GDL, i.e. a GDL with liquid water formed

by condensation assuming that the other parameters (operating temperature, pressure, etc) are set and thus not varied. The method to compute this diagram is described in Chapter 5, see also Straubhaar et al. (2016). The condensation diagram obtained for the values of model parameters is shown in Fig.3. The line in this figure marks the boundary between the "dry" operating conditions and the "wet" boundary conditions and corresponds to the curve $\bar{i}_c(RH)$, where $\bar{i}_c$ is, for a given *RH*, the "critical" current density, i.e. the minimum mean current density leading to condensation.

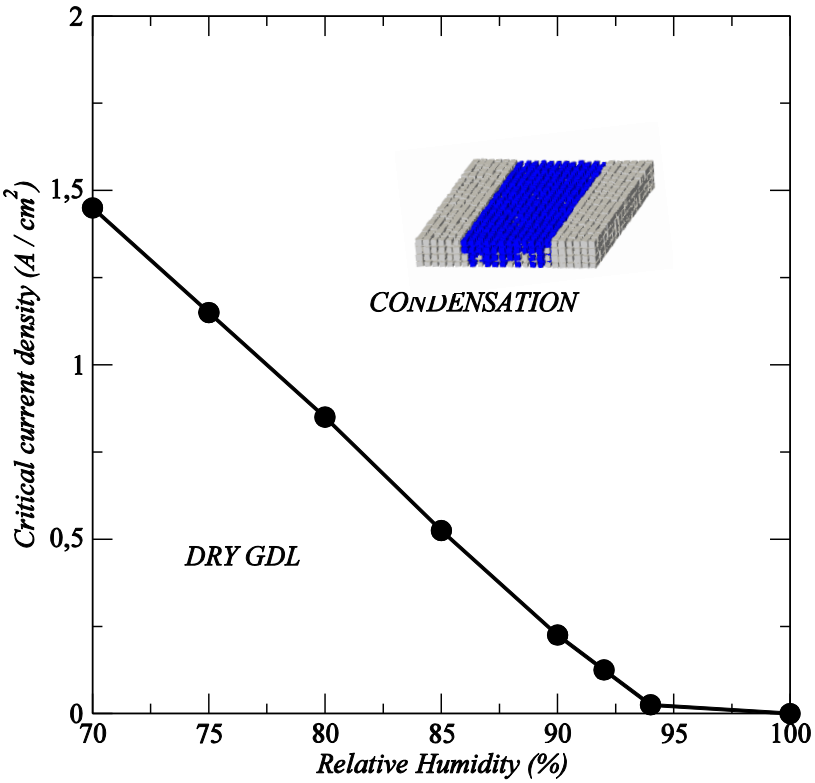


Figure 3: Condensation diagram.

In relation with the experimental results shown in Fig. 1, this diagram indicates that liquid water due to condensation is present in the DM for a sufficiently high mean current density (~ 0.8 A/cm²) for *RH* = 80 %. However, if one interprets the formation of the minimum in the current density transverse distribution as due to the formation of liquid water, then the experimental results reported in Fig. 2 would suggest that liquid water occurs for *RH* = 50% for a sufficiently high mean current density. This is not consistent with the condensation diagram depicted in Fig. 3. As discussed in Chapter 5, the condensation diagram is highly dependent on the DM and MPL properties. For example, with the properties used in Straubhaar et al. (2016), the occurrence of liquid water takes place at significantly smaller *RH* and mean current density than indicated in Fig.3. In other terms, it would be not difficult and still consistent with the values of DM and MPL properties available in the literature to set the properties so as to obtain liquid water formation at lower RH than indicated in Fig.3. For the

sake of consistency with other chapters, we have decided, however, to keep the properties indicated in Tables 1 and 2 which lead to the condensation diagram of Fig.3.

## 4.2 Liquid water distribution

Fig. 4 shows a typical liquid water distribution within the DM resulting from the condensation process. As can be seen the liquid water preferentially forms in the region below the rib, which corresponds to the region of lower temperatures within the DM and to the region of longer diffusion path for the water vapor. One can refer to Chapter 5 for more details on the notion of diffusion path and to Straubhaar et al. (2016) as regards the process of condensation in the GDL. As pointed out in Straubhaar et al. (2016), the preferential formation of liquid water in the rib area is in agreement with in situ experimental observations, e.g. Oberholzer and Boillat (2014). The fact that the liquid water is mostly below the rib and the regions of the DM below the channels are free of liquid water is referred to as the separation effect (see again Straubhaar et al. (2016) for more details).

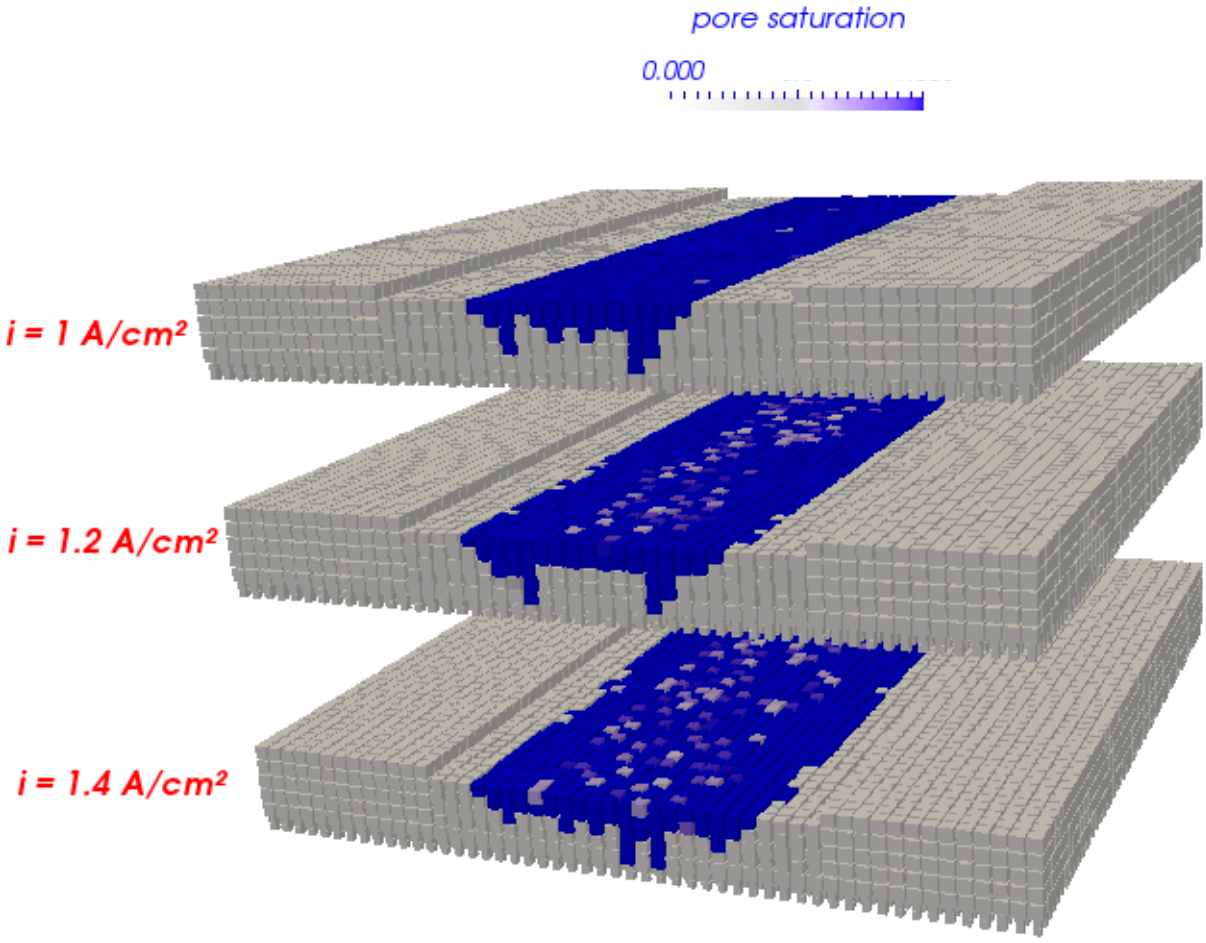


Figure 4: Typical water distribution (in blue) within the DM resulting from the condensation process: $RH$ = 80 %, $T$ = 80°C, $P_{O2}/P$ = 21%.

As illustrated in Fig.4 and expected from a physical standpoint, the region occupied by liquid water below the rib within the DM increases when the mean current density is increased.

Similarly as reported in Straubhaar et al. (2016), the overall liquid saturation also increases when the relative humidity is greater in the channel.

These two features, i.e. the increase in saturation when either the mean current density or the channel relative humidity are increased, are in a good qualitative agreement with in-situ experiments as reported in Straubhaar et al. (2016). This is also illustrated below from the consideration of the saturation transverse and through-plane saturation profiles.

The liquid distribution in the DM is also illustrated from the plots of the transverse in-plane and through plane saturation profiles.

As illustrated in Fig.5, the transverse in-plane saturation is the fraction of the pore space occupied by liquid water in a longitudinal vertical plane (vertical in the representation of Fig. 5). Similarly, the through plane saturation is the fraction of the pore space occupied by liquid water in a horizontal plane in Fig.5. There are six rows of pores to represent the DM in the through-plane direction. Therefore, the through plane saturation profile is formed by the saturation computed in each of these six rows. In the plots of the through plane saturation profile, the MPL is on the left side and the interface with the channel / rib area is on the right side.

The saturation profiles obtained from the simulations for the case $RH$ = 80% are shown in Fig.6. As can be seen and consistently with the condensation diagram depicted in Fig.3, there is no liquid water forming in the DM for the mean current density lower than 1 A/cm$^2$ in Fig.6. The overall saturation increases with the current density (for $\bar{i} > 0.8$ A/cm$^2$ in Fig.6) but the liquid water remains confined below the rib area.

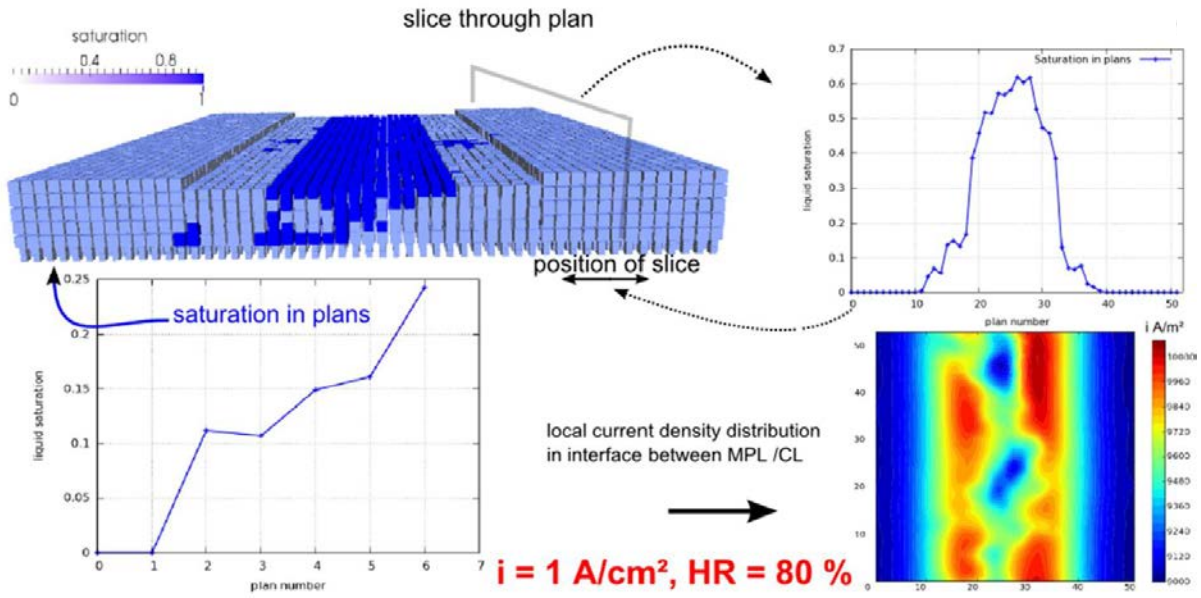


Figure 5: Definition of in plane (top figures) and through plane (figure on the bottom left) saturations in the DM. For the through plane saturation profile, the MPL is on the left side and the interface with the channel / rib area is on the right side. The color map shows an example of current distribution at the interface between the MPL and the CL.

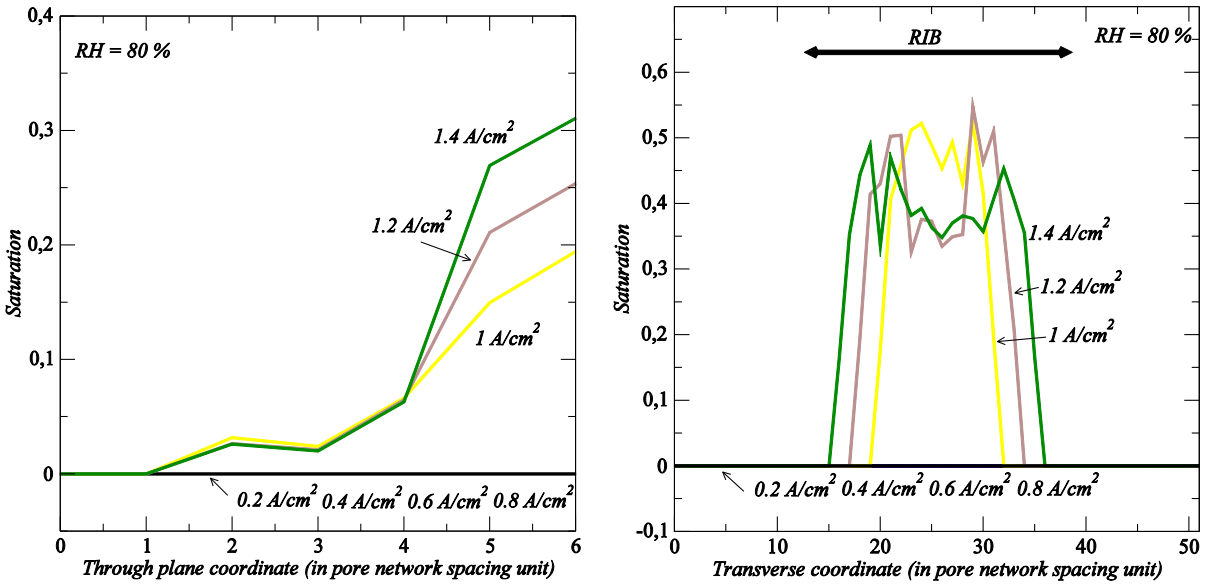


a) through plane b) in plane

Figure 6: Impact of mean current density on saturation profiles for *RH* = 80%: a) through plane saturation profile (MPL on the left, rib-channel on the right), b) in plane saturation profile.

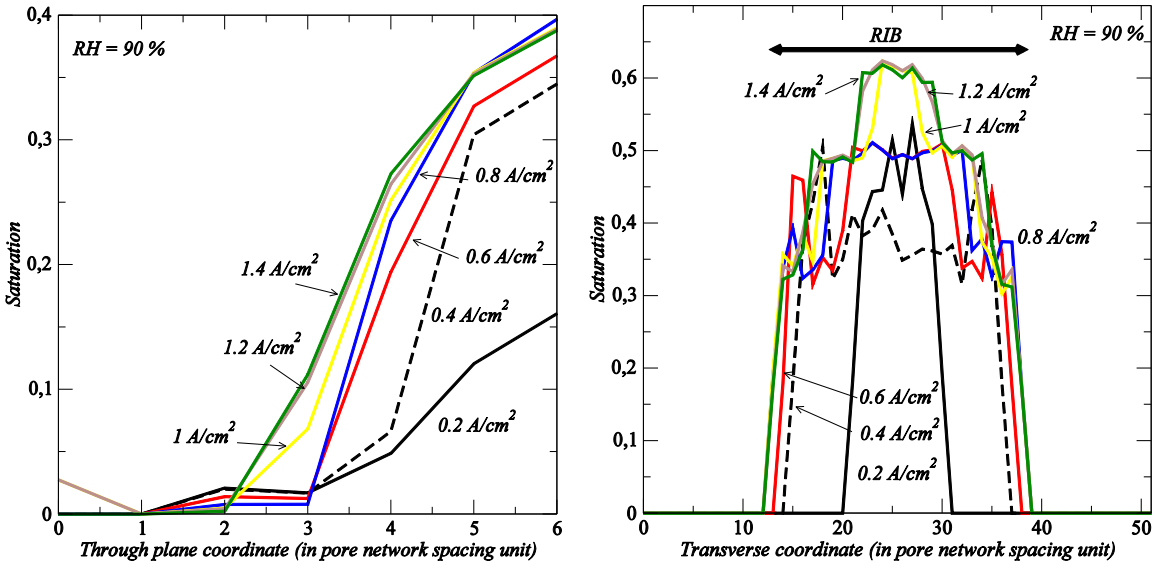


b) through plane b) in plane

Figure 7: Impact of mean current density on saturation profiles for RH = 90%: a) through plane saturation profile (MPL on the left, rib-channel on the right), b) in plane saturation profile.

As can be seen from Fig.7 and also from the condensation diagram (Fig.3), liquid water begins to form for a much lower mean current density when the relative humidity in the channel is increased (from 80% in Fig.6 to 90% in Fig.7). As already mentioned this is in agreement with in-situ experimental observations, e.g. Straubhaar et al. (2016). Consistently, the overall saturation is greater for a given mean current density when the channel relative humidity is increased (as can be seen from the comparison between Fig.6 and Fig.7). Here again, the liquid water remains confined below the rib region area, even for the greatest tested mean current density (1.4 A/cm$^2$).

## 4.3 Local current density distribution

Examples of current density distributions at the CL–MPL interface obtained from the simulations are depicted in Fig.8. As can be seen, there is clear change in the position of the current intensity maximum when the mean current density is increased. Consider for example the color maps for *RH* = 90 % in Fig. 8 and look at the line corresponding to the rib median axis (this corresponds to the vertical dashed median line in Fig.8). This line corresponds to a maximum in current density for $\bar{i} = 0.2$ A/cm$^2$ whereas it corresponds to a minimum in current density for $\bar{i} = 0.8$ and $\bar{i} = 1.4$ A/cm$^2$.

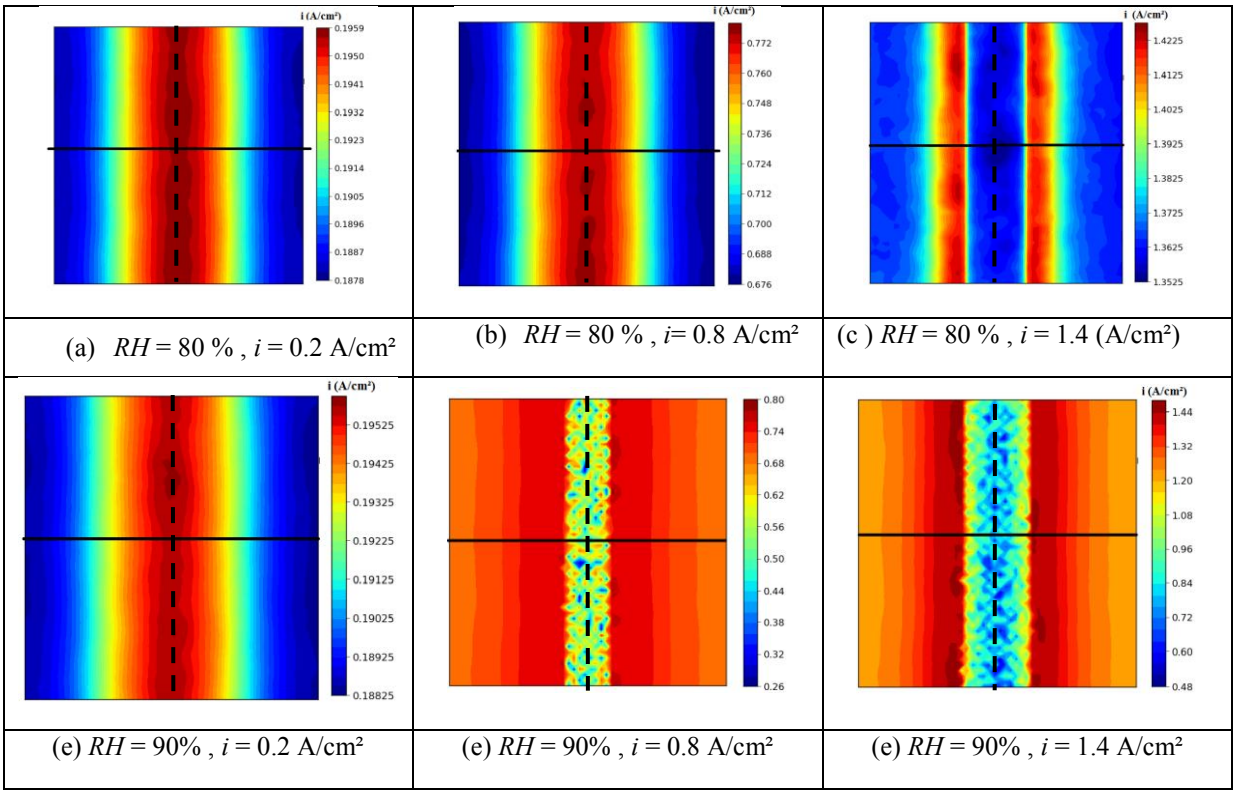


(a) *RH* = 80 % , *i* = 0.2 A/cm² | (b) *RH* = 80 % , *i*= 0.8 A/cm² | (c ) *RH* = 80 % , *i* = 1.4 (A/cm²)

(e) *RH* = 90% , *i* = 0.2 A/cm² | (e) *RH* = 90% , *i* = 0.8 A/cm² | (e) *RH* = 90% , *i* = 1.4 A/cm²

Figure 8: Impact of mean current density on the current density distribution at the CL/GDL interface for *RH* = 80 % (top row) and 90 % (bottom row).

Still more interesting are the current density profiles (at the CL-MPL interface) depicted in Fig.9. They first clearly show that the local current density is uniform between rib and channel for low mean current densities (<0.2 A/cm²). Then, a maximum of local current density appears below the rib as the mean current density is increased. For even higher mean

current density (~ 1A/cm²), the local current density below the rib is no more a maximum and can even be a well marked minimum for a high relative humidity in the channel (RH = 90%, Fig. 9b).The greater the mean current density, the more marked the minimum.

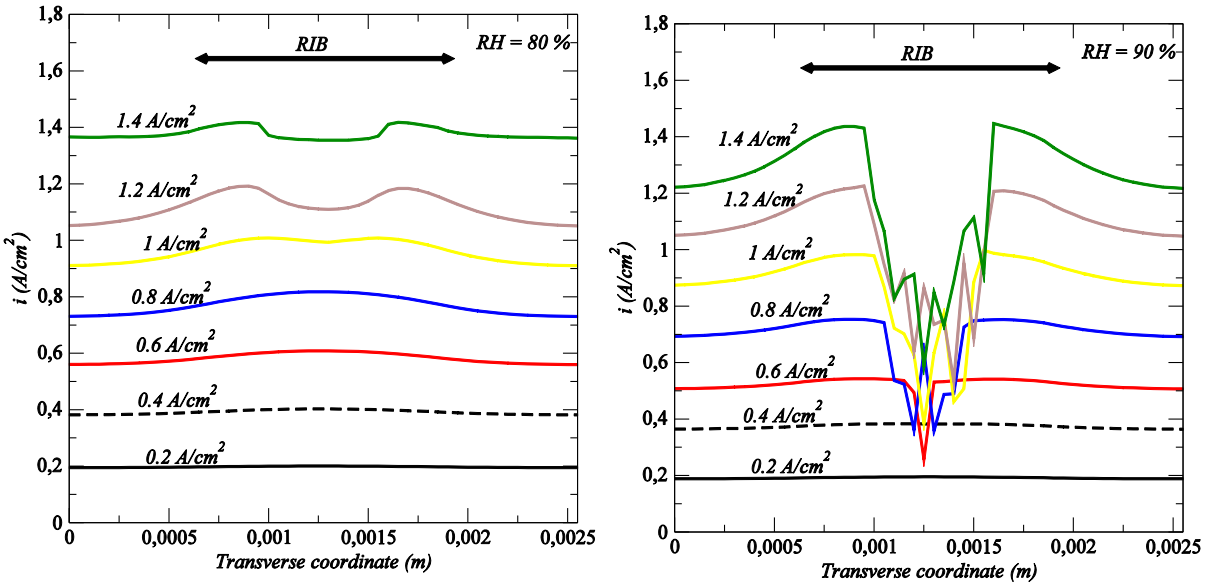


a) b)

Figure 9: Current intensity transverse profiles at the CL – MPL interface for various mean current densities: a) *RH* = 80%, b) *RH* = 90%.

These profiles are in a qualitative agreement with the experimental profiles in Fig.2. Note the local maximum in current density along the edges of the rib (rib / channel transition region) in Fig.9 for the highest mean current densities. Although less clearly, this is also visible in Fig.2.

The comparison between the saturation profiles in Fig.6 (*RH* = 80%) and 7 (*RH* = 90%) and the current density profiles in Fig.9 clearly show a direct correlation between the formation of the current density minimum below the rib and the formation of liquid water due to condensation. For the case *RH* = 80%, there is no liquid water for $\bar{i} < 1$ A/cm$^2$. For this range of current density ([0-0.8]), Fig.9 indicates a maximum in current density in the region corresponding to the rib median axis. A similar maximum is also visible in the experimental results for the sufficiently low mean current densities. By contrast, the region corresponds to a local minimum in current density in the range [1 -1.4 A/cm$^2$]) when there is a sufficient amount of liquid water in the GDL. For *RH* = 90%, liquid water is present for all the considered current densities. However, it can be seen from Fig.7 that there is a significantly greater amount of liquid water in the range of mean current densities [0.6 – 1.4 A/cm$^2$]. This is the range where the minimum in the current density in the region of the rib median axis is increasingly more marked as the mean current density increases.

The current density reversal effect, i.e. the fact that the current density below the rib median axis rather corresponds to a local maximum in current density at low mean current densities and to a minimum when the mean current density is sufficiently high can be quantitatively illustrated from the competition of $\delta i$ defined as

$$\delta i = \frac{1}{12} \sum_{j=n_{\min}}^{j=n_{\max}} (i(j) - \bar{i}) \qquad (1)$$

where *i(j)* is the current density along the current density transverse profile located in the row #*j* counted from the left side of the GDL unit cell. The transverse profiles depicted in Fig.9 are constructed from 52 discrete values corresponding to the number of pores (52) in the transverse direction. Then $n_{min}$ (= 21) and $n_{max}$ (=32) corresponds to the central region of the rib (the width of the rib counted in number of pores is 26, the rib extents from the rows #14 to #39, the rows 21 to 32 thus correspond to the central region of the rib illustrated in Fig.10). Thus $\delta i$ corresponds to the mean deviation between the current density in the central region of the rib and the mean current density. $\delta i > 0$ corresponds to the existence of a local maximum in the rib central region whereas $\delta i < 0$ corresponds to a local minimum.

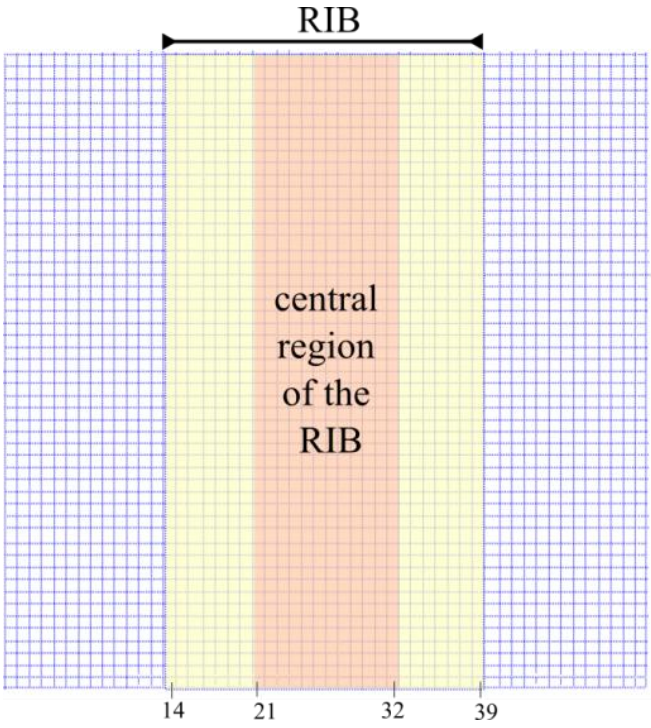


Figure 10: Rib region and central region of the rib

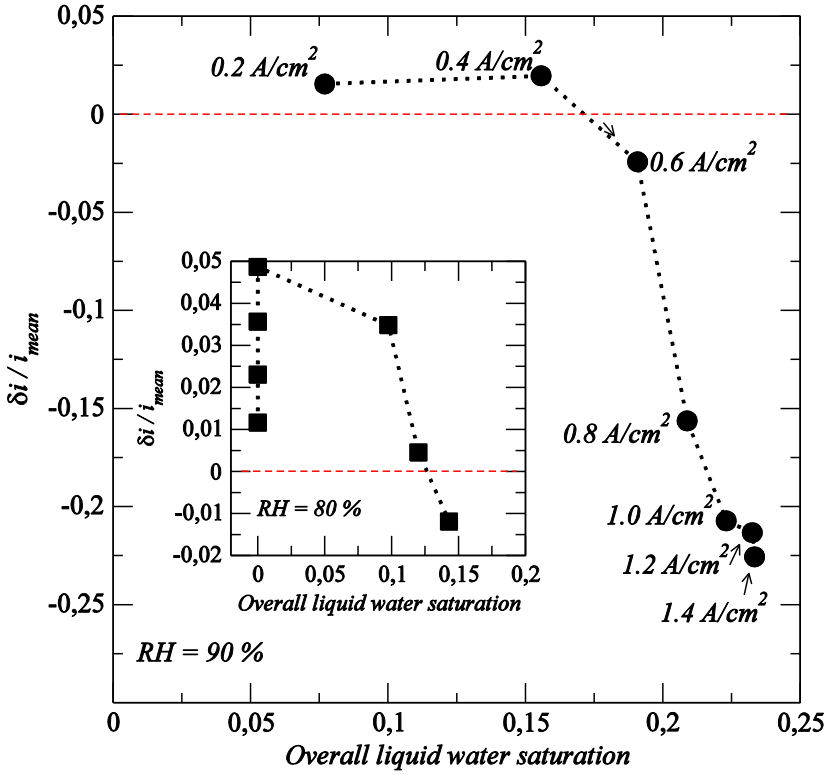


Figure 11: Current density mean deviation in the central region of the rib as a function of the overall liquid saturation; the black squares in the inset (RH 80%) correspond to the same mean current densities as the black dots (RH 90%).

The computation of $\delta i$ leads to the results depicted in Fig.11. They clearly illustrate that the current density reversal effect below the rib region can be directly interpreted as a consequence of the growth of the zone occupied by liquid water in the region of the DM below the rib.

## 5. Discussions

The main idea to explain the results discussed in the previous section, i.e. the current density reversal effect below the rib, is to consider that the development of the liquid region below the rib affects the oxygen access to the region of the catalyst layer located below the central region of the rib as well as the distribution of water vapor in this region.

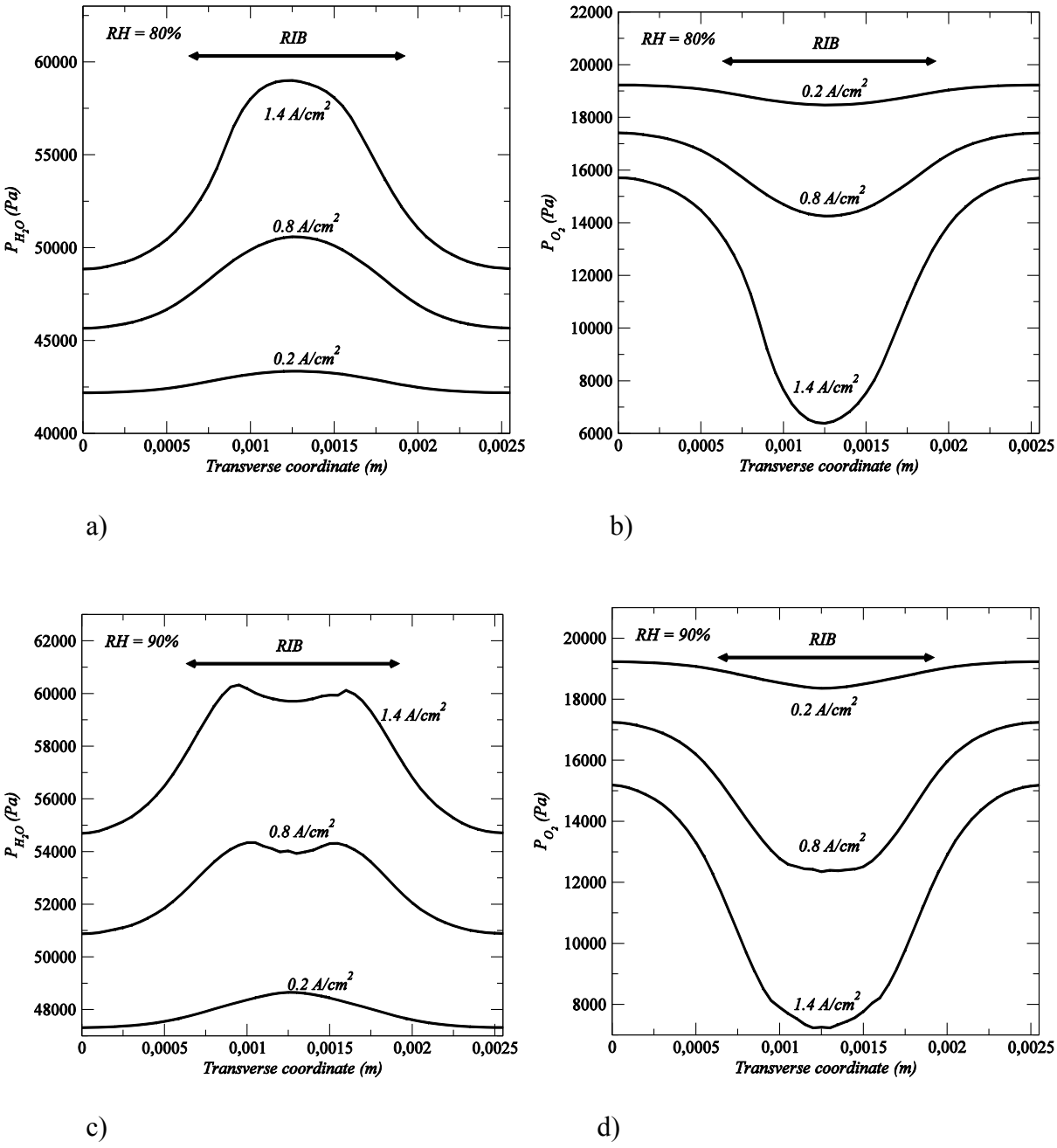


Figure 12: Water vapor and oxygen partial pressure transverse profiles at the CL – MPL interface for various mean current densities: a) b) *RH* = 80%, c) d) *RH* = 90%.

As illustrated in Fig. 4, the growth of the liquid zone in the DM reduces the fraction of the pore space available for the transport of the oxygen in this region. The consequence is a decreasing in the oxygen partial pressure at the MPL – DM interface in this region as the liquid zone grows. This is illustrated in Fig. 12, which shows that the effect is quite marked. The transverse distribution in oxygen is only slightly non-uniform at low mean current densities. The minimum in oxygen partial pressure for the lower mean current density is then attributed to the longer diffusion path between the channel and the central region of the rib compared to the region of the CL-GDL interface located below the channel. The minimum in

oxygen partial pressure becomes much more marked compared to the region below the channel when the liquid water zone develops below the rib. The trend is exactly the opposite regarding the water vapor partial pressure. As illustrated in Fig.12, the central region below the rib corresponds to a maximum in water vapor partial pressure. This maximum is due to the longer diffusion path from this region to the channel when the DM is dry (sufficiently low current densities). The maximum is much more marked when liquid water forms in the DM below the rib. As the liquid water zone develops, the water vapor partial pressure at the CL-GDL interface below the rib central region tends to get closer to the saturation water vapor pressure since menisci progressively get closer to this interface. This explains the change in the curves shape in Fig.12c (which corresponds to the case *RH* =90 % and thus to an important development of the liquid water zone), from a dome to a hat profile shape. This change is strongly correlated to the change in the transverse saturation profile depicted in Fig.7b.

However, the link with the current densities variations depicted in Fig. 9 is less straightforward than one might think at first glance.

As presented in Chapter 3, our model relies on the Butler-Volmer equation (Erdey-Gruz, 1930; Mann et al., 2006), which provides the relation between current density $i_{bv}$ and the overpotential $\eta$:

$$i_{bv} = i_0 \left( \exp\left(\frac{\alpha n F}{RT}\eta\right) - \exp\left(-\frac{(1-\alpha) n F}{RT}\eta\right)\right) \quad (2)$$

where $R = 8.3$ J/(mol.K) is the ideal gas constant, $T$ is the temperature, $F = 96485.3$ A/mol is the Faraday constant and $n = 2$ ($n$ is the number of chemical species involved in the reaction).

In Eq.(2), the exchange current density $i_0$ is expressed as:

$$i_0 = n\, k_0 \, \exp\left(-\frac{A_0}{RT}\right)\left(a_{O_2}^{\gamma_{O_2}}\right)^{1-\alpha}\left(a_{H_2O}^{-\gamma_{H_2O}}\right)^{\alpha} \quad (3)$$

in which $k_0 = 4.2.10^{-8}$ m. s$^{-1}$ , $A_0 = 24360$ J. mol$^{-1}$, $\alpha = 0.6$,$\gamma_{O_2} = 0.41$ ,$\gamma_{H_2O} = 2.04$ (as discussed in Chapter 4). In Eq.(3), $a_{O_2} = \frac{P_{O_2}}{P_{ref}}$, $a_{H_2O} = \frac{P_{H_2O}}{P_{sat}}$ are the oxygen and water activity respectively ($P_{O_2}$ and $P_{H_2O}$ are the oxygen and water vapor partial pressures in the gas phase within the catalyst layer).

Eq. (3), and thus also Eq.(2), is therefore directly dependent on the composition of the gas phase in oxygen and water vapor at the MPL – DM interface (assuming that the composition within the MPL and the CL is close to the composition at the MPL - DM interface or at least follows a similar spatial variation).

It can be seen from Eq.(3) that the current density decreases with a decreasing oxygen partial pressure. However it increases with an increasing water vapor partial pressure. Thus we cannot readily conclude from Fig.12 that $i_0$ decreases below the rib as a result of liquid zone growth.

The variation of $i_0$ is plotted in Fig.13. As can be seen the trend is in accordance with the results depicted in Fig.9, i.e. a local minimum in $i_0$ forms below the central region of the rib for a sufficiently high mean current density. This indicates that the impact of the liquid zone growth on the distribution of $P_{O2}$ has more impact on $i_0$ than the distribution of $P_{H2O}$ (which would tend to lead to a local maximum in $i_0$ and not a local minimum). However, the main point indicated by Fig.13 is that the amplitude of the $i_0$ variations is much too weak to fully explain the results plotted in Fig.9.

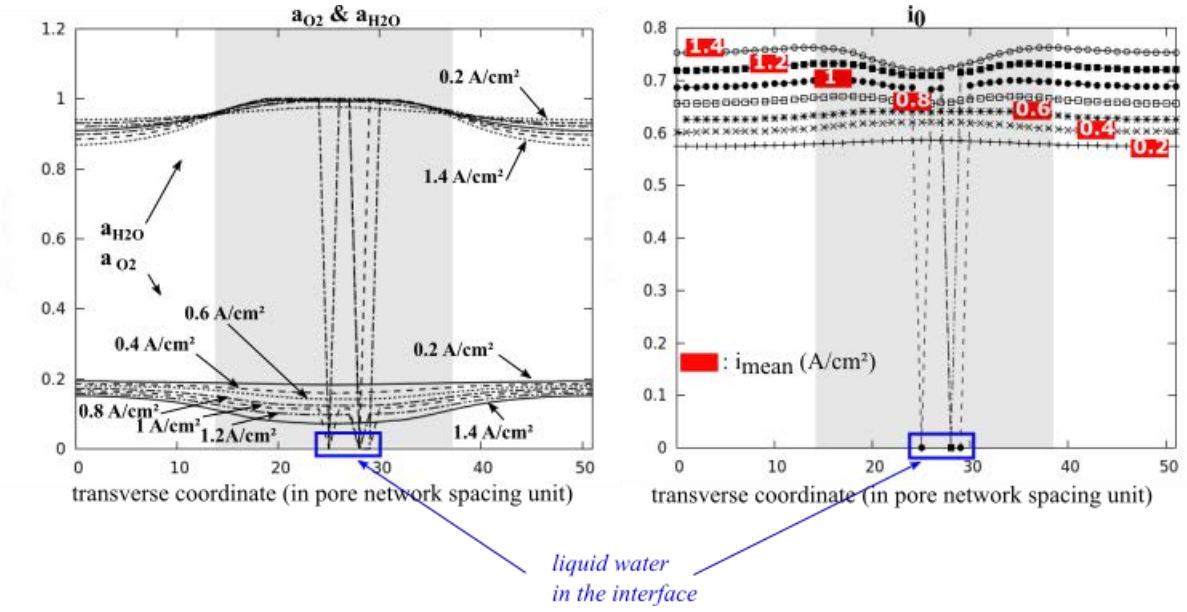


Figure 13: Transverse profiles of $i_0$, $a_{O2}$ and $a_{H2O}$ at the CL – MPL interface for various mean current densities for $RH = 90\%$.

Returning to Eq.(2), this is an indication that the dominant factor in the transverse variation of $i_{bv}$ must be the transverse variation in the overpotential $\eta$ (the temperature varies only slightly along the CL-MPL interface). In fact, in our model we first determine the electronic potential $\psi_c$ which is related to the overpotential $\eta$ through the series of equations (see Chapter 3):

$$\begin{cases} E_{rev} = \frac{\Delta H - T\Delta S}{nF} + \frac{RT}{nF} ln\left(a_{O_2}^{\frac{1}{2}} a_{H_2} a_{H_2O}^{-1}\right) \\ \psi_c = E_{rev} + \eta + \phi_c \\ \eta = -\frac{RT}{(1-\alpha)nF} ln\left(-\frac{i_{bv}}{i_0}\right) \\ \phi_c = \phi_a + R_m i_{bv} \end{cases} \quad (4)$$

where it turns out that the thermodynamic potential $E_{rev}$ (~ 1.22V) is dominated by the first term ($\frac{\Delta H - T\Delta S}{nF}$) and thus varies quite weakly with the activities $a_{O2}$ and $a_{H20}$. Also it can be noted that the membrane resistance $R_m$ is on the order of 5 $10^{-6}$ $\Omega/m^2$ for a well hydrated membrane. Thus the term $R_m i_{bv}$ in Eq.(4) is on the order of 0.05 V (50 mV). Note that by convention the current density is negative ($i < 0$) in Eq.(4). Thus Fig.4 actually shows the absolute value of current density $i$.

Fig.14 shows the transverse variations of $\psi_c$ for the cases $\bar{i}$ =0.2 and 0.8 A/cm$^2$. As can be seen, the electric potential $\psi_c$ varies little in the transverse direction when there is no liquid water formation ($\bar{i}$ =0.2 A/cm2) whereas the variation is noticeable in the presence of a liquid zone (RH =90% $\bar{i}$ = 0.8 A/cm$^2$) with a traverse variation of the order of 30 mV and a complete change in the profile (local maximum in $\psi_c$ below the central region of the rib in the presence of liquid water whereas a local minimum is observed when the DM is dry).

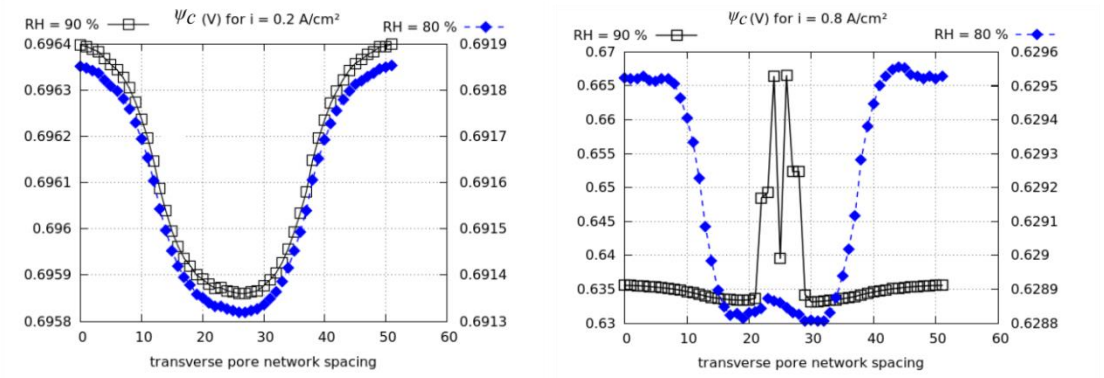


Figure 14: Transverse profiles of electronic potential $\psi_c$ at the CL – MPL interface for two mean current densities for *RH*= 80 % and *RH* = 90%.

Also the analysis of the two contributions to $\psi_c$, namely $\eta$ and $R_m i$ (note that $\phi_a$=0 by convention) shows that there are both of the same order of magnitude and varies like $\psi_c$. Thus, this confirms that the greater source of transverse variation in Eq.(2) is $\eta$ (and not $i_0$). Since $\eta$, $R_m i$ and $i$ are coupled through Eqs. (2-4), this, however, do not provide a clear-cut explanation (we face a "chicken ($\eta$) and egg ($i$)" problem). Since it is clear from Eqs. (2-4) that the solution to electronic transport problem (i.e. $i$, $\psi_c$) depends of the activities of $O_2$ and $H_2O$, we can finally only conclude that combination of the activities variations due to the liquid zone growth and the coupling between the various transport phenomena expressed in part by Eqs. (2-4) lead to the observed current reversal effect.

Our conclusion is therefore that the observed current density reversal effect as the mean current density is increased is essentially due to the development of the condensation liquid water zone below the rib. It can be argued, however, that the effect is observed for somewhat higher relative humidities in the channel compared to the experimental results depicted in Fig.2. Again, the condensation diagram for our model (Fig.3) does not necessarily correspond to the experimental situation. This is because we did no try to impose in our model the parameters corresponding to the experiments. For instance with the parameters used in Straubhaar et al. (2016), we believe that the obvious similarities between the experimental data and the simulations would have been still more striking.

## 5. Conclusions

A numerical model of the cathode side at the rib-channel scale was used to investigate the impact of mean current density on the current density distribution at the catalyst layer – GDL interface. A key aspect of this model is to simulate the liquid water formation process in the diffusive medium due to condensation. This aspect of the model was performed thanks to a pore network model using a recently proposed condensation algorithm.

The simulation shows that a current density reversal effect in the region of the diffusion medium below the rib with the current density region in the rib median axis region changing from a local maximum to a local minimum as the mean current density is increased. The simulations indicate that this variation in the structure of the current density distribution is directly correlated to the development of the condensation liquid water zone below the rib.

This is explained by the impact of the liquid region growth on the oxygen and water vapor concentration fields in the region of the GDL below the rib, which in turn affects the current density via the Butler-Volmer equation.

Interestingly, the simulation results are in good qualitative agreement with experimental results based on in-situ measurements.

The favorable comparison between the experiments and the simulations can also be viewed as an additional confirmation of the relevance of the condensation as major mechanism of liquid water formation in GDL in an operating fuel cell.

# References

Erdey-Gruz T., M. Volmer Z. Phys. Chem. (A) 150, 203-213 (1930).

Freunberger S. A., M.Reum, J.Evertz, A.Wokaun, F.N. Büchi, Measuring the Current Distribution in PEFCs with Sub-Millimeter Resolution, *Journal of The Electrochemical Society,* 153 (11), A2158-A2165 (2006)

Mann, R.F., J.C. Amphlett, B.A. Peppley, C.P. Thurgood, Application of Butler–Volmer equations in the modelling of activation polarization for PEM fuel cells, *Journal of Power Sources* 161, 775–781, (2006).

Rachidi S., Développement et exploitation d'une micro-instrumentation pour les piles à combustible de type PEMFC, Thèse Université de Poitiers (2011).

Straubhaar S., J.Pauchet, M. Prat, Pore network modelling of condensation in gas diffusion layers of proton exchange membrane fuel cells, submitted (2016)

# Chapter 7
# Impact of wettability on condensation pattern in the gas diffusion layer


## Abstract

The loss in hydrophobicity of the GDL is widely considered as a possible phenomenon contributing to the fuel cell progressive performance loss (aging). The loss in hydrophobicity is modeled here considering that the fraction of hydrophilic elements (pores or throats) in the network used to represent the diffusion medium GDL can vary between zero (purely hydrophobic network) and 1 (purely hydrophilic network). The impact of the hydrophobicity loss is studied from pore network simulations considering the condensation scenario for three different cases of the initial distribution of the hydrophobic agent within the network, various channel relative humidities and various mean current densities. A loss in performance, characterized by a greater invasion of the DM in liquid water and a diminished oxygen access, to the CL is found for intermediate values of the fraction of hydrophilic elements. The impact of the loss in hydrophobicity is found to be more marked for the lower values of the channel relative humidities tested.


## 1. Introduction

As discussed in Chapter 5 & 6, condensation is a key mechanism of liquid water formation in the GDL, at least for sufficiently high operating temperatures ($T \sim 80°C$). As in Chapter 5 & 6, the GDL is considered here as a simple two-layer assembly of the diffusive medium (DM) and the microporous layer (MPL). In Chapter 5 & 6 as well as in Straubhaar et al. (2016), it was assumed that the DM was perfectly hydrophobic. This means that the contact angle was supposed constant throughout the medium and greater than 90 °. It is indeed well known that the DM is generally treated so as to be hydrophobic thanks to a hydrophobic agent, most often PTFE, supposedly carpeting the fibers of the DM, Inoue et al. (2013). The contact angle for water on PTFE is approximately $\theta \sim 110$ - 120°. As discussed in previous works, e.g. Chapuis et al. (2008), the hydrophobic treatment favors the formation of capillary fingers when liquid water displaces the gas phase in the DM. As discussed in Chapuis et al. (2008), capillary fingering patterns facilitate the gas access to the catalyst layer (CL) compared to the compact invasion pattern expected in a hydrophilic system. However, it is somewhat unclear whether this also holds in the same way when the liquid water forms by condensation. Furthermore, it often happens that the hydrophobic agent is not uniformly distributed within the DM, which leads to the consideration of DM of mixed wettability. A DM of mixed wettability is a DM in which hydrophilic and hydrophobic regions coexist within the DM. An extreme but relatively frequently encountered case of DM of mixed wettability is when the hydrophobic agent is present only in the very first layers of the system on both sides of the DM without any PTFE in the layers located further inside the DM, e.g. Thomas et al. (2015). A related issue is the progressive loss of the PTFE during the operation of the system, e.g. Pulloor et al. (2011), Pauchet et al. (2012). This process is considered as one of the

degradation mechanisms leading to the progressive loss in fuel cell performance. Starting from a uniformly hydrophobic DM, the simple "aging" model considered in Pauchet et al. (2012) was to assume that the pores in the DM could completely lose their hydrophobicity randomly with the idea that the fraction of hydrophilic pores progressively increases over time from zero (initial perfectly hydrophobic state) to a high fraction of hydrophilic pores (a fraction of 100 % hydrophilic pores corresponds to a perfectly hydrophilic system). The contact angle was assumed to be the contact angle of water on carbon ($\theta$ ~ 80°) in the hydrophilic pores.

It is important to note that the studies reported in Pulloor et al. (2011) and Pauchet et al. (2012) were based on the scenario referred to as the "liquid" invasion scenario in which water enters the DM from the CL /MPL region directly in liquid phase (scenario #1). By contrast, we consider in this chapter the "vapor" scenario, also referred to as the condensation scenario (scenario #2), where liquid water forms in the GDL as a result of the condensation of the water vapor.

The objective is therefore to shed light on the impact of wettability on the liquid water distribution within the DM resulting from condensation.

## 2. Modeling

The computational model is the one described in Chapter 3 and is therefore the same as the one used in Chapters 5 and 6 for the study of the condensation diagram and the current intensity distribution at the GDL inlet (GDL/Catalyst layer (CL) interface, respectively).

Again, the parameters in our model are specified so as to be representative of SGL 25BC.

As mentioned in the introduction and sketched in Fig.1, the GDL is considered as a two-layer porous system, made of a "fibrous" Diffusion Medium (DM) and of a Micro-Porous-Layer (MPL) coated on the DM. The MPL penetration into the DM is not considered in this study.

The computational domain is depicted in Fig.1. It corresponds to an elementary unit cell containing a bipolar plate rib and two gas half channels. The geometrical dimensions of the various layers are specified in Fig.1. For the GDL, the indicated thickness corresponds to the uncompressed GDL, i.e. approximately below the channels.

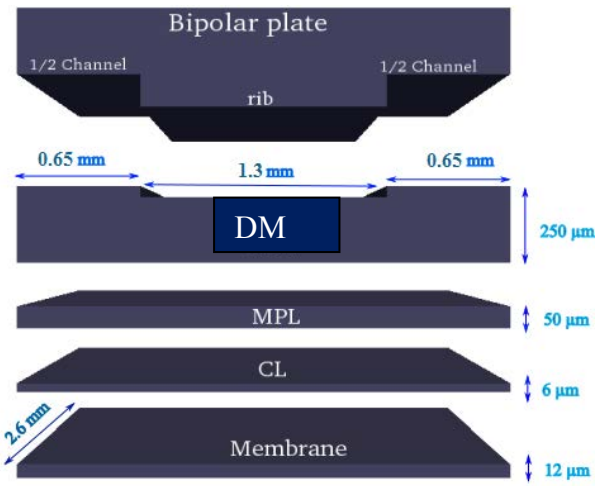


Figure 1: Computational domain.

The properties of the various layers have been specified as explained in previous chapters. There are summarized in Tables 1- 2 for the MPL and the GDL.

Table 1 : MPL properties.

| | *Effective thermal conductivity* ($Wm^{-1}K^{-1}$) | *Effective electrical conductivity* (S/m) | *Effective diffusion coefficient* | *Thickness* (*µm*) | *Porosity* |
|---|---|---|---|---|---|
| *Symbol* | $\lambda$ | $\sigma$ | $D^*/D$ | | |
| | 2.5 | 2500 | 0.04 | 50 | 0.4 |

Table 2: DM properties (corresponding to SGL 25 BC).

| | *DM thickness* (*µm*) | | *Porosity* (%) | |
|---|---|---|---|---|
| *Symbol* | $\delta$ | $\delta_{uc}$ | $\varepsilon_c$ | $\varepsilon_{uc}$ |
| | 200 | 250 | 0.72 | 0.8 |
| | *Effective thermal conductivity* ($Wm^{-1}K^{-1}$) | | | |
| *symbol* | $\lambda_{//c}$ | $\lambda_{//uc}$ | $\lambda\perp_c$ | $\lambda\perp_{uc}$ |
| | 6.9 | 4.9 | 0.35 | 0.17 |
| | *Effective electrical conductivity* (S/m) | | | |
| *symbol* | $\sigma_{//c}$ | $\sigma_{//uc}$ | $\sigma\perp_c$ | $\sigma\perp_{uc}$ |
| | 5000 | 4000 | 254 | 138 |
| | *Effective diffusion coefficient (-)* | | | |
| *symbol* | $D_{//c}/D$ | $D_{//uc}/D$ | $D\perp_c/D$ | $D\perp_{uc}/D$ |
| | 0.5 | 0.6 | 0.12 | 0.2 |

The useful properties of the other layers, namely the catalyst layer (CL) and the membrane are given in Chapter 4 together with the model used to compute the current density distribution (Chapter 3).

The GDL is represented by a 52x52x7 cubic pore network (the figures indicate the number of pores along the directions of a Cartesian grid), see Chapter 3 for more details. As discussed for instance in Straubhaar et al. (2016), the pore network (PN) representation is convenient for simulating the formation of liquid water by condensation in the DM. The condensation PN algorithm described in Straubhaar et al. (2016) is used. The main features of this algorithm are summarized in Chapter 3. However, it should be noted again that the DM was supposed uniformly hydrophobic in Straubhaar et al. (2016). The local invasion rules in a hydrophilic system or a system of mixed wettability are somewhat more complex as described in Chapter 3, see also Pulloor et al. (2011), Pauchet et al. (2012), Ceballos and Prat (2013). This is because the local menisci displacement rules in hydrophilic regions require distinguishing the pore invasion from the throat invasion (in a hydrophobic region, the local menisci

displacement rules are only controlled by the throats). Also, it is necessary to take into account the cooperative effects between adjacent throat menisci in the pore invasion mechanisms. Thus, here, the algorithm presented in Straubhaar et al. (2016) was extended so as to take into the local wettability conditions.
The fraction of hydrophilic throat and pores in a given region of the DM is denoted by $f$ : $f = 0$ ( $f$ = 100 % respectively) means that all pores and throats in this region are hydrophobic (hydrophilic respectively).
The simulations presented in what follows were performed for the values of operating conditions and parameters reported in Tables 1-2 and Table 3.

Table 3. Simulation conditions ($T$ is the bipolar plate temperature equal to the gas temperature, $P$ the total gas pressure, $p_{O2}$ the oxygen partial pressure in the channel, $RH$ the relative humidity in the channel); $\beta_{H2O}$ and $\beta_T$ are the mass flow rate and heat transfer rate partition coefficients; $\eta$ is the nucleation parameter (see Chapters 3 or 4)

| $T$ (°C) | $i$ (A/cm$^2$) | $RH$ (%) | $P$ (bar) | $p_{O2}$ / $P$ | $\beta_T$ | $\beta_{H2O}$ | $\eta$ |
|---|---|---|---|---|---|---|---|
| 80 | 1-1.5 | 80-95 | 1.5 | 0.21 | 0.8 | 0.8 | 1 |

## 3. The three cases

As briefly discussed in the introduction, various situations can be considered as regards the distribution of the hydrophobic agent. Fig.2 illustrates the situation where the hydrophobic agent could be essentially present along the external surfaces of the DM and seemingly not present (or much less present) further inside the DM.

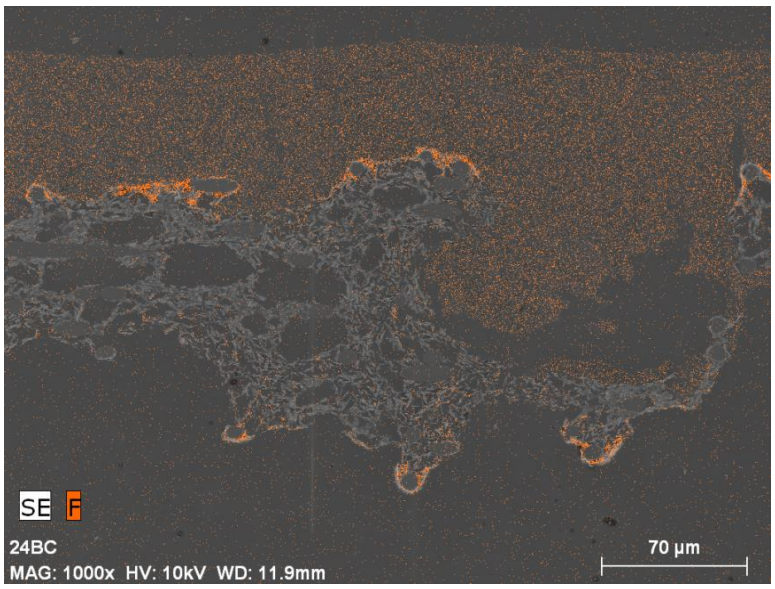


Figure 2: Example of heterogeneous hydrophobic agent (orange pixels) distribution within the GDL (image from Thomas et al. (2015)). The hydrophobic agent is present everywhere within the MPL (top layer with orange pixels almost evenly distributed) whereas the image suggests that the wettability could be different along the edges of the DM (bottom layer with clear top and bottom zones of higher concentration in hydrophobic agent) from the region further inside the DM. Note also the interpenetration of the MPL and the DM suggesting that considering the DM / MPL interface as a flat dividing surface is a somewhat too rough assumption.

In the present chapter, three cases are distinguished regarding the initial distribution of the hydrophobic agent. The three cases are illustrated in Fig.3. Also, in what follows, "degradation" means the variation of the fraction $f$ of hydrophilic pores: $f$ = 0 in a non-degraded region, $f$ = 100 % when this region is fully degraded. Typically, we will look at what happens in the DM when $f$ varied from $f$ = 0 (initial state) to $f$ = *1* in the considered region.

In case 1 the hydrophobic agent is homogenously distributed in all the DM. Thus, $f$ = 0 everywhere within the DM in the initial state. The degradation, i.e. the variation of $f$, is considered as "homogenous". This means that the pores and throats labelled as hydrophilic for a given value of $f$ are selected randomly. There is no preferential localization effects in the variation of the wettability , i.e. under the rib or below the channel for example, for case #1.

In case 2 the hydrophobic agent is present only in the first rows of pores along the outer surfaces of DM (two first rows of pores and throats on the channel –rib side, first row of throats and pores on the CL side). The two rows of pores further inside the DM are supposed fully hydrophilic. This case could approximately mimic the situation depicted in Fig. 2 (again if one considerers that the hydrophobic agent is not present at all in the middle layers). The variation of $f$ in the rows of pores initially uniformly hydrophobic is homogeneous, i.e. the hydrophilic pores and throats are selected randomly without preferential localization effect.

In case 3, the initial distribution of the hydrophobic agent is exactly the same as for case 2. The difference lies in the fact that only the pores and throats below the channels can become hydrophilic. Thus the degradation, i.e. the variation of $f$, takes place only in the two first rows of pores and throats in contact with the channels. Thus it is assumed here that the degradation takes place preferentially below the channels and that there is no degradation below the rib. As for case 2, the two rows inside the DM are fully hydrophilic.

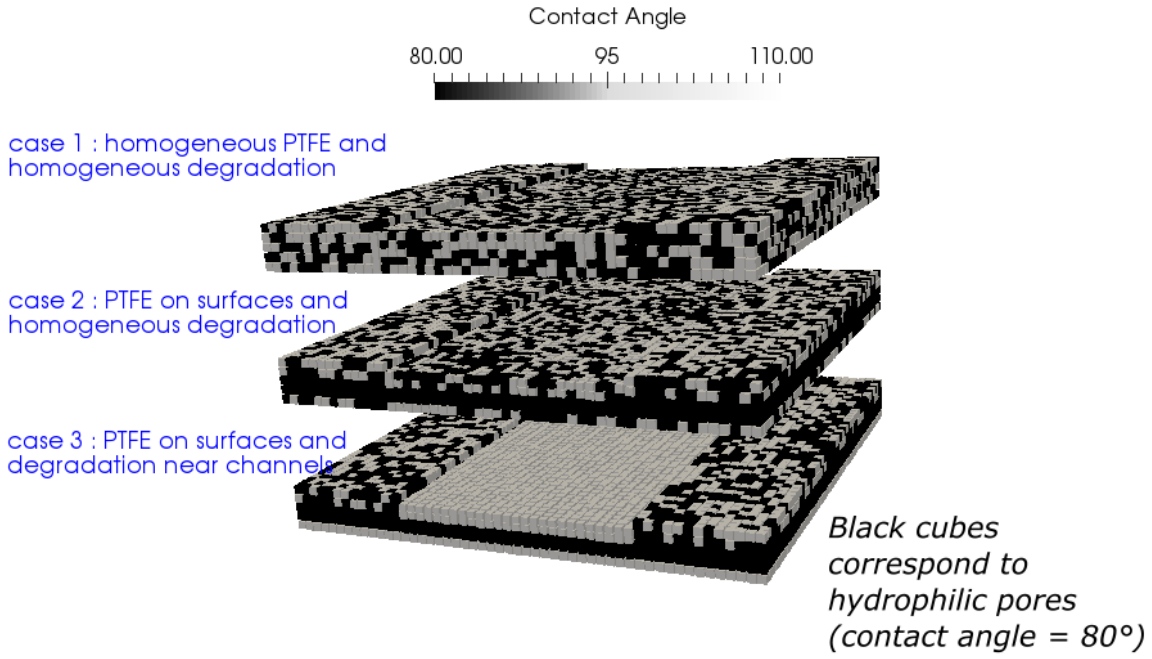


Figure.3: Illustration of the three cases for $f$ = 50%

# 4. Results

## 4.1 Main results for scenario #1 (invasion in liquid phase)

For convenience, the main results obtained within the framework of scenario #1 (invasion in liquid phase from the adjacent MPL or CL) and reported in Pulloor et al; (2011) are briefly summarized in this section. This will facilitate the comparisons between the two scenarios, i.e. liquid invasion vs condensation. Note that only case #1 was considered in Pulloor et al. (2011).

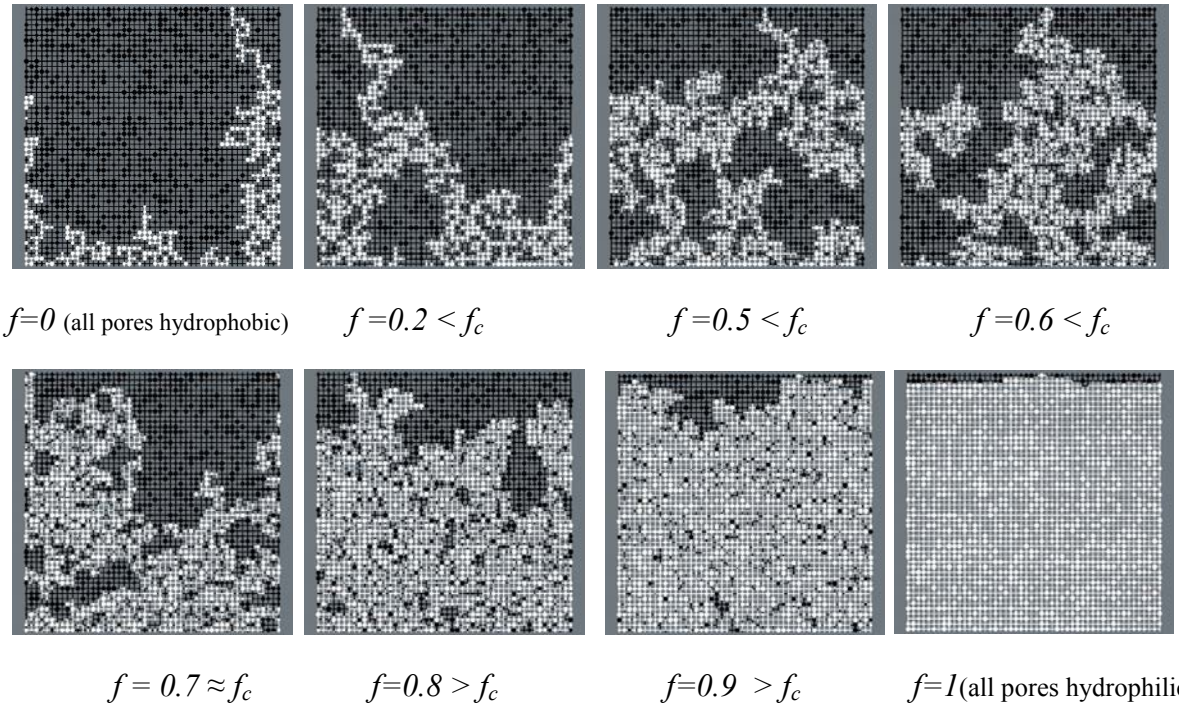


Figure 4: Case 1 for scenario #1. Invasion patterns for various values of the hydrophilic pore-throat fraction $f$ in a 2D 50 x 50 square network. The invading fluid (water in white) is injected from the bottom. The defending fluid (in black) escapes from the top. A capillary fingering pattern is observed for $f \sim 0$. A compact pattern is obtained for $f \sim 1$. The pattern obtained for $f \sim f_c$ resembles the capillary fingering pattern but actually results from the fact the percolating subnetwork formed by the hydrophilic pores and throats is a percolation cluster. An invasion percolation cluster ($f \sim 0$) is about the same fractal object as the hydrophilic pores percolation cluster ($f \sim f_c$). This is why both cases ($f \sim 0$ and $f \sim f_c$) lead to the same type of phase distribution despite the change in the local mechanisms controlling the growth of the liquid/gas interface in the hydrophobic regions and the hydrophilic ones respectively. For this bond-site percolation network, the percolation threshold $f_c$ is approximately equal to 0.7 (in 2D).

The typical variation of the invasion pattern at breakthrough with the "wettability", i;e. $f$, within the framework of scenario #1 is depicted in Fig.4 whereas the variations of the overall liquid saturation at breakthrough $S_{BT}$ and of the through-plane effective diffusion coefficient $D_{eff}$ (characterizing the gas access through the DM) are shown in Fig.5. As can be seen from Fig.5, the variations of $S_{BT}$ and $D_{eff}$ are minor until $f$ reaches the network percolation threshold $f_c$. Then $S_{BT}$ sharply increases and $D_{eff}$ sharply decreases for $f$ increasing above $f_c$ ($f_c$ ~50% in 3D).

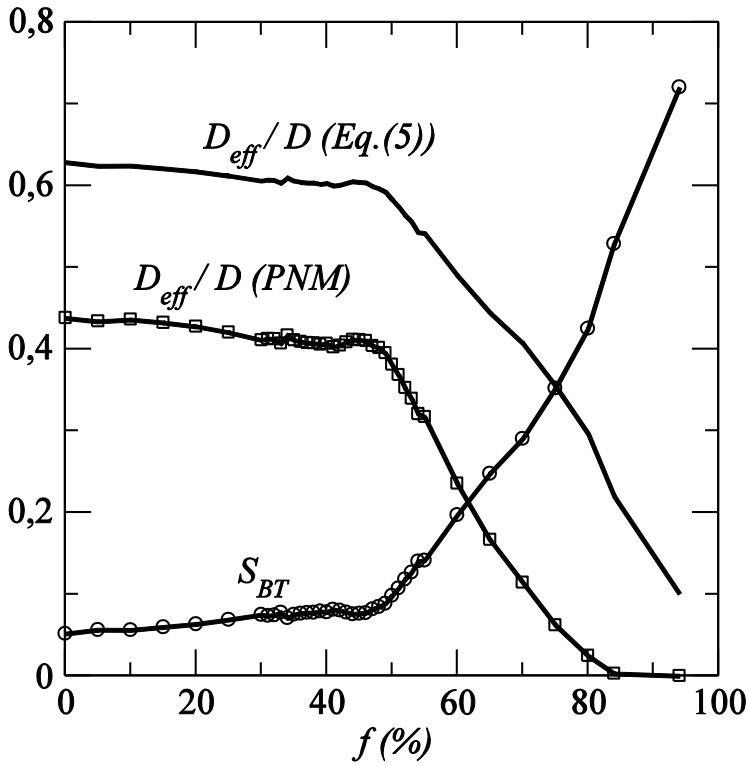


Figure 5: Case #1 with scenario #1. Variation of saturation at breakthrough ($S_{BT}$) and through-plane binary effective diffusion coefficient at breakthrough (PNM) as a function of the fraction of hydrophilic elements $f$ (from Pulloor et al. (2011)).

## 4.2 Condensation diagram

With the assumptions made in our model, the wettability conditions in the DM have no effect on the condensation diagram (see Chapter 5). This is because we implicitly assumed that the presence of the hydrophobic agent do not modify the DM gas diffusion and thermal properties. However, one can argue that the hydrophobic agent can partially occupied the throats and pores and therefore can alter the diffusion properties. Also as reported in Sadeghifar et al. (2013), the presence of the hydrophobic agent can affect the effective thermal conductivity of the DM. Thus, the condensation diagram could actually be (slightly ?) modified by the variations in the DM transport properties due to the loss of hydrophobic agent.

## 4.3 Impact of *f* on the liquid phase distributions (condensation scenario)

Fig.6 shows how the liquid distribution varies within the DM when the fraction of hydrophilic elements $f$ is varied for case 1 whereas similar information is provided in Fig.7 for case 2. As can be seen liquid water remains mostly confined below the rib for all the values of $f$ tested. However, one can observe a significant transverse invasion for $f \sim 60$ -70% when the channel relative humidity is sufficiently low ($RH = 80$ % in Fig.6 and Fig.7).

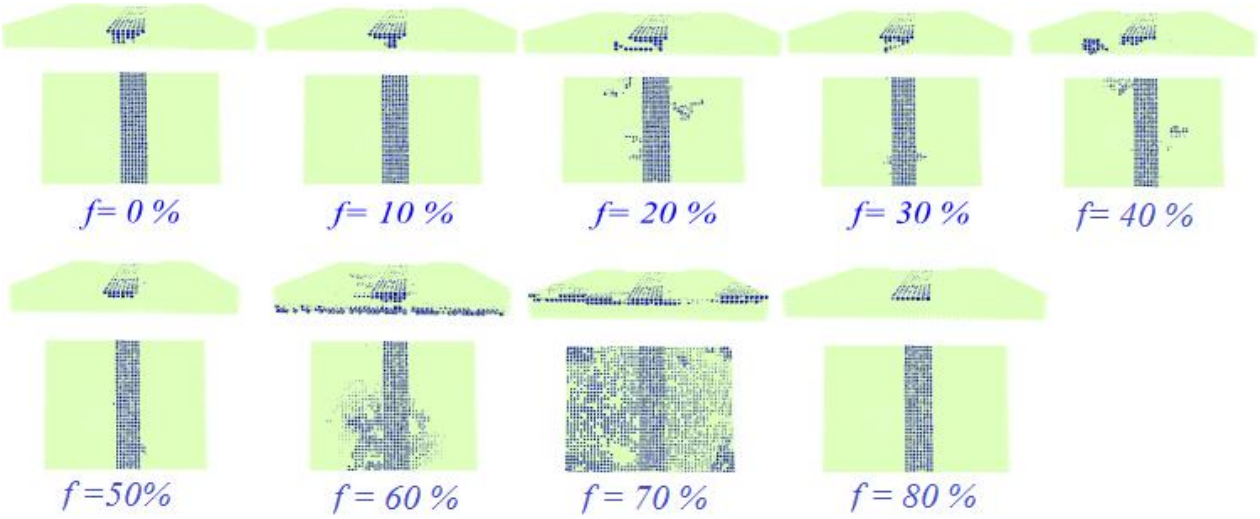


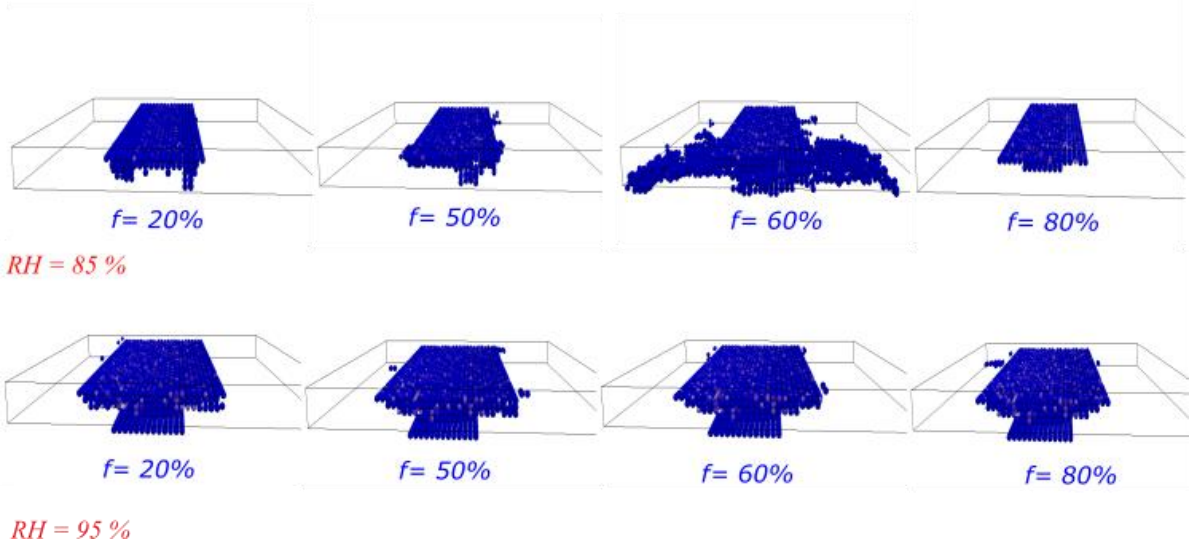


Figure 6: Typical liquid water (in blue) distribution in case 1 for $i$ = 1 A/cm$^2$ for various channel relative humidities ($RH$) and various fractions $f$ of hydrophilic elements (pores and throats).

Also the situation is not significantly different between case #1 and case #2 on the basis of the phase distributions depicted in Figs.6 and 7. This is somewhat counter-intuitive since one might have expected a more marked invasion of the fully hydrophilic middle region with case 2. The effect is however visible if one compares the patterns for $f$ = 60% and $f$ = 70% between Fig.6 and Fig.7 for $RH$ = 80%.

The situation is therefore quite different from the one observed with scenario #1 (liquid injection). As reported in Pulloor et al. (2011) and illustrated in Fig.4, see also Ceballos et Prat (2013), the phase distribution is greatly affected when $f$ is greater than the percolation threshold of network with the network becoming fully liquid saturated for $f$ ~100%. By contrast, the patterns for $f$ = 20% and $f$ =80% are almost identical in Figs.6 and 7.

This is interpreted by the fact that the final invasion shape in the case of the condensation scenario results from a balance between condensation and evaporation. This is sketched in Fig.8. Accordingly, for a given current density, the liquid must reach a region closer to the channel when $RH$ is high compared to the same case with a lower $RH$ (this is because the

evaporation rate is globally proportional to the difference in water vapor pressure between the channel and the evaporation front within the DM and inversely proportional to the distance from the front to the channel). This is clearly visible from Figs. 6 and 7.

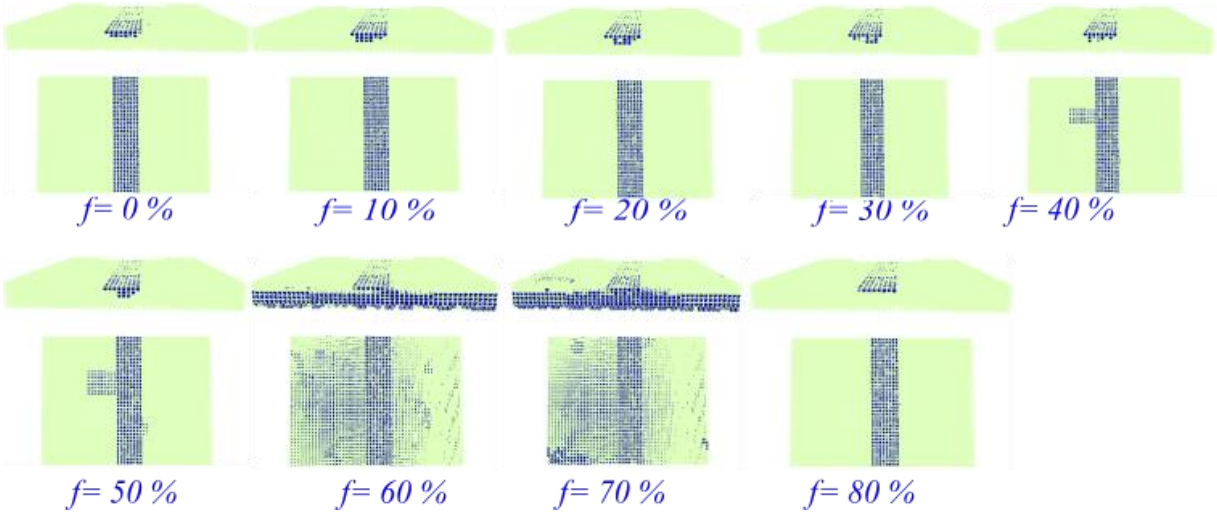


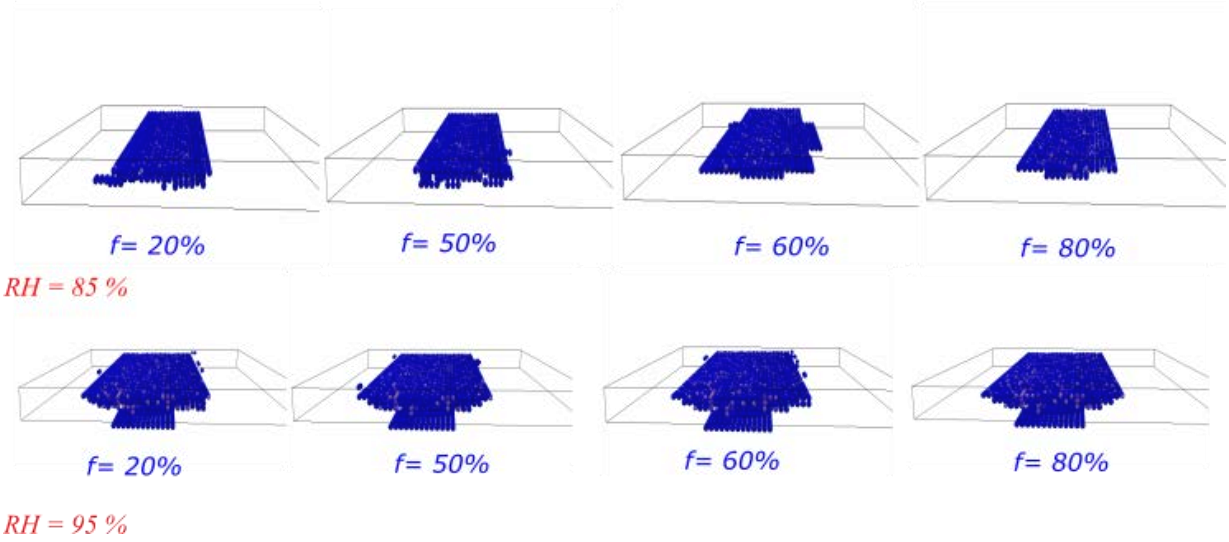


Figure 7: Typical liquid water (in blue) distribution in case 2 for $i$ = 1 A/cm$^2$ and for various channel relative humidities ($RH$) and various fractions $f$ of hydrophilic elements (pores and throats).

The liquid zone hull (the envelop surface of the liquid region), which is also the place of the phase change (evaporation or condensation), might not strongly dependent on the local growth rules of the liquid clusters, i.e. eventually on the wettability. This is probably in part due to the diffusive screening of liquid fingers forming in the hydrophobic case (evaporation or condensation rates are important at the tips of fingers and not within the "fjords" of the liquid clusters). Thus the fact that the clusters are a priori much less compact in the hydrophilic case compared to a fully hydrophilic case could have a limited effect on the final shape of the condensation –evaporation surface.

As a results, the impact of *f* is mostly sensitive for intermediate values (*f* ~60 – 70 %) and not too high *RH* ,i.e. *RH* ~ 80 %) when the growth of the liquid zone is impacted by the preferential invasion of hydrophilic elements.
Consistently with the results depicted in Figs.6 and 7, changing the wettability, i.e. *f*, has absolutely no impact for case #3. In fact, no liquid water forms at the channel-DM interface under the considered conditions. Thus, modifying the wettability in this region of the DM has no impact. For this reason, considerations are mostly given to cases #1 and 2 in what follows unless otherwise mentioned.
Further insights on the impact of wettability can be gained from the consideration of overall saturation.

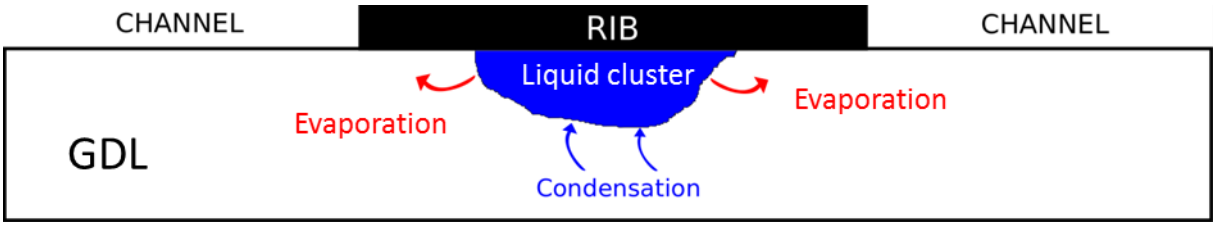


Figure 8: Illustration that the computed liquid water distribution corresponds to a steady state where the evaporation rate at the boundary of each liquid cluster exactly compensates the condensation rate (from Straubhaar et al. 2016).

## *4.4* Variations of overall liquid saturation with *f*

### 4.4.1 Impact of channel relative humidity

Fig.9 shows the variation of overall liquid saturation (fraction of pores and throats in the whole network occupied by liquid water) as a function of *f* for various relative humidies *RH* in the channel and a given mean current density ($i$ = 1A /cm$^2$). The results correspond to mean values over 10 realizations of network. First as reported in Straubhaar et al. (2016), it can be seen that the overall saturation increases with an increasing *RH* in the purely hydrophobic cases. A similar variation is observed for *f* = 100 % (fully hydrophilic DM). Somewhat counter-intuitively, the overall saturation is less for a 100% hydrophilic network than for a 100% hydrophobic network (except for the case RH = 95% in Fig.9). Again, this is probably due to the compact invasion pattern when the network is sufficiently hydrophilic.
The situation is, however, more complex for intermediate values of *f*. For example, the saturation for *f* =70% at *RH* =80% is much higher than at *RH* = 90 or 95 %.
The case with the highest tested *RH* (*RH* =95% in Fig.9) leads to relatively low variations of the overall saturation with the change in wettability *f*. The overall saturation stays close to 0.09 with however slightly greater saturations for *f* in the range [10% -50%]
The most striking feature in Fig.9 is perhaps than the variation of the overall saturation does not monotonically vary with *f* . This is in full contrast with the variations obtained under scenario #1 (Pulloor et al. (2011)) showing that the overall saturation sharply increases with an increasing *f* for *f* above the network percolation network (see Fig.4).
As can be seen from Fig.9, the lower the relative humidity (in the range tested, which correspond to the range for which condensation is obtained of course), the greater the impact

of *f*. The impact is quite significant for *f* in the range [60 -70%], which corresponds to the quite visible impact on the liquid patterns shown in Fig.6 (case 1) and Fig.7 (case 2).

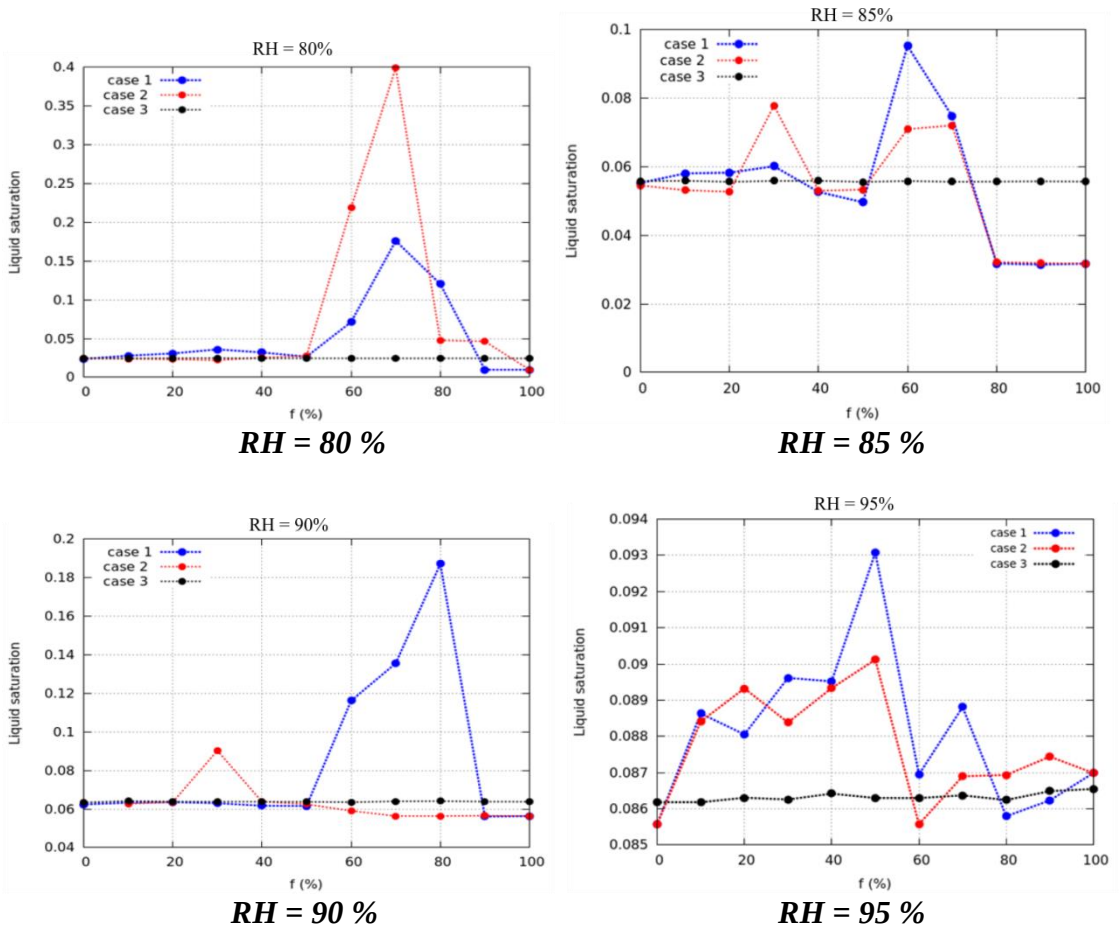


Figure 9: Variations of overall saturation as a function of *f* for the three cases for four different values of the channel relative humidity and $i$ = 1 A / cm$^2$. Data correspond to mean values over ten realizations of network.

### 4.4.2 Impact of current density

Fig.10 shows the influence of *f* on the overall liquid saturation *S* for three various mean current densities and *RH* = 80%. The variation of *S* with *i* for a purely hydrophobic network (*f* = 0%) is similar to the one reported in Straubhaar et al. (2016). The greater the current density, the greater the saturation. The variation is similar in a fully hydrophilic network as shown in Fig. 10. In the intermediate situations, i.e. 0 < *f* <100% (and especially for *f* ~60 -70 %), this trend is not verified. For example for case #2 and *f* =70% , this is exactly the opposite variation which is found (the greater the current density, the lower the saturation).

Again the range of intermediate values in *f* , namely *f* ~60 -70 %, has on the whole a much greater impact with significantly greater saturation (note that this is however not observed for case 2 and $i$ =1.5 A/cm$^2$).

As already observed and illustrated in Fig.11, *f* has no impact for case 3 since again liquid water is no present in the region where *f* is varied in case 3.

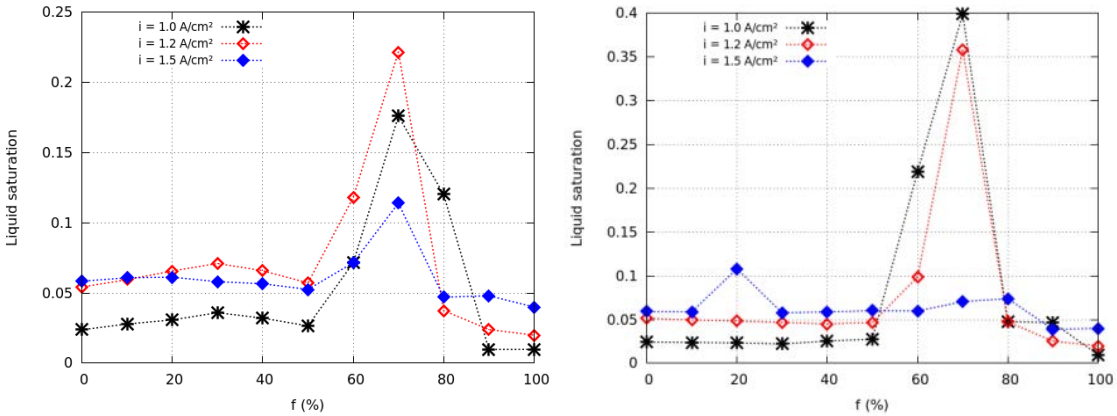


Case #1 Case #2

Figure 10: Cases #1 and 2: Variations of overall saturation as a function of hydrophilic elements *f* for three values of the mean current density (*i*=1A/cm², 1.2 A/cm², 1.5 A/cm²); *RH* = 80 % and *T* = 80 °C. Data correspond to mean values over ten realizations of network.

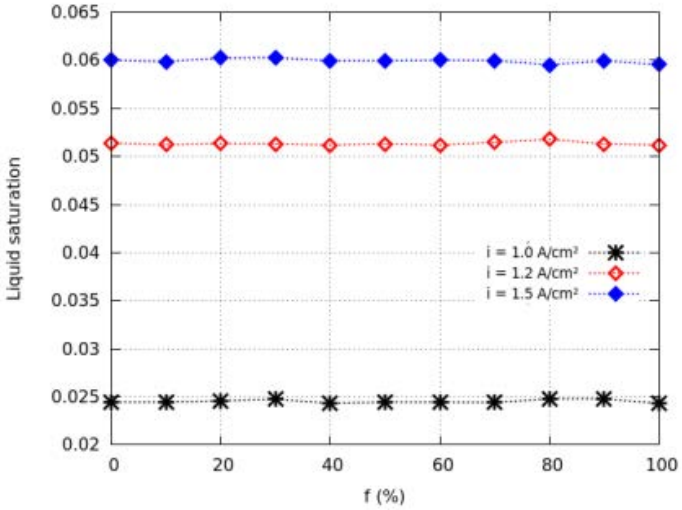


Case 3

Figure 11: Case #3: Variations of overall saturation as a function of hydrophilic elements *f* for three values of the mean current density (*i* = 1A/cm², 1.2 A/cm², 1.5 A/cm²); *RH* = 80 % and *T* = 80 °C. Data correspond to mean values over ten realizations of network.

## 4.5 Impact on gas diffusion properties

Fig.12 shows the variation of through plane effective diffusion coefficient (computed as explained in Chapter 1) with the fraction of hydrophilic elements *f*. There is an obvious and expected direct correlation between the variations of $D_{eff}$ and the variation of the overall saturation *S*. The greater the saturation, the lower the effective diffusion coefficient. This was expected since oxygen is transported only in the fraction of the pore space free of liquid water (dissolved oxygen transport is neglected).

Here again, the variation of $D_{eff}$ is quite different from the one reported in Pulloor et al. (2011) for scenario #1 (see Fig.5), consistently with the quite different impact of *f* on the overall saturation between scenario #1 and scenario #2

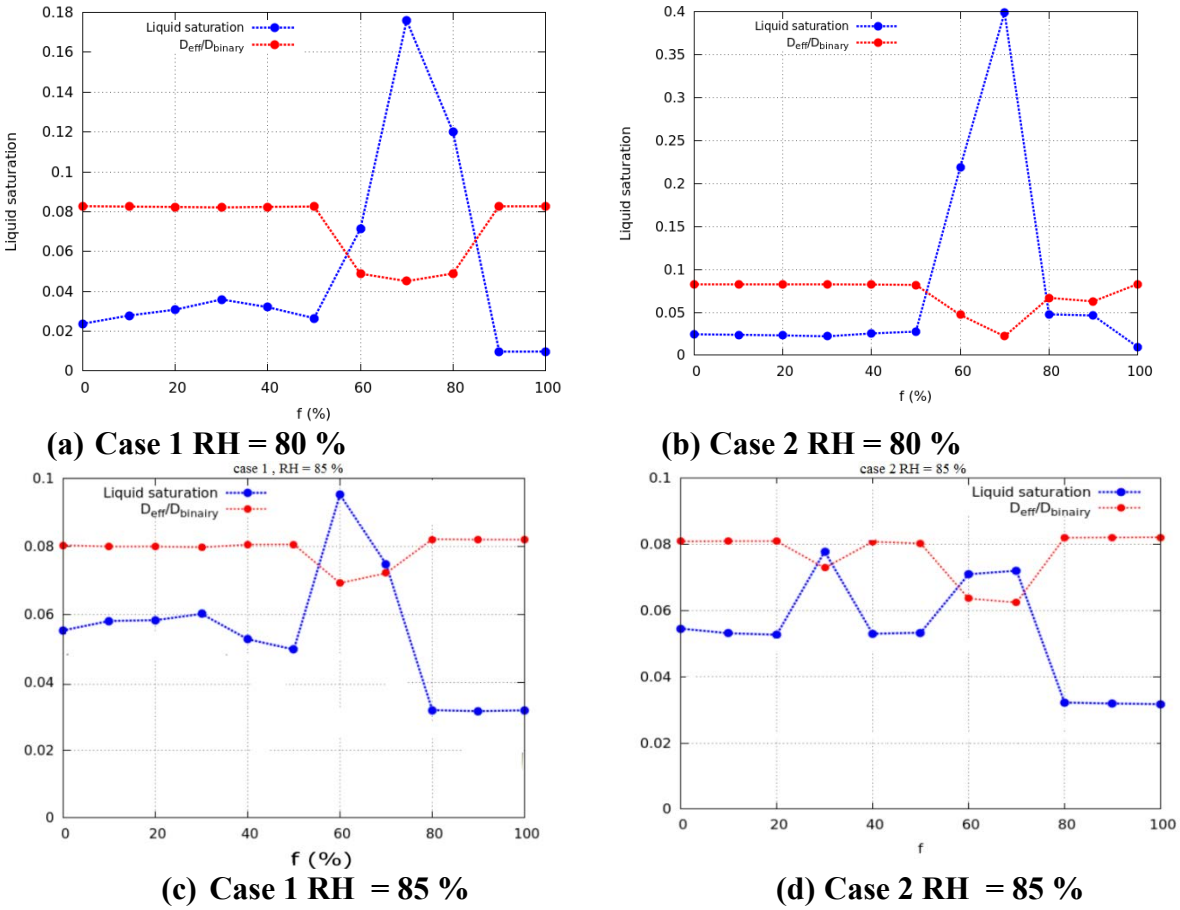


Figure 12: Variations of overall saturation and through plane effective diffusion coefficient as a function of $f$ for $RH$ = 80 % and 85 % for case #1 and case #2 ($i$ = 1 A/cm2, $T$ = 80°C). Data corresponds to mean values over ten realizations of network.

## 5. Conclusions

In this chapter, preliminary results on the impact of wettability on the condensation scenario were reported. The wettability was characterized by the fraction $f$ of hydrophilic throats and pores in the network used to represent the diffusion medium (coarser medium of the GDL). The complementary fraction 1-$f$ was supposed hydrophobic. Three cases were distinguished depending on the initial of the hydrophobic agent within the DM.

The results present some quite significant differences with previous results obtained within the framework of scenario #1 (liquid injection). The most striking one is the fact that a fully hydrophilic network leads to results comparable, or even better, than a fully hydrophobic network.

However, there exists an intermediate range of $f$, close to 60 – 70 % in our examples leading to significant performance degradations (i.e. higher overall saturations and lower values in the through plane effective diffusion coefficient in our simulations). This was more marked for the lowest channel relative humidity $RH$ considered in our simulations. The interpretation is as follows. First a lower $RH$ makes more likely the in –depth invasion of the diffusion medium (as opposed to a greater $RH$ that makes more likely the transverse invasion toward

the channel). Second, intermediate values of $f$ favor the formation of hydrophilic sub-networks. These sub-networks are preferentially invaded and can transport the liquid water within the middle rows of network away from the rib area. More detailed analyses are however needed to confirm this.

**References**

L. Ceballos, M. Prat, Slow invasion of a fluid from multiple inlet sources in a thin porous layer: influence of trapping and wettability, Phys. Rev. E 87, 043005 (2013)

O. Chapuis, M. Prat, M. Quintard, E. Chane-Kane, O. Guillot, N. Mayer, Two-phase flow and evaporation in model fibrous media. Application to the gas diffusion layer of PEM fuel cells, J. of Power Sources, 178, 258 -268 (2008).

G. Inoue, N. Ishibe, Y. Matsukuma, M. Minemoto, Understanding Mechanism of PTFE distribution in Fibrous Porous Media, ECS Transactions 50(2):461-468 ·(2013)

S. Pulloor Kuttanikkad, M. Prat, J. Pauchet, Pore-network simulations of two-phase flow in a thin porous layer of mixed wettability: Application to water transport in gas diffusion layers of proton exchange membrane fuel cells, J. of Power Sources 196, pp. 1145–1155 (2011)

J. Pauchet, M. Prat, P. Schott, S. Pulloor Kuttanikkad, Performance loss of proton exchange membrane fuel cell due to hydrophobicity loss in gas diffusion layer: Analysis by multiscale approach combining pore network and performance modelling, Int. J. of Hydrogen Energy. 37 (2), pp. 1628 – 1641 (2012)

H.Sadeghifar, N.Djilali, M.Bahrami, Effect of PTFE on thermal conductivity of gas diffusion layers of PEM fuel cells, Proceedings of the ASME 2013 11th Fuel Cell Science, Engineering and Technology Conference FuelCell2013, July 14-19, Minneapolis, MN, USA (2013)

B.Straubhaar, J.Pauchet, M. Prat, Pore network modelling of condensation in gas diffusion layers of proton exchange membrane fuel cells, submitted (2016)

Y. R. J. Thomas, A. Benayad, M.Schroder, A. Morin, J.Pauchet, New Method for Super Hydrophobic Treatment of Gas Diffusion Layers for Proton Exchange Membrane Fuel Cells Using Electrochemical Reduction of Diazonium Salts, ACS Appl. Mater. Interfaces, 7, 15068−15077 (2015).

# Conclusion et perspectives

Les travaux présentés dans cette thèse ne sont pas tout à fait ceux qui étaient initialement prévus, du moins en ce qui concerne l'exploitation du modèle du chapitre 3 vis-à-vis de la perte des performances. Les problèmes de dégradations n'ont été en réalité que légèrement abordés avec le chapitre 7 concernant l'impact de la mouillabilité sur les « patterns » de condensation.

Ceci s'explique principalement par un changement de paradigme concernant la formation de l'eau liquide dans le support de la GDL, c'est-à-dire le « diffusion medium » (DM) avec les définitions utilisées dans ce travail. Même à l'échelle d'un « simple » problème d'ingénieur, les changements de paradigme demandent un certain temps d'appropriation et rencontrent des résistances somme toute classiques, dès lors qu'il s'agit de quitter un système de pensée largement accepté. En clair, cela a pris du temps de passer du scenario #1 (invasion en phase liquide depuis la MPL ou la couche catalytique (CC)) qui prévalait en début de thèse au scenario #2 (condensation), qui est celui maintenant considéré comme le plus représentatif.

L'idée que la condensation puisse être un mécanisme important avait été mise en avant par différents auteurs, e.g. Nam et Kaviany (2003), Basu et al (2009), Caulk et Baker (2010,2011), Owejan et al. (2010), Alink et Gerteisen (2013), Thomas et al. (2012-2014), mais n'avait pas reçu la considération qu'elle méritait dans les travaux basés sur les modèles de réseau de pores.

Le premier modèle réseau de pores bâti pour le scenario de condensation est celui proposé dans la thèse de Straubhaar (2015). Cette thèse a montré que le scenario de condensation était nettement plus cohérent avec les visualisations expérimentales in-situ de l'eau ainsi qu'avec plusieurs autres observations expérimentales comme l'impact de la densité de courant moyenne ou de l'humidité dans le canal sur les profils de saturation, du moins pour les températures de fonctionnement classiques autour de 80°C. La situation est cependant peut-être plus complexe et reste à clarifier aux températures nettement plus basses. Ceci justifie de ne pas abandonner pour l'instant le scenario 1 dont nous avons étudié certains aspects dans les chapitres 1 et 2.

Il est évident que la question des mécanismes du transfert d'eau est absolument centrale. Une modélisation erronée de ceux-ci conduirait fatalement à des simulations erronées de la perte de performance (dégradation).

Comparé au travail de Straubhaar, notre contribution majeure a été de proposer un modèle couplé DM-MPL-CC ou encore réseau de pores (DM)-continu (autres composants). Dans le modèle proposé dans Straubhaar (2015), la réaction électrochimique n'est pas modélisée explicitement. La densité de courant et la tension sont considérées comme des données d'entrée. Grâce à notre modèle couplé, nous pouvons calculer la distribution de la densité de courant au sein du domaine de calcul (comme d'autres grandeurs telles que la concentration en oxygène). Ceci a permis d'obtenir les très intéressants résultats, du moins nous semble-t-il, du chapitre 6 sur le phénomène d'inversion de courant (le lieu du maximum en densité de

courant sous la dent devient le lieu d'un minimum en densité de courant) lorsque la densité de courant moyenne augmente. Dans le contexte des deux scenarios, il s'agit d'un élément de plus en faveur du scenario de condensation. Ceci permet aussi de proposer une interprétation cohérente aux résultats expérimentaux obtenus dans la thèse de Rachidi (2011).
L'importance de bien identifier le scenario le plus correct a été aussi indirectement illustré par les résultats du chapitre 7 sur l'impact de la mouillabilité sur la distribution de l'eau liquide se formant par condensation. Alors, que l'impact de la variation de la mouillabilité sur l'accès de l'oxygène à la CC est spectaculaire dans le cas du scenario #1, e.g. Pulloor Kuttanikkad et al. (2011), l'effet est beaucoup plus faible dans le cadre du scenario de condensation. C'est une conséquence du fait que la distribution de l'eau liquide résulte d'un équilibre entre évaporation et condensation. C'est cet équilibre qui impose la forme de la distribution indépendamment de la mouillabilité. Il faut cependant distinguer la gamme des humidités relatives proches de la valeur critique (valeur de l'humidité relative en dessous de laquelle toute l'eau peut transférer en phase vapeur sans qu'il y ait condensation au sein du support de GDL) où l'impact peut être marqué.
De même l'interprétation du rôle de la MPL vis-à-vis du transfert d'eau est fort différent suivant le scenario. Dans le cas du scenario 1, la MPL a un rôle de filtre réduisant le nombre de points d'injection liquide au sein du support (ce qui améliore l'accès des gaz). Ceci a été étudié en détail au chapitre 2. Dans le cas du scenario de condensation (scenario 2), l'impact bénéfique de la MPL est dû à son rôle de barrière capillaire. Elle bloque l'avancée de l'eau liquide se formant par condensation dans le support vers la couche catalytique.

Le scenario le plus probable (du moins, comme indiqué plus haut, aux températures proches de 80°C) étant très clairement le scenario de condensation, nous nous trouvons dans une situation considérablement clarifiée pour évoquer la principale perspective à ce travail. Celle-ci concerne essentiellement l'exploitation du modèle présenté au chapitre 3 vis-à-vis de la perte en performance (dégradation). Il est intéressant de rappeler à ce propos que le scenario de condensation est intimement lié à l'existence de variations de température au sein du support de GDL, c'est-à-dire aux transferts thermiques. Par ailleurs, des corrélations ont été établies entre hétérogénéités de température et dégradations, e.g. Nandjou (2015). C'est donc bien le triptyque couplé transfert d'eau – transfert de chaleur – phénomènes de dégradations qui doit être pris en compte pour prédire la perte de performance.
Les autres perspectives évidentes concernent d'une part l'amélioration du modèle et d'autre part son extension à un assemblage complet anode-cathode, les transferts d'eau étant dépendant aussi des conditions à l'anode. Pour ce qui concerne l'amélioration du modèle, une perspective immédiate serait d'abandonner le modèle par compartiment dans la couche active et de le remplacer par un modèle continu classique.

**Références**

R.Alink and D.Gerteisen, Modeling the liquid water transport in the gas diffusion layer for polymer electrolyte membrane fuel cells using a water path network, Energy 6 (2013) 4508-4530.
S.Basu, C.Y.Wang and K.S.Chen, Phase Change in a Polymer Electrolyte Fuel Cell, Journal of The Electrochemical Society 156 (6) (2009) B748-B756.

D.A.Caulk and D.R. Baker, Heat and water transport in hydrophobic diffusion media of PEM fuel cells, Journal of The Electrochemical Society 157 (8) (2010) B1237-B1244.

D.A.Caulk and D.R. Baker, Modeling two-phase water transport in hydrophobic diffusion media for PEM fuel cells, Journal of The Electrochemical Society 158 (4) (2011) B384-B393.

J.H. Nam and M. Kaviany, Effective diffusivity and water-saturation distribution in single- and two layer PEMFC diffusion medium, Int. J. of Heat and Mass Transfer, 46 (2003) 4595-4611.

F.Nandjou, Local study of temperature distribution in P.E.M fuel cells for automotive applications. Correlation between local temperature and degradations, Ph.D thesis, Grenoble Alpes University, (2015).

J.P. Owejan, J.E. Owejan, W. Gu, T.A. Trabold, T.W. Tighe and M.F. Mathias, Water transport mechanisms in PEMFC gas diffusion layers, Journal of The Electrochemical Society 157 (2010) B1456–B1464.

S. Pulloor Kuttanikkad, M. Prat, J. Pauchet, Pore-network simulations of two-phase flow in a thin porous layer of mixed wettability: Application to water transport in gas diffusion layers of proton exchange membrane fuel cells, *J. of Power Sources* 196, pp. 1145–1155 (2011)

S.Rachidi, Développement et exploitation d'une micro-instrumentation pour les piles à combustible de type PEMFC, Thèse Université de Poitiers (2011).

B.Straubhaar, Pore network modelling of condensation in gas diffusion layers of PEMFC, Ph.D thesis, Toulouse University (2015)

A.Thomas, G.Maranzana, S. Didierjean, J. Dillet and O. Lottin, Thermal Effect on Water Transport in Proton ExchangeMembrane Fuel Cell, Fuel Cells 12 (2) (2012) 212–224.

A.Thomas, G. Maranzana, S. Didierjean, J. Dillet and O. Lottin, Measurements of electrode temperatures, heat and water fluxes in PEMFCs: conclusions about transfer mechanisms, Journal of The Electrochemical Society 160 (2) (2013) F191-F204.

A.Thomas, G. Maranzana, S. Didierjean, J. Dillet and O. Lottin, Thermal and water transfer in PEMFCs: Investigating the role of the microporous layer, International Journal of Hydrogen Energy 39(6) (2014) 2649–2658.